Turbulent mixing in temporally evolving stratified channel flow, an investigation through direct numerical simulations

VASSILI ISSAEV

B.Eng (Hons)

THE UNIVERSITY OF SYDNEY

Supervisor: Nicholas Williamson
Associate Supervisor: Steven Armfield

A thesis submitted in fulfilment of
the requirements for the degree of
Doctor of Philosophy

School of Aerospace, Mechanical and Mechatronic Engineering
Faculty of Engineering and Information Technology
The University of Sydney
Australia

21 December 2022

This page is intentionally left blank.

Declaration

I hereby declare that all the work presented within this thesis is solely my own. At time of writing, to the best of my knowledge, the work presented is original unless otherwise indicated by reference to other studies. No part of this thesis has been submitted for consideration of any other degree.

Vassili Issaev

21st of December 2022

This page is intentionally left blank.

Acknowledgements

I would like to express profound thanks and gratitude to my supervisors Dr. Nicholas Williamson and Prof. Steven Armfield for their patience, knowledge, insight and guidance throughout my PhD candidature. Without their help and support I would never have dreamed of completing a task as daunting as PhD thesis. In particular I cannot begin to express my thanks for the generosity of Nick with his time and patience during both the COVID pandemic and his first years of fatherhood. Our weekly discussions were not only crucial to the completion of the thesis but have left with a much deeper interest and appreciation of fluid mechanics as a whole. I would like to further express thanks to the other member of the FLuD research group: Michael, Vanja, Kris, Layth, Kai-Chun, Cindy and many more for their help and insight throughout my time as a PhD student.

I would like to deeply thank Dr. Stuart Norris for allowing me to use his numerical solver as the main tool through which to conduct my research. and His prompt and detailed support in any technical issues I have faced with SnS throughout my time as PhD student have been invaluable to the outcome of my research.

I am eternally grateful to my parents Vlad and Galina who have provided me with love and care throughout not only my PhD candidature but my entire life. Throughout my life they have always endeavored to foster a sense of inquisitiveness and curiosity in me which I believe has been crucial in the success of my research presented within this thesis.

Finally and most importantly I would like to thank my partner Hikaru for her endless love and support that she has provided me throughout this entire process. She has had to deal with the emotional roller coaster of living with a PhD student with weeks of frustration and misery as well as the occasional moment of triumph. She has always believed in me throughout this entire time and has continued to push me to pursue excellence in both my research and all other aspects my life. I love you and could not have done this without you.

Abstract

Turbulent flows affected by stable density stratification occur ubiquitously in wide range of geophysical and environmental flows such as the ocean, the atmosphere or rivers and lakes. Within such flows the process of turbulent mixing plays a leading order role in numerous physical and ecological processes such as the vertical transport of heat, salt and nutrients as well as being vital to accurately predict global energy circulation models. A better understanding of the flow dynamics and the mechanisms that govern turbulent mixing as well as its accurate prediction in stratified flows is therefore crucial to accurately resolve such processes. If stratified flow is constrained by physical boundaries perpendicular to the gravitational vector, then the flow develops into a distinctly vertically inhomogeneous state that adds an additional layer of complexity into the mixing dynamics of the flow. Motivated by the stratified river flows of Australia, this thesis aims to enhance our knowledge and understanding of turbulent mixing in vertically inhomogeneous stratified flows through an extensive set of direct numerical simulations (DNS) of stratified channel flow.

By performing a canonical 'sunrise' DNS of initially isothermal turbulent channel flow subject to sudden radiative heating we demonstrate that the flow undergoes an initial 'rapid' suppression of turbulence due the reduction of the fluctuating vertical velocity component w' from the sudden introduction of stable stratification. The flow 'slowly' recovers towards a stationary state as the flow accelerates and the mean shear develops such that equilibrium is achieved in the turbulent kinetic energy and momentum flux balances. We demonstrate that for the temporally evolving flow, the global suppression of turbulent mixing defined by bulk measures of the eddy diffusivity and viscosity is well predicted by the mixed bulk parameter $Ri_\tau^{-1}Re_\tau$, where Ri_τ and Re_τ are the friction Richardson and Reynolds numbers respectively such that mixing within the flow becomes strongly suppressed for $Ri_\tau^{-1}Re_\tau \lesssim 10$ and approaches neutral conditions for $Ri_\tau^{-1}Re_\tau \gtrsim 100$. We find that the convergence of the flow towards stationarity is a globally parabolic process such that the flow at all

depths simultaneously obtains equilibrium in the buoyancy and momentum fluxes. Scaling arguments are presented to demonstrate that this process may be parameterized through bulk flow properties such that the flow achieves equilibrium at $Ri_\tau^{-1/2}(t/T_\tau) \approx 2$ provided that $Ri_\tau^{-1}Re_\tau \lesssim 100$, where t is the measured time from its initial isothermal state and T_τ is the bulk friction time scale. We propose that the bulk scaling presented could lend itself as a useful forecasting tool for the onset of suppressed mixing in real stratified river flows.

By considering instantaneous horizontal planar averages of the temporally evolving flow we observe three distinctly different mixing regimes separated by transitional values of turbulent Froude number Fr: a weakly stratified regime for $Fr > 1$, an intermediate regime for $0.3 < Fr < 1$ and a saturated regime for $Fr < 0.3$. The mixing coefficient Γ is well predicted by the parametrization schemes of Maffioli *et al.* (2016) and Garanaik & Venayagamoorthy (2019) across all three regimes through instantaneous measurements of Fr and the ratio L_E/L_O, where L_E and L_O are the Ellison and Ozmidov length scales respectively. The flux Richardon number R_f shows linear dependence on the gradient Richardson number Ri_g up to a transitional value of $Ri_g = 0.25$ past which it saturates again to a constant value independent of Fr or Ri_g. By examining the flow as a balance of inertial, shear and buoyancy forces, we derive physically based scaling relationships to demonstrate that $Ri_g \sim Fr^{-2}$ and $Ri_g \sim Fr^{-1}$ in the weakly and moderately stratified regimes and that Ri_g becomes independent of Fr in the saturated regime. Our scaling analysis and results suggest that an extended range of the $L_E/L_O \sim Fr^{-1}$ scaling of Garanaik & Venayagamoorthy (2019) in the intermediate regime manifests due to the influence of mean shear. Hence we directly reconcile the Fr, Ri_g and L_E/L_O frameworks across all three mixing regimes for our shear driven flow.

By adapting the density inversion criterion method of Portwood *et al.* (2016) for our flow, we demonstrate that the flow may be robustly separated into regions of active turbulence for which $Re_B \gtrsim \mathcal{O}(10)$ and quiescent fluid where $Re_B \lesssim \mathcal{O}(10)$, where Re_B is the buoyancy Reynolds number. The intermittency in the surface heated channel flow spontaneously manifests as a deformed horizontal interface between the upper quiescent and lower turbulent flow. We find the region just below the interface is characterized by vigorous and efficient energetic mixing from Kelvin-Helmholtz type overturning instabilities, with the thickness

of the interfacial layer being proportional to the Ellison length L_E. The resulting vertical intermittency profile quantified through a depth varying turbulent volume fraction is accurately predicted by a local Monin-Obukhov length normalized in viscous wall units Λ^+ such that the flow begins to display intermittency within the parameter range of $2.5 \lesssim \Lambda^+ \lesssim 260$. We find the 'turbulent' flow within this region to be described by constant critical gradient Richardson and turbulent Froude numbers of $Ri_{g,c} \approx 0.2$, $Fr_c \approx 0.3$ and $\Gamma_c \approx 0.25$, suggesting that for our flow, critical mixing conditions arise from the intermittency resulting from stratification. By considering conditional averages of both the 'turbulent' and 'quiescent' flow separately within this critical regime, we find that the 'turbulent' flow continues to display a $\Gamma \sim Fr^{-1}$ relationship in the limit of $Fr < Fr_c$, while the quiescent flow shows no correlation between Γ and Fr. We demonstrate that for stratified open channel flow, the emergence of an asymptotic 'saturated' Γ regime in the limit of a low 'global' Fr occurs directly due to intermittency and increasing contributions to measurements of Γ from the quiescent flow.

This page is intentionally left blank.

Authorship attribution statement

Chapter §3 is based on the following planned publication:

Issaev, Vassili, Williamson, N. & Armfield, S. W. Transient response and transition to equilibrium of turbulent open channel flow subject to stratification through radiative heating. Planned for submission to *Journal of Fluid Mechanics* in 2022.

Chapter §4 is based on the following publication:

Issaev, Vassili, Williamson, N., Armfield, S. W. & Norris, S. E. 2022. Parameterization of mixing in stratified open channel flow. *Journal of Fluid Mechanics* 935, publisher: Cambridge University Press.

Chapter §4 is based on the following publication:

Issaev, Vassili, Williamson, N. & Armfield, S. W. 2022. Intermittency and critical mixing in stratified channel flow. *Journal of Fluid Mechanics* (submitted).

As first author in all these publications, I was responsible for the both the setup and running of the simulations. I was responsible for the post-process of the resulting raw data and the analysis of the processed results. The initial drafts and subsequent revisions of all publications were written by me and represent original research that I have conducted. The publications are not subject to any contractual agreements with third parties that would restrict their usage within this thesis.

Student: Vassili Issaev

Signature.....Date.....

Supervisor: Dr Nicholas Williamson

Signature.....Date.....

This page is intentionally left blank.

Contents

This page is intentionally left blank.

CHAPTER 1

Introduction

1.1 Stably stratified turbulent flows, context and significance

Turbulent flows being characterized by highly disordered vortical motions are ubiquitous across a large variety of naturally occurring flows. In particular, in the context of geophysical turbulent flows such as the ocean, atmosphere, rivers or lakes, such flows are often affected by stable density stratification. That being, that the density of the fluid increases in the direction of the gravitational force. Stable stratification occurs in geophysical flows due to temperature differences as the hotter fluid expands and becomes less dense, usually driven by solar radiative heating (or the absence of, in the case of the nocturnal atmosphere), or due to variable active scalar concentration (salinity in aqueous flows, moisture in the atmosphere). In stably stratified flows, when a dense parcel of fluid is advected upwards by turbulent motions into a relatively less dense background fluid, gravitational buoyancy acts to exert a restoring force. This inhibits vertical fluid displacements and under sufficient strength of stratification may act to 'modify' the turbulence structure into a anisotropic state (Riley & Lelong, 2000; Billant & Chomaz, 2001).

In turbulent flows 'mixing' occurs as turbulent eddying motions act to stir the fluid, dispersing fluid particles and irreversibly homogenizing (mixing) the scalar fields within the flow. Understanding the dynamics and mechanism by which turbulent mixing occurs within stratified flows as well as its accurate estimation is crucial to numerous geophysical applications such as: global ocean circulation models, atmospheric climate and pollutant dispersion models, global energy budget calculation, nutrient transport in rivers, estuaries and lakes (Gregg, 1987; Fernando, 1991; Turner & Erskine, 2005). As an example, in the ocean, turbulent mixing

defined through a measured 'eddy diffusivity' (to be defined in more detail in §1.3), may vary by orders of magnitude (Ivey *et al.*, 2018). As many of the mechanisms underlying turbulent mixing in stratified flows remain poorly understood, this creates a significant amount of uncertainty and often error in current mixing models (Gregg *et al.*, 2018).

A particular motivation behind this study are the regulated river flows of Australia. Turbulent mixing in such flows is the primary mechanisms responsible for the vertical transport of key nutrients absorbed at the water-air interface critical for the ecological health of the system such as carbon dioxide or dissolved oxygen. In summer and during periods of low rain, Australian rivers and estuaries may become persistently strongly stratified such that there is a significant reduction of turbulent mixing in the upper layer of the flow. It has been shown that this reduced mixing and subsequent non-uniform distribution of the aforementioned nutrients has been shown to facilitate severely harmful ecological events Turner & Erskine (2005). Reduction in flow rates and turbulent mixing has been linked to harmful cyanobacterial blooms such as that in 2016 which forced the closure of a 1600 km long stretch of the Murray river (Brooks *et al.*, 2016). Long periods of strong strong stratification and reduced mixing, followed by rapid extreme mixing events have been proposed as a primary cause for the low levels of dissolved oxygen resulting in the mass fish kills seen in the Darling river in 2019 (Vertessy *et al.* (2019)). The financial cost of such ecological damage can be severe. As such, a better understanding of the mechanisms by which turbulent mixing and its suppression manifests in stratified river flows is a key aim of this thesis.

1.2 Fundamental background theory

1.2.1 Governing equations of motion

Geophysical flows are characterized by their enormous scale, however turbulent mixing is inherently a dissipative process that occurs at the smallest scales of turbulence (Caulfield & Peltier, 2000; Peltier & Caulfield, 2003). As such, direct numerical simulations (DNS) as employed in this dissertation, which resolves the smallest scales of motion computationally,

lends itself as a logical method by which to investigate mixing within stratified flows at a fundamental level. DNS modelling of stratified flow requires defining an appropriate set of governing equations which are then discretized and solved numerically. For the purpose of this thesis we will assume the scale of the flows in question is sufficiently modest such that the effect of the earths rotation may be seen as negligible relative to buoyancy and may be neglected. The governing equations of motion for an incompressible fluid with constant fluid properties defining the conservation of momentum and mass, i.e. the Navier-Stokes equations under the Oberbeck-Boussinesq assumptions read as

$$\frac{\partial \boldsymbol{u}}{\partial t} + (\boldsymbol{u}\cdot\boldsymbol{\nabla})\boldsymbol{u} = -\frac{\nabla p^*}{\rho_0} + \nu\nabla^2\boldsymbol{u} - \frac{\rho'}{\rho_0}g\boldsymbol{e}_z, \tag{1.1}$$

$$\boldsymbol{\nabla}\cdot\boldsymbol{u} = 0, \tag{1.2}$$

where ρ' is the density pertubation of the fluid, ρ_0 is the mean or background density, $\boldsymbol{u}$ is the flow velocity, $p^* = p + \rho_0 g\boldsymbol{e}_z$ the combined pressure term which incorporates the hydrostatic pressure portion of the gravitational term, t is the time, ν is the kinematic viscosity and g is the gravitational acceleration. In this thesis we define that in the Eulerian reference frame gravity acts in $-\delta_{i3}$ or $-z$ direction. Note that the derivation of (1.1-1.2) stems from the primary Oberbeck-Boussinesq assumption that for most geophysical flows, the density perturbations are small relative to the background density (i.e. $\rho' \ll \rho_0$) and can be neglected in in the equations of motion with the exception of the gravitational term.

For closure of the governing equations it is clear that an additional scalar transport equation is required to determine ρ'. We now take the critical assumption that variations in density due to concentration(i.e. salinity) are negligible such that they occur solely due to variations in temperature θ . Hence we assume a linear transform from fluid temperature to density perturbation is given by the equation of state

$$\rho' = \rho_0(1 - \beta\theta'), \tag{1.3}$$

where β is the constant of thermal expansion. Assuming that θ' is a conserved scalar that satisfies an advection-diffusion transport equation we can write a similar transport equation

for ρ' of the form

$$\frac{\partial \rho'}{\partial t} + (\boldsymbol{u}\cdot\boldsymbol{\nabla})\rho' = \kappa\nabla^2\rho', \tag{1.4}$$

where κ is the molecular diffusivity of heat. Finally for consistency with past work of stratified flow we define $b = -\rho' g/\rho_0$ as the 'buoyancy' or reduced gravity variable to arrive at the set of governing equations that fully define stratified flow:

$$\frac{\partial \boldsymbol{u}}{\partial t} + (\boldsymbol{u}\cdot\boldsymbol{\nabla})\boldsymbol{u} = -\frac{\nabla p^*}{\rho_0} + \nu\nabla^2\boldsymbol{u} + b\boldsymbol{e}_z, \tag{1.5}$$

$$\frac{\partial b}{\partial t} + (\boldsymbol{u}\cdot\boldsymbol{\nabla})b = \kappa\nabla^2 b, \tag{1.6}$$

$$\boldsymbol{\nabla}\cdot\boldsymbol{u} = 0. \tag{1.7}$$

Note that these equations are generic and describe all stratified flow under the assumptions outlined above and do not include forcing terms or boundary fluxes which may vary with individual flow configuration, provided the boundary conditions and initial mean profiles of $\overline{\boldsymbol{u}}$ and $\overline{b}$ similarly satisfy the Oberbeck-Boussinesq assumptions. We will cover our adaption of (1.5-1.7) and their numerical discretization in more detail in §2.

1.2.2 Turbulent mixing and energetics

As discussed in §1.1 mixing in stratified flows is fundamentally linked to energetics and the conversion of turbulent kinetic energy (TKE) into potential energy (PE) through mixing as denser fluid is advected upwards through turbulent motions.

We note the flow velocity $\boldsymbol{u}$ and buoyancy b may be decomposed into their mean and fluctuating components such that

$$\boldsymbol{u} = \overline{\boldsymbol{u}} + \boldsymbol{u}', \qquad b = \overline{b} + b', \tag{1.8a, b}$$

where the overbar denotes some appropriate ensemble average that is flow specific. Hence we can define the 'turbulent' component of the kinetic energy as

$$E_K = \frac{1}{2}(\overline{u_i' u_i'}). \tag{1.9}$$

By substituting (1.8) into the momentum equation (1.5) and multiplying through by $\boldsymbol{u'}/2$ it is possible to derive an evolution equation for E_K (Pope, 2000). Under the assumption of homogeneity in the horizontal plane, it reads

$$\frac{\partial E_K}{\partial t} = P - \epsilon_K - B + D_\nu + T_K + \Pi, \tag{1.10}$$

where terms on the RHS going from left to right are: the production term, the turbulent buoyancy flux, the dissipation rate of turbulent kinetic energy, the viscous transport term, the turbulent convection term and the pressure transport term, where

$$\begin{aligned} &P = -\overline{u_i' w'}\tfrac{\partial \overline{u_i}}{\partial z}, \quad \epsilon_K = 2\nu\overline{s_{ij}' s_{ij}'}, \quad B = \overline{-b'w'} \\ &D_\nu = \nu\left(\tfrac{\partial^2 E_K}{\partial z^2}\right), \quad T_K = -\tfrac{\partial}{\partial z}(\overline{w' E_K}). \quad \Pi = -\tfrac{\partial}{\partial z}(\overline{w'p'}), \end{aligned} \tag{1.11a-f}$$

where $s_{ij}' = 1/2(\partial u_i'/\partial x_j + (\partial u_j'/\partial x_i)$ is the pertubation deformation tensor. Here the most significant difference to incompressible flow in the absence of buoyancy, is the inclusion of the buoyancy flux B. Under the assumption that in turbulent stratified flows that the turbulent buoyancy flux acts downwards (upwelling of dense fluid) such that $B \geq 0$, B therefore acts as a kinetic energy sink or 'toll' the flow has to pay that transfers TKE into PE. Accordingly in literature B is often interpreted as the mixing rate within stratified flows (Osborn, 1980; Ivey & Imberger, 1991; Shih *et al.*, 2005). We note that B is not always strictly positive definite. If the flow approaches very stable conditions, B may act as a reversible conduit of energy from PE back to TKE, we will discuss this in more detail shortly.

Analogously by substituting (1.8) into the transport equation for b (1.6) and multiplying through by $b'/2N^2$, we can obtain an evolution equation for the buoyancy variance $\overline{b'^2}/2$. Where $N = (\partial\overline{b}/\partial z)^{1/2}$ is square root of the background stratification known as the buoyancy frequency. Under similar assumptions of homogeneity in the horizontal plane, the equation reads

$$\frac{1}{N^2}\frac{\partial(\overline{b'^2}/2)}{\partial t} = B - \chi + D_\kappa + T_b, \tag{1.12}$$

where the terms on the RHS going left to right are: the production term which is exactly the buoyancy flux B, the rate of buoyancy variance destruction, diffusive transport term, turbulent

convection term defined as:

$$\chi = \frac{\kappa}{N^2}\overline{\left(\frac{\partial b'}{\partial x_j}\right)^2}, \qquad D_\kappa = \frac{\kappa}{N^2}\left(\frac{\partial^2 \overline{b'^2}}{\partial z^2}\right), \qquad T_b = -\frac{1}{2N^2}\frac{\partial}{\partial z}(\overline{w'b'^2}). \qquad (1.13a, b, c)$$

It is clear that B features in both (1.10) and (1.12) as a kinetic energy sink and as the source of buoyancy variance respectively. Note in both (1.10) and (1.12) we have omitted the mean convection term as the term becomes identically zero under the assumption of homogeneity in the horizontal plane.

As outlined in the seminal work of Osborn & Cox (1972), a further key insight is that if the flow is sufficiently far from physical boundaries such that it may be considered quasi-homogeneous as in the ocean interior, the transport terms D_ν, T_K, Π in (1.10) and D_κ, T_b in (1.12) may be neglected such that the steady-state evolution equations read

$$P \approx B + \epsilon_K, \qquad (1.14)$$

$$B \approx \chi. \qquad (1.15)$$

If the flow satisfies these conditions, it is said to be in a state of 'local equilibrium'. However, under very stable conditions, instantaneous 'counter-gradient' measurements of $B < 0$ may be observed, as propagating internal waves and convective instabilities act to transfer PE back into TKE (Taylor *et al.*, 2005; Venayagamoorthy & Koseff, 2016; Howland *et al.*, 2020). Osborn & Cox (1972) argue that provided the conditions of (1.14-1.15) are satisfied, then χ which is inherently a small scale and positive definite quantity, is a more sensible measure of irreversible mixing than B.

If an additional condition is met that the background stratification N^2 is invariant in space and time then χ estimates the irreversible conversion of available potential energy (APE) into background potential energy (BPE), this being a primary quantity of interest in global energetics models (Caulfield, 2020). Here APE is the portion of the total potential energy that may be converted back into kinetic energy. While BPE is the minimum potential energy of the flow after an adiabatic resorting of the buoyancy field and is not available to the flow (Lorenz, 1955). In a key study, using the APE framework, Winters *et al.* (1995) develop an analytical expression for the irreversible diapycnal density flux. Caulfield & Peltier (2000)

and Peltier & Caulfield (2003) extend this concept to demonstrate that for closed systems, the framework may be employed to derive a global instantaneous irreversible mixing rate $\mathcal{M}^*$. The use of this framework has been particularly prevalent in DNS studies of singular shear instability mixing events to better understand the transient dynamics and accurately quantity irreversible turbulent mixing across the entire mixing cycle (Basak & Sarkar, 2006; Mashayek *et al.*, 2013; Salehipour & Peltier, 2015; Salehipour *et al.*, 2015; Mashayek *et al.*, 2017; VanDine *et al.*, 2021). Expanding on this, Scotti & White (2014) present a theoretical formulation for the calculation of 'local' APE in stratified flows. Recent DNS studies of Zhou *et al.* (2017*b*) of stratified plane Couette flow and Smith *et al.* (2021) of forced free shear flow have adapted this theory to show that local irreversible mixing for vertically inhomogeneous flows can defined in this framework. However in both cases the limitation being that the flow must be symmetrical about a central shear interface where the local irreversible mixing is appropriately defined.

In inhomogeneous flows, the χ and the APE framework are not always appropriate. In vertically inhomogeneous flows where the presence of physical boundaries cannot be neglected such as rivers or lakes, or temporally evolving flows in which flow properties rapidly change with time the local equilibrium assumptions in $(1.14 - 1.15)$ no longer hold true. This effectively invalidates the use of χ as a measure of mixing or energy conversion between TKE and PE. Meanwhile the APE framework requires full knowledge of the flow field such that adiabatic resorting of the density field is possible, knowledge only available in DNS.

For a wide range of flows, particularly if they are spatio-temporally inhomogeneous, B remains the primary method of defining the local mixing rate.

1.2.3 Eddy diffusivity and mixing efficiency

Despite the complexity of turbulent mixing in stratified flows, in geophysical applications it is most commonly modelled through a one-dimensional simple flux-gradient eddy diffusivity K_ρ. From an applications perspective, K_ρ remains the primary quantity of interest and its accurate estimation remains the primary and most controversial objective of stratified mixing research

to date (Ivey *et al.*, 2018). K_ρ can be readily derived by taking the Reynolds decomposition of b in (1.8) to arrive at an evolution equation for the mean buoyancy $\overline{b}$ which reads

$$\frac{\partial \overline{b}}{\partial t} = \frac{\partial(\overline{-b'w'})}{\partial z} + \kappa \frac{\partial^2 \overline{b}}{\partial z^2} = \frac{\partial}{\partial z}\left(\overline{-b'w'} + \kappa \frac{\partial \overline{b}}{\partial z}\right). \tag{1.16}$$

Recalling that $\overline{-b'w'} = B$ and $\partial \overline{b}/\partial z = N^2$, we can rewrite this as

$$\frac{\partial \overline{b}}{\partial t} = \frac{\partial}{\partial z}\left((\kappa + K_\rho)N^2\right), \tag{1.17}$$

where

$$K_\rho = \frac{B}{N^2}. \tag{1.18}$$

It is clear that again the mixing defined through B (assuming that $B > 0$) acts to enhance the diapycnal diffusion of heat transfer. In most turbulent geophysical flows it is assumed that molecular diffusion of heat is negligible to that of turbulent mixing such that $K_\rho \gg \kappa$.

In his key study, Osborn (1980) presents a simple model for K_ρ which remains widely used to this day, which reads

$$K_\rho = \frac{B}{N^2} = \frac{\epsilon_K}{\epsilon_K}\frac{B}{N^2} = \Gamma \frac{\epsilon_K}{N^2}, \tag{1.19}$$

where $\Gamma = B/\epsilon_K$ is the flux coefficient. From the perspective of field data interpretation, as ϵ_K and N^2 can be inferred from field measurements far more easily than B, quantifying K_ρ comes down to the estimation of Γ. Due to the ubiquitous measurements in the ocean and laboratory experiments with upper limit of $\Gamma \leq 0.2$, Osborn (1980) argued for the use of a constant value of $\Gamma = 0.2$ for oceanic modelling. He argued based on the assumption of local equilibrium of TKE for steady-state flow (i.e. $P \approx B + \epsilon_K$), the ratio of the kinetic energy lost due to the buoyancy 'toll', to that being produced must have an upper limit to sustain turbulence. This being defined as the flux Richardson number $Ri_f = B/P$, where Ri_f is commonly referred to as the 'mixing efficiency'. Hence he shows that

$$Ri_f = \frac{B}{P} \approx \frac{B}{B + \epsilon_K} = \frac{1}{1 + \Gamma}, \tag{1.20}$$

and argues that an upper limit for Ri_f implies an upper limit for Γ. Expanding on this work, by omitting the assumption of local equilibrium assumption or stationarity Ivey & Imberger

(1991) define an instantaneous flux Richardson number R_f

$$R_f = \frac{B}{B + \epsilon_K}, \tag{1.21}$$

such that the equality the relationship between R_f and Γ in (1.20) does not rely on assumptions of energetic equilibrium. They interpret it as the instantaneous mixing efficiency defining the ratio of TKE lost to buoyancy to the total loss of TKE in the flow and similarly argue that an upper limit pertains to R_f for sustained turbulence.

Citing the assumption of local equilibrium such that $B \approx \chi$, Osborn & Cox (1972) argue for similar reasons outlined in §1.2.2 that is more logical to infer the eddy diffusivity through χ such that

$$K_\rho \approx \frac{\chi}{N^2}. \tag{1.22}$$

A key recent study by Taylor *et al.* (2019) of high resolution DNS of stratified turbulence simulates the 'vertical sampling' typically done in microstructure profiling of the ocean. They confirmed that inferring K_ρ directly through χ rather than B required appreciably less samples to acquire an accurate estimate of K_ρ. However accurate direct measurements of χ require the resolution of the smallest diffusive scales of turbulence, which presents a significant challenge in the field and the technology to achieve this has been only recently developed (Moum & Nash, 2009; Waterhouse *et al.*, 2014). Following the logic of Osborn & Cox (1972) it follows that K_ρ may be similarly parameterized as in (1.19) such that

$$K_\rho \approx \frac{\chi}{N^2} = \Gamma_\chi \frac{\epsilon_K}{N^2}, \tag{1.23}$$

where $\Gamma_\chi = \chi/\epsilon_K$, analogous to its counterpart defined through B. Note that similarly a mixing efficiency η can be defined

$$\eta = \frac{\chi}{\chi + \epsilon_K}, \tag{1.24}$$

which can be analogously linked to Γ_χ as in (1.20). A large amount of recent studies regarding the estimation of mixing within stratified flows where the local equilibrium assumption is valid have investigated mixing through the in (1.23) (Venayagamoorthy & Stretch, 2010;

de Bruyn Kops, 2015; Maffioli *et al.*, 2016; Venayagamoorthy & Koseff, 2016; Garanaik & Venayagamoorthy, 2018; Howland *et al.*, 2020, 2021).

Similarly, through the APE framework Caulfield & Peltier (2000) define an irreversible mixing efficiency

$$\eta^* = \frac{\mathcal{M}^*}{\mathcal{M}^* + \epsilon_K}. \tag{1.25}$$

Salehipour & Peltier (2015) further demonstrate that within this framework an irreversible diapycnal diffusivity K_ρ^* can be analogously defined and parameterized of the form

$$K_\rho^* = \frac{\mathcal{M}^*}{N_*^2} = \Gamma_{\mathcal{M}} \frac{\epsilon_K}{N_*^2}, \tag{1.26}$$

where N_*^2 is the adiabatically sorted mean stratification profile and $\Gamma_{\mathcal{M}} = \mathcal{M}^*/\epsilon_K$.

However since the work of Osborn (1980), a large amount of observational, experimental and numerical studies have demonstrated that all definitions of the flux coefficient are not constant and may significantly vary across a wide range of parameters, often significantly exceeding the proposed 'Osborn' upper limit of $\Gamma = 0.2$ (Shih *et al.*, 2005; Ivey *et al.*, 2008; García-Villalba & del Álamo, 2011; Chung & Matheou, 2012; Maffioli *et al.*, 2016; Ijichi & Hibiya, 2018; Garanaik & Venayagamoorthy, 2019; Howland *et al.*, 2020; Issaev *et al.*, 2022). As outlined above, obtaining direct and accurate measurements of B, χ or $\mathcal{M}^*$ outside of laboratory experiments or DNS is highly challenging. Hence the accurate estimation of the eddy diffusivity for practical purpose, reduces down to the need to accurately parameterize an appropriate definition of Γ from readily available quantities.

1.3 Parametrization of Γ

A significant challenge within the study of stratified turbulent mixing is the plethora of varied parametrization schemes for Γ and the subsequent ambiguity in the relationship between the different parameters across varying classes of flows (Gregg *et al.*, 2018).

In an influential paper, Shih *et al.* (2005), present a parametrization of Γ based on the buoyancy Reynolds number Re_B, often also referred to as the activity parameter or Gibson number Gn

(Portwood *et al.*, 2016). Where

$$Re_B = \frac{\epsilon_K}{N^2\nu}. \tag{1.27}$$

Using the results from their DNS data set they empirically propose that for $7 \leq Re_B \leq 100$ Γ is constant (seemingly in agreement with Osborn), $\Gamma \sim Re_B^{1/2}$ for $Re_B \geq 100$ and for $Re_B \leq 7$, the flow approaches quasi-laminar conditions such that turbulent mixing becomes of the same order as molecular diffusion. Since their study the use of Re_B has been prevalent in global models and is particularly appealing as it goes hand in hand with the Osborn model for K_ρ such that

$$\frac{K_\rho}{\kappa} = \Gamma\frac{\epsilon_K}{N^2\kappa} = \Gamma\frac{\nu}{\nu}\frac{\epsilon_K}{N^2\kappa} = \Gamma PrRe_B, \tag{1.28}$$

where $Pr = \nu/\kappa$ is the molecular Prandtl number which is assumed to be constant. The model suggests that the diapycnal diffusivity may be fully parametrized by the singular and relatively easy to measure parameter Re_B. However, since then numerous studies have demonstrated that the transition away from a constant Γ regime does not display universal dependence on a singular value of Re_B with reported transitional values varying between $\mathcal{O}(10^1) \leq Re_B \leq \mathcal{O}(10^4)$ (Lozovatsky & Fernando, 2013; Scotti & White, 2016; Issaev *et al.*, 2022). In particular, a key recent DNS study of high resolution homogeneous sheared stratified flow by Portwood *et al.* (2019) demonstrated that provided the flow maintains sufficient dynamic range, Γ displays no dependence on Re_B within their full parameter range presented of $36 \leq Re_B \leq 900$.

To explain this we note that Re_B can be expressed as a ratio of length scales such that

$$Re_B = \left(\frac{L_O}{L_K}\right)^{4/3}, \tag{1.29}$$

where L_O is the Ozmidov length describing the maximum conceptual size of an isotropic eddy that is not confined by stable stratification, while L_K is the well known Kolmogorov microscale describing the smallest scale of turbulence, where

$$L_O = \left(\frac{\epsilon_K}{N^3}\right)^{1/2}, \qquad L_K = \left(\frac{\nu^3}{\epsilon_K}\right)^{1/4}. \tag{1.30a, b}$$

In a key study Maffioli *et al.* (2016) argue that if Γ is primarily determined by the how 'strong' the stratification is within the flow, then Re_B is not an appropriate paramater to define

Γ as it does not define the strength of stratification but rather is a measure of the inertial range of the flow. Billant & Chomaz (2001) show that Re_B may be considered a 'mixed' parameter comprised out of intrinsic flow paramaters such that

$$Re_B = Re_T Fr^2, \tag{1.31}$$

where Re_T is the turbulent Reynolds number, analogous to a classic definition of the Reynolds number $Re = UL/\nu$ (see Billant & Chomaz (2001) for a full derivation) comparing viscous to inertial forces and Fr is the turbulent Froude number defined as

$$Re_T = \frac{E_K^2}{\epsilon_K \nu}, \qquad Fr = \frac{\epsilon_K}{N E_K}. \tag{1.32a, b}$$

Note that Fr can also be interpreted as a ratio of length scales, as shown in Lindborg (2006)

$$Fr = \left(\frac{L_O}{L_I}\right)^{2/3}, \tag{1.33}$$

where L_I is the inertial turbulent length scale that conceptually defines the size of the largest energy containing eddies in isotropic turbulence (Pope, 2000), defined as

$$L_I = \frac{E_K^{3/2}}{\epsilon_K}. \tag{1.34}$$

Accordingly Fr represents a measure of how deformed the large energetic scales are due to stratification, i.e. how strong the stratification is. Maffioli *et al.* (2016) argue that provided Re_T is sufficiently high, then Γ should show a dependence on Fr. They provide physically based scaling arguments to show two limits: For $Fr \gg \mathcal{O}(1)$ dubbed 'weakly stratified' flow they derive $\Gamma \sim Fr^{-2}$, consistent with the arguments of Ivey & Imberger (1991). And for or $Fr \ll \mathcal{O}(1)$ 'strongly stratified' flow they argue that Γ will grow independent of Fr and approach a constant value. In particular their arguments presented for the latter case stem from the underlying theory of Billant & Chomaz (2001) and Lindborg (2006) regarding the distinguished limit of $Re_T \gg \mathcal{O}(1)$ and $Fr \ll \mathcal{O}(1)$ for 'strongly stratified turbulence' expected in the highly energetic atmosphere and ocean. This also being commonly referred to as the 'layered anisotropic stratified turbulence' (LAST) regime (Falder *et al.*, 2016). Numerous studies from varying flow configurations since then have shown strong support for

this parametrization (Garanaik & Venayagamoorthy, 2019; Howland *et al.*, 2020; Smith *et al.*, 2021; Issaev *et al.*, 2022).

Garanaik & Venayagamoorthy (2019) expand upon this work to propose a separate 'moderately stratified' - $Fr = \mathcal{O}(1)$ regime where both buoyancy and inertial forces are significant and derive scaling arguments to propose a novel $\Gamma \sim Fr^{-1}$ relationship within this regime, showing a range of varied data that supports this scaling. However, the underlying arguments of Garanaik & Venayagamoorthy (2019) regarding this 'intermediate' regime remains an area of debate in stratified turbulence literature (Caulfield, 2021; Mashayek *et al.*, 2021).

Maffioli *et al.* (2016) argue that previous observation of correlation between Γ and Re_B in past studies where Re_T is often kept constant, stems from an inherent relationship between Fr and Γ. It should be noted that Re_B is still a relevant parameter in the estimation of Γ. It is a general consensus in stratified flow literature that $Re_B \geq \mathcal{O}(10)$ is a requirement for sustained turbulence Smyth & Moum (2000); Brethouwer *et al.* (2007); Portwood *et al.* (2016) (directly analogous to the finding of a $Re_B \leq 7$ diffusive regime in Shih *et al.* (2005)). Below this the flow is not 'energetic' enough to maintain vigorous or efficient mixing such that Γ drops towards zero. It has been suggested that multi-parameter frameworks may be necessary to fully capture the complex dynamics and accurately parametrize Γ (Mater & Venayagamoorthy, 2014; Salehipour *et al.*, 2016).

For flows in the presence of mean shear, the parametrization of Γ has been frequently explored in literature through the gradient Richardson number Ri_g, where

$$Ri_g = \frac{N^2}{S^2}, \tag{1.35}$$

where $S = \partial\overline{u}/\partial x$ is the mean shear rate. Note that Ri_g can be similarly expressed as a ratio of length scales such that

$$Ri_g = \left(\frac{L_C}{L_O}\right)^{4/3}, \tag{1.36}$$

where

$$L_C = \left(\frac{\epsilon_K}{S^3}\right)^{1/2} \tag{1.37}$$

is the Corssin scale, analogously to L_O representing the upper limit of an isotropic eddy not distorted by the means shear. Hence, Ri_g can be seen as a competition between the turbulence enhancing force of the mean shear and the suppression of turbulent motions from buoyancy.

Throughout numerous studies of varied flow configurations, it has been repeatedly shown that for stationary turbulent shear flows, Ri_g approaches and upper limit ranging between $0.16 \lesssim Ri_g \lesssim 0.25$, under which R_f and hence Γ displays a linear monotonic dependence on Ri_g Armenio & Sarkar (2002); Taylor *et al.* (2005); García-Villalba & del Álamo (2011); Chung & Matheou (2012); Deusebio *et al.* (2015); Karimpour & Venayagamoorthy (2015); Zhou *et al.* (2017*a*); Issaev *et al.* (2022). As outlined in Caulfield (2021), the theory underlying this result stems from the assumption that for steady stratified shear flow, the mean shear dominates flow dynamics such that the stratification is inherently 'weak' such that the mixing of the buoyancy field is lock-in-step with the mixing of momentum resulting in a turbulent Prandtl number Pr_T of unity, where

$$Pr_T = \frac{K_M}{K_\rho}, \tag{1.38}$$

where K_M is the eddy viscosity defined for sheared flow as

$$K_M = \frac{\overline{-u'w'}}{S}. \tag{1.39}$$

Assuming that in sheared flow $P = \overline{-u'w'}S$, we can obtain

$$Pr_T = \frac{K_M}{K_\rho} = \frac{\overline{-u'w'}N^2}{BS} = \frac{PN^2}{BS^2} = \frac{Ri_g}{Ri_f} \approx 1, \tag{1.40}$$

recovering the linear relationship between the mixing efficiency and Ri_g. For large Ri_g, there exists no universal behaviour for Γ. Using DNS data, Venayagamoorthy & Koseff (2016) propose an empirical fit suggesting Γ should remain constant at Ri_g, analogous to the strongly stratified scaling of Maffioli *et al.* (2016). However, it has also been observed that Γ may reduce as Ri_g exceeds some critical value (Shih *et al.*, 2005; Zhou *et al.*, 2017*b*).

Considering the aforementioned observations of an upper limit for a stationary Ri_g, is it still unclear if shear flow can maintain active turbulence at high Ri_g. The issue is further complicated if we consider that Ri_g and Fr may not be independent parameters. For the

weakly stratified limit, Maffioli *et al.* (2016) present scaling arguments leading to $Ri_g \sim Fr^{-2}$. Yet for $Fr \lesssim \mathcal{O}(1)$ the relationship between Fr and Ri_g and therefore how the Fr and Ri_g mixing parametrization frameworks reconcile has not been addressed in current literature. Caulfield (2021) argues that due the relationship between shear and inertial forces, an upper limit on Ri_g implies a lower limit on Fr and therefore stratified shear flow may be unable to access the 'strongly stratified' regime. Similarly it has been shown using scaling analysis and DNS data, that for some flows $Ri_g \sim Re_B^{-1}$ (Riley & deBruynKops, 2003; Hebert & de Bruyn Kops, 2006), such that high Ri_g flow in some instances may be interpreted as low Re_B 'diffusive' flow in which the concept of a 'turbulent' mixing efficiency begins to somewhat lose relevance. This creates a complex and ambiguous parameter space where conceptually $\Gamma = f(Ri_g, Fr, Re_B)$, and where all these parameters may be also interconnected, not to mention molecular fluid properties defined by varied Pr (Caulfield, 2021).

On the basis of past works (Ivey & Imberger, 1991; Smyth & Moum, 2000; Smyth *et al.*, 2001; Mater *et al.*, 2013; Mashayek *et al.*, 2017), Garanaik & Venayagamoorthy (2019) further presents arguments showing that Fr may be inferred through the length scale ratio L_E/L_O, where

$$L_E = \frac{b'_{\text{rms}}}{N^2} \tag{1.41}$$

is the Ellison length describing the extent of vertical fluid displacements and can be interpreted as the characteristic size of overturns in stratified flow (Ellison, 1957). on the basis that L_E has been shown to correlate linearly to the Thorpe length L_T which is relatively easy to measure from one dimensional profiles in the field, Garanaik & Venayagamoorthy (2019) argue that Γ may be inferred through the length scale ratio L_T/L_O, which is significantly easier to measure than Fr. Where L_T similarly describes the vertical extent of overturns and is defined through a one dimensional adiabatic reordering of the density field (see Thorpe (1973)). They present a varied DNS set which shows support for their scaling and parametrization.

A recent study by Mashayek *et al.* (2021), present an alternative parametrization through L_T/L_O (R_{OT} in their study) based on the concepts of time-dependant mixing and self-organized criticality in stratified shear flow (to be discussed in more detail in §1.5). Most

notably, in the limit of high L_T/L_O their parametrization does not predict an asymptotic Γ regime as in Garanaik & Venayagamoorthy (2019), but rather suggests Γ continues to grow large. They present a varied oceanic data-set which shows strong support for their scaling.

It is clear that there is still a considerable amount of ambiguity in the literature as to how parametrization frameworks for Γ through Re_B, Fr, Ri_g and L_T/L_O reconcile(or contradict) across the multitude of proposed mixing regimes and complex multi-parameter space. Many of the frameworks discussed have been derived under the assumption of homogeneity and stationarity, and tested within idealized triply-periodic DNS where such assumptions are enforced. However real flows can exhibit strong spatial and temporal variability resulting from the inherent intermittency of stratified flow at finite Re_B as stratification suppresses turbulence (Portwood *et al.*, 2016). Furthermore, the presence of physical boundaries may impose vertical inhomogeneity further complicating the mixing dynamics of the flow. Clearly there is a need for more robust testing of the aforementioned parmaterization schemes in a variety of spatio-temporally inhomogeneous flows and a deeper investigation into the relationships between the parameters across varying flow regimes.

1.4 Vertical inhomogeneity in wall bounded stratified flows

Motivated by the ocean interior where such assumptions are valid, many numerical investigations into stratified flows have employed triply-periodic homogeneous domains with a linear stratification (i.e. $N = \text{const}$) (Shih *et al.*, 2005; Lindborg, 2006; Brethouwer *et al.*, 2007; de Bruyn Kops, 2015; Maffioli *et al.*, 2016; Portwood *et al.*, 2019). However, many naturally occurring flows such as the atmospheric boundary layer or stratified river flows, the presence of physical boundaries cannot be ignored and creates an additional confinement scale within the flow, which introduces vertical inhomogeneity in the stratification profile (i.e. $N = f(z)$). If mean shear is also present, (usually as a result of friction at the wall) then this creates a complex set of flow dynamics in which $S, N = f(z)$ and where local shear instability and wall generated turbulence may interact and co-exist in one flow domain.

Past studies on wall bounded stratified flows in which gravity acts perpendicular to the wall can be largely subdivided into two classes of flows. One where the flow is driven by a pressure gradient in the streamwise direction, namely channel flow (Komori *et al.*, 1983; Garg *et al.*, 2000; Armenio & Sarkar, 2002; Taylor *et al.*, 2005; García-Villalba & del Álamo, 2011; Flores & Riley, 2011; Williamson *et al.*, 2015; Buren *et al.*, 2017; Kirkpatrick *et al.*, 2019, 2020; Atoufi *et al.*, 2020, 2021). The second being that where the flow is driven by shear resulting from moving boundaries, namely Taylor-Couette and plane-Coutte flow (Oglethorpe *et al.*, 2013; Deusebio *et al.*, 2015; Zhou *et al.*, 2017*b*,*a*). The former having the appeal of *a priori* knowledge of the momentum flux profiles due to the force balance between the shear stress and pressure gradient. And the latter having the appeal of constant buoyancy and momentum flux profiles in the core of flow.

A reoccurring theme in both classes of flows is that despite the vertical inhomogeneity of the mean gradient profiles S, N, in steady-state and away from the physical boundaries, the central flow approaches a state of quasi local equilibrium as defined by (1.14-1.15). This creates an inhomogeneous flow where local based parametrization frameworks may be tested across a broad paramater range within a single flow domain. As mean shear is usually present within wall-bounded flows, the Ri_g framework has been extensively tested in the aforementioned studies. With noteable exceptions (Zhou *et al.*, 2017*b*,*a*), the Fr and L_E/L_O frameworks remain largely untested in wall-bounded flows nor is it clear as to the relationship between these parameters in such inhomogeneous flows. Furthermore, the vast majority of the aforementioned studies focus on the statistically stationary flow where the flow dynamics can be analyzed without additional complexities of time-dependant processes. It remains unclear when the assumptions of local equilibrium become valid and subsequently if the paramatrization frameworks remain relevant in temporally evolving wall bounded flows.

In the context of stratified river flows which form one of the primary motivators of this study, Williamson *et al.* (2015) present its canonical representation as a DNS configuration for stratified open channel flow subject to surface radiative heating modelled through the Beer-Lambert law. Their study focuses on the stationary case and in particular finds that the flux profiles of both buoyancy and momentum are distinctly inhomogeneous, with no constant

flux regions observed. However, an appreciable region of local equilibrium still manifests within the channel within which the $P \approx B + \epsilon_K$ and $Ri_g \sim R_f$ relationships are observed.

The study of Kirkpatrick *et al.* (2019) expand on this to explore the temporally evolving canonical 'sunset' case of the destratification of the stationary stratified flow after the removal of the radiative heat source. In Kirkpatrick *et al.* (2020) they further add the additional control parameter of upper surface cooling to expedite the destratification process. They find that at a bulk parameter level the destratification of the flow is well described and can be predicted by two time varying parameters: the friction Reynolds and Richardson numbers defined as

$$Re_\tau = \frac{u_\tau \delta}{\nu}, \qquad Ri_\tau = \frac{\Delta \bar{b} \delta}{u_\tau^2}, \tag{1.42a, b}$$

where u_τ is the so called friction velocity, δ is the channel height and $\Delta \bar{b}$ is the mean buoyancy (temperature) difference across the channel. They show that the destratifying channel maintains a state of local equilibrium for the majority of the destratification process as the flow relaxes back into a neutral state within which the $Ri_g \sim R_f$ parameterization remained valid. Analogously they found that the upper limit of $\Gamma \approx 0.2$ that manifests in the stationary state similarly remains for a long period of the flows evolution.

However, the 'sunrise' analogue of this configuration (i.e. a turbulent neutral channel subject to sudden radiative heating) remains uninvestigated. Hence with direct applicability to stratified river flows, it remains unclear as to the validity of local equilibrium assumptions nor the $Ri_g, Fr, L_E/L_O$ based parametrization frameworks within such a flow configuration. To our knowledge no comprehensive description of the transient response with respect to the vertical structure of the channel for the 'sunrise' case exists in literature through DNS investigation.

1.5 Intermittency and criticality in stratified flows

If stabilizing forces of stratification overcome that of inertia and the production of turbulence through shear instabilities, then turbulence may collapse and the flow may partially relaminarize such that turbulent and non-turbulent phases may co-exist in a stable state (Brethouwer

et al., 2012; Deusebio *et al.*, 2015). Oceanic and atmospheric flows have been frequently observed to display strong spatio-temporal intermittency with patches of weakly stratified energetic turbulence encompassed in strongly stratified yet essentially quasi-laminar flow (Baker & Gibson, 1987; Van de Wiel *et al.*, 2002).

Portwood *et al.* (2016) observe strong intermittency in their high resolution DNS at 'global' values of $Fr = 0.015$, $Re_B = 13$ and demonstrate that although turbulent patches account for only a small fraction of the flow domain, they account for the vast majority of turbulent mixing within the flow. They further find that the conditionally averaged values of Re_B vary by multiple orders of magnitude between the turbulent and quiescent regions. They find a distinct bimodal distribution of ϵ_K, χ within their flow. Similar bimodal observations of the dissipation rates and variability in Re_B were made in the DNS de Bruyn Kops (2015) as the flow became more anisotropic with increased stratification. It becomes an open question whether the distinguished limit of the LAST regime as described by Billant & Chomaz (2001) ($Re_B \gg \mathcal{O}(1)$, $Fr \ll \mathcal{O}(1)$) is physically possible in a 'local' sense. Indeed the underlying theory presented in Billant & Chomaz (2001) suggests strongly stratified flow will spontaneously organize into 'layers' or 'pancakes' of well mixed weakly stratified flow separated by interfaces at much stronger stratification. Strong evidence for such anisotropic layering has been observed in numerous studies (Lindborg, 2006; Brethouwer *et al.*, 2007; Waite, 2011; Maffioli & Davidson, 2016; Maffioli, 2017; de Bruyn Kops & Riley, 2019; Howland *et al.*, 2020). This creates appreciable challenges in inferring a singular global measure of Γ as used in oceanic models, where the parameters from which it is inferred are calculated from measurements within finite spatial and temporal windows and are inherently local.

In sheared flows, intermittency is often linked to Ri_g. In his seminal work, through inviscid linear stability theory Miles (1961) defined an upper limit of $Ri_{g,c} = 1/4$ for the formation of shear instabilities in steady stratified shear flows. Accordingly a vast amount of literature both experimental and numerical has investigated on the transition to turbulence and evolution of a mixing event due to the formation of shear instabilities (Caulfield & Peltier, 2000; Peltier & Caulfield, 2003; Basak & Sarkar, 2006; Smyth & Moum, 2000; Smyth *et al.*, 2001; Thorpe

et al., 2013; Mashayek *et al.*, 2013; Salehipour & Peltier, 2015; Salehipour *et al.*, 2015; Mashayek *et al.*, 2017; Howland *et al.*, 2018; Lewin & Caulfield, 2021, 2022). And although it has been found that $Ri_g = 1/4$ is not a strict limit for transition to turbulence, it has been generally established that it cannot exceed this value by any significant margin. This being seemingly in direct agreement with the frequent observation of similar upper limits on Ri_g, Ri_f for steady state flow observed in numerous past studies as discussed in §1.3. However it is still open to debate whether the critical limits are defined by stability and intermittency or if the overlap is simply 'fortuitous' (Zhou *et al.*, 2017*a*), warranting further investigation.

Based on the frequency of oceanic observations where $Ri_g \approx 1/4$, Thorpe & Liu (2009) hypothesise that by adjusting its mean gradients, stratified shear flows naturally converges to this 'marginally unstable' state and slight variations in shear or stratification cause the flow to oscillate between states of stability and instability. Salehipour *et al.* (2018) and Smyth *et al.* (2019) expand on this to describe this a state of 'self-organized criticality' (SOC) frequently observed in other natural systems. This concept of SOC lies at the heart of the R_{OT} parametrization scheme of Mashayek *et al.* (2021) who argue that although R_{OT} and Γ may vary, the significant majority of mixing occurs at this naturally occurring critical or 'optimal' state where $R_{OT} \approx 1$. Here 'optimal' implies that energy being injected into the flow through overturns is precisely at the wavelength corresponding to the upper limit of the inertial sub-range of the flow. However it is still unclear how local intermittency and relaminarization come into play within this conceptual framework, nor has this framework been explored in detail in vertically inhomogeneous flows.

In wall-bounded flows, the collapse of turbulence and intermittency has been frequently explored through the Monin-Obhukov (M-O) framework. In the context of the atmospheric boundary layer, M-O scaling suggests that the flow can be described by two parameters: the distance from the wall z defining a confinement scale and the M-O length L defining the competition between the forces of the shear and buoyancy at the wall defined as

$$L = \frac{u_\tau^3}{b^* \kappa_c}, \tag{1.43}$$

where b^* is the surface buoyancy flux and $\kappa_c = 0.4$ is the von Karman's constant. Flores & Riley (2011) find that the collapse of turbulence in bottom-cooled open-channel is well predicted by a critical value of the parameter $L^+ = Lu_\tau/\nu$. Here L^+ is the M-O length normalized by the viscous wall-unit (ν/u_τ) such that L^+ may be considered a 'mixed' parameter that compares the forces of shear, buoyancy and viscosity analogous to Re_B. Deusebio *et al.* (2015) similarly show that L^+ serves as an excellent predictor of intermittency in stratified plane Couette flow. Expanding on past atmospheric studies such as Nieuwstadt (1984) or Sorbjan (1986), Chung & Matheou (2012) expand on this work to show that local intermittency can be predicted similarly with a normalized 'local' M-O length $\Lambda^+ = \Lambda u_*/\nu$ where

$$\Lambda = \frac{u_*^3}{B\kappa_c}, \qquad u_* = \overline{-u'w'}^{1/2}. \tag{1.44a, b}$$

It still remains unclear how L^+ or Λ^+ scaling of intermittency applies (or whether it applies at all) to stratified flows such as rivers or lakes where the buoyancy flux into the flow occurs at the upper water-air interface rather than at the bottom wall as in the case of the atmosphere.

It becomes clear that to accurately parameterize mixing in intermittent stratified flows from finite local measurements, a thorough understanding is required of the mechanisms by which intermittency manifests, both the flow dynamics in the separate turbulent/quiescent regions as well as a robust quantification and prediction of intermittency. All these being areas of current investigation in stratified flow literature.

1.6 Primary goals and thesis layout

It is clear that a more thorough understanding of turbulent mixing and its parametrization in stratified flows is still required within existing literature and in particular with respect to vertically and temporally inhomogeneous and intermittent flows. Additionally it is clear that there is a gap in current literature describing the transient response of a turbulent open channel flow subject to sudden stratification with extensive DNS data. Motivated by stratified river flows, this thesis employs a 'sunrise' scenario variant (to be defined in detail in §2) of the

stratified open channel flow DNS configuration of Williamson *et al.* (2015) to address the following open questions and core aims of this thesis:

(1) What is the transient response of the vertical energetic structure of a neutral turbulent channel to the sudden imposition of stable stratification through radiative heating?
(2) In the context of stratified river flows, can the onset of globally suppressed turbulent mixing and the time scale under which equilibrium is achieved be predicted through a bulk flow parameterization of easily measurable quantities in the field?
(3) Can Γ be accurately parameterized through Re_B, Fr, Ri_g and L_E/L_O frameworks in our spatio-temporally inhomogeneous channel flow within which the assumptions of local equilibrium are invalid?
(4) How do these frameworks and the relationships between the varying parameters reconcile (or contradict) across the varying mixing regimes and what are the subsequent implications for current mixing models for stratified shear flow?
(5) How does intermittency due to stable stratification manifest within surface heated stratified channel flow and can it be quantified and parameterized through Monin-Obhukov scaling?
(6) How does the inherent intermittency in stratified flow effect the parameterization of Γ in the limit of low Fr and how does this reconcile with the theory of self organized criticality and 'optimal' mixing in stratified shear flows?

To that end the remainder of this thesis is structured as follows

In chapter §2 a description of the DNS configuration for temporally evolving stratified open channel flow as well the numerical method used is presented. The numerical method is validated through near-wall spectra of the initial condition.

In chapter §3 we present a thorough qualitative and quantitative description regarding the transient response of a neutral turbulent open channel flow subject to sudden radiative heating with emphasis on the energetic vertical structure of the flow. Physically based scaling arguments are presented to derive a bulk property parametrization for both the global suppression

of mixing and the time scale under which the flow obtains stationarity. A model for the bulk stratification rate is proposed and its limitations discussed.

In chapter §4 we present a thorough evaluation as to the efficacy of Re_B, Fr, Ri_g and L_E/L_O paramterization frameworks for Γ in temporally evolving stratified open channel flow. Three separate mixing regimes are established based on values of Fr and scaling arguments are presented to determine the relationship between all four non-dimensional parameters across all regimes. The implications of the results for other stratified shear flows are discussed.

In chapter §5 an adaptation of the unstable density gradient criterion method of Portwood *et al.* (2016) is presented for stratified open channel flow such that instantaneous realisations of the flow are robustly separated into turbulent and quiescent regions. The intermittency and its quantification is parameterized through local M-O scaling. The vertical energetic structure of the flow with respect to the two flow regimes are investigated and evidence is presented for self-organized criticality within the intermittent regions of the flow. Implications for the parametrization of Γ within an intermittent flow are discussed and it is directly shown that for stratified channel flow that a constant Γ regime occurs due to intermittency.

In chapter §6 the major findings within this thesis are summarized and direction for future work is discussed.

CHAPTER 2

Numerical method

2.1 Flow configuration

The flow configuration of our DNS employs the framework of Williamson *et al.* (2015) for stationary radiatively heated open channel flow as a canonical representation of stratified river flow. For our DNS we consider not only the stationary flow but also the temporally evolving case as an initially isothermal neutral open channel flow is subject to radiative heating and evolves towards a stationary stably stratified state. A schematic depicting our flow configuration is presented in figure 2.1. The flow is periodic in the streamwise (x) and spanwise (y) directions and is driven by a constant pressure gradient in x. The top and bottom boundary conditions are free-slip adiabatic and no-slip adiabatic respectively. The flow is subject to a depth varying volumetric temperature source $q(z)$, modelled on the principle of

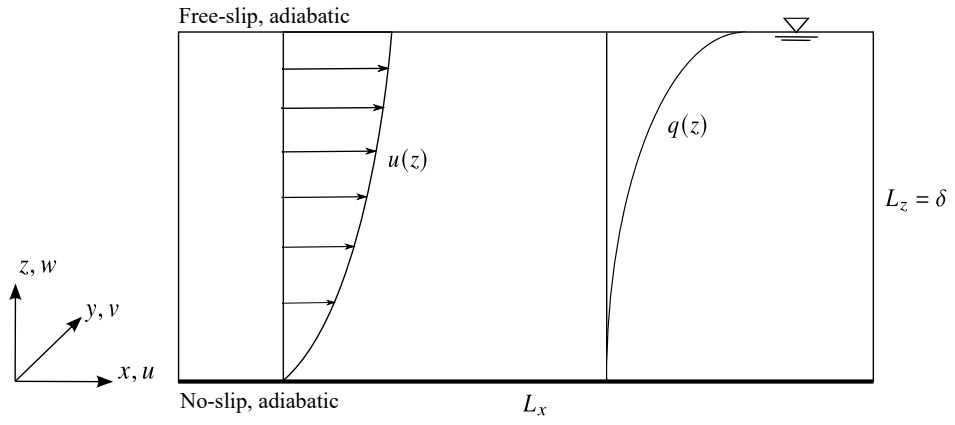

FIGURE 2.1: Schematic diagram of the flow configuration, domain is periodic in x and y.

Beer-Lambert's law and defined as

$$q(z) = \frac{I_s \alpha}{C_P \rho_0} e^{(z-\delta)\alpha}, \tag{2.1}$$

where I_s is the radiant surface heat flux, α is the absorption coefficient and δ is the channel height, C_p is the specific heat and ρ_0 is the reference fluid density. Hence we can define both the domain-averaged mean heat source and representative heat source respectively as

$$\langle q \rangle = \frac{1}{\delta} \int_0^\delta q(z) dz, \qquad q_N = \frac{1}{\delta^2} \int_0^\delta (\langle q \rangle - q(z))(z - \delta) dz. \tag{2.2a, b}$$

Here q_N can be considered analogous to that of a surface heat flux in an iso-flux flow configuration and defines a characteristic heat input into the channel by accounting for the turbidity of the flow. Subsequently, under the Oberbeck-Boussinesq assumption, the governing equations for our flow, i.e. the incompressible Navier-Stokes equations are

$$\boldsymbol{\nabla \cdot u} = 0, \tag{2.3}$$

$$\frac{\partial \boldsymbol{u}}{\partial t} + \boldsymbol{u \cdot \nabla u} = -\frac{\nabla p^*}{\rho_0} + \nu \nabla^2 \boldsymbol{u} + b \boldsymbol{e}_z + F \boldsymbol{e}_x, \tag{2.4}$$

$$\frac{\partial b}{\partial t} + \boldsymbol{u \cdot \nabla} b = \kappa \nabla^2 b + g \beta q(z), \tag{2.5}$$

Where $b = -g\rho/\rho_0$ is the buoyancy, g is the gravitational acceleration, ν is the kinematic viscosity, κ is the thermal diffusivity, F is the driving mean pressure gradient and β is the coefficient of thermal expansion such that the transform from fluid temperature (θ) to density (ρ) is given by the equation of state

$$\rho = \rho_0 (1 - \beta \theta). \tag{2.6}$$

And our initial and boundary conditions are explicitly defined as

$$z = 0: \quad u = v = w = 0, \quad \frac{\partial b}{\partial z} = 0. \tag{2.7}$$

$$z = \delta: \quad \frac{\partial u}{\partial z} = \frac{\partial v}{\partial z} = w = 0, \quad \frac{\partial b}{\partial z} = 0. \tag{2.8}$$

$$t = 0: \quad b = 0 \tag{2.9}$$

and where the initial condition for the velocity field is to be defined in §2.2. Our flow is then fully defined by four non-dimensional parameters: The initial friction Reynolds number Re_τ^0, the molecular Prandtl number Pr, the turbidity parameter $\alpha\delta$ that controls the vertical heating profile and an initial bulk stability parameter λ^0, defined as

$$Re_\tau^0 = \frac{u_\tau^0 \delta}{\nu}, \qquad Pr = \frac{\nu}{\kappa}, \qquad \alpha\delta, \qquad \lambda^0 = \frac{\delta}{\mathcal{L}^0}. \tag{2.10a-d}$$

Here, u_τ^0 is the initial equilibrium friction velocity defined as

$$u_\tau^0 = \left(\frac{\tau_w^0}{\rho_0}\right)^{1/2}, \tag{2.11}$$

where τ_w^0 is the initial equilibrium viscous shear stress at the bottom wall. The stability parameter of our λ^0 flow is defined in the Monin-Obhukov framework as the ratio of the domain confinement scale δ to bulk Obhukov length $\mathcal{L}_0$ defined as

$$\mathcal{L}^0 = \frac{(u_\tau^0)^3}{g\beta q_N \delta}. \tag{2.12}$$

We note that this formulation of the Obhukov length which accounts for our volumetric heat source is analogous to the standard definition used in atmospheric literature $L = u_\tau^3/\kappa_c b_*$ (Flores & Riley, 2011), where the term $g\beta q_N \delta$ can be considered analogous to the surface buoyancy flux b_*. Furthermore, as derived in Williamson *et al.* (2015), for high $\alpha\delta$ we can obtain

$$q_N \approx \frac{I_S}{\delta}\left(\frac{1}{2} - \frac{1}{\alpha\delta}\right)^{-1}, \tag{2.13}$$

such that we can redefine

$$\mathcal{L}^0 = \frac{(u_\tau^0)^3}{g\beta I_s/(\rho_0 C_p)}\left(\frac{1}{2} - \frac{1}{\alpha\delta}\right)^{-1}. \tag{2.14}$$

We note that for our simulations we have defined our parameters using the initial friction velocity u_τ^0. In our flow, we maintain a constant pressure gradient in the stream wise direction that is balanced by the downward momentum flux across the channel and reflected in the measured shear stress at the wall. In this sense u_τ^0 represents both the initial and final equilibrium value of the friction velocity of the flow. However as will be shown throughout the study, the sudden effects of stable stratification act to suppress the turbulent component

of the momentum flux causing an imbalance in the stream wise momentum equation and subsequent reduction of u_τ, which varies in time as the flow transitions towards its final equilibrium state. As such, when presenting statistics within this study that incorporate the time varying u_τ, rather than the initial equilibrium value of u_τ^0, it is implicit that this corresponds to the measurement of the friction velocity at time t.

We can further define our governing equations in non-dimensional form. Firstly, we note that the dimensional temperature θ at time t is decomposed into the statistically steady temperature fluctuation deviating from a domain-averaged mean, defined as

$$\theta(\boldsymbol{x}, t) = \theta(\boldsymbol{x}, t)' + \langle\theta(t)\rangle. \tag{2.15}$$

and under the assumptions that no heat is lost through the boundaries it follows that

$$\frac{\partial\langle\theta(t)\rangle}{\partial t} = \frac{\langle q\rangle}{\rho_0 C_p}, \tag{2.16}$$

By defining u_τ^0 and δ as the characteristic velocity and length scales respectively we can then define a characteristic temperature scale

$$\theta_N = \frac{q_N \delta}{\rho_0 c_p u_\tau^0}. \tag{2.17}$$

And hence we can define a non-dimensional temperature and heat source

$$\hat{\theta}(\boldsymbol{x}, t) = \frac{\theta(\boldsymbol{x}, t) - \langle\theta(t)\rangle}{\theta_N}, \qquad \hat{q}(z) = \frac{q_I(z) - \langle q\rangle}{q_N}, \tag{2.18a, b}$$

leading to our non-dimensional buoyancy variable

$$\hat{b} = \lambda^0 \hat{\theta}. \tag{2.19}$$

Next we non-dimensionalize our remaining dimensional variables in (2.3-2.5) about u_τ^0, δ and ρ_0 such that

$$\hat{\boldsymbol{x}} = \frac{\boldsymbol{x}}{\delta}, \qquad \hat{\boldsymbol{u}} = \frac{\boldsymbol{u}}{u_\tau^0}, \qquad \hat{t} = \frac{t u_\tau^0}{\delta}, \qquad \hat{p^*} = \frac{p^*}{\rho_0 (u_\tau^0)^2} \tag{2.20a - d}.$$

Accordingly the governing equations in (2.3-2.5) expressed in non-dimensional form become

$$\boldsymbol{\nabla}\cdot\hat{\boldsymbol{u}} = 0, \tag{2.21}$$

$$\frac{\partial \hat{\boldsymbol{u}}}{\partial \hat{t}} + \hat{\boldsymbol{u}} \cdot \boldsymbol{\nabla} \hat{\boldsymbol{u}} = -\nabla \hat{p^*} + \frac{1}{Re_\tau^0} \nabla^2 \hat{\boldsymbol{u}} + \hat{b} \boldsymbol{e}_z + \boldsymbol{e}_x, \tag{2.22}$$

$$\frac{\partial \hat{b}}{\partial \hat{t}} + \hat{\boldsymbol{u}} \cdot \boldsymbol{\nabla} \hat{b} = \frac{1}{Pr Re_\tau^0} \nabla^2 \hat{b} + \lambda^0 \hat{q}, \tag{2.23}$$

We have selected this open channel flow configuration for three reasons. Firstly, as discussed in §1, our DNS configuration of a stratified open channel flow heated through radiative surface heating is a canonical representation of stratified river flow and in particular the regulated river flows in inland Australia, where the accurate estimation and prediction of diapycnal mixing remains an important task. Secondly, the use of an adiabatic bottom boundary has been shown to ensure that while the bulk flow becomes stratified, the near-wall turbulence structure remains relatively unchanged by the effects of buoyancy (Taylor *et al.*, 2005; Williamson *et al.*, 2015). As will be shown in §5, this creates a distinctly inhomgeneous intermittency profile, allowing for simulations to be run at higher levels of buoyancy strength than iso-flux or fixed buoyancy boundary conditions where the relaminarization and collapse of turbulence inherently occurs at the wall (Flores & Riley, 2011; García-Villalba & del Álamo, 2011; Deusebio *et al.*, 2015; Zhou *et al.*, 2017*a*). Thirdly, relative to a surface flux boundary condition, use of the volumetric heat source shifts the pycnolcine deeper into the channel away from the upper boundary, creating an appreciable region in the central bulk flow of significantly stronger stratification (Williamson *et al.*, 2015). This subsequently allows us to access regimes of lower Fr (higher Ri_g) further away from the top boundary. Accordingly this allows us to explore local correlations between mixing properties and non-dimensional parameters at a low Fr range without additional complication from boundary confinement effects which may influence the mixing dynamics (Flores *et al.*, 2017).

2.2 Direct numerical simulations

Equations (2.21- 2.23) were solved using the SnS code, fractional-step finite-volume solver as outlined in Norris (2000) and Armfield *et al.* (2003). The code has since been verified and employed in a range of high resolution DNS studies (Williamson *et al.*, 2015; Ke *et al.*, 2019, 2020, 2021). The advective spatial derivatives are discretized using fourth-order

Case	Re_τ^0	λ^0	Pr	$\alpha\delta$	$L_x \times L_y \times L_z$	$N_x \times N_y \times N_z$	$\frac{t_{\text{final}}}{T_\tau^0}$
R400L0.02	400	0.02	1	8	$2\pi\delta \times \pi\delta \times \delta$	$512 \times 512 \times 150$	15
R400L0.1	400	0.1	1	8	$2\pi\delta \times \pi\delta \times \delta$	$512 \times 512 \times 150$	15
R400L0.25	400	0.25	1	8	$2\pi\delta \times \pi\delta \times \delta$	$512 \times 512 \times 150$	15
R400L0.5	400	0.5	1	8	$2\pi\delta \times \pi\delta \times \delta$	$512 \times 512 \times 150$	50
R400L0.5AD32	400	0.5	1	32	$2\pi\delta \times \pi\delta \times \delta$	$512 \times 512 \times 150$	40
R400L0.5PR0.5	400	0.5	0.5	8	$2\pi\delta \times \pi\delta \times \delta$	$512 \times 512 \times 150$	40
R400L1	400	1	1	8	$2\pi\delta \times \pi\delta \times \delta$	$512 \times 512 \times 150$	50
R400L1LD	400	1	1	8	$8\pi\delta \times 2\pi\delta \times \delta$	$2560 \times 1280 \times 150$	40
R400L2	400	2	1	8	$2\pi\delta \times \pi\delta \times \delta$	$512 \times 512 \times 150$	90
R900L1	900	1	1	8	$2\pi\delta \times \pi\delta \times \delta$	$1152 \times 1152 \times 450$	40
R900L1AD16	900	1	1	16	$2\pi\delta \times \pi\delta \times \delta$	$1152 \times 1152 \times 450$	10
R900L2	900	2	1	8	$2\pi\delta \times \pi\delta \times \delta$	$1152 \times 1152 \times 450$	10
R900L5	900	5	1	8	$2\pi\delta \times \pi\delta \times \delta$	$1152 \times 1152 \times 450$	10

TABLE 2.1: List of DNS performed and relevant parameters

central differencing, whilst other spatial derivatives are calculated using second-order central differencing. Cell-face velocities are calculated using Rhie-Chow momentum interpolation and the time-advancement is performed using a second-order Adams-Bashforth scheme.

A detailed list of simulations performed is presented in Table 2.1. Our simulations cover two friction Reynolds number of $Re_\tau^0 = 400, 900$. The stability parameter varies in the range of $\lambda^0 = 0.02 - 5$, such that our simulations cover stability regimes varying from passive scalar flow to extremely stable. We keep the turbidity parameter constant at $\alpha\delta = 8$ for all simulations with two control cases of $\alpha\delta = 32, 16$ for our $Re_\tau^0 = 400, 900$ cases respectively. For all cases we keep $Pr = 1$ for computational efficiency with the exception of a single $Pr = 0.5$ case to test our bulk flow parametrization in §3.

Our choice of grid resolution closely follows past studies of stratified wall-bounded turbulence (García-Villalba & del Álamo, 2011; Deusebio *et al.*, 2015; Williamson *et al.*, 2015), we discretize our domain as follows. For all simulations the stream and span-wise grid size in initial viscous wall units is kept constant at $\Delta x_0^+ = 5$ and $\Delta y_0^+ = 2.5$. The vertical grid size for the $Re_{\tau,0} = 400$ simulations is logarithmically stretched from $\Delta z_0^+ = 0.4$ at the wall to $\Delta z_0^+ = 4$ at $z = 0.25$ where it stays constant to the half channel height $z = 0.5$. The vertical

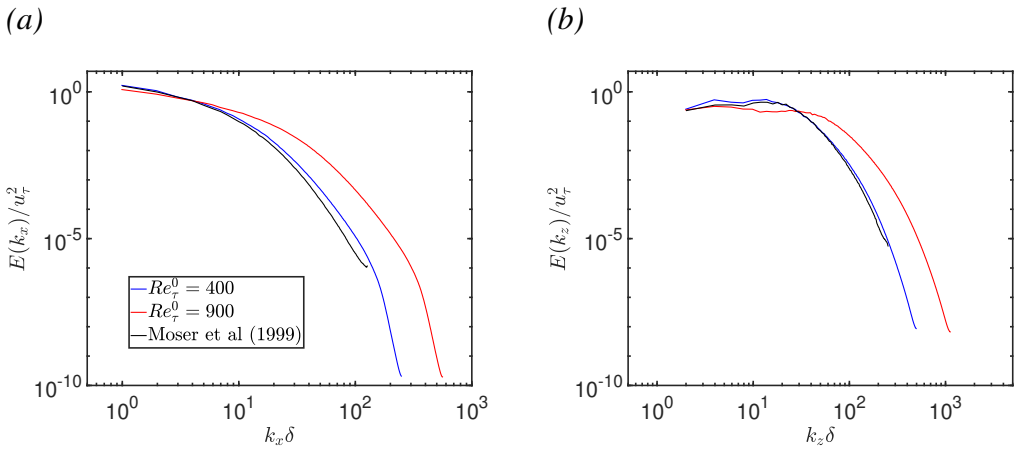

FIGURE 2.2: (a) Stream-wise and (b) span-wise energy spectra of the initial state of the flow at $t = 0$ for both values of Re_τ at a vertical location of $z^+ = 10$. Included in both figures is the data of Moser *et al.* (1999) at $z^+ = 10$ and $Re_\tau = 395$.

grid spacing in the top half of the channel is then set as symmetrical about the midpoint axis to ensure accurate resolution of viscous near surface mechanics (Calmet & Magnaudet, 2003). A similar procedure for the vertical grid size of the $Re_{\tau,0} = 900$ simulations was employed with a further refinement of $\Delta z_0^+ = 2.5$ in the bulk of the flow. To maintain accurate resolution of the viscosity affected near-wall and near-surface regions we ensure that we have more than ten grid points within a $\Delta z_0^+ = 10$ distance from either boundary.

The initial simulation field is of fully developed statistically stationary neutral open channel flow at a given Re_τ^0. To validate the grid resolution of our flow, figure 2.2 shows the streamwise and spanwise energy spectra $E(k_x), E(k_z)$for both $Re_\tau^0 = 400, 900$ initial conditions at $z^+ = 10$ roughly corresponding to the peak in turbulence production P. For reference we also plot the spectra from the $Re_\tau = 395$ DNS of Moser *et al.* (1999). The results show well developed spectra with no truncation at high wavelengths, with excellent agreement between our $Re_\tau^0 = 400$ case and that of Moser *et al.* (1999).

For all simulations we then initialize the isothermal buoyancy field $b = 0$ at $t = 0$ and simultaneously switch on the volumetric heat source and the effects of buoyancy. For all simulations, transient data has been recorded at non-dimensional time intervals of $\Delta t/T_\tau^0 = 0.02$ up to the non-dimensional time of $t/T_\tau^0 = 10$ to ensure accurate representation of the

temporal effects during the early rapid adjustment period of the flow. Here $T_\tau^0 = \delta/u_\tau^0$ is the initial friction (advection) time scale of the flow. For $t/T_\tau^0 > 10$, changes in the flow become smoother and data is collected at non-dimensional time intervals of $\Delta t/T_\tau^0 = 0.1$.

We acknowledge past studies that have shown that the size of the domain may effect the intermittent regime where laminar and turbulent patches coexist, such that a smaller domain often leads to earlier laminarization for the same set of bulk parameters Flores & Riley (2011); García-Villalba & del Álamo (2011); Brethouwer *et al.* (2012); Deusebio *et al.* (2015). However as shown in Williamson *et al.* (2015), our adiabatic bottom boundary condition ensures that the near-wall region remains fully turbulent unlike the afforementioned studies where intermittency in the near-wall region leads to a collapse of turbulence across the whole domain. Hence we do not expect the domain size to significantly influence the results presented in this study. Accordingly for computational efficiency we keep the domain size constant at $L_x \times L_y \times L_z = 2\pi\delta \times \pi\delta \times \delta$ across all simulations with the exception of case R400L1LD (long domain) for which the domain size is increased to $L_x \times L_y \times L_z = 8\pi\delta \times 2\pi\delta \times \delta$ to demonstrate the independence of our results on the domain size. This is shown in chapter 5.3.

CHAPTER 3

Transient response and transition to equilibrium of stratified open channel flow

---

In this chapter we investigate the transient response of neutral/isothermal turbulent open channel flow subject to sudden radiative heating. We present a detailed qualitative description of the change in the vertical structure of the flow as the flow transitions towards a stationary stratified state. In particular we focus on the bulk flow parameterization of globally suppressed turbulent mixing as well as the time scale under which the flow obtains stationarity.

The contents of this chapter are based on the following manuscript:

Issaev, Vassili, Williamson, N., Armfield, S. W. & Norris, S. E. Transient response and transition to equilibrium of turbulent open channel flow subject to stratification through radiative heating. Planned for submission to *Journal of Fluid Mechanics* in 2022.

3.1 Introduction

Turbulent flows subject to radiative solar, heating resulting in a vertically inhomogeneous stable density stratification profile are prevalent in an geophysical context such as rivers, lakes and estuaries. As a result of the stratification, buoyancy acts to suppress turbulent mixing in a non-uniform manner with the suppression being most pronounced at the upper surface where the radiative heating is most concentrated (Williamson *et al.*, 2015). In particular, such flows are also typically defined by a non-uniform mean shear profile that results from the friction at the bottom boundary which drives the generation of turbulence in the flow. In a broad sense the flow can be described as a competition between the dampening effects of

stable stratification and the turbulence enhancing effects of the mean shear which both vary significantly with depth creating a complex set of inhomogeneous and interconnected flow dynamics.

As discussed in §1, Williamson *et al.* (2015) present a DNS configuration for stably stratified open channel flow subject to radiative heating modelled through the Beer-Lambert Law as a canonical representation of stratified river flow. In their study analyse the statistically stationary flow, both at a bulk and local level. In particular, they find that at their paramater range, the upper portion of the channel approaches quasi-laminar conditions with severely reduced mixing, the onset of which is well predicted by a stationary 'bulk' Obhukov Reynolds number $Re_{\mathcal{L}}$ within the Monin-Obhukov framework. This being analogous to L^+ used in atmospheric studies. Following their work Kirkpatrick *et al.* (2019) examine a canonical 'sunset' case by employing the same framework to examine the temporally evolving 'destratifying' flow in which the stationary stable flow reverts back to a neutral state after the sudden removal of the radiatiave heating. They find that the evolution and properties of the transient flow can well described by the time dependant friction Reynolds and Richardson numbers Re_τ and Ri_τ, both being bulk parameters that may be easily obtained from field measurements in real river flows. In particular, they show that a bulk destratification rate $\mathcal{D}$ of the channel flow can be well parameterized by Ri_τ alone. In their subsequent work Kirkpatrick *et al.* (2020) in which a similar 'sunset' case is examined but with the addition of upper surface cooling, they similarly find that $\mathcal{D}$ displays a clear dependence on Ri_τ as well as a convective Richardson number Ri_*. It however remains unclear whether a singular Ri_τ parametrization of an analogous bulk 'stratification' rate for an idealised 'sunrise' scenario in which an initially neutral turbulent open channel flow is subject to sudden radiative heating is valid. Furthermore, a bulk flow parametrization for the time-varying flow that predicts the onset of reduced turbulent mixing also remains uninvestigated in current literature.

The temporally evolving 'stratifying' case has also been explored by Flores & Riley (2011) in the context of the development of the stable nocturnal boundary layer modelled as turbulent open channel flow subject to sudden bottom wall cooling. They demonstrate that for the stratifying case in which relaminarization and intermittency is an inherent feature of the flow,

Ri_τ alone is insufficient to predict the behaviour of the flow as the molecular properties of the fluid also becomes an important parameters of the temporally evolving flow such that the collapse of turbulence is well predicted by 'hybrid' buoyancy Reynolds number in the Monin-Obhukov framework Re_L. However, drawing direct comparisons of their work to the framework of Williamson *et al.* (2015) must be treated with caution as in former case the collapse of turbulence occurs at the wall whilst in the latter the suppression of turbulence is a 'top-down' due to the concentration of radiative heating at the upper surface.

In particular, a key finding of Williamson *et al.* (2015) was that the central bulk flow of the channel was in a state of local energetic equilibrium such that $P \approx B + \epsilon_K$ and displays properties similar to that of homogeneous stratified shear flow (Shih *et al.*, 2000, 2005; Chung & Matheou, 2012). In this regime they found that despite the strong vertical inhomogeneity, the mixing efficiency defined through the flux Richardson number R_f approached a classic 'Osborne' limit of $R_{f,c} \approx 0.17$ Osborn (1980). Similarly, they found the gradient Richardson number also approached a critical limit of $Ri_{g,c} \approx 0.2$. Similar values have been also reported in a variety of stationary stratified shear flows both homogeneous and wall-bounded (Armenio & Sarkar, 2002; Shih *et al.*, 2005; García-Villalba & del Álamo, 2011; Chung & Matheou, 2012; Deusebio *et al.*, 2015; Zhou *et al.*, 2017*a*).

In Kirkpatrick *et al.* (2019) for the destratyfying case, it was shown that the state of local equilibrium persisted for a long period of the destratification process and hence the upper limits of R_f and Ri_g remained valid for the duration of the flow's evolution. However, as will be shown in §3.4, during the initial transitional period of the flow for our evolving stratifying case, local values of R_f and Ri_g may greatly exceed these limit values analogously to studies of stratified free shear flow during initial development of shear instabilities (Caulfield & Peltier, 2000; Mashayek *et al.*, 2013; Salehipour & Peltier, 2015; Salehipour *et al.*, 2015; Mashayek *et al.*, 2017). Accordingly, a natural question that presents itself is: when is stationarity in our 'sunrise' case reached such that the critical assumptions are valid? And is it possible to predict the time scale at which this occurs through bulk flow parameters?

In light of the discussion presented above, we present this chapter which employs direct numerical simulations (DNS) to address a relatively focused and central theme which may be subdivided into two open questions in literature:

(1) In the 'sunrise' case for stratified open channel flow, can the stratification rate and onset of globally reduced mixing be accurately predicted through bulk flow parameters?
(2) At what time in the flows evolution, does the channel flow obtain stationarity such that critical limit conditions may be assumed and can this similarly be predicted through a bulk flow parametrization?

To that end, the remainder of this chapter is structured as follows: in §3.2 we present our list of DNS used for this chapter. In §3.3 we briefly present a theoretical background of the governing equations that describe the flow's transition to stationarity. In §3.4 we demonstrate the initial time-dependence of our flow on the development of the buoyancy field and demonstrate that after this period, the mixing properties within the flow become insensitive to global temporal effects and can be described by local scaling. In §3.5 we present a qualitative overview of the bulk and local flows transition towards equilibrium conditions. In §3.6 we present scaling analysis to predict the transition towards a suppressed mixing regime through bulk flow parameters. In §3.7 we investigate the transition of the buoyancy and momentum fluxes towards equilibrium conditions and provide a bulk parameter scaling to predict the equilibrium time scale. In §3.8 we define a bulk stratification rate and provide scaling analysis to present its bulk flow parametrization. And in §3.9 we summarize our key findings in this chapter.

3.2 List of DNS used and notation

Table 3.1 presents a list of the DNS used within this chapter. As our overreaching aim of this chapter is to provide a bulk flow paramaterization for the time scale that determins the transition to equilibrium, we only consider DNS that have been run until statationarity that is obtained at the equilbrium time t_e (to be defined in more detail in §3.7). The DNS considered

Case	Re_τ^0	λ^0	Pr	$\alpha\delta$	$L_x \times L_y \times L_z$	$N_x \times N_y \times N_z$	$\frac{t_{\text{final}}}{T_\tau^0}$	$\frac{t_e}{T_\tau^0}$	Ri_τ^{final}
R400L0.02	400	0.02	1	8	$2\pi\delta \times \pi\delta \times \delta$	$512 \times 512 \times 150$	15	4	0.4
R400L0.1	400	0.1	1	8	$2\pi\delta \times \pi\delta \times \delta$	$512 \times 512 \times 150$	15	5	2.5
R400L0.25	400	0.25	1	8	$2\pi\delta \times \pi\delta \times \delta$	$512 \times 512 \times 150$	15	6.5	11.5
R400L0.5	400	0.5	1	8	$2\pi\delta \times \pi\delta \times \delta$	$512 \times 512 \times 150$	50	15	34.9
R400L0.5PR0.5	400	0.5	0.5	8	$2\pi\delta \times \pi\delta \times \delta$	$512 \times 512 \times 150$	40	12	20.7
R400L0.5AD32	400	0.5	1	32	$2\pi\delta \times \pi\delta \times \delta$	$512 \times 512 \times 150$	40	15	52.7
R400L1	400	1	1	8	$2\pi\delta \times \pi\delta \times \delta$	$512 \times 512 \times 150$	50	30	113.8
R400L2	400	2	1	8	$2\pi\delta \times \pi\delta \times \delta$	$512 \times 512 \times 150$	90	50	338.2
R900L1	900	1	1	8	$2\pi\delta \times \pi\delta \times \delta$	$1152 \times 1152 \times 450$	40	33	201.1

TABLE 3.1: List of DNS considered within this chapter 3. t_{final} corresponds to the total simulation time, t_e corresponds to the time to obtain equilibrium, Ri_τ^{final} corresponds to final(stationary) measured friction Richardson number as defined in (1.42). $T_\tau^0 = \delta/u_\tau^0$ is the initial advection/friction time scale

tests both Re_τ values, varying flux profiles through $\alpha\delta$ and a range of λ that varies from extremely stable to essentially neutral flow. For computational efficiency we do not test values of $Pr = 7$ typical when considering the diffusivity of heat in water. However we probe the sensitivity of our results to Pr by considering a singular $Pr = 0.5$ case.

For this chapter, we define that any flow variable at a spatial location $\mathbf{x}$ and time t can be decomposed into a horizontally averaged mean and fluctuating components denoted with an overbar and prime respectively, such that

$$f(\mathbf{x}, t) = \overline{f}(z, t) + f'(\mathbf{x}, t) \tag{3.1}$$

and where the mean at a vertical location of z is calculated through a volumetric integral across the horizontal plane at time t

$$\overline{f}(z, t) = \frac{1}{L_x L_y} \int_0^{L_x} \int_0^{L_y} f(\mathbf{x}, t) dx dy. \tag{3.2}$$

Similarly, we define that unless otherwise explicitly stated, it is implicit that flow statistics composed out of the velocity and buoyancy fields are presented as horizontal averages of that quantity at location z and time t as defined in (3.2). Furthermore, we define that the $\langle . \rangle$

operator indicates a domain averaged value across the entire channel such that

$$\langle f(t)\rangle = \frac{1}{V}\int_0^{L_x}\int_0^{L_y}\int_0^{L_z} f(\mathbf{x},t)dxdydz. \tag{3.3}$$

3.3 Theoretical Background

We consider the response of the buoyancy and velocity fields of an initially isothermal neutral channel subject to radiative heating through $q(z)$ and the subsequent sudden stabilizing effects of buoyancy. Under the assumption of homogeneity in the horizontal plane the evolution equations for the mean buoyancy and streamwise velocity become

$$\frac{\partial\overline{b}}{\partial t} = \frac{\partial(\overline{-b'w'})}{\partial z} + \kappa\frac{\partial^2\overline{b}}{\partial z^2} + g\beta q(z) = \frac{\partial\mathcal{B}}{\partial z} + g\beta q(z) \tag{3.4}$$

$$\frac{\partial\overline{u}}{\partial t} = F\boldsymbol{e}_x + \frac{\partial(\overline{-u'w'})}{\partial z} + \nu\frac{\partial^2\overline{u}}{\partial z^2} = F\boldsymbol{e}_x + \frac{\partial\mathcal{M}}{\partial z}, \tag{3.5}$$

where $\mathcal{B}$ and $\mathcal{M}$ are the total vertical buoyancy and momentum fluxes respectively which can be decomposed into their turbulent and laminar components such that

$$\mathcal{B} = \underbrace{\overline{-b'w'}}_{\text{Turbulent } \mathcal{B}_t} + \underbrace{\kappa\frac{\partial\overline{b}}{\partial z}}_{\text{Molecular } \mathcal{B}_m} \tag{3.6}$$

and

$$\mathcal{M} = \underbrace{\overline{-u'w'}}_{\text{Turbulent } \mathcal{M}_t} + \underbrace{\nu\frac{\partial\overline{u}}{\partial z}}_{\text{Molecular } \mathcal{M}_m} . \tag{3.7}$$

$\mathcal{B}$ thus represents the pathway for buoyancy (heat) to be redistributed vertically throughout the channel through both turbulent mixing and molecular diffusion, while $\mathcal{M}$ acts to oppose the driving pressure gradient to achieve equilibrium in the stream-wise momentum equation (Pope, 2000). Furthermore for clarity, we note that both $\mathcal{B}$ and $\mathcal{M}$ can be directly related to the idea of an eddy diffusivity/viscosity hypothesis (Pope, 2000) such that:

$$\mathcal{B} = (K_\rho + \kappa)N^2, \qquad \mathcal{M} = (K_M + \nu)S. \tag{3.8a, b}$$

Where $N = (\partial\overline{b}/\partial z)^{1/2}$ is the buoyancy frequency, $S = \partial\overline{u}/\partial z$ is the mean shear, K_ρ is the eddy diffusivity and K_M is the eddy viscosity defined as

$$K_\rho = \frac{\overline{-b'w'}}{N^2}, \qquad K_M = \frac{\overline{-u'w'}}{S}. \tag{3.9a, b}$$

Subsequently, when $\mathcal{B}$ and $\mathcal{M}$ both achieve their respective equilibrium values for all vertical locations within the channel, the mean buoyancy and velocity fields attain stationarity.

Williamson *et al.* (2015) (Henceforth denoted WAKN15) demonstrate that for the stationary case the equilibrium value of total buoyancy flux $\mathcal{B}_E$ can be anlytically derive such that

$$\mathcal{B}_E = \frac{g\beta I_S}{C_P\rho_0\delta}\left(z(1 - e^{(z-\delta)\alpha})\right). \tag{3.10}$$

For our initially isothermal flow where $\mathcal{B} = \mathcal{B}_t = \mathcal{B}_d = 0$ at $t = 0$, the convergence towards buoyancy flux equilibrium can be defined through the fraction $\mathcal{B}/\mathcal{B}_E$ which transitions from zero to unity.

Similarly, through (3.5), an expression for the equilibrium value of the total momentum flux $\mathcal{M}_E$ can be derived such that

$$\mathcal{M}_E = \tau_w\left(1 - \frac{z}{\delta}\right) = u_\tau^2\left(1 - \frac{z}{\delta}\right), \tag{3.11}$$

We again note that in our evolving flow τ_w and hence u_τ vary in time due to the suppressing effects of stable stratification. In this sense a ratio of $\mathcal{M}/\mathcal{M}_E = 1$ represents an quasi-equilibrium state where any local variations in the momentum flux are captured through instantaneous measurements of u_τ.

The transition to equilibrium can also be considered from an energetics perspective by considering the budget for the turbulent kinetic energy $E_K = 1/2(\overline{u_i'u_i'})$ and under the assumption of homogeneity in the horizontal plane, the evolution equation for E_K at a given depth z can be written as:

$$\frac{\partial E_K}{\partial t} = P - \epsilon_K - B + D_\nu + T_K + \Pi, \tag{3.12}$$

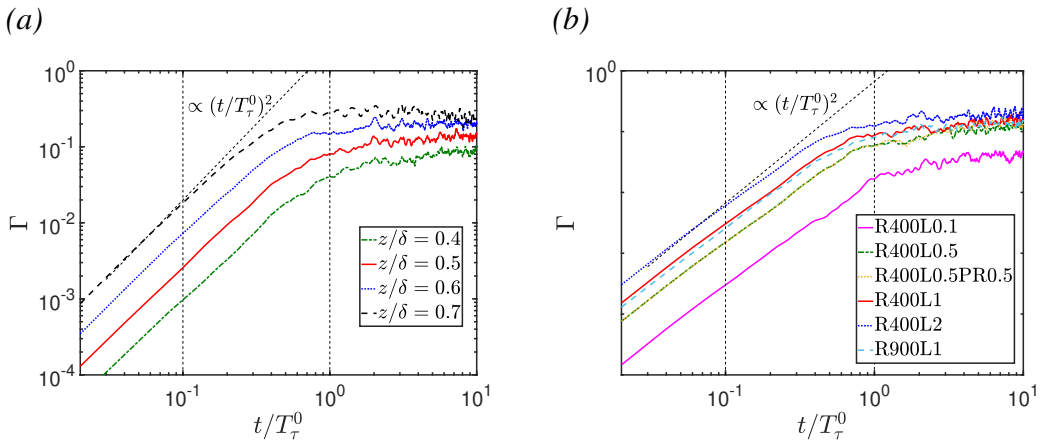

FIGURE 3.1: Mixing coefficient Γ plotted against non-dimensional time t/T_τ^0 (a) at varying vertical locations for case R900L1 (b) at a vertical location of $z = 0.5$ for a range of simulations. Vertical dashed lines in both figures represent $t/T_\tau^0 = 0.1$ and $t/T_\tau^0 = 1$, diagonal dashed line represents a line proportional to $(t/T_\tau^0)^2$

where terms going from left to right are: the unsteady term, the production term, the turbulent buoyancy flux , the dissipation rate of turbulent kinetic energy, the viscous transport term, the turbulent convection term and the pressure transport term, where

$$\begin{aligned} P &= -\overline{u'w'}S, \quad \epsilon_K = \nu\overline{\left(\frac{\partial u_i'}{\partial x_j}\right)^2}, \quad B = \overline{-b'w'} \\ D_\nu &= \nu\left(\frac{\partial^2 E_K}{\partial z^2}\right), \quad T_K = -\frac{\partial}{\partial z}(\overline{w'E_K}), \quad \Pi = -\frac{\partial}{\partial z}(\overline{w'p'}). \end{aligned} \tag{3.13}$$

We note that B and $\mathcal{B}_t$ are identical and are presented with different notation in this paper with respect to the context in which they are used. In this sense, the sudden introduction of the B term in (3.12) drives the imbalance in the transient energetics as the flow begins to pay its 'kinetic energy toll' to mix the stabilizing buoyancy field (Osborn, 1980).

3.4 Initial time dependence

We first briefly consider the initial time dependence exhibited by our flow properties related to the buoyancy field due to our idealised initial condition of $b = 0$ by plotting $\Gamma = B/\epsilon_K$ as a function of time across a range of vertical locations and simulations in figure 3.1 which has been chosen arbitrarily as a parameter that contains quantities relating to the buoyancy

field to illustrate our point. From the results we observe that Γ initially grows proportional to $(t/T_\tau^0)^2$ and shows clear time dependence up to approximately one eddy turnover time unit ($t/T_\tau^0 \approx 1$). We consider the transport equation for the horizontally averaged mean buoyancy $\overline{b}$ in (3.4). By taking the vertical derivative $\partial/\partial z$ we can obtain the evolution equation for N^2

$$\frac{\partial N^2}{\partial t} = \underbrace{\frac{\partial^2 \mathcal{B}_t}{\partial z^2}}_{\text{Turbulent}} + \underbrace{\frac{\partial \mathcal{B}_m}{\partial z}}_{\text{Molecular}} + \underbrace{\frac{\partial}{\partial z} g\beta q(z)}_{\text{Source}}. \tag{3.14}$$

For our simulations with initial condition $b = 0$ we make the assumption that the turbulent and diffusive terms (first and second terms on the RHS) are negligible at the start of the simulation and the equation reduces to

$$\frac{\partial N^2}{\partial t} = \frac{\partial}{\partial z} g\beta q(z). \tag{3.15}$$

Integrating forward in time from the initial reference time of $t = 0$ we arrive at estimate of $N^2(t)$ at a given horizontal plane

$$\int_0^t \frac{\partial N^2}{\partial t} dt = \int_0^t \frac{\partial}{\partial z} g\beta q(z) dt \quad \Rightarrow \quad N^2(t) = \frac{\partial}{\partial z} g\beta q(z) qt. \tag{3.16}$$

Hence it is clear that initially $N^2 \sim t$. For the remainder of this section, in the interest of simplification, we drop the notation (t), however the dependence on time of flow properties remains implicit. Performing a similar analysis as in the scaling arguements of Garanaik & Venayagamoorthy (2019), we consider the turbulent vertical displacement of a fluid parcel $L_{disp} = w't$. The fluctuating buoyancy b' can therefore be estimated as

$$b' \sim L_{disp} N^2 = w' N^2 t = w' \frac{\partial}{\partial z} g\beta q(z) t^2 \sim t^2. \tag{3.17}$$

If we take one further assumption that buoyancy initially acts as a passive scalar, then it follows that flow properties related to the velocity field are not a strong function of t and remain initially unchanged by the introduction of the buoyancy field. We can thus construct an initial time dependant expression for any flow property that incorporates the buoyancy field. Consider for example the buoyancy flux such that

$$B = \overline{-b'w'} \sim t^2. \tag{3.18}$$

By similar logic we can obtain an expression for Γ

$$\Gamma = \frac{B}{\epsilon_K} \sim t^2, \tag{3.19}$$

as clearly demonstrated in figure 3.1 for all cases where $\Gamma \sim (t/T_\tau^0)^2$ until approximately one tenth of the characteristic eddy turnover time unit, corresponding to the estimate for the time taken for energy injected at large scales to travel down the energy cascade to the dissipative range and hence effect the flow field (see Pope (2000)). Past this timescale buoyancy begins to affect the flow, nullifying our assumption of buoyancy acting as a passive scalar. Meanwhile we expect the turbulent and diffusive terms in (3.14) to become appreciable and influence the growth of N^2, causing it to diverge from a linear $N^2 \sim t$ growth. This creates a set of complex dynamics, causing the buoyancy field to exhibit non-linear time-dependence as the flow adjusts to the sudden imposition of buoyancy. This time-dependence lasts of the order of one eddy turnover time unit ($t/T_\tau^0 \approx 1$) across all simulations and vertical locations, suggesting the adjustment to the buoyancy field is a global rather than local process. For $t/T_\tau^0 \gtrsim 1$ temporal variability becomes negligible and Γ begins to evolve at a quasi-steady rate. We note similar dependence on the initial eddy turnover timescale has been observed in previous studies with distinctly different flow configurations yet with a similar $b = 0$ initial condition (Métais & Herring, 1989; Venayagamoorthy & Stretch, 2006; Maffioli & Davidson, 2016), suggesting some universality on the eddy turnover timescale for the non-linear adjustment of the flow. Subsequently we can expect that for $t \gtrsim 1$, mixing defined through B and hence Γ and K_ρ become independent of the initial condition and evolve relative to local processes. Furthermore, it follows that for $t/T_\tau^0 \gtrsim 1$ we can expect locally based parametrization schemes for mixing to become applicable to our flow.

3.5 Flow evolution overview

In this section we present a qualitative overview of the flow's evolution from an initially neutral isothermal state to that of stationary stably stratified turbulence. Where relevant, we present the data for our high Reynolds number simulation R900L1 as a representative case that displays behaviour typical of all simulations. We further note that to to minimize

noise and present clear behavioural trends when presenting vertical profiles, transient data is averaged across intervals of $\Delta t/T_\tau^0 = 0.5$ non-dimensional time units using a centrally weighted moving average filter.

3.5.1 Response of bulk flow parameters

At a global level the transient response of open-channel flow can be described by the evolution of the (time-varying) friction Reynolds (Re_τ) and Richardson numbers (Ri_τ), which are defined as

$$Re_\tau = \frac{u_\tau \delta}{\nu}, \qquad Ri_\tau = \frac{\Delta \bar{b} \delta}{u_\tau^2}, \tag{3.20a, b}$$

where $\Delta \bar{b} = \bar{b}(\delta) - \bar{b}(0)$ is the buoyancy difference across the channel. As demonstrated in Kirkpatrick *et al.* (2019) (henceforth denoted as KWAZ19), it is further useful to consider both Re_τ and Ri_τ as a competition of timescales such that

$$Re_\tau = \frac{T_\tau}{T_\nu}, \qquad Ri_\tau = \frac{T_\tau^2}{T_N^2}, \tag{3.21a, b}$$

where T_τ, T_ν and T_N are the bulk friction, viscous and buoyancy timescales respectively defined as

$$T_\tau = \frac{\delta}{u_\tau}, \qquad T_\nu = \frac{u_\tau^2}{\nu}, \qquad T_N = \left(\frac{\Delta \bar{b}}{\delta}\right)^{-1/2} \tag{3.22a, b, c}$$

Hence, Re_τ and Ri_τ can be interpreted as the competition between the time scale associated with large domain-scale shear induced motions against the dampening effects of viscous and buoyancy processes respectively.

Figure 3.2(a) shows the evolution of Re_τ normalized by the initial/final Reynolds number Re_τ^0 plotted against t/T_τ^0 for all simulations. From the results it is clear that the evolution of the flow can be broadly described by two periods. Firstly, as outlined in Buren *et al.* (2017) by considering the budget for the Reynolds stress term $\overline{-u'w'} = \mathcal{M}_t$, it can be shown that the flow undergoes a 'suppression' or 'decay' period during which the sudden effects of stable stratification act to suppress local turbulence through the dampening of the vertical velocity fluctuation w' and subsequently the the turbulent momentum flux $\mathcal{M}_t$. This creates an inbalance between the pressure gradient and the total momentum flux which subsequently

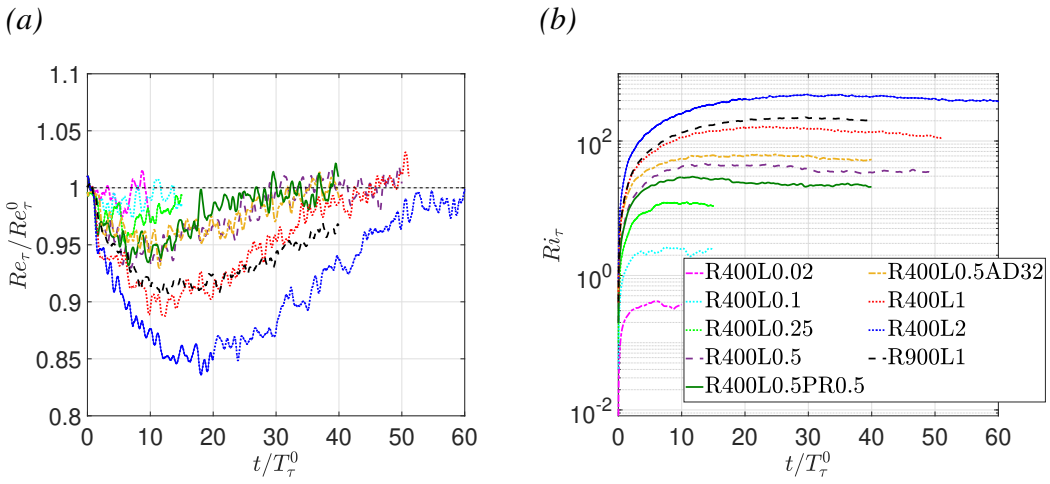

FIGURE 3.2: Time response of bulk flow properties plotted against t/T^0_τ. (a) Time varying friction Reynolds number Re_τ normalized by initial/final friction Reynolds number Re^0_τ, (b) Friction Richardson number Ri_τ.

causes a global suppression of turbulence across the channel and is reflected in the drop of Re_τ. As the flow accelerates to develop the mean shear profile such that $\mathcal{M}_m$ increases to account for the inbalance, the flow is able to extract more energy from the mean shear and subsequently undergoes a 'recovery' period in which turbulence re-intensifies across the channel and Re_τ grows to converge towards its final stationary value. We observe that through the increase of the stability parameter λ^0 or reduction of inertial range through decreasing Re^0_τ, the duration and severity of the 'suppression' period is amplified. Meanwhile, changes in turbidity profile $\alpha\delta$ or Pr cause relatively negligible effects on the transient response of Re_τ.

The 'suppression' and 'recovery' behaviour is also evident in the evolution of Ri_τ plotted against t/T^0_τ in figure 3.2(b). During the initial 'suppression' period, Ri_τ grows monotonically with time to a clear peak as $\Delta\overline{b}$ grows with the increasing stratification profile, while u_τ is suppressed. During the 'recovery' period, the increase in turbulent mixing in the upper channel causes $\Delta\overline{b}$ to marginally decrease, while the convergence towards momentum flux equilibrium is reflected in an according increase in u_τ. Subsequently Ri_τ decreases slightly in the 'recovery' period before plateauing at its final stationary value. We observe that with increasing λ^0, both the growth rate and final value of Ri_τ is increased. Through comparison of cases R900L1 and R400L1, we can observe that an increase in Re^0_τ causes an increase to both

the initial growth rate and final value of Ri_τ. This can be explained under the consideration that near the free surface and at our parameter range, stable stratification suppresses turbulence to the extent that the flow relaminarizes and enters a diffusive regime. Within this regime turbulent mixing is so severely suppressed, that the vertical transport of heat is almost entirely governed by the process of molecular diffusion. As the heat input through $q(z)$ is concentrated near the free surface and within this quasi-laminar regime, an increase in Re_τ^0 acts to reduce the molecular and hence effective diffusivity within this region. This subsequently reduces the downward transport of heat within this regime and causes the heat to be essentially 'trapped' within the upper layer of the channel. Accordingly this is reflected in an increase of $\Delta\bar{b}$ and Ri_τ. Analogously, increasing the concentration of heat input near the surface with increasing turbidity parameter $\alpha\delta$ or reduction of diffusivity with increasing Pr causes qualitatively similar behaviour.

3.5.2 Flow visualizations

Figures 3.3 and 3.4 show the evolution of the buoyancy (b) and dissipation rate of turbulent kinetic energy (ϵ_K) fields respectively in the $x-z$ plane for our representative case R900L1, which provide visual evidence for the 'suppression' and 'recovery' behaviour described in §3.5.1. We note at $t/T_\tau^0 = 33$ the flow obtains both buoyancy and momentum flux equilibrium, as will be shown in further detail in §3.7.

Initially we observe that the channel has a turbulence structure typical of a turbulent neutral boundary layer, characterized by large wall-generated turbulent structures of size $\mathcal{O}(\delta)$ dominating the interior layer. Meanwhile as demonstrated in §3.4, during the initial adjustment period of $t/T_\tau^0 < 0.1$, buoyancy acts purely as a passive scalar and grows directly proportional to $q(z)$. As buoyancy suppresses the turbulence in the bulk of the channel, the mean flow subsequently accelerates to create the mean shear profile and account for the momentum inbalance. Due to the increasing strength of stable stratification and relaxation of the mean shear at the top boundary, we observe the formation of a quasi-laminar region developing at the free surface where turbulent mixing is essentially suppressed. We further observe the formation of braided-eye overturning type shear instabilities that show similarity to the well

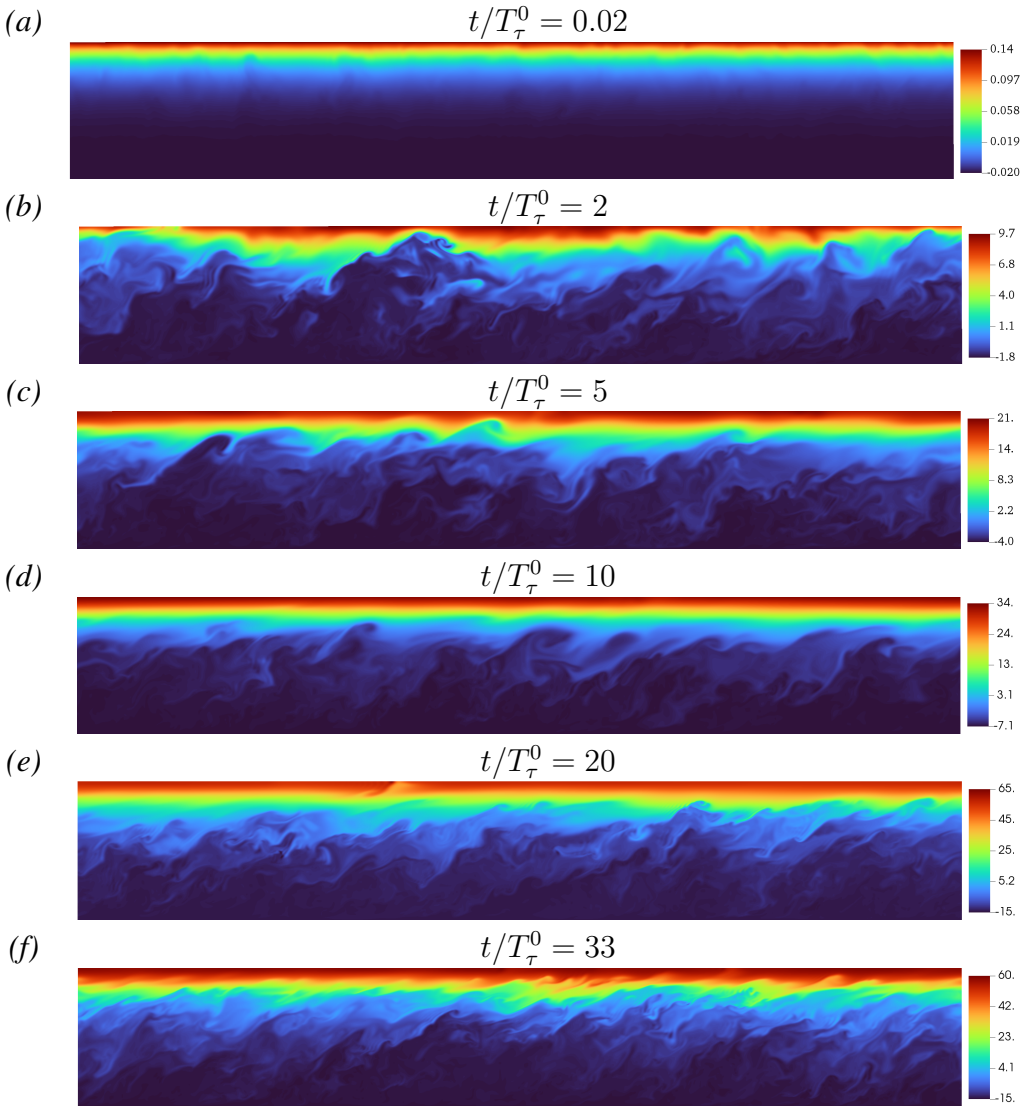

FIGURE 3.3: Evolution of instantaneous flow visualizations in the vertical (x, z) plane for case R900L1 of the buoyancy field b. Colour scale is linear and varies in each image to highlight features. Flow is moving left to right.

known Kelvin-Helmholtz instability (KHI) forming in the bulk flow shear layer, causing overturning of the buoyancy interface as the overturning structures are ejected from the shear layer towards the free surface. By $t/T_\tau^0 = 10$ the 'suppression' of turbulence in the central and upper channel is most significantly pronounced and the extent of the quasi-laminar region thickness reaches a maximum value with a clearly defined sharp buoyancy interface. As the flow continues to accelerate and is able to extract more energy from the increasing mean shear in the channel, the flow transitions into the 'recovery' period and we clearly observe

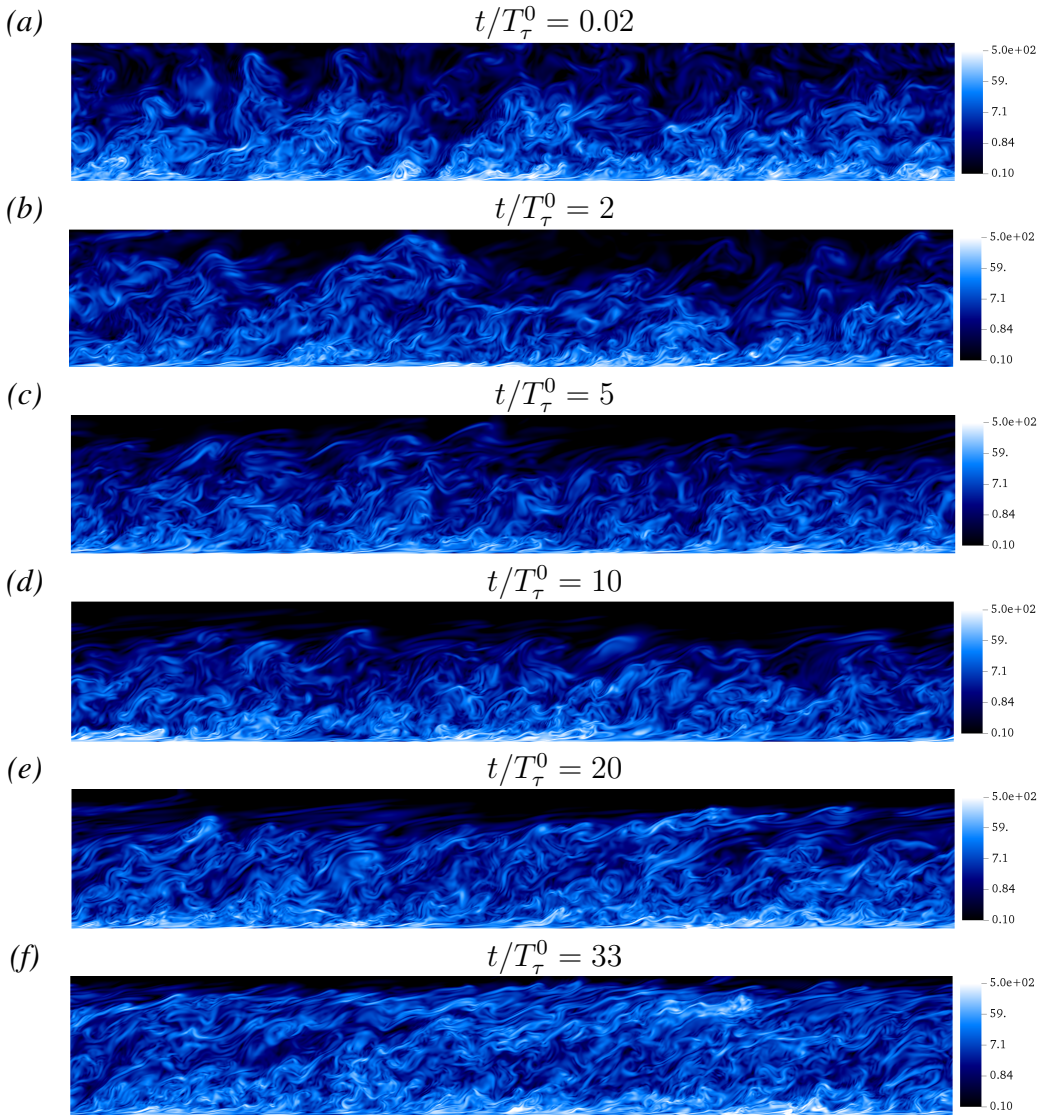

FIGURE 3.4: Evolution of instantaneous flow visualizations in the vertical (x, z) plane for case R900L1 of the dissipation rate of kinetic energy field ϵ_K. Colour scale is logarithmic and is constant for all images to highlight turbulence intesnity. Flow is moving left to right.

that turbulence in the bulk of the channel reintensifies with the increasing development of small-scale dissipative structures, similar to the stationary results of WAKN15 and KWAZ19. As the channel continues to 'recover', the thickness of the quasi-laminar region is significantly reduced and the overturning events at the turbulent-laminar interface become more frequent extending all the way to free surface. In contrast, the turbulence structure in the lower and near-wall regions is only weakly effected by stable stratification.

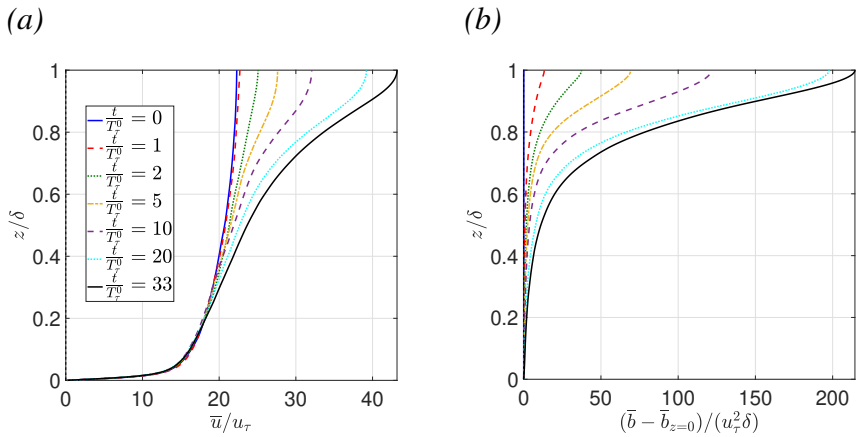

FIGURE 3.5: Evolution in time of the vertical profiles of: (a) mean streamwise velocity $\overline{u}$. (b) Mean buoyancy $\overline{b}$. All data plotted for case R900L1

3.5.3 Evolution of mean flow profiles

We first consider the evolution of the vertical mean flow profiles for our representative case R900L1.

Figure 3.5(a) shows the evolution in time of vertical profiles of the mean streamwise velocity $\overline{u}$ normalized by u_τ and $u_\tau^2\delta$ respectively. The profile initially displays typical behaviour for neutral channel turbulent flow (Moser *et al.*, 1999), with rapid growth of the velocity within the inner boundary layer before approaching a plateau in the bulk of the channel. Within the bulk of the flow, as the shear develops to account for the suppression of turbulence, we observe an increase in the mean velocity until the final profile displays clear inflectional behaviour consistent with the stationary results of WAKN15.

Figure 3.5(b) similarly shows the evolution time of vertical profiles of the mean buoyancy $\overline{b}-\overline{b}_{z=0}$ normalized by $u_\tau^2\delta$. From its initial isothermal state, the mean buoyancy profile shows steady development across the channel throughout the entire evolution of the flow as the mean stratification profile develops. In particular the inhomogeneity of the flow's stratification profile becomes apparent with a clear concentration of high buoyancy near the upper portion of the channel where the heating is strongest and where we have visually observed the formation of a quasi-laminar layer in figures (3.3- 3.4).

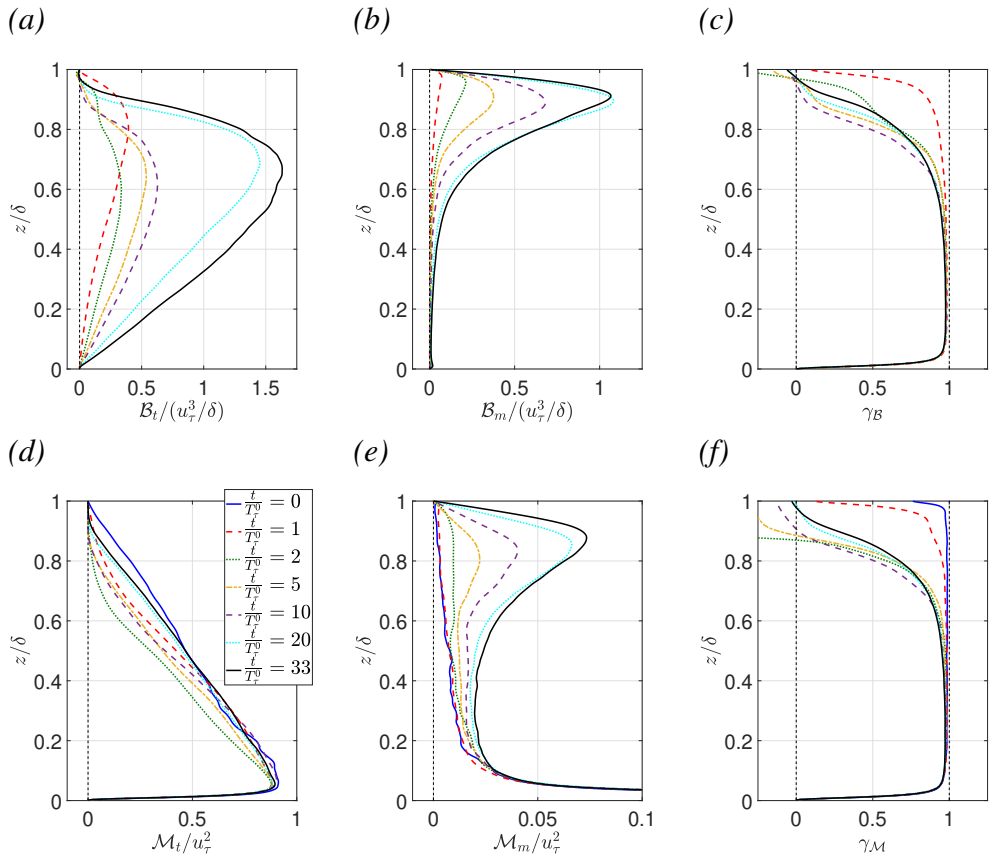

FIGURE 3.6: (a) Evolution of the turbulent buoyancy flux $\mathcal{B}_t$, (b) molecular buoyancy flux $\mathcal{B}_m$ and (c) buoyancy flux turbulent fraction $\gamma_\mathcal{B}$ as a function of z/δ. (d-f) Evolution of the turbulent momentum flux $\mathcal{M}_t$, Same as (a-c) but for the momentum flux $\mathcal{M}$. All data plotted for case R900L1

3.5.4 Evolution of the buoyancy and momentum fluxes

We now consider the evolution of the turbulent and molecular components of the buoyancy and momentum fluxes. All figures within this section again present results from our representative case R900L1.

Figures 3.6 (a) and (b) show the evolution in time of vertical profiles of $\mathcal{B}_t$ and $\mathcal{B}_m$ non-dimensionolized by u_τ^3/δ. From the results we observe rapid growth in both $\mathcal{B}_t$ and $\mathcal{B}_m$ across the entire channel depth from its initial isothermal state as the flow responds to the radiative heating. As demonstrated previously, during the initial adjustment time of one eddy turnover time unit, it can be readily derived that initially the development of the fluxes evolve according

to

$$\mathcal{B}_m(z,t) \sim \frac{\partial}{\partial z}\kappa g\beta q(z)t, \qquad \mathcal{B}_t(z,t) \sim w'^2\frac{\partial}{\partial z}g\beta q(z)t^2. \tag{3.23a, b}$$

Hence explaining the initial rapid growth of both buoyancy fluxes across the channel. As the fluxes develop and the turbulent and molecular terms in (3.14) no longer become negligible, the peaks progressively shift away from the free surface towards towards their stationary values as dictated through the boundary conditions and reflected in (3.10). By $t/T_\tau^0 \approx 5$, in agreement with our visual observations of re-laminarazition at the free surface, a region develops for $0.9 < z/\delta < 1$ where turbulent mixing is fully suppressed and $\mathcal{B}_t \approx 0$. Within this region we observe counter-gradient behaviour in $\mathcal{B}_t$ as observed in numerous past studies of very stable flow (Armenio & Sarkar, 2002; García-Villalba & del Álamo, 2011; Williamson *et al.*, 2015; Howland *et al.*, 2020). As the flow continues to evolve and enters the 'recovery' period, both $\mathcal{B}_t$ and $\mathcal{B}_m$ continue to display steady growth across the channel until they reach a state of quai-stationarity at $t/T_\tau^0 \approx 33$, corresponding to the plateau in Ri_τ observed in figure 3.2. Furthermore, as the turbulence intensity within the channel continues to recover, the subsequent increase in mixing within the upper portion of the channel acts to reduce the thickness of the upper quasi-laminar layer. This is reflected in the reduction of the region where $\mathcal{B}_t \approx 0$ during the 'recovery' period and is in direct agreement with our visual observations from figures 3.3 and 3.4.

It is useful to also consider the relative contribution to the total buoyancy flux from its individual components. We subsequently define $\gamma_\mathcal{B}$ as the turbulent buoyancy flux fraction such that

$$\gamma_\mathcal{B} = \frac{\mathcal{B}_t}{\mathcal{B}_t + \mathcal{B}_m}. \tag{3.24}$$

We note that $\gamma_\mathcal{B}$ can be directly linked to the eddy diffusivity K_ρ as it can be readily shown that

$$\gamma_\mathcal{B} = \frac{\mathcal{B}_t}{\mathcal{B}_t + \mathcal{B}_m} \equiv \frac{B}{(K_\rho + \kappa)N^2} = \frac{K_\rho}{K_\rho + \kappa} \tag{3.25}$$

Figure 3.6(c) shows the temporal evolution of the vertical profile of $\gamma_\mathcal{B}$. The results again strongly depict the 'suppression' and 'recovery' behaviour that define our flow. Initially for $0 < t/T_\tau^0 < 1$ while buoyancy essentially acts as a passive scalar we observe that the majority of the total buoyancy flux is comprised of its turbulent component. This is analogous to say

that $K_\rho/\kappa \gg \mathcal{O}(1)$ for the entire channel depth, with the exception of the near-wall and near-surface regions where the viscous and diffusive forces strongly effect the flow (Pope, 2000; Calmet & Magnaudet, 2003). As turbulent mixing is suppressed and the mean stratification profile develops we observe that $\gamma_{\mathcal{B}}$ decreases within the vertical range $z/\delta \gtrsim 0.5$, with the suppression being most severe at $t/T_\tau^0 \approx 10$ in agreement with our earlier observations. During the 'recovery' period, turbulence re-intensifies and $\gamma_{\mathcal{B}}$ begins to increase again in the upper half of the channel before reaching its stationary value at $t/T_\tau^0 \approx 33$. Conversely, within the lower vertical extent of $z/\delta \lesssim 0.5$ where the flow is only weakly effected by stratification, $\gamma_{\mathcal{B}}$ experiences negligible changes throughout the entirety of the flows evolution. We note that in the quasi-laminar layer $\gamma_{\mathcal{B}} < 0$ due to the counter gradient fluxes within this regime.

Figures 3.6(d) and (e) show the evolution in time of vertical profiles of $\mathcal{M}_t$ and $\mathcal{M}_m$ non-dimensionolized by u_τ^2. From the results we observe a defining feature of our temporally evolving flow. Due to the suppression of w' through the sudden imposition of stable stratification, the turbulent momentum flux $\mathcal{M}_t$ rapidly drops from its initial value across the entire channel with the exception of the near-wall region. We further note that this suppression is a relatively 'rapid' process is most severe in the very initial stages of the flows evolution for $0 \lesssim t/T_\tau^0 \lesssim 2$, past which the turbulent momentum flux begins to slowly recover towards stationarity. In contrast to the 'rapid' suppression of $\mathcal{M}_t$, the acceleration of the mean flow and development of the mean shear profile reflected in $\mathcal{M}_m$ is a relatively 'slow' process with a clear delay period of $t/T_\tau^0 \approx 1$ during which the shear profile remains unchanged. It is this disparity between the 'rapid' suppression of the turbulent momentum flux and the 'slow' acceleration of the mean flow that defines the shear stress in-balance accross the channel and drives the structural changes within the flow. This behaviour directly agrees with that observed in the studies of neutral channel flow suddenly subject to bottom surface cooling (Flores & Riley, 2011; Atoufi *et al.*, 2020). Furthermore, the turbulent momentum flux $\mathcal{M}_t$ approaches zero in the upper quasi-laminar region with similar counter-gradient behaviour. Within this region where the total momentum flux is predominantly provided through viscous diffusion, we observe that the mean shear profile reflected through $\mathcal{M}_m$ displays a linear profile away from the free surface as dictated by (3.11).

Figure 3.6(f) shows the evolution of the vertical profile of the turbulent momentum flux fraction $\gamma_{\mathcal{M}}$, which can similarly be defined through the eddy viscosity K_M, such that

$$\gamma_{\mathcal{M}} = \frac{\mathcal{M}_t}{\mathcal{M}_t + \mathcal{M}_m} = \frac{K_M}{K_M + \nu} \tag{3.26}$$

From the results we observe that the evolution of $\gamma_{\mathcal{M}}$ displays qualitatively similar behaviour to that of $\gamma_{\mathcal{B}}$. Initially in its neutral state $\gamma_{\mathcal{M}} \approx 1$ for almost the entire channel depth with the exception of the near-wall and near-surface regions. In the upper half of the channel $\gamma_{\mathcal{M}}$ analogously displays 'suppression' and 'recovery' behaviour and in the bottom half remains relatively unchanged throughout the entire evolution of the flow. Again we observe negative values for $\gamma_{\mathcal{M}}$ within the upper quasi-laminar layer due to the development of counter-gradient fluxes.

3.5.5 Evolution of dominant energetic terms

We also consider the transient response of the flow from the perspective of energetics. Figure 3.7 shows the evolution of the vertical profiles of the individual terms within the turbulent kinetic energy budget defined in (3.12) for case R900L1.

Figure 3.7(a) shows the evolution of E_K normalized by u_τ^2. The results similarly demonstrate clear 'suppression' and 'recovery' behaviour that defines the evolution of our flow. E_K is initially reduced across the entire channel with the exception of the near-wall region as turbulence is suppressed. We again observe that this suppression is 'rapid' with the majority of the suppression occurring within the $0 < t/T_\tau^0 < 2$ non-dimensional time period and remains in this suppressed state until approximately $t/T_\tau^0 \approx 10$ when the flow enters the 'recovery' period. Within the upper quasi-laminar layer of $z/\delta \gtrsim 0.9$ we observe that turbulent kinetic energy is almost entirely suppressed and $E_K \approx 0$.

Figures 3.7(b-d) show the evolution of the dominant terms within the budget P, ϵ_K and B normalized by u_τ^3/δ. We note that as $B = \mathcal{B}_t$, figure 3.7(d) is identical to figure 3.7(a) and has been included again for clarity with respect to the energetic response of the flow.

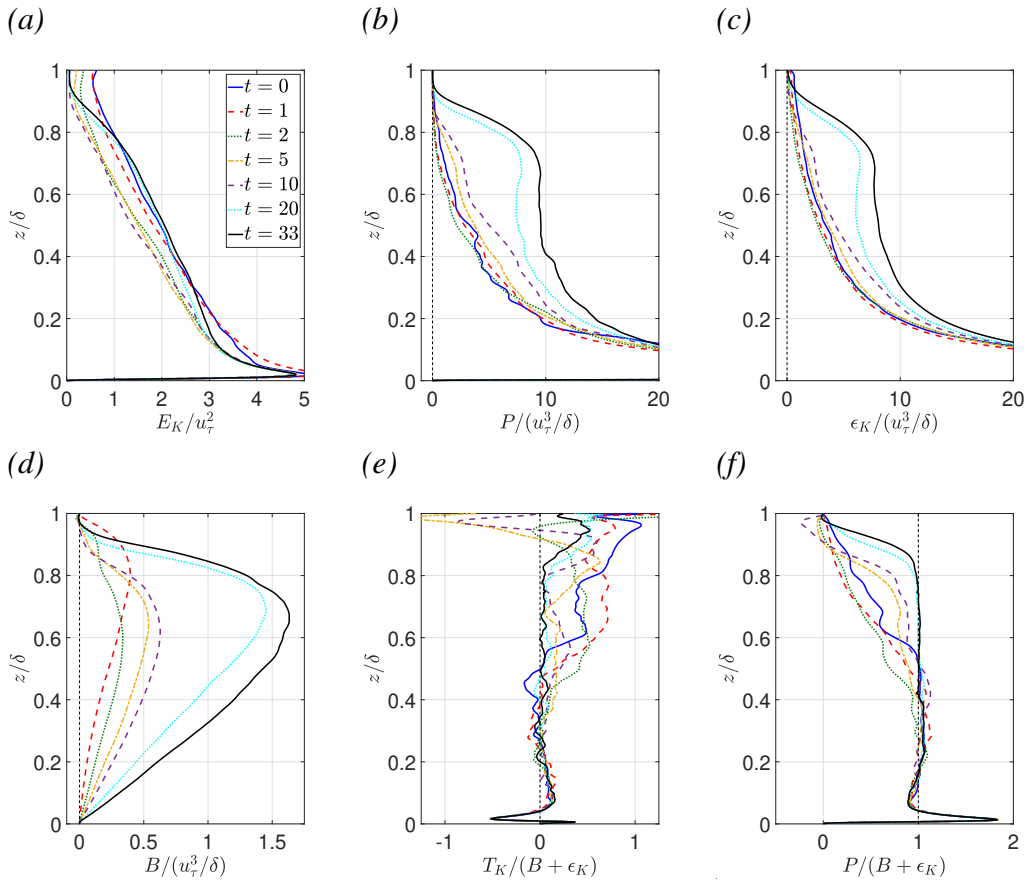

FIGURE 3.7: Evolution of the vertical profiles of key energetic quantities: (a) the turbulent kinetic energy E_K, (b) TKE production term P, (c) TKE dissipation rate ϵ_K, (d) turbulent buoyancy flux B, (e) the normalized turbulent convection term $T_K/(B+\epsilon_K)$, (f) local energetic equilibrium ratio $P/(B+\epsilon_K)$. All data plotted for case R900L1

From the results we can observe qualitatively similar behaviour in the evolution of the production and dissipation terms. with the exception of the near-wall region, we observe that both P and ϵ_K are reduced relative to their initial profiles during the initial suppression period of $0 < t/T_\tau < 2$ as w' is suppressed. We note the drop in P is marginally more severe than ϵ_K as the growing stratification profile initially constrains the larger scales associated with production before the smaller dissipative scales (Lindborg, 2006). In combination with the sudden development of the buoyancy flux which acts as a kinetic energy sink, this drives the kinetic energy imbalance within the flow causing the global drop in E_K across the channel. As the flow accelerates, the increasing mean shear allows the central bulk flow to extract more turbulent kinetic energy from the mean flow locally through shear instabilities rather than

wall-generated structures from below. Subsequently, both P and ϵ_K begin to recover and eventually exceed their respective initial values with a clear secondary peak forming in the region of maximum shear at $0.7 < z/\delta < 0.8$ in agreement with our visual observations of vigorous overturning driven mixing within this region.

Figures 3.7(e) shows the evolution of the turbulent convection transport terms T_K, normalized by the total loss of TKE: $B + \epsilon_K$. We observe that in the initial neutral state, for $z/\delta \gtrsim 0.5$ turbulent convection T_K acts as an appreciable source of E_K as wall generated turbulence is ejected upwards from the wall. This falls in agreement with the stationary results for $\lambda = 0$ of Williamson *et al.* (2015) and the DNS study of neutral channel flow of Moser *et al.* (1999). This region grows to $z/\delta \gtrsim 0.3$ during the initial suppression period of $0 < t/T_\tau^0 < 2$ as $\overline{-u'w'}$ and hence local production through P is rapidly suppressed. As the increasing mean shear causes P to grow in the central shear layer we observe that the relative contribution to E_K through turbulent convection continues to decrease in the bulk of the flow as T_K eventually becomes negligible in the energetic budget. In the final quasi-stationary state T_K is only appreciable in the near-surface and and near-wall regions, consistent with the stationary results of Williamson *et al.* (2015).

Figure 3.7(h) shows the production term P normalized by $(B + \epsilon_K)$ and depicts the local equilibrium ratio such that a value of $P/(B + \epsilon_K) \approx 1$ represents an energetic state of the flow that is in balance between the inherently local terms P, B, ϵ_K. As discussed in §1, the assumption of $P/(B + \epsilon_K) \approx 1$ is regularly invoked in literature, in particular with respect to parametrization mixing models for the eddy diffusivity K_ρ (Osborn & Cox, 1972; Osborn, 1980; Shih *et al.*, 2005; Gregg *et al.*, 2018). From our results it is clear that in the case of the developing channel flow, this assumption is significantly invalid for the majority of the flows evolution. In its initial neutral state, the flow is only in a state of equilibrium within region of $50 \lesssim z^+ \lesssim 0.5Re_\tau$ in agreement with the studies of Moser *et al.* (1999) and Williamson *et al.* (2015). During the initial suppression period of $0 < t/T_\tau^0 < 2$ we observe that the equilibrium region shrinks to an upper limit of $z/\delta \approx 0.3$ as local production is suppressed and turbulent convection becomes important in the vertical transport of TKE. Past this, the increasing mean shear and local production causes the local equilibrium ratio to recover towards unity within

the region of $z^+ \gtrsim 50$ and $z/\delta \lesssim 0.8$. Above this depth, the flow deviates from a state local equilibrium as the transport terms become appreciable. As we have visually observed in figures 3.3 and 3.4, this upper region approaches a quasi-laminar state. It is hence unclear whether this deviation from local equilibrium occurs due to the surface confinement effects described in Calmet & Magnaudet (2003) or due the laminarization of the flow. As surface confinement effects are outside the scope of this dissertation, we leave this as room for future work. Accordingly, the significant takeaway from these results is that unlike the destratifying case of KWAZ19 where local equilibrium is maintained for the majority of the destratification process, for a significant portion of our flows evolution, the local equilibrium assumption within the upper half of the channel becomes strictly invalid.

3.6 Prediction of suppressed mixing regime

In the context of the discussion presented in §1 regarding the stratified river flows of Australia that form the motivation behind this thesis, we seek to define a bulk flow parametrization for the global suppression of turbulent mixing across the channel. We propose that suitable bulk metrics of turbulent mixing across the channel are the normalized domain averaged eddy diffusivity and viscosity of the form

$$\frac{\langle K_\rho \rangle}{\kappa} = \frac{\frac{1}{\delta}\int_0^\delta K_\rho dz}{\kappa}, \qquad \frac{\langle K_M \rangle}{\nu} = \frac{\frac{1}{\delta}\int_0^\delta K_M dz}{\nu}. \tag{3.27a, b}$$

Initially we consider the scaling of the bulk averaged eddy diffusivity $\langle K_\rho \rangle$, which can recast using dimensional analysis of the form

$$\langle K_\rho \rangle \sim U_*^2 T_*, \tag{3.28}$$

where U_* and T_* are the velocity and time scales pertinent to the global state of the flow. We note this is analogous to a classic mixing length argument of the form $K_\rho \sim L_* U_*$ as it can clearly be shown that the pertinent mixing length $L_* = U_* T_*$.

Firstly, we take the assumption that the turbulent mixing within the flow is predominantly shear driven such that we expect the friction velocity which defines the shear in the flow to be the pertinent velocity scale such that $U_* = u_\tau$.

Secondly, we hypothesise that the global flow may be loosely described by two limit regimes. One where the effect of stable stratification is relatively negligible and the flow approaches neutral conditions and the mixing of the buoyancy field may be treated as a passive scalar. Within this regime we expect the eddy turnover time scale to define the dynamics of the flow such that $T_* \sim T_\tau$. Accordingly we obtain:

$$\langle K_\rho \rangle \sim u_\tau^2 T_\tau = u_\tau^2 \frac{\delta}{u_\tau} = u_\tau \delta. \tag{3.29}$$

Normalizing both sides by $\kappa(\nu/\nu)$ we obtain:

$$\frac{\langle K_\rho \rangle}{\kappa} \sim \frac{u_\tau \delta}{\kappa} = \frac{u_\tau \delta}{\kappa} \frac{\nu}{\nu} = PrRe_\tau. \tag{3.30}$$

A such the resulting scaling suggests that the global mixing of the buoyancy field displays no dependence on the stratification of the flow, analogous to that of neutral channel flow (Moser *et al.*, 1999).

Conversely, we propose that for flow where stable stratification strongly suppresses the turbulent fluxes as seen in figures 3.6(c.f), it is reasonable to assume that processes occurring at the global buoyancy time scale dominate the flow, such that $T_* \sim T_N$. This is in direct agreement with the experimental results of Buren *et al.* (2017) where it was shown that the global time scale T_N scaled the late time evolution of the Reynolds stresses of the flow in a stable boundary layer. Hence, we obtain:

$$\langle K_\rho \rangle \sim u_\tau^2 T_N = u_\tau^2 \frac{\delta^{1/2}}{\Delta \bar{b}^{1/2}}. \tag{3.31}$$

We can hence obtain an expression in terms of Ri_τ of the form:

$$\langle K_\rho \rangle \sim u_\tau^2 \frac{\delta^{1/2}}{\Delta \bar{b}^{1/2}} \frac{\delta^{1/2}}{\delta^{1/2}} = Ri_\tau^{-1/2} u_\tau \delta \tag{3.32}$$

and similarly by normalizing both sides by $\kappa(\nu/\nu)$ we obtain the final result:

$$\frac{\langle K_\rho \rangle}{\kappa} \sim PrRi_\tau^{-1/2} Re_\tau. \tag{3.33}$$

We note a similar $Ri_\tau^{-1/2}$ dependence on the evolution of the total buoyancy flux and stratification rate was empirically observed in KWAZ19.

To predict the global eddy viscosity $\langle K_M \rangle$, we take the assumption that for the majority of the domain (excluding flow close to either boundary), the local turbulent Prandtl number $Pr_T = K_M/K_\rho$ is approximately unity such that $K_M \sim K_\rho$. As will be shown directly in §5, we have directly shown this to hold for our flow for both the transitional and stationary flow. Hence we similarly obtain two scaling results. For the passive scalar regime we obtain:

$$\frac{\langle K_M \rangle}{\nu} \sim \frac{\langle K_\rho \rangle}{\nu} \sim \frac{u_{\tau\delta}}{\nu} = Re_\tau \tag{3.34}$$

and for the suppressed regime we obtain:

$$\frac{\langle K_M \rangle}{\nu} \sim \frac{\langle K_\rho \rangle}{\nu} \sim Ri_\tau^{-1/2} \frac{u_{\tau\delta}}{\nu} = Ri_\tau^{-1/2} Re_\tau. \tag{3.35}$$

Lastly, a suitable parameter is needed to define the separation of the two regimes. For the stationary case WAKN15 demonstrate that $Re_{\mathcal{L}^0}$ becomes a suitable bulk parameter for the prediction of globally supressed turbulent mixing across the channel, where

$$Re_{\mathcal{L}^0} = \frac{u_\tau^0 \mathcal{L}^0}{\nu}. \tag{3.36}$$

We note that $Re_{\mathcal{L}^0}$ is analogous to the non-dimensional Obhukov length L^+ used in atmospheric literature to predict the collapse of the nocturnal boundary layer (Flores & Riley, 2011; Chung & Matheou, 2012). However for our developing case however $Re_{\mathcal{L}^0}$ loses relevance as the definition of $\mathcal{L}^0$ in (2.14) inherently assumes a stationary and fully developed buoyancy flux profile.

It is however well established that 'locally' the onset of a diffusive regime marked by reduced mixing is well predicted by the buoyancy Reynolds number $Re_B = \epsilon_K/N^2\nu$ (Billant & Chomaz, 2001; Shih *et al.*, 2005; Portwood *et al.*, 2016; Issaev *et al.*, 2022). We can

directly relate this to our estimates of global mixing through bulk parameters by taking two assumptions. Firstly, we assume the established inertial scaling for channel flow of $\epsilon_K \sim u_\tau^3/\delta$ (Moser *et al.*, 1999). Secondly, following the work of KWAZ19, we assume that the local mean buoyancy gradient evolves proportionally to the mean global buoyancy difference across the channel such that $N^2 \sim \Delta\bar{b}/\delta$ such that we obtain:

$$Re_B = \frac{\epsilon_K}{N^2\nu} \sim \frac{u_{\tau^3}\delta}{\Delta\bar{b}\nu\delta} = \frac{u_{\tau^3}}{\Delta\bar{b}\nu}. \tag{3.37}$$

Furthermore, as derived in Billant & Chomaz (2001), in the same sense that Re_B is a 'mixed' parameter such that $Re_B = Re_T Fr^2$, where Re_h and Fr are the turbulent Reynolds number and Froude number respectively, it can be readily shown that the bulk parameter $u_\tau^3/\Delta\bar{b}\nu$ is analogously a mixed parameter that can be decomposed into Re_τ and Ri_τ such that

$$\frac{u_{\tau^3}}{\Delta\bar{b}\nu} = \frac{u_\tau^2}{\Delta\bar{b}\delta}\frac{u_\tau\delta}{\nu} = Ri_\tau^{-1}Re_\tau. \tag{3.38}$$

Accordingly, to account for the viscous and buoyancy forces which may conceivably suppress mixing in the channel, we propose that $Ri_\tau^{-1}Re_\tau$ will act as a logical global parameter for the onset of a reduced mixing regime for our temporally evolving flow analagous to Re_B. Furthermore from figure 3.2, we note that the rate of change in Re_τ is very small relative to Ri_τ during the transitional period of the flow. Hence Re_τ can be assumed to be essentially constant such that we can reasonably approximate:

$$Ri_\tau^{-1/2}Re_\tau \approx Ri_\tau^{-1/2}Re_\tau^0. \tag{3.39}$$

To test our analysis, figures 3.8(a,b) show $\langle K_\rho\rangle/\kappa Pr$ and $\langle K_M\rangle/\nu$ plotted against $Ri_\tau^{-1}Re_\tau$ respectively for all simulations, excluding the data for the adjustment period of $t/T_\tau^0 < 1$. From the results it is clear that our hypothesis is correct and we observe the two limit cases for the global levels of turbulent mixing. For $Ri_\tau^{-1}Re_\tau \gtrsim 100$ the flow approaches an asymptotic mixing state where stratification only weakly suppresses turbulent mixing and both $\langle K_\rho\rangle/\kappa$ and $\langle K_M\rangle/\nu$ appear to plateau to a constant asymptotic value that varies with Pr and Re_τ. This is in agreement with our above analysis suggesting that for the passive scalar regime, global values of turbulent mixing depend only on Pr and Re_τ which remain essentially

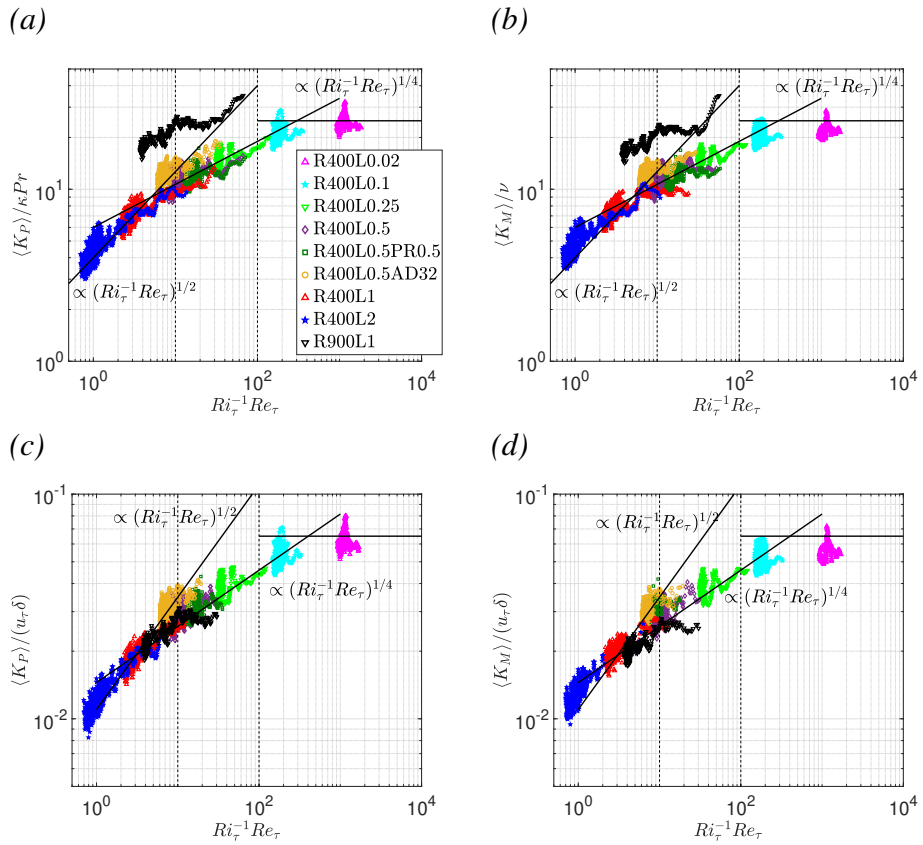

FIGURE 3.8: Normalized, instantaneous measurements of bulk eddy $\langle K_\rho \rangle$ and viscosity $\langle K_M \rangle$ plotted against $Ri_\tau^{-1}Re_\tau$. (a) $\langle K_\rho \rangle/\kappa Pr$ (b) $\langle K_m \rangle/\nu$. (c) $\langle K_\rho \rangle/(u_\tau \delta)$. (d) $\langle K_m \rangle//(u_\tau \delta)$. Vertical dashed lines indicate $Ri_\tau^{-1}Re_\tau = 10, 100$. Solid diagonal lines indicate lines $\propto (Ri_\tau^{-1}Re_\tau)^{1/2}, (Ri_\tau^{-1}Re_\tau)^{1/4}$. All data plotted for $t/T_\tau^0 > 1$

constant for this regime. This is conceptually consistent with the work of Chung & Matheou (2012) who show that for neutral sheared flow, K_ρ/κ and K_M/ν approach asymptotic values defined by the molecular properties, and the ratio of an appropriately defined confinement scale to the Kolmogorov scale.

For $Ri_\tau^{-1}Re_\tau \lesssim 10$ we observe that the channel flow enters a regime of suppressed mixing with clear dependence on the mixed parameter of the form:

$$\frac{\langle K_\rho \rangle}{\kappa Pr} \sim \frac{\langle K_m \rangle}{\nu} \sim (Ri_\tau^{-1}Re_\tau)^{1/2}. \tag{3.40}$$

This result is directly in agreement with our above analysis suggesting a $Ri_\tau^{-1/2}$ dependence on the evolution of the turbulent fluxes for the buoyancy effected regime.

For flow where $10 \gtrsim Ri_\tau^{-1}Re_\tau \lesssim 100$, we observe an intermediate regime where buoyancy begins to suppress turbulent mixing, but at a lesser extent than the $Ri_\tau^{-1/2}$ scaling for a buoyancy dominated regime. Within this regime, from our observation we empirically propose a $(Ri_\tau^{-1}Re_\tau)^{1/4}$ scaling to account for this behaviour which can conceptually be interpreted as a regime where both T_τ and T_N are equally significant.

Due to the clear dependence of the asymptotic values on the molecular properties, we can present the results in a way that clearly shows the separation of the two regimes. We do this by renormalizing bulk eddy diffusivity and viscosity by $\kappa/u_\tau\delta$ and $\nu/u_\tau\delta$ respectively such that we obtain

$$\frac{\langle K_\rho\rangle}{\kappa}\frac{\kappa}{u_\tau\delta} = \frac{\langle K_\rho\rangle}{u_\tau\delta}, \qquad \frac{\langle K_m\rangle}{\nu}\frac{\nu}{u_\tau\delta} = \frac{\langle K_m\rangle}{u_\tau\delta}. \tag{3.41a, b}$$

We note that this formulation can be interpreted in the form of a classic mixing length argument such that the eddy diffusivity term becomes

$$\frac{K_\rho}{u_\tau\delta} = \frac{\overline{-b'w'}}{N^2u_\tau\delta} \sim \frac{b'w'}{N^2u_\tau\delta} \sim \frac{L_E}{\delta}\frac{w'}{u_\tau} \sim \frac{L_E}{\delta}, \tag{3.42}$$

where $L_E = b'_{\text{rms}}/N^2$ is the Ellison length scale describing the size of overturning eddies within the flow (Shih *et al.*, 2005). Analogously, the eddy viscosity term can be interpreted as

$$\frac{K_m}{u_\tau\delta} = \frac{\overline{-u'w'}}{Su_\tau\delta} = \frac{L_M}{\delta}\frac{(\overline{-u'w'})^{1/2}}{u_\tau} \sim \frac{L_M}{\delta}, \tag{3.43}$$

where $L_M = \overline{-u'w'}/S$ is the well known mixing length. In this sense the ratios $\langle K_\rho\rangle/u_\tau\delta$ and $\langle K_M\rangle/u_\tau\delta$ can be interpreted as the bulk ratios of the two respective large energetic length scales L_E and L_M to the confinement scale δ which we expect to asymptote to an upper limit in the neutral case as shown in Chung & Matheou (2012). Furthermore, as has been previously shown in past studies of stratified sheared flow (Mater & Venayagamoorthy, 2014; Issaev *et al.*, 2022), the size of the overturns is well approximated by the mixing length such that $L_E \sim L_M$. Hence we expect both qualitatively and quantitatively similar behaviour in $\langle K_\rho\rangle/u_\tau\delta$ and $\langle K_M\rangle/u_\tau\delta$.

Figures 3.8(c,d) show the ratios $\langle K_\rho\rangle/u_\tau\delta$ and $\langle K_M\rangle/u_\tau\delta$ plotted against $Ri_\tau^{-1}Re_\tau$. Presented in this manner the data across all simulations collapses well on singular lines of scaling that depict qualitatively similar behaviour to figure 3.8(a) and (b) with a clear separation of

the asymptotic passive scalar and suppressed mixing regimes, separated by the transitional value of $Ri_\tau^{-1}Re_\tau = 10$.

The collapse of the results presented within this section across the entire parameter set suggest that the mixed parameter $Ri_\tau^{-1}Re_\tau$ is a relatively robust measure of the global levels of turbulent mixing across the channel. However, we acknowledge that at the limited parameter range explored within this thesis (particularly our modest values of Re_τ), it remains unclear if the transitional values of $Ri_\tau^{-1}Re_\tau \approx 10$ and 100 will hold universally for all Re_τ, Ri_τ and Pr. We suggest rather than exact transitional values, the results within this section should be viewed more broadly such that $Ri_\tau^{-1}Re_\tau = \mathcal{O}(10), \mathcal{O}(100)$ that roughly separate the clearly differing mixing regimes within flow. As such we propose that the results presented here could form the groundwork for the forecasting of reduced mixing rates at the upper layer in real stratified river flows where the bulk flow properties u_τ and $\Delta\bar{b}$ can be readily obtained from field measurements.

3.7 Transition to equilibrium flow

3.7.1 Convergence of buoyancy and momentum fluxes towards equilibrium

In the context of a 'sunrise' scenario for stratified river flow, a central aim of this chapter is the accurate prediction of the time scale at which the flow obtains stationarity as an initially isothermal channel flow is subject to radiative heating. As outlined in §1.2, at a local level the flow's transition to equilibrium conditions can be described by the convergence of the total buoyancy and momentum fluxes towards their respective equilibrium values defined by the ratios $\mathcal{B}/\mathcal{B}_E$ and $\mathcal{M}/\mathcal{M}_E$ respectively. To investigate this, we first consider figure 3.9 which shows $\mathcal{B}/\mathcal{B}_E$ plotted as a function of t/T_τ^0 over a wide range of depths and different simulations.

From the global results we can make two key observations. Firstly, it is clear that from the initially isothermal state of $\mathcal{B} = 0$, the development of the total buoyancy flux and the

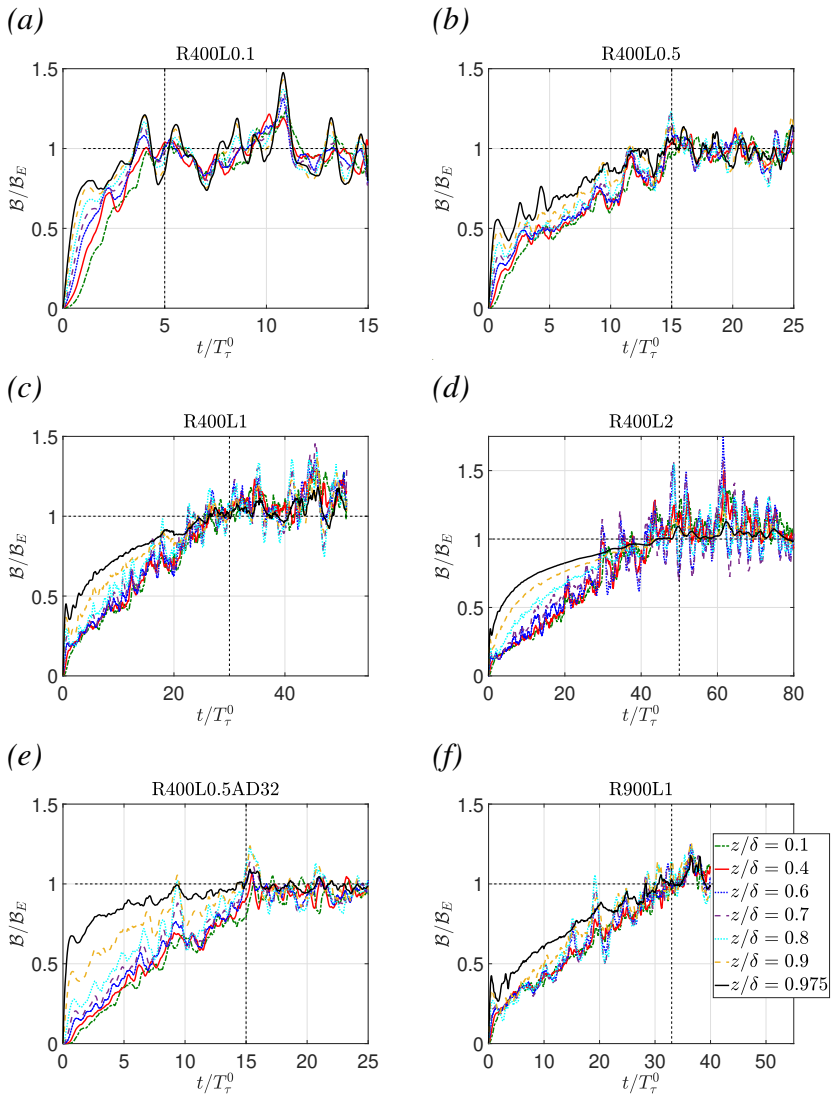

FIGURE 3.9: Evolution for of the local buoyancy flux convergence ratios $\mathcal{B}/\mathcal{B}_E$ as a function of t/T_τ^0 for a range of simulations. Vertical dashed lines correspond to approximate visually estimated values of the final equilibrium convergence time.

transition to buoyancy flux equilibrium is a global process such that local equilibrium at any depth z is obtained simultaneously across the entire channel depth. We note that for all cases this time at which each simulation obtains equilibrium corresponds directly to a plateau of Ri_τ observed in figure 3.2 and is tabulated within table 3.1 as t_e.

Secondly we can observe that initially during the adjustment period of $t/T_\tau^0 \approx 1$, $\mathcal{B}$ grows rapidly and varies with vertical location as both $\mathcal{B}_t$ $\mathcal{B}_m$ evolve according to (3.23). Past this

time scale, the local convergence of the total buoyancy flux towards equilibrium follows an essentially linear monotonically increasing trajectory regardless of depth or local levels strength of stratification. The exception to this behaviour are vertical locations within the upper quasi-laminar regime where the total buoyancy flux is comprised almost entirely of its molecular component (i.e. $\gamma_{\mathcal{B}} \approx 0$). Within this regime where the turbulent fluxes and hence the turbulent term in (3.14) are heavily suppressed, the background stratification N^2 and subsequently $\mathcal{B}_m$ initially grow at a relatively more rapid rate than that of the turbulent flow within the channel. The final equilibrium convergence time however remains constant.

We further observe that these two findings hold irrespective of the external parameter set Re_τ^0, λ^0, $\alpha\delta$. The results subsequently suggest that although the mixing of the buoyancy field at a given depth is a local process that is defined by the relevant local scales pertinent to the varying mixing regimes within the flow (as will be shown in §4), the convergence towards an equilibrium buoyancy flux profile in time is rather a global phenomenon that we expect to scale with bulk flow properties similarly to the prediction of the bulk measures of eddy diffusivity and viscosity as in §3.6.

Through comparison of cases R400L0.5 and R400L1 it is clear that for a given Re_τ an increase in stratification strength through λ^0 (decreasing $Ri_\tau^{-1}Re_{\tau)}$ acts to increase the thickness of the quasi-laminar layer and hence an increasing portion of the upper channel deviates from the constant trajectory towards equilibrium. Analogously through comparison of cases R400L1 and R900L1, a decrease in Re_τ^0 acts causes a similar effect. Similarly, through increasing turbidity parameter $\alpha\delta$ we see an increase in Ri_τ. Hence, the increase in heating near the upper surface causes larger local buoyancy gradients and contributions from $\mathcal{B}_m$ to the total buoyancy flux causing similar deviation from a constant trajectory towards equilibrium.

Figure 3.10 shows the evolution of the momentum flux equilibrium ratio $\mathcal{M}/\mathcal{M}_E$ for the same extended data set presented in figure 3.9. During the initial suppression period of $0 \lesssim t/T_\tau^0 \lesssim 2$ where $\mathcal{M}_t$ is rapidly suppressed and before the mean shear has begun to develop, the total momentum flux is accordingly reduced for all simulations. The severity of the suppression relative to equilibrium is accordingly amplified with increasing distance from the wall due to the inhomogeneity of the flow as both the strength of stratification

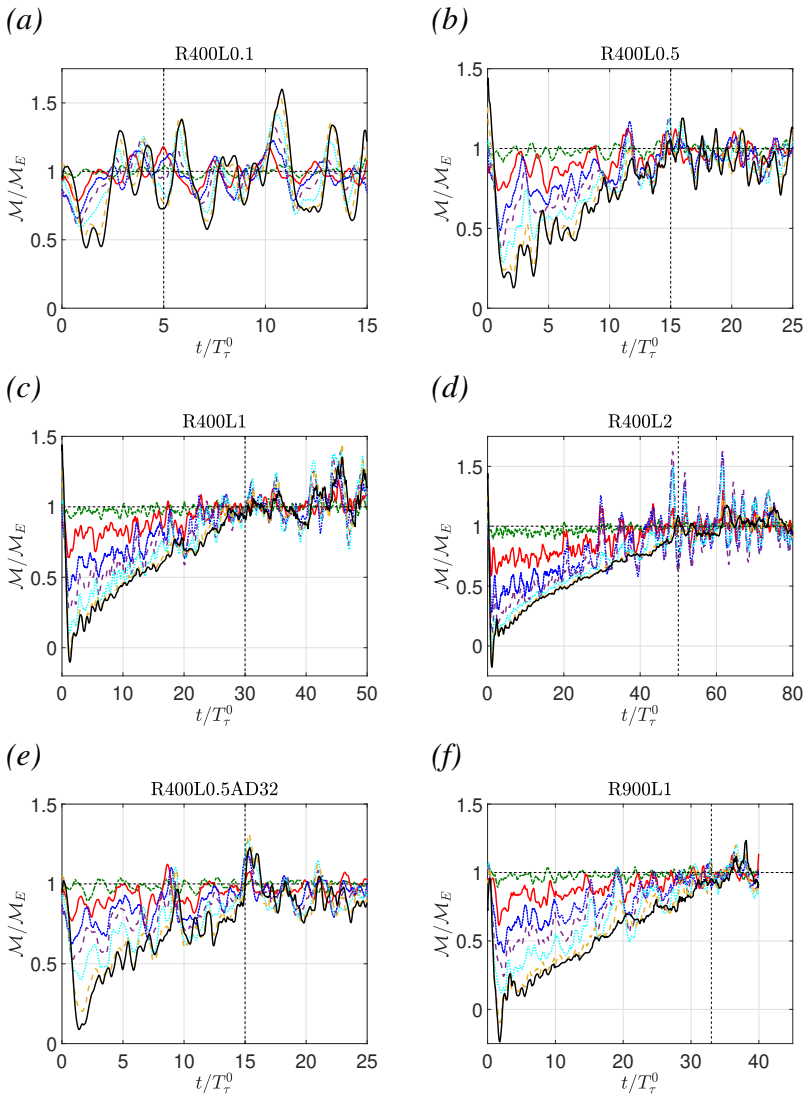

FIGURE 3.10: Evolution for of the local momentum flux convergence ratios $\mathcal{M}/\mathcal{M}_E$ as a function of t/T_τ^0 for a range of simulations. Vertical dashed lines correspond to approximate visually estimated values of the final equilibrium convergence time. Legend same as for figure 3.9.

increases whilst the turbulence intensity decreases. Similarly, increases in λ^0 or decreases in Re_τ further amplify the suppression and deviation from momentum flux equilibrium. Past the initial suppression, the mean shear profile begins to develop and the momentum flux recovers monotonically towards equilibrium. Most significantly we observe that the convergence towards momentum flux equilibrium is similarly a global process governed by a single convergence time at which the entire channel obtains $\mathcal{M}/\mathcal{M}_E = 1$ simultaneously. Furthermore, we observe that this convergence time is identical to that of the buoyancy flux

equilibrium convergence time indicating that a single convergence time scale governs the transitional process of the channel.

Past this equilibrium time-scale the total momentum flux continues to evolve directly proportional to u_τ^2 towards full stationarity of the flow field. As such, the results suggest that for our temporally evolving channel flow in which the buoyancy flux profile and therefore the stabilizing force on the velocity field is still developing, caution should be advised in the inference of the local momentum flux from instantaneous measurements of the friction velocity u_τ.

From the results above it is clear that a single global time scale exists that defines the transition of the channel at any depth z towards buoyancy and momentum flux equilibrium which we explicitly define as:

$$t_E = t\left(\frac{\mathcal{B}(z)}{\mathcal{B}_E(z)} = 1\right) = t\left(\frac{\mathcal{M}(z)}{\mathcal{M}_E(z)} = 1\right) \tag{3.44}$$

Subsequently we can define global convergence ratios for the buoyancy and momentum fluxes of the form

$$\left\langle \frac{\mathcal{B}}{\mathcal{B}_E} \right\rangle = \frac{1}{\delta}\int_0^\delta \frac{\mathcal{B}}{\mathcal{B}_E} dz, \qquad \left\langle \frac{\mathcal{M}}{\mathcal{M}_E} \right\rangle = \frac{1}{\delta}\int_0^\delta \frac{\mathcal{M}}{\mathcal{M}_E} dz. \tag{3.45a, b}$$

And due to the approximate monotonic convergence behaviour of the fluxes it is clear that

$$t_E = t\left(\left\langle \frac{\mathcal{B}}{\mathcal{B}_E} \right\rangle = 1\right) = t\left(\left\langle \frac{\mathcal{M}}{\mathcal{M}_E} \right\rangle = 1\right). \tag{3.46}$$

Figures 3.11(a) and (b) show the evolution of the global convergence ratios $\langle \mathcal{B}/\mathcal{B}_E \rangle$ and $\langle \mathcal{M}/\mathcal{M}_E \rangle$ for all simulations plotted against t/T_τ^0. From the results it is clear that the evolution of the global flux convergence ratios display the same qualitative behaviour as that of the local convergence ratios $\mathcal{B}/\mathcal{B}_E$ and $\mathcal{M}/\mathcal{M}_E$. Furthermore, in agreement with our hypothesis of a single convergence time scale we observe that the time taken for the global convergence ratios to reach equilibrium are identical to that of the local flow observed in figures 3.9 and 3.10.

We also consider the global convergence of the flow towards a quasi-stationary energetic state by plotting the domain averaged turbulent kinetic energy $\langle E_K \rangle$ normalized by u_τ^2 and plotted

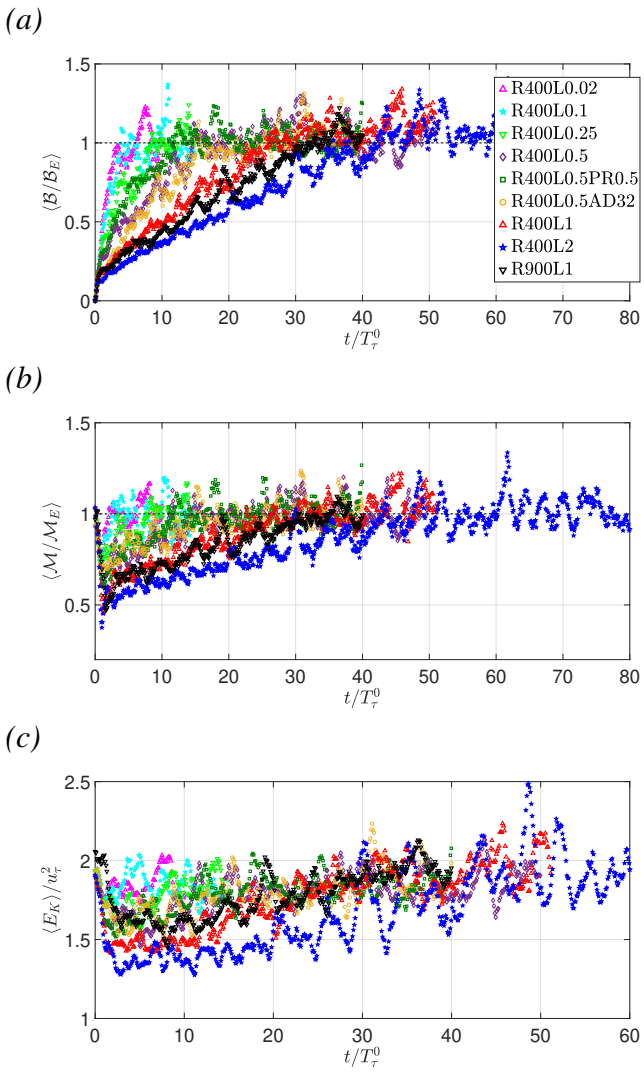

FIGURE 3.11: (a) Global convergence statistics plotted against t/T_τ^0 for all simulations. (a) Global buoyancy flux convergence ratio $\langle \mathcal{B}/\mathcal{B}_E \rangle$.(b) Global momentum flux convergence ratio $\langle \mathcal{M}/\mathcal{M}_E \rangle$. (c) Normalized domain averaged turbulent kinetic energy $\langle E_K \rangle / u_\tau^2$.

against t/T_τ^0 for all simulations in figure 3.11(c). From the results it becomes clear that the single convergence time scale t_e defines not only the convergence towards equilibrium of the buoyancy and momentum fluxes but also a defines the time for which the flow obtains a state of energetic quasi-stationarity. This result implies a globally parabolic process with respect to the convergence of the flow field towards statistical stationary and is not overly surprising given the coupled nature of the governing equations of the flow in (2.3-2.5). We again note

the high frequency oscillations due to the internal wave field in all three figures for the bulk flow quantities.

3.7.2 Prediction of the global convergence time scale

We now consider the scaling of the global buoyancy flux convergence ratio $\langle \mathcal{B}/\mathcal{B}_E \rangle$. In the previous section we have observed that the development of the total buoyancy flux and convergence towards equilibrium is a global process described by a single convergence time scale t_e and monotonic growth towards unity of the ratio $\langle \mathcal{B}/\mathcal{B}_E \rangle$ respectively. Due to the clear observation of monotonic growth of $\mathcal{B}$ with respect to time, we can simplify the global integral $\langle \mathcal{B}/\mathcal{B}_E \rangle$ as two separate integrals such that

$$\left\langle \frac{\mathcal{B}}{\mathcal{B}_E} \right\rangle = \frac{1}{\delta} \int_0^\delta \frac{\mathcal{B}_T}{\mathcal{B}_E} dz \sim \frac{\int_0^\delta \mathcal{B}_T dz}{\int_0^\delta \mathcal{B}_E dz}. \tag{3.47}$$

The integral in the denominator subsequently can be readily derived analytically to obtain

$$\int_0^\delta \mathcal{B}_E dz = g\beta q_N \delta^2. \tag{3.48}$$

Next we recast the total buoyancy flux $\mathcal{B}$ in terms of the classic eddy diffusivity formulation as defined in (3.8) such that the numerator in (3.47) becomes

$$\int_0^\delta \mathcal{B} dz = \int_0^\delta (\mathcal{B}_t + \mathcal{B}_m) dz = \int_0^\delta (K_\rho + \kappa) \frac{\partial \overline{b}}{\partial z} dz. \tag{3.49}$$

Further, by considering the results of figure 3.6 and 3.8, we take the assumption that when considering the integral across the entire channel depth, the dominant contribution to the total buoyancy flux is through turbulent mixing rather than molecular diffusion such that

$$\int_0^\delta (K_\rho + \kappa) \frac{\partial \overline{b}}{\partial z} dz \approx \int_0^\delta K_\rho \frac{\partial \overline{b}}{\partial z} dz. \tag{3.50}$$

In the context of a global convergence towards equilibrium, K_ρ in this instance represents a global level of eddy diffusivity such that we can adopt the bulk scaling derived in §3.6. Hence, following our analysis that for flow where $Ri_\tau^{-1} Re_\tau \lesssim 100$ and stratification actively suppresses and modifies turbulent mixing, we take the bulk scaling of $K_\rho \sim Ri_\tau^{-1/2} u_\tau \delta$ derived in (3.32).

Next we consider that in the context of the global stratification process and the heating of the channel from its initial isothermal state, the $\partial\bar{b}/\partial z$ term in (3.50) represents the transient development of the buoyancy gradients due to the externally imposed heat input into the flow through the representative bulk heat source q_N and is inherently dependant on the total time t for which the external forcing has been applied. Accordingly we can obtain

$$\frac{\partial\bar{b}}{\partial z} \sim \frac{g\beta q_N t}{\delta}, \tag{3.51}$$

In this sense, $g\beta q_N t/\delta$ represents the total buoyancy input into the channel from the initial isothermal reference state of $b = 0$ at $t = 0$ distributed across the channel height δ. We note here that we fundamentally differ from the analysis in KWAZ19 in which the absence of the forcing term that depends on t suggests that the appropriate scaling for this term is $\partial\bar{b}/\partial z \sim \Delta\bar{b}/\delta$. We can thus substitute (3.32) and (3.51) into (3.50) to obtain

$$\int_0^\delta K_\rho \frac{\partial\bar{b}}{\partial z} dz \sim \int_0^\delta Ri_\tau^{-1/2} u_\tau \delta \left(\frac{g\beta q_N t}{\delta}\right) dz = Ri_\tau^{-1/2} u_\tau \delta g\beta q_N t. \tag{3.52}$$

Following which we can substitute (3.48) and (3.52) back into (3.47) to obtain

$$\frac{\int_0^\delta \mathcal{B} dz}{\int_0^\delta \mathcal{B}_E dz} \sim \frac{Ri_\tau^{-1/2} u_\tau \delta g\beta q_N t}{g\beta q_N \delta^2} = \frac{Ri_\tau^{-1/2} u_\tau t}{\delta}. \tag{3.53}$$

Now, we recall that $\delta/u_\tau = T_\tau$ to obtain the final scaling for the global convergence ratio such that:

$$\left\langle \frac{\mathcal{B}}{\mathcal{B}_E} \right\rangle \sim \frac{Ri_\tau^{-1/2} u_\tau t}{\delta} = Ri_\tau^{-1/2}\left(\frac{t}{T_\tau}\right); \qquad \left\langle \frac{\mathcal{B}}{\mathcal{B}_E} \right\rangle \leq 1 \tag{3.54}$$

Furthermore, as we have observed that the transition to equilibrium is governed by a single time scale t_e, we expect the evolution of the domain averaged momentum flux and turbulent kinetic energy to similarly display a dependence on $Ri_\tau^{-1/2}(t/T_\tau)$. To test the scaling derived in (3.54), we plot $\langle \mathcal{B}/\mathcal{B}_E \rangle$, $\langle \mathcal{M}/\mathcal{M}_E \rangle$ and $\langle E_K \rangle/u_\tau^2$ against $Ri_\tau^{-1/2}(t/T_\tau)$ for all simulations in figure 3.12.

With the exception of case400L0.02 the results in figure 3.12(a) show clear support for the proposed scaling in (3.54) with a distinct collapse of the data as $\langle \mathcal{B}/\mathcal{B}_E \rangle$ displays clear linear

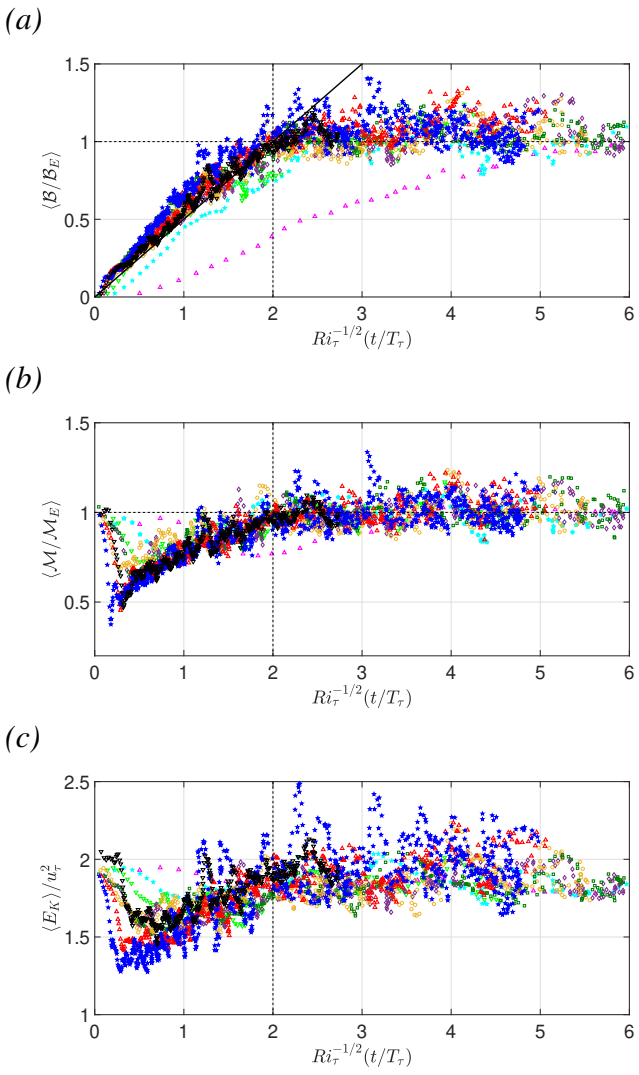

FIGURE 3.12: (a) Global convergence statistics plotted against $Ri_\tau^{-1/2}(t/T_\tau)$ for all simulations. (a) Global buoyancy flux convergence ratio $\langle \mathcal{B}/\mathcal{B}_E \rangle$. Solid black line indicates linear fit of $\langle \mathcal{B}/\mathcal{B}_E \rangle = 0.5 Ri_\tau^{-1/2}(t/T_\tau)$. (b) Global momentum flux convergence ratio $\langle \mathcal{M}/\mathcal{M}_E \rangle$. (c) Normalized domain averaged turbulent kinetic energy $\langle E_K \rangle / u_\tau^2$. Legend same as figure 3.11

dependence on $Ri_\tau^{-1/2}(t/T_\tau)$ such that we can approximate

$$\left\langle \frac{\mathcal{B}}{\mathcal{B}_E} \right\rangle \approx 0.5 Ri_\tau^{-1/2} \left(\frac{t}{T_\tau} \right); \qquad \left\langle \frac{\mathcal{B}}{\mathcal{B}_E} \right\rangle \leq 1 \tag{3.55}$$

until the flow transitions to equilibrium at $Ri_\tau^{-1/2}(t/T_\tau) \approx 2$. Figure 3.12(b) further confirms the universal scaling of the convergence of the flow towards equilibrium with a clear collapse of the data and an identical final convergence of $\langle \mathcal{M}/\mathcal{M}_E \rangle \approx 1$ at $Ri_\tau^{-1/2}(t/T_\tau) \approx 2$ for all

simulations (again with the exception of case R400L0.02). Similar behaviour is shown in figure 3.12(c) for the scaling of the global energetic equilibrium confirming our assumptions.

For case R400L0.02 we observe clear disagreement with our scaling. This is conceptually consistent with our analysis in §3.6 as flow in this simulation is described by $Ri_\tau^{-1}Re_\tau \gg 100$ and may hence be considered essentially neutral turbulent open channel flow. In this sense we do not expect T_N to be a relevant time scale in the evolution of the flow and hence our Ri_τ scaling becomes invalid.

3.7.3 Convergence of local mixing diagnostics

We note that a global transition to quasi-stationarity of the flow can also be interpreted as a state of the flow in which the local mixing properties reach their respective stationary values. Furthermore, the global convergence of the turbulent fluxes towards equilibrium suggest that the time scale of t_e should similarly govern this process.

To demonstrate this we consider the instantaneous flux and gradient Richardson number R_f and Ri_g defined as:

$$R_f = \frac{B}{B+\epsilon_K}, \qquad Ri_g = \frac{N^2}{S^2}. \tag{3.56a, b}$$

As discussed in §3.1, it has been shown for a variety of channel flow configurations, that for the stationary case and under sufficiently stable conditions, R_f and Ri_g approach their respective critical values of $R_{f,c} \approx 0.17 - 0.2$ and $Ri_{g,c} \approx 0.2 - 0.25$ (Armenio & Sarkar, 2002; Taylor *et al.*, 2005; García-Villalba & del Álamo, 2011; Williamson *et al.*, 2015). And for flow where $Ri_g < Ri_{g,c}$ it has been shown in numerous studies that the two paramaters display a linear correlation such that $R_f \sim Ri_g$.

Figure 3.13 shows the evolution of the vertical profiles of Ri_g and R_f for case R900L1. The results clearly show that for most of the flows evolution towards stationarity, in the upper portion of the channel, R_f and Ri_g may significantly exceed their critical values and become uncorrelated. Analytically this can be explained for our particular flow by the slow response of S and ϵ_K, while B and N^2 grow rapidly according to (3.23). Conceptually this is consistent

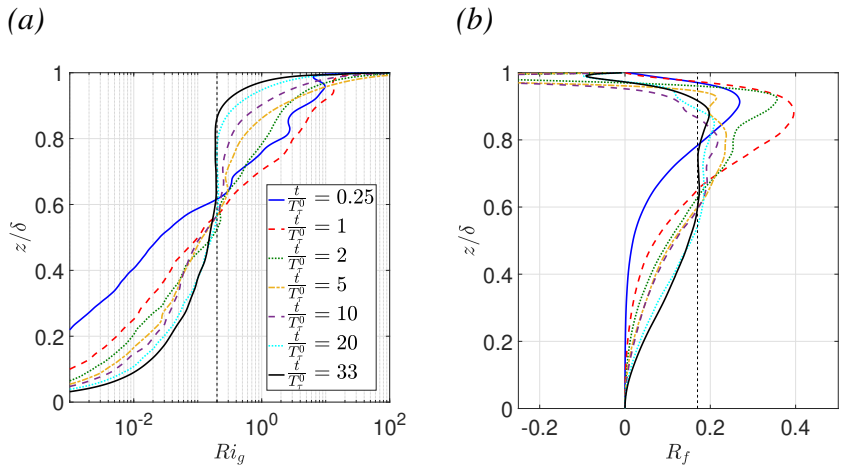

FIGURE 3.13: Evolution of the vertical profiles of: (a) Gradient Richardson number Ri_g, vertical dashed line indicates $Ri_g 0.2$. (b) Instantaneous flux Richardson number R_f, vertical dashed line indicates $R_f = 0.17$. Data for case R900L1

with past studies of stratified shear layers that show appreciably higher values of R_f and Ri_g during the initial 'roll-up' of an overturning shear instability structure (Mashayek *et al.*, 2017). Conversely in the lower portion of the channel, the slow development of the buoyancy fluxes causes R_f and Ri_g to slowly and monotonically grow towards their stationary values. In the final stationary state we observe that a region develops in the core of the channel where Ri_g and R_f approach their established critical limits of 0.2 and 0.17 respectively, consistent with WAKN15. In the upper quasi-laminar layer we observe Ri_g grows very large as the upper boundary conditions causes a relaxation of the mean shear while R_f grows small and becomes negative due to the counter gradient fluxes in this region.

We hence test whether our bulk scaling for the global convergence of buoyancy and momentum fluxes to equilibrium similarly applies to Ri_g and R_f. To investigate this we plot R_f and Ri_g against $Ri_\tau^{-1/2}(t/T_\tau)$ for all simulations with the exception of case R400L0.02 at varying depths $z/\delta = 0.4, 0.6, 0.8$ in figure 3.14. Note we have omitted the plot of R_f at $z/\delta = 0.8$ for case R400L2 in figure 3.14(g) as at this location the flow is essentially laminar and measurements of R_f become extremely noisy as both B and ϵ_K go to zero. From the results it becomes clear that our assumption is valid and the results suggest that $Ri_\tau^{-1/2}(t/T_\tau) \approx 2$ corresponds to a global time scale under which the 'local' mixing diagnostics similarly reach

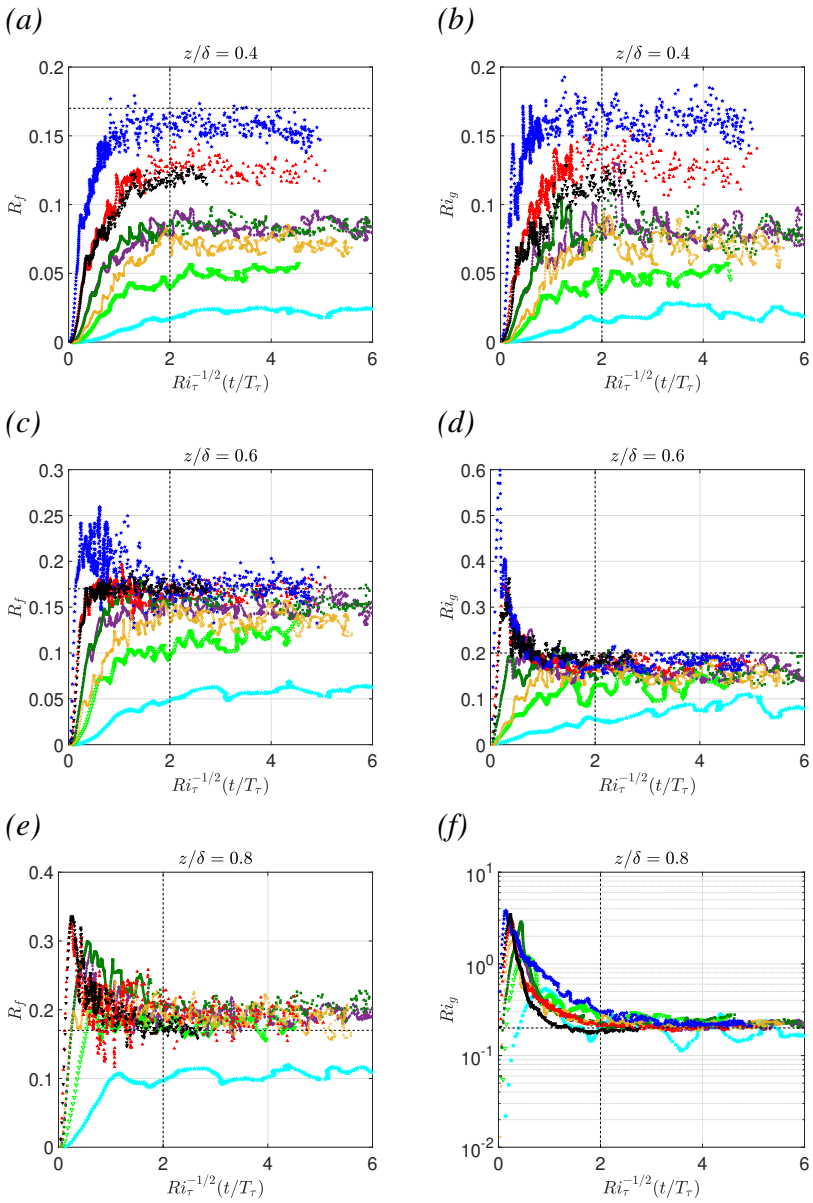

FIGURE 3.14: Flux Richardson R_f and gradient Richardson Ri_g numbers plotted against $Ri_\tau^{-1/2}(t/T_\tau)$ at varying depths for all simulations (with the exception of case R400L0.02). (a-b) $z/\delta = 0.4$. (c-d) $z/\delta = 0.6$. (e-f) $z/\delta = 0.8$. Horizontal dashed lines in (c),(e),(g) indicate $R_f = 0.17$. Horizontal dashed lines in (d),(f),(h) indicate $Ri_g = 0.2$. Same legend as for figure 3.11.

their respective stationary values, regardless of the external parameter set and hence initial rapid growth rate of R_f and Ri_g during the adjustment period of $t/T_{\tau,0} < 1$. Although not shown here, similar behaviour occurs for other mixing diagnostics composed of N, S and the energetic quantities in (3.12) (e.g. Fr, Re_B). Hence analogous to the invalidity of the local

equilibrium assumption, it is clear that in the transitional flow for $Ri_\tau^{-1/2}(t/T_\tau) < 2$ care must be taken when assuming classic critical limits on mixing diagnostics and their respective parameters.

In the context of a global process governing the flows convergence to equilibrium, the results presented within figure 3.14 are somewhat reminiscent of the results of Salehipour *et al.* (2018) who demonstrate the convergence of R_f, Ri_g in stratified free shear flow towards their critical value regardless of initial condition. Accordingly our results further present strong mounting evidence for the case of self-organization in sheared stratified flow towards an 'optimal' or 'critical' state of 'marginal stability' as argued for by Thorpe & Liu (2009) and Smyth *et al.* (2019). This will be explored in much more detail in §5.

3.8 Global stratification rate and comparison with Kirkpatrick *et al.* (2019)

A key finding of KWAZ19 in their study of the destratifying case after the removal of the radiative heat source, was to present a parametric estimate of the bulk destratification rate $\partial\Delta\bar{b}/\partial t$ through measurements of Ri_τ. In its its nondimensional form the the model reads:

$$\frac{T_\tau}{\Delta\bar{b}}\frac{\partial\Delta\bar{b}}{\partial t} = -2.1Ri_\tau^{-1/2}; \qquad Ri_\tau > 15. \tag{3.57}$$

We can derive a similar expression for stratifying case based on the scaling analysis for buoyancy flux convergence derived in §3.7. We recall the evolution for the buoyancy gradient N^2 in (3.14) which can be recast in terms of the total buoyancy flux $\mathcal{B}$ such that

$$\frac{\partial N^2}{\partial t} = \frac{\partial^2 B}{\partial z^2} + \kappa\frac{\partial N^2}{\partial z} + \frac{\partial}{\partial z}g\beta q(z) = \frac{\partial^2 \mathcal{B}}{\partial z^2} + \frac{\partial}{\partial z}g\beta q(z). \tag{3.58}$$

Integrate (3.58) across the channel height δ

$$\int_0^\delta \frac{\partial N^2}{\partial t}dz = \int_0^\delta \left(\frac{\partial^2 \mathcal{B}}{\partial z^2} + \frac{\partial}{\partial z}g\beta q(z)\right)dz. \tag{3.59}$$

leads to an evolution equation for the buoyancy difference across the channel of the form

$$\frac{\partial \Delta \overline{b}}{\partial t} = \int_0^\delta \left(\frac{\partial^2 \mathcal{B}}{\partial z^2} \right) dz + \left(\frac{\partial}{\partial z} g\beta q(z) \right) dz. \tag{3.60}$$

Next we recall provided that $Ri_\tau^{-1} Re_\tau \lesssim 100$ we recall our observation that with the exception of the quasi-laminar regime, the local convergence of $\mathcal{B}(z)$ towards equilibrium follows a single constant trajectory which we estimate to scale as the global convergence ratio such that

$$\frac{\mathcal{B}(z,t)}{\mathcal{B}_E(z)} \approx 0.5 Ri_\tau^{-1/2} \frac{t}{T_\tau} \tag{3.61}$$

Accordingly, we can make the approximation that the first term on the LHS of (3.60) becomes

$$\int_0^\delta \left(\frac{\partial^2 \mathcal{B}}{\partial z^2} \right) dz \sim 0.5 Ri_\tau^{-1/2} \frac{t}{T_\tau} \int_0^\delta \left(\frac{\partial^2 \mathcal{B}_E(z)}{\partial z^2} \right) dz. \tag{3.62}$$

Furthermore, it can be readily derived that

$$\int_0^\delta \left(\frac{\partial^2 \mathcal{B}_E(z)}{\partial z^2} \right) dz = \frac{g\beta I_S \alpha}{C_P \rho_0}, \tag{3.63}$$

which leads to

$$\int_0^\delta \left(\frac{\partial^2 \mathcal{B}}{\partial z^2} \right) dz \sim -0.5 Ri_\tau^{-1/2} \frac{t}{T_\tau} \frac{g\beta I_S \alpha}{C_P \rho_0}. \tag{3.64}$$

Next it can again be readily derived that

$$\int_0^\delta \left(\frac{\partial}{\partial z} g\beta q(z) \right) dz = \int_0^\delta \left(\frac{g\beta I_S \alpha^2}{C_P \rho_0} e^{(z-\delta)\alpha} \right) dz = \frac{g\beta I_S \alpha}{C_P \rho_0}. \tag{3.65}$$

Finally we can substitute (3.64) and (3.65) into (3.60) to obtain

$$\frac{\partial \Delta \overline{b}}{\partial t} = \frac{g\beta I_S \alpha}{C_P \rho_0} \left(1 - 0.5 Ri_\tau^{-1/2} \frac{t}{T_\tau} \right), \tag{3.66}$$

For brevity, we define a non-dimensional stratification rate $\mathcal{S}$ such that

$$\mathcal{S} = \frac{C_P \rho_0}{g\beta I_S \alpha} \frac{\partial \Delta \overline{b}}{\partial t} \tag{3.67}$$

and hence (3.66) can be expressed in non-dimensional form such that:

$$\mathcal{S} = 1 - 0.5 Ri_\tau^{-1/2} \frac{t}{T_\tau}. \tag{3.68}$$

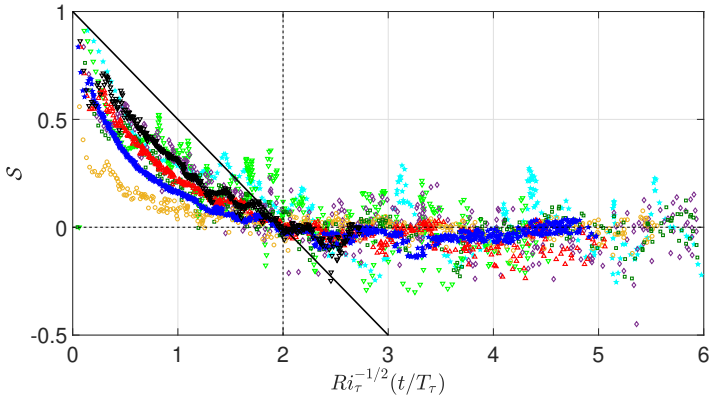

FIGURE 3.15: Normalized global stratification rate $\mathcal{S}$ plotted against $Ri_\tau^{-1/2}(t/T_\tau)$ for all simulations (with the exception of case R400L0.02). Solid black line indicates projected linear fit of $\mathcal{S} = 1 - 0.5Ri_\tau^{-1/2}(t/T_\tau)$. Same legend as for figure 3.11

Accordingly in agreement with our results in §3.7, it is clear from the derivation above that when $Ri_\tau^{-1/2}(t/T_\tau) \approx 2$, the bulk stratification rate of change will become zero and $\Delta\bar{b}$ reaches its stationary value. We investigate the above analysis by plotting $\mathcal{S}$ against $Ri_\tau^{-1/2}(t/T_\tau)$ for all simulations (with the exception of case R400L0.02) in figure 3.15. A line depicting the linear relationship defined in (3.54) is shown for reference.

From the results we again confirm that $Ri_\tau^{-1/2}(t/T_\tau) \approx 2$ indeed corresponds to the global equilibrium time scale past which $\mathcal{S}$ reduces zero for all cases. However for the transitional state of the flow where $Ri_\tau^{-1/2}(t/T_\tau) < 2$, we do not observe a universal collapse of the data on a single line of scaling as for the buoyancy flux convergence ratio $\langle \mathcal{B}/\mathcal{B}_E \rangle$ or in the destratifying case of KWAZ19. Rather the evolution of $\mathcal{S}$ displays a non-linear dependence on $Ri_\tau^{-1/2}(t/T_\tau)$ which varies significantly with the entire external parameter set $(Re_\tau^0, \lambda^0, Pr, \alpha\delta)$.

To investigate this we consider that the derivation of the scaling for $\mathcal{S}$ in (3.68) stems from the assumption that our global scaling for the buoyancy flux convergence is applicable at a local level. As shown in figure 3.9 this assumption breaks down for vertical locations near the top boundary within the quasi-laminar regime. Furthermore, as is evident from (3.60), the evolution of $\mathcal{S}$ depends strongly on the second derivative term $\partial^2\mathcal{B}/\partial z^2$. As outlined

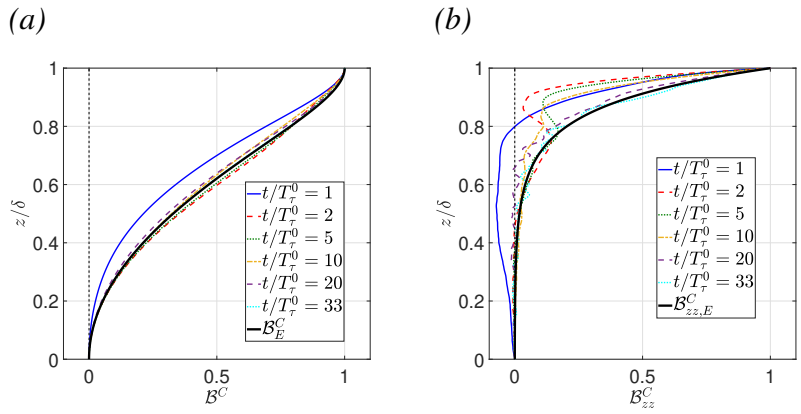

FIGURE 3.16: Evolution of the vertically integrated cumulative normalized functions (a) $\mathcal{B}^C$ and (b) $\mathcal{B}^C_{zz}$ plotted against z/δ for case R900L1.

in KWAZ19 (see their figure 27), unlike the buoyancy flux $\mathcal{B}$ which is relatively evenly distributed across the channel depth, the majority of the contribution to $\partial^2\mathcal{B}/\partial z^2$ occurs very close to the upper surface. To demonstrate this we define the vertically integrated cumulative normalized functions for $\mathcal{B}$ and $\partial^2\mathcal{B}/\partial z^2$ such that

$$\mathcal{B}^C(z,t) = \frac{\int_0^z \mathcal{B}(z,t)dz}{\int_0^\delta \mathcal{B}(z,t)dz}, \qquad \mathcal{B}^C_{zz}(z,t) = \frac{\int_0^z \frac{\partial^2\mathcal{B}(z,t)}{\partial z^2}dz}{\int_0^\delta \frac{\partial^2\mathcal{B}(z,t)}{\partial z^2}dz}, \tag{3.69a, b}$$

Figures 3.16(a) and (b) shows the transient evolution of $\mathcal{B}^C$ and $\mathcal{B}^C_{zz}$ respectively for our representative case R900L1. For reference we also plot the projected cumulative functions based on our assumption of $\mathcal{B} = 0.5\mathcal{B}_E Ri_\tau^{-1/2}(t/T_\tau)$ in (3.48) denoted as $\mathcal{B}^C_E$ and $\mathcal{B}^C_{zz,E}$ respectively.

With the exception of the initial development period, it is clear from from figure 3.16(a) that our estimation of $\mathcal{B}^C_E$ through the scaling in (3.48) is valid displaying excellent agreement with $\mathcal{B}^C$ for the most of the flows evolution. Furthermore, it is clear from the profiles of $\mathcal{B}^C$ that the total buoyancy flux is quite evenly distributed across the channel depth and accordingly explains the excellent agreement of the results for the buoyancy flux convergence presented in figure 3.12.

Conversely, from the profiles of $\mathcal{B}^C_{zz}$ in figure 3.16(b) it is clear that the vast majority of the total contribution to $\partial^2\mathcal{B}/\partial z^2$ occurs very close the free surface where the heating is strongest

and where the flow enters the diffusive regime for most simulations. Within this region, for the majority of the flows evolution our estimation of a constant growth rate of $\partial^2\mathcal{B}/\partial z^2$ in time breaks down with poor agreement between the measured data and our estimation of $\mathcal{B}^C_{zz,E}$ through (3.48). We note that this effect is strongly amplified with increasing turbidity parameter $\alpha\delta$ or with an increased thickness of the quasi-laminar layer through a reduction of Re^0_τ or increase of λ^0. Subsequently this explains the disagreement from a linear dependence of $\mathcal{S}$ on $Ri_\tau^{-1/2}(t/T_\tau)$ in figure 3.15 with clear sensitivity to the external parameter set.

We note however from the results of our weakly stratified cases R400L0.1 and R400L0.25 where the flow remains fully turbulent all the way to the free surface, we still observe disagreement from our fit of linear estimation through (3.48). This can be explained if we consider that during the initial development period of $t/T^0_\tau \lesssim 1$, our linear fit model inherently breaks down near the upper surface due to the growth of $\mathcal{B}$ and $\partial^2\mathcal{B}/\partial z^2$ proportional to $q(z)$ as dictated by (3.23). As seen from figure 3.2(b), for these two low λ^0 cases, during this initial period the flow is always described by $Ri_\tau \approx \mathcal{O}(1)$ and hence $Ri_\tau^{-1/2} \approx \mathcal{O}(1)$. Hence for these cases where the suppression of the turbulent flow is negligible and where the flow reaches stationarity quite rapidly, the initial development period of $t/T^0_\tau \approx \mathcal{O}(1)$ also corresponds to $Ri_\tau^{-1/2}(t/T_\tau) \approx \mathcal{O}(1)$. Accordingly the flow only briefly enters the transitional period of the flow which is both independent of the initial condition and yet sufficiently far from equilibrium conditions to observe a linear fit to the stratification rate $\mathcal{S}$.

Conversely, in KWAZ19 it was found that the collapse of the quasi-laminar upper layer is a very rapid process that occurs within approximately $t/T_\tau \approx \mathcal{O}(1)$ eddy turn over time units. Similarly in their study, the removal of the external forcing through the heat source dictates that the RHS of (3.60) is reduced only to the second derivative term. Hence the destratification rate evolves due to local processes reflecting the evolution of $\mathcal{B}$ that we expect to linearly depend on $Ri_\tau^{-1/2}$. Accordingly in their study, an assumption of fully turbulent flow independent of external forcing or time across the entire channel becomes valid. Hence explaining the collapse of their results for the destratification rate on a single line of scaling. As such, consider that $\partial^2\mathcal{B}/\partial z^2$ in both the initial transient period and later recovery period depends so strongly only local processes that vary strongly with vertical location. The results

hence suggest that for the heating 'sunrise' case where partial relaminarization and the initial condition complicates the process, the prediction of a global stratification rate through a singular bulk parameter framework may not be possible as in the destratifying case. However the final stratification time at $Ri_\tau^{-1/2}(t/T_\tau) = 2$ for all simulations remains clear.

3.9 Conclusion

In this chapter we have investigated the transition of turbulent open channel flow from a neutral to a stably stratified state as the channel is subject so sudden radiative heating across a wide external parameter set. In particular the emphasis of our study falls on the quantification and prediction of the flows transition to an equilibrium state.

We find that the the transient response of the channel is largely described by two transient periods. Firstly, the flow undergoes an initial 'rapid' suppression period where the imposition of stable stratification acts to suppress the Reynolds stress $-\overline{u'w'}$ dampening turbulence production across the channel. Secondly, the flow transitions to an equilibrium state in a relatively 'slow' recovery period that is defined by the acceleration of the mean flow and development of the mean shear profile in the bulk of the channel.

By defining a bulk measure of the turbulent mixing in the channel through $\langle K_\rho \rangle / \kappa$ and $\langle K_M \rangle / \nu$ we demonstrate that the transition away from an asymptotic(neutral) to a heavily suppressed mixing regime in the channel is well predicted by the mixed bulk parameter criterion of $Ri_\tau^{-1} Re_\tau \lesssim 10$ and approaches neutral conditions for $Ri_\tau^{-1} Re_\tau \gtrsim 100$. We provide scaling arguments to show that for the suppressed mixing regime the bulk values of the normalized eddy diffusivity and viscosity show dependence on Pr, Ri_τ and Re_τ, while in the weakly stratified asymptotic regime, buoyancy acts as a passive scalar and the only influencing parameters are Pr and Re_τ.

We find that the transition to an equilibrium quasi-stationary state defined by the vertical buoyancy flux and momentum flux convergence ratios $\mathcal{B}/\mathcal{B}_E = 1$ and $\mathcal{M}/\mathcal{M}_E = 1$ is a global process governed by a single global equilibrium time scale such that the flow obtains

local flux equilibrium at all depths simultaneously across the channel. We find that this global time scale also corresponds to a state of energetic quasi-stationarity at which E_K/u_τ^2 and the mixing diagnostics R_f and Ri_g reach their respective stationary values irrespective of the initial deviation in the adjustment period of the flow. By defining the turbulent fluxes through the eddy diffusivity/viscosity hypothesis we employ our previously derived scaling arguments to demonstrate that the convergence of the fluxes and turbulent kinetic energy within the flow scales directly with the bulk flow properties $Ri_\tau^{-1/2}(t/T_\tau)$ and the flow obtains equilibrium at $Ri_\tau^{-1/2}(t/T_\tau) = 2$ for all simulations across the entire external parameter range provided that buoyancy is an influencing factor in the flow such that $Ri_\tau^{-1}Re_\tau \lesssim 100$. In the context of the $Ri_\tau^{-1/2}$ dependence of the fluxes found in the studies of Kirkpatrick *et al.* (2019) and Kirkpatrick *et al.* (2020), the results suggest a degree of universality to this result.

By applying our derived scaling of the global flux convergence ratio $\langle \mathcal{B}/\mathcal{B}_E \rangle$ to the local buoyancy flux $\mathcal{B}(z)$ we subsequently provide scaling analysis to demonstrate that a non-dimensional bulk stratification rate $\mathcal{S}$ similarly displays a clear dependence on $Ri_\tau^{-1/2}$ analogous to the destratification rate $\mathcal{D}$ in Kirkpatrick *et al.* (2019) . However, due to the coexistence of an upper quasi-laminar layer with the bulk turbulent flow as well as the initial time dependence of the isothermal flow, we find that $\mathcal{S}$ does not evolve on singular lines of scaling as in Kirkpatrick *et al.* (2019) but rather displays a clear dependence on the entire external parameter set ($Re_\tau^0, \lambda^0, Pr, \alpha\delta$) as well as local time-varying dynamics of the flow suggesting a singular universal bulk scaling for $\mathcal{S}$ may not be possible.

As our temporally evolving DNS is an idealised representation of a 'sunrise' scenario of stratified river flow, we consider our results in this context. As an example, in times of draught in Australia flow rates in rivers can be reduced to the extent such that measurements of the friction velocity and river depth have been observed at values $u_\tau \approx 0.002m/s$ and $\delta \approx 4m$ (Webster *et al.*, 1996; Bormans & Webster, 1998). This results in highly turbulent flow where $Re_\tau \approx \mathcal{O}(10^5)$ and $\lambda \approx 10$ yet where the typical advection time scale is $T_\tau \approx \mathcal{O}(10^3)s$. In contrast, from our results the least stratified (yet not neutral) case R400L0.1 has a transitional period towards equilibrium that lasts $t/T_\tau \approx 5$ eddy turnover units. In this sense it becomes clear that our results for the temporally evolving open channel flow become

very physically relevant as the transitional period can extend for the entire duration of a day. Accordingly it remains to be seen how our results at modest Re_τ and λ within our idealised DNS configuration pertain to real river flows and presents a clear direction for future work.

We note in our study we have limited ourselves to $Pr = 0.5$ and 1 for numerical efficiency. In stratified river flows, typical values are $Pr \approx 6 - 7$. Hence it remains unclear how our results pertain directly in this context. However considering the scaling arguments for t_e presented in §3.7 which do not consider molecular properties and the clear collapse of both Pr cases in our study we argue that the final convergence time of $Ri_\tau^{-1/2}(t/T_\tau) = 2$ will display a degree of universality for stratified open channel flow at higher Pr.

CHAPTER 4

Parameterization of mixing in temporally evolving stratified open channel flow

---

In this chapter we perform a robust investigation into the parameterization of the flux coefficient Γ through $Fr, Ri_g, L_E/L_O$ and Re_B frameworks for temporally evolving stratified open channel flow. We explore how the varying parametrization frameworks and their underlying scaling arguments pertain and reconcile to the dynamically different mixing regimes defined by a local measure of Fr. In particular we employ our data-set in which the majority of the flow is described by $Fr \approx \mathcal{O}(1)$ to investigate the 'intermediate' mixing regime proposed by Garanaik & Venayagamoorthy (2019) and discuss the potential differences in the parameterization of mixing within this regime for flow with and without mean shear.

The contents of this chapter are based on the following publication:

Issaev, Vassili, Williamson, N., Armfield, S. W. & Norris, S. E. 2022 Parameterization of mixing in stratified open channel flow. *Journal of Fluid Mechanics* 935, publisher: Cambridge University Press.

4.1 Introduction

As outlined in §1, central to the quantification and estimation of mixing in stratified flows are the diapycnal diffusivity K_ρ and the mixing efficiency coefficient Γ, which are linked through the relation

$$K_\rho = \Gamma \frac{\epsilon_K}{N^2} \tag{4.1}$$

where $\Gamma = R_f/(1 - R_f)$, R_f is the mixing efficiency or flux Richardson number, ϵ_K is the dissipation rate of turbulent kinetic energy and N is the buoyancy frequency. Historically, Osborn (1980) argued that under equilibrium conditions Γ can be assumed to have a constant value of 0.2, however it has since been demonstrated that Γ can significantly vary with respect to the energetic state of the flow (Shih *et al.*, 2005; Ivey *et al.*, 2008; Venayagamoorthy & Koseff, 2016). As such, numerous parametrization schemes have been proposed in the literature to estimate Γ based on relevant non-dimensional parameters. However, as summarized in Gregg *et al.* (2018), a significant challenge within the study of stratified turbulence is the plethora of varied parametrization schemes for Γ and the subsequent ambiguity in the relationship between the different parameters. Further, as outlined by Caulfield (2021) a limitation of numerous parametrization frameworks is that they are derived under the assumptions of homogeneity and stationarity and further tested within idealised triply-periodic domains where such homogeneity and stationary is enforced and the statistics are correlated after appropriate spatial and temporal averaging. Although such flows are extremely useful for evaluating flow properties at a precise parameter range, real flows however can exhibit significant variability in time and space, often resulting in disparity between instantaneous correlations of flow properties to their respective non-dimensional parameters relative to a statistically stationary case. In this context, our spatio-temporally inhomogeneous channel flow in which no local parameters are externally enforced or known *a priori*, presents a robust testing ground for such schemes as well as a distinct opportunity to investigate the relationships and similarities between the varied parametrization frameworks.

Historically, due to the relative ease of measuring mean gradients, parametrization of the mixing efficiency in wall-bounded and shear flows has focused on the gradient Richardson number $Ri_g = N^2/S^2$, where S is the mean shear. Throughout numerous studies it has been repeatedly shown that for stationary shear flows and within the upper limit of $Ri_g \lesssim 0.25$, the mixing efficiency displays a monotonic, essentially linear dependence on Ri_g (Armenio & Sarkar, 2002; Taylor *et al.*, 2005; García-Villalba & del Álamo, 2011; Chung & Matheou, 2012; Deusebio *et al.*, 2015; Karimpour & Venayagamoorthy, 2015; Zhou *et al.*, 2017*a*). Although the deviation of a monotonic relationship between Γ and Ri_g at $Ri_g = 0.25$ is conceptually consistent with the idea of critical gradient Richardson number $Ri_{g,c} = 0.25$

proposed in the seminal work of Miles (1961) as the idealised threshold for the formation of local shear instabilities, however it remains unclear if stability is in fact the mechanism for the departure from monotonic behaviour or the value of $Ri_g = 0.25$ is simply 'fortuitous' Salehipour *et al.* (2018)). The critical value itself as applied to real three dimensional flows is an area of debate in itself (Galperin *et al.*, 2007).

In a recent study Maffioli *et al.* (2016) (henceforth referred to as MBL16 in this chapter) presented scaling arguments to propose an alternative parametrization framework through the turbulent Froude number $Fr = \epsilon_K / N E_K$, where E_K is the turbulent kinetic energy. In their paper and under the assumption of sufficiently high Reynolds number, they classify stratified turbulence into the 'strongly stratified' - $Fr \ll \mathcal{O}(1)$ and 'weakly stratified' - $Fr \gg \mathcal{O}(1)$ regimes with $\Gamma \sim$ constant and $\Gamma \sim Fr^{-2}$ scaling relationships respectively. Garanaik & Venayagamoorthy (2019) (henceforth referred to as GV19 in this chapter) expand upon this idea to propose a separate 'moderately stratified' - $Fr = \mathcal{O}(1)$ regime where both buoyancy and inertial forces are significant and derive scaling arguments to propose a novel $\Gamma \sim Fr^{-1}$ relationship within this regime. Expanding on similar concepts from past works such as Ivey & Imberger (1991) and Smyth *et al.* (2001), they further propose that Fr and subsequently Γ can be inferred from the ratio of L_E/L_O across all three regimes, where L_E is the overturning Ellison length scale and L_O is the Ozmidov lengthscale, with the underlying concept being that L_E has been proven to correlate directly to the easily measurable overturning Thorpe lengthscale L_T (Smyth & Moum, 2000; Mater *et al.*, 2013), thus inferring the mixing efficiency through field measurements of L_T/L_O becomes a conceivably easier task rather than directly through Fr. As Fr is a parameter composed of fundamental turbulent flow properties that inherently exists in stratified turbulence irrespective of physical boundaries or mean shear, MBL16 and GV19 hence both argue that a Fr based framework may present a degree of universality across a broad range of stratified flows. However the testing of its applicability to wall-bounded and shear flows remains relatively limited, in particular for stronger stratification levels of $Fr < 1$.

The concept of a single unifying parametrization scheme becomes somewhat complicated when considering that in the presence of mean shear, Ri_g and Fr may not be independent

parameters, in fact it has been suggested that a multi-parameter framework may be necessary to accurately describe the mixing dynamics when both shear and buoyancy forces are present within the flow (Mater & Venayagamoorthy, 2014). The two frameworks are reconciled for weakly stratified flow ($Fr \gg \mathcal{O}(1)$ or $Ri_g \ll \mathcal{O}(1)$) as it can readily be shown that $Ri_g \sim Fr^{-2}$ (Zhou *et al.*, 2017*a*). However in the moderately and strongly stratified regimes the relationship between Ri_g and Fr remains unclear. The underlying basis for the scaling in the strongly stratified regime of MBL16 draws directly from established strongly stratified turbulence theory of a regime defined by $Fr \ll \mathcal{O}(1)$ and $Re_B \gg \mathcal{O}(1)$ (Billant & Chomaz, 2001; Riley & deBruynKops, 2003; Lindborg, 2006; Brethouwer *et al.*, 2007), where $Re_B = \epsilon_K/N^2\nu$ is the buoyancy Reynolds number and ν is the kinematic viscosity. As summarized in the review of Caulfield (2021), it is however still an open question whether sheared stratified turbulence can access this regime in the sense described. For instance, Thorpe & Liu (2009) hypothesise that sheared stratified turbulence inherently self-regulates within a loop between states of marginal stability and instability. Recent studies have shown support for such self-regulatory behaviour that appears to drive sheared Holmboe instability (HBI) or 'scouring' driven turbulence towards a state described by the classic Miles and Osborne estimates of a critical gradient Richardson number $Ri_{g,c} \approx 0.25$ and mixing efficiency $\Gamma_c \approx 0.2$ (Salehipour *et al.*, 2018; Smyth *et al.*, 2019). The matter becomes even further complicated if we consider that in weakly stratified flows, Ri_g and Re_B can also become deeply correlated such that $Ri_g \sim Re_B^{-1}$ (Riley & deBruynKops, 2003; Hebert & de Bruyn Kops, 2006; Chung & Matheou, 2012), where Re_B itself has been a parameter widely used to parametetrize mixing (Shih *et al.*, 2005). Thus creating a complex multi-parameter space in which Γ, Ri_g, Fr, Re_B may all conceivably be interdependent in varying ways across varying energetic regimes.

In particular, the dynamics and relationships between these key parameters in the intermediate $Fr = \mathcal{O}(1)$ regime remains relatively uninvestigated in the literature. Motivated by oceanic and atmospheric flows, recent high resolution body-forced numerical studies have predominantly focused on the 'strongly stratified' regime (Brethouwer *et al.*, 2007; Maffioli *et al.*, 2016; Maffioli, 2017; Portwood *et al.*, 2016; Taylor *et al.*, 2019). Meanwhile studies with temporally evolving simulations tend to traverse this regime temporarily between states of weak and strong stratification, or vice-versa (Shih *et al.*, 2005; Maffioli & Davidson, 2016; Garanaik &

Venayagamoorthy, 2018) rather than in a forced quasi-stationary state. However, a key study by Portwood *et al.* (2019) demonstrated that in stationary sheared stratified turbulence with a broad range of Re_B, and where Fr and Ri_g were allowed to evolve as free parameters, the flow 'tuned' to fixed values of $Ri_g \approx 0.16$, $Fr \approx 0.5$ and $\Gamma \approx 0.2$, independent of Re_B. In the context of the self-regulatory behaviour described previously, such results suggest that the $Fr = \mathcal{O}(1)$ regime may have significant relevance across a variety of sheared stratified flows and warrants deeper investigation.

In light of the discussion presented above, we summarise the main concepts and subsequent open questions we aim to address within this chapter:

(1) In the context of our highly spatio-temporally inhomogenous flow, can Γ be accurately parametrized through instantaneous measurements of $Fr, Ri_g, L_E/L_O$ or Re_B?
(2) Are these frameworks interconnected and if so how are they and the relationships between their relative parameters reconciled across the different mixing regimes?
(3) What are the limitations on their applicability to open channel flow?

To that end, the remainder of this chapter is structured as follows. in §4.2 we present our list of DNS performed in this chapter. In §4.3 we present a brief qualitative overview of our flows evolution and demonstrate the local parameter range of Fr and Re_B available within our flow. In §4.4 we examine the applicability of $Fr, Ri_g, L_E/L_O$ and Re_B based parametrization frameworks for both the mixing efficiency as well as the energetic state of the flow itself and subsequently derive relationships between all four non-dimensional parameters across the varying flow regimes within the channel. Finally in §4.5 we discuss our main findings within the study and their direct implications to the parametrization of mixing within stratified turbulence.

Case	Re_τ^0	λ^0	Pr	$\alpha\delta$	$L_x \times L_y \times L_z$	$N_x \times N_y \times N_z$	$\frac{t_{\text{final}}}{T_\tau^0}$
R400L0.5	400	0.5	1	8	$2\pi\delta \times \pi\delta \times \delta$	$512 \times 512 \times 150$	10
R400L1	400	1	1	8	$2\pi\delta \times \pi\delta \times \delta$	$512 \times 512 \times 150$	10
R400L2	400	2	1	8	$2\pi\delta \times \pi\delta \times \delta$	$512 \times 512 \times 150$	10
R900L1	900	1	1	8	$2\pi\delta \times \pi\delta \times \delta$	$1152 \times 1152 \times 450$	10
R900L1AD16	900	1	1	16	$2\pi\delta \times \pi\delta \times \delta$	$1152 \times 1152 \times 450$	10
R900L2	900	2	1	8	$2\pi\delta \times \pi\delta \times \delta$	$1152 \times 1152 \times 450$	10
R900L5	900	5	1	8	$2\pi\delta \times \pi\delta \times \delta$	$1152 \times 1152 \times 450$	10

TABLE 4.1: List of DNS performed in chapter 4 and relevant parameters

4.2 List off DNS performed and notation

Table 4.1 presents the list of DNS considered within this chapter. As one of the aims of this chapter is to investigate how the parameterization frameworks apply to temporally evolving in which the local equilibrium assumptions are strictly invalid (see §3), we consider only flow within the first ten eddy turnover units. This allows to us consider our entire high resolution $Re_\tau = 900$ data-set. As Pr effects on local mixing parameterization fall at $Pr = 1$. We demonstrate the independence of our results on the buoyancy flux profile by considering a singular $\alpha\delta = 16$ case at high Reynolds number. Furthermore, as we are again primarily interested in flow moderately or strongly effected by stable stratification (i.e $Fr \lesssim \mathcal{O}(1)$), we only consider DNS at $\lambda^0 \geq 0.5$.

We again define that flow statistics and non-dimensional parameters unless otherwise stated are presented as horizontal averages at time t denoted by the $(\bar{\cdot})$ operator.

4.3 Flow overview

4.3.1 Qualitative description and local parameter range

A defining feature of our DNS configuration is that as the channel transitions from a neutral to stratified state, the local flow at any given vertical location z evolves through a broad range of non-dimensional parameters such that at any point in time, the flow contains regions of both

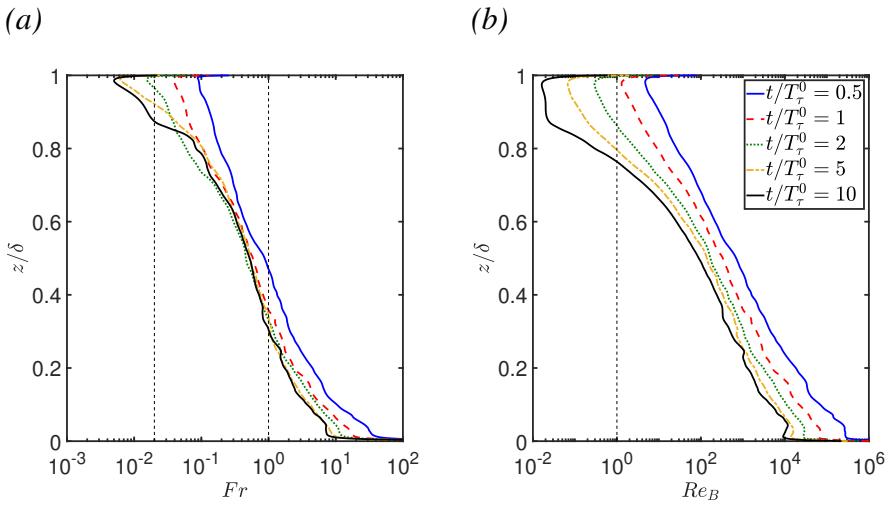

FIGURE 4.1: Evolution in time of key local parameters as a function of z/δ for case R900L2. (a) turbulent Froude number Fr, vertical dotted lines left to right represent $Fr = 0.02$ (as the upper limit for the strongly stratified regime outlined in Lindborg (2006)) and $Fr = 1$, (b) buoyancy Reynolds number Re_B, vertical dotted line represents $Re_B = 1$

high and low Fr simultaneously. This creates a data-set that traverses a variety of energetic regimes within a single simulation and where the flow, both mean and fluctuating evolves in a relatively natural way without external imposition. We briefly present the local parameter range available within our data set through figure 4.1 showing the temporal evolution of Fr and Re_B as a function of z for case R900L2 which shows behaviour typical of our flow, where we redefine

$$Fr = \frac{\epsilon_K}{N E_K}, \qquad Re_B = \frac{\epsilon_K}{N^2 \nu}, \tag{4.2a, b}$$

where $\epsilon_K = \nu(\partial u_i'/\partial x_j)^2$, $E_K = 1/2(\overline{u_i' u_i'})$ and $N = (\partial \bar{b}(z)/\partial z)^{1/2}$. From figure 4.1(a) we observe that the flow obtains a Fr range that encapsulates all three energetic mixing regimes proposed by GV19. Of particular interest is that within the central portion of the channel, Fr stabilizes within approximately one eddy turnover unit ($t \approx 1$) and obtains an appreciable depth range for the so called 'moderately stratified regime' where $Fr = \mathcal{O}(1)$ in an energetically 'quasi-stationary' state such that turbulent properties adapt rapidly to the evolving buoyancy gradient N in order to obtain energetic equilibrium. As outlined in §4.1, in previous numerical studies this regime is only often temporarily traversed as a transient state and subsequently there is a lack of data-points in available literature within this regime.

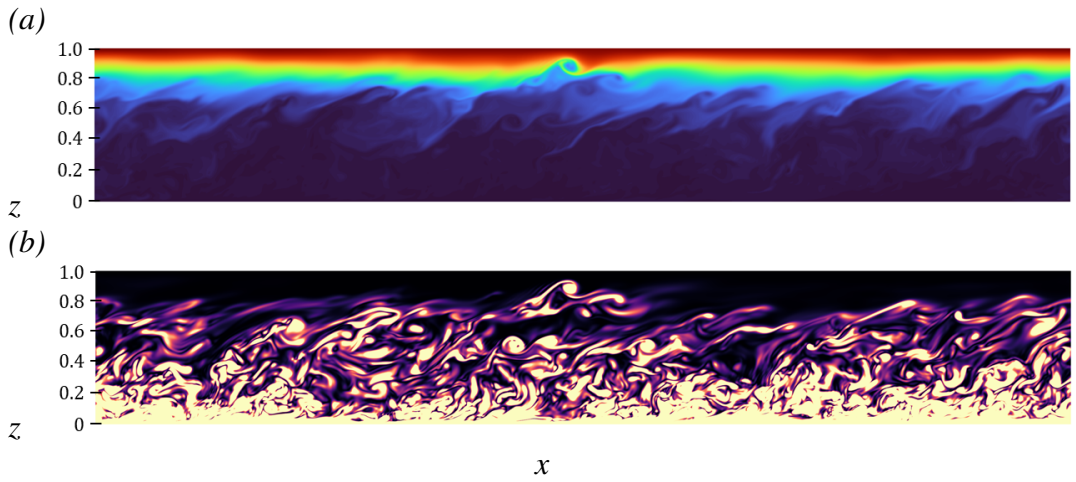

FIGURE 4.2: Instantaneous flow visualizations in the vertical (x, z) plane at $t = 5$ for case R900L2 of (a) the buoyancy field b and (b) enstrophy field $|\boldsymbol{\omega}^2|$. Flow is moving left to right. Color scale in both figures is linear.

As such our flow and extensive data-set of $Fr = \mathcal{O}(1)$ allows us to examine the mixing properties and scaling relationships within this regime in much greater detail than has been previously reported.

Although the flow achieves $Fr < 0.02$ close to the free surface, our simulations are not able to access the 'strongly stratified regime' in the same sense as outlined in Billant & Chomaz (2001) or Brethouwer *et al.* (2007). This is made evident in figure 4.1(b), which demonstrates that for our flow configuration as we approach the free surface, the stratification grows stronger and a reduction in Fr inevitably leads to a reduction in Re_B, leading to the relaminarization of the flow. Subsequently at our parameter range, regions within our flow of very low Fr are more indicative of a diffusive regime as described by Brethouwer *et al.* (2007), where $Re_B < 1$ and the flow is dominated by viscous effects and strong vertical shearing at large scales.

This is made clear if we consider the instantaneous visualizations of the buoyancy b and enstrophy $|\boldsymbol{\omega}^2|$ fields in the vertical (x, z) plane at $t/T_\tau^0 = 5$ in figure 4.2 for case R900L2. We can clearly observe that the flow is separated into three distinct regimes relative to the vertical coordinate z. A lower near wall regime, where due to the adiabatic boundary condition, the boundary layer turbulence structure remains relatively unchanged by the effects

of stratification. A central region within which turbulent structures exhibit the characteristic 'lean' of sheared stratified turbulence and where we again observe the formation of distinct braided eye overturning structures within the shear layer, causing highly vigorous and energetic mixing. And finally an upper quasi-laminar or diffusive regime where turbulence is essentially suppressed by the effects of buoyancy and separated by a sharp buoyancy interface that experiences sporadic overturning by turbulent structures. Thus, the turbulence structure visually observed in figure 4.2 corresponds closely to the three regimes defined by Fr and Re_B in figure 4.1.

4.3.2 A note on the mixing efficiency

Throughout this thesis we defer to a definition of the instantaneous mixing efficiency through R_f and Γ as defined in Ivey & Imberger (1991)

$$R_f = \frac{B}{B + \epsilon_K}, \qquad \Gamma = \frac{R_f}{1 - R_f} = \frac{B}{\epsilon_K}, \tag{4.3a, b}$$

where $B = \overline{-b'w'}$ is the buoyancy flux. As discussed in §1, the vertical buoyancy flux however not only incorporates the small scale irreversible mixing rate (the quantity of interest) but also large scale reversible stirring processes (Caulfield & Peltier, 2000; Peltier & Caulfield, 2003). As such, for linearly stratified flows a more robust definition of the irreversible mixing rate is usually defined through the destruction rate of buoyancy variance χ (Maffioli *et al.*, 2016; Venayagamoorthy & Koseff, 2016; de Bruyn Kops & Riley, 2019; Howland *et al.*, 2020), where

$$\chi = \frac{\kappa}{N^2} \overline{\left(\frac{\partial b'}{\partial x_j} \right)^2}. \tag{4.4}$$

For χ to accurately represent the irreversible conversion of kinetic to available potential energy, a fundamental condition is that the local buoyancy period $N(z)$ must be invariant in both space and time (Caulfield, 2020), a condition that is inherently unsatisfied within our temporally evolving inhomogeneous channel flow (see figure 3.6).

As discussed in §1, an alternative framework is through the adiabatic resorting of the buoyancy in the z_* coordinate space of Winters *et al.* (1995) to obtain an irreversible mixing rate $\mathcal{M}$ and

subsequently an irreversible mixing efficiency $\eta = \mathcal{M}/(\mathcal{M} + \epsilon_K)$ (Caulfield & Peltier, 2000). In past studies Zhou *et al.* (2017*b*) and Smith *et al.* (2021) have shown that the framework may be also applied to inhomogeneous shear flows to evaluate irreversible mixing across a midplane shear interface through appropriate spatial and temporal integration over the shear layer.

However, in stratified open-channel flow where we are interested in investigating the correlation between mixing efficiency and local flow parameters across a broad range of vertical locations, rather than a single central shear layer, the z_* framework presents obvious limitations. We note, the aim of this chapter is not to quantify an exact measure of the irreversible mixing efficiency, but rather to investigate its behavioural trends across different mixing regimes and the subsequent implications on the relationships between varying non-dimensional parameters at a given vertical location. Furthermore, as shown in Venayagamoorthy & Koseff (2016), we expect that in the weakly and moderately stratified regimes the differences in the definitions of mixing efficiency to be relatively small and the qualitative behaviour to remain similar. As such our definition of mixing efficiency through (4.4) still accurately capture the dynamics of interest to our study.

4.4 Parametrization of mixing efficiency, applicability and comparison

We now turn to the main theme of this chapter. In this section we explore the parametrization of mixing efficiency in our temporally evolving inhomegenous flow through the $Fr, Ri_g, L_E/L_O$ and Re_B methods. We then use the Fr based framework of MBL16 and GV19 as a base case scenario to further investigate the relationships and similarities between the varying frameworks and relevant non-dimensional parameters across the varying mixing regimes.

4.4.1 $Fr - \Gamma$ framework and moderately stratified regime scaling

To begin we first explicitly test the novel $\Gamma - Fr^{-1}$ scaling relationship derived in GV19 for the $Fr = \mathcal{O}(1)$ regime. The authors argue that the pertinent timescales for B and ϵ_K are the buoyancy and inertial timescales $T_N = 1/N$ and $T_L = E_K/\epsilon_K$ respectively. And under the assumption of a stationary linearly stratified flow they obtain

$$B \sim \chi \sim \frac{w'^2}{T_N}, \qquad \epsilon_K \sim \frac{w'^2}{T_L}. \tag{4.5a, b}$$

Thus they obtain the new scaling for the irreversible mixing coefficient $\Gamma = B/\epsilon_K \sim \chi/\epsilon_K \sim T_L/T_N = Fr^{-1}$. For the purpose of generality we take one further assumption that at $Fr = \mathcal{O}(1)$ the separation of vertical and horizontal velocity scales is still relatively small and hence we can approximate $w'^2 \sim E_K$. We can thus rewrite (4.5) in the classic form of velocity and length scales $\epsilon \sim u^3/l$ as

$$B \sim \chi \sim \frac{E_K}{T_N} \sim \frac{E_K^{3/2}}{L_N}, \qquad \epsilon_K \sim \frac{E_K}{T_L} \sim \frac{E_K^{3/2}}{L_I}, \tag{4.6a, b}$$

where

$$L_N = \frac{E_K^{1/2}}{N}, \qquad L_I = \frac{E_K^{3/2}}{\epsilon_K}. \tag{4.7a, b}$$

Here L_N is an energetic buoyancy length scale constructed as a result of dimensional analysis and can be taken to represent the conceptual size of large energy containing eddies when the effects of buoyancy are significant. L_N has also been shown to be an accurate indicator of the size of overturns when $Fr < 1$ (Mater *et al.*, 2013). L_I is the well known inertial energy-containing turbulent length scale (Pope, 2000). Such that for the moderately stratified regime we obtain $\Gamma = B/\epsilon_K \sim \chi/\epsilon_K \sim L_I/L_N = Fr^{-1}$, the same scaling as GV19. If considered in the context of the strongly stratified turbulence theory of Billant & Chomaz (2001) and Lindborg (2006) it can be readily seen that L_N and L_I have physical analogues in the vertical and horizontal integral scales $l_v \sim u_h/N$ and $l_h \sim u_h^3/\epsilon_K$ respectively, where u_h is the horizontal velocity scale.

As discussed in §4.3, the definition of χ as an irreversible mixing rate in the derivation above is not equivalent to that of an instantaneous local $\chi(z)$ as measured within our flow, hence

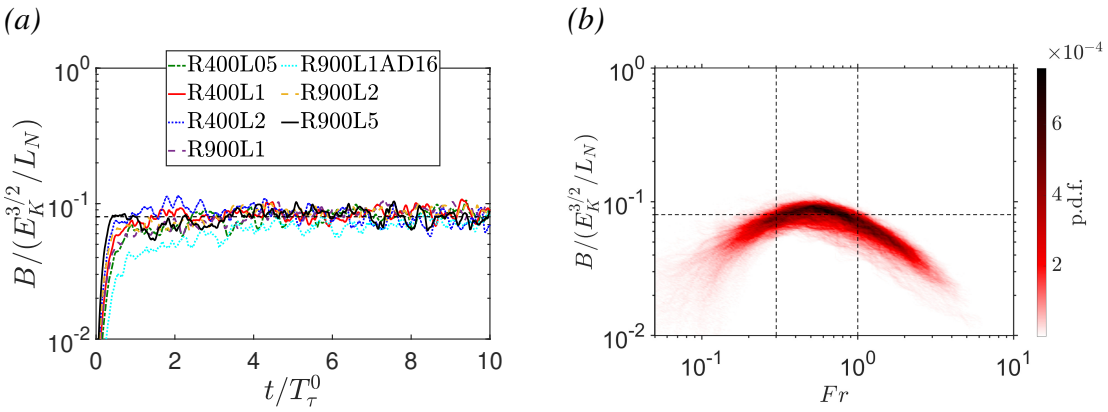

FIGURE 4.3: Buoyancy flux B normalized by $E_K^{3/2}/L_N$, (a) as a function of time t for all simulations at a vertical location of $z = 0.5$, (b) as a function of the turbulent Froude number Fr presented as a 2-D p.d.f. for $t/T_\tau^0 > 1$ and $0.2 \leq z/\delta \leq 0.8$. Vertical dashed lines indicate $Fr = 0.3$ and $Fr = 1$. Dashed horizontal line in both figures indicates empirical constant of 0.08

and without loss of generality we explore these scaling proposals through the buoyancy flux B instead. Figure 4.3(a) shows B normalized by $E_K^{3/2}/L_N$ as function of time at a vertical location of $z = 0.5$, corresponding to a location in the flow where $Fr = \mathcal{O}(1)$ and $Re_B \gg \mathcal{O}(1)$ for all simulations. For the proposed scaling to hold, we expect the former ratio to approach a constant value of $\mathcal{O}(1)$. We further note that it is sufficient to show the B scaling alone to validate the $\Gamma \sim Fr^{-1}$ assumption, as it can readily be shown that $\epsilon_K/(E_K^{3/2}/L_I) = (\epsilon_K/E_K^{3/2})/(\epsilon_K/E_K^{3/2}) = 1$.

In agreement with our analysis in §3.4 we observe the scaling does not hold for $t < 1$ during the transient adjustment period, past which the results clearly show an agreement with the scaling in (4.6) such that $B/(E_K^{3/2}/L_N)$ approaches a constant value of approximately 0.08 across all simulations and appears invariant in time. When considered in the context of our temporally inhomogeneous flow where not only the turbulent properties but also the background stratification N^2 is evolving in time, the result implies that the above scaling for B in (4.6) is both valid and relatively robust. This is further made evident in figure 4.3(b) which shows the two-dimensional probability density function (p.d.f.) of Fr and the ratio $B/(E_K^{3/2}/L_N)$ for all simulations. Due to the initial time dependence observed in §3.4 we exclude the data for $t < 1$ in the construction of the p.d.f. Furthermore, as the confinement

effects of the top and bottom boundaries are outside the scope of this chapter we also exclude the data for $z/\delta < 0.2$ and $z > 0.8$. The vertical limits of $z/\delta = 0.2$ and $z/\delta = 0.8$ have been chosen as the approximate values within which fully developed open channel flow has been shown to obtain local energetic equilibrium (Williamson *et al.*, 2015; Kirkpatrick *et al.*, 2019). It is indeed clear from the results that $B/(E_K^{3/2}/L_N) \approx 0.08$ and remains constant only for a regime within the bounds of $0.3 \lesssim Fr \lesssim 1$, presenting further strong evidence for the argument of GV19 for the existence of a separate intermediate energetic regime that exists in a quasi-stationary state and not as a transient transition between the weakly and strongly stratified regimes. We note that the value of $Fr = 0.3$ is in direct agreement with the transitional value observed in MBL16 towards the asymptotic Γ regime within their study, suggesting some level of universality to this transitional value. We now turn our attention to the Fr based parametrization of the mixing efficiency. Figure 4.4(a) shows the two dimensional p.d.f. of Fr and Γ for all simulations constructed out of the data within the range of $t/T_\tau^0 > 1$ and $0.2 \leq z/\delta \leq 0.8$.

From the results we observe that Γ collapses well across all three energetic regimes and respective scaling relationships proposed by MBL16 and GV19. Although we only access a very small section of the weakly stratified regime, we observe a distinct Fr^{-2} slope developing in the high Fr range similar to that observed in the Couette flow studies of Zhou *et al.* (2017*a*,*b*). Crucially in agreement with our analysis above, we observe that within a range of $0.3 \lesssim Fr \lesssim 1$ where the majority of our data is concentrated, Γ collapses across all simulations and depths with a distinct Fr^{-1} scaling, providing further strong evidence for the existence of a distinctly separate intermediate regime as proposed by GV19. Unlike MBL16 however, who find that $Fr = 0.3$ corresponds to a peak in mixing efficiency, we observe no non-monotonic behaviour in Γ, rather the transition at $Fr = 0.3$ corresponds to a saturation of the mixing efficiency, with Γ displaying independence of Fr and trending towards an empirically observed asymptotic value of $\Gamma \approx 0.3$. The asymptotic value being significantly higher than the upper limit of 0.2 proposed by Osborn (1980), is more reminiscent of the higher values of cumulative mixing efficiency seen in studies of KHI induced mixing (Salehipour & Peltier, 2015; Mashayek *et al.*, 2017; Salehipour *et al.*, 2018), seemingly in

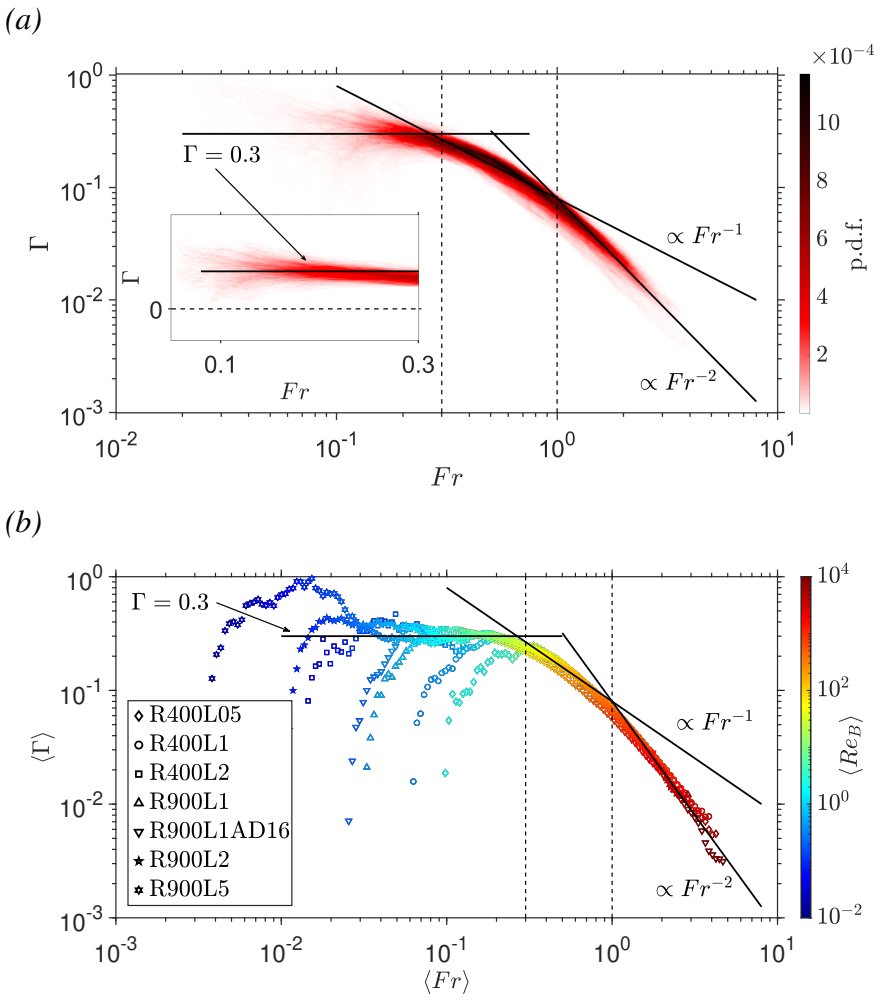

FIGURE 4.4: (a) Two dimensional p.d.f. of the turbulent Froude number Fr and the mixing coefficient Γ constructed out of the instantaneous data of all simulations within the range of $t/T_\tau^0 > 1$ and $0.2 \leq z/\delta \leq 0.8$. The axes on the insert within the figure are presented on a linear scale. (b) Fr bin-averaged mixing coefficient $\langle \Gamma \rangle$ plotted against bins of corresponding turbulent Froude number $\langle Fr \rangle$ for all data points within $t/T_\tau^0 > 1$ and $z/\delta > 0.2$. Solid lines indicate the proposed scaling of MBL16 and GV19 as well as empirically observed $\Gamma = 0.3$. Vertical dashed lines indicate $Fr = 0.3$ and $Fr = 1$

agreement with our visual observations of highly energetic overturning driven mixing events within our flow.

With further decreasing Fr we observe a significant amount of scatter in the data. This can be explained as the flow transitions towards the diffusive regime and both B and ϵ_K grow very small and a minor change in either of the two quantities causes large variation

in Γ. Additionally, as has been reported in the study García-Villalba & del Álamo (2011), channel flow within this regime becomes increasingly affected by the propagation of internal gravity waves as well as counter-gradient fluxes resulting from convective instabilities in the flow (Taylor *et al.*, 2005). This results in instantaneous measurements of B becoming strongly susceptible to contamination from these reversible processes, subsequently causing our measurements of Γ within this regime to show significant scatter about its asymptotic mean value. Furthermore, as discussed in Venayagamoorthy & Koseff (2016) the presence of the counter-gradient fluxes may cause the observed saturated mean value of $\Gamma = 0.3$ to underestimate the true irreversible mixing efficiency. However, as can be observed from the insert in figure 4.4(a) which presents the same data on a linear-linear axes, the observed frequency of counter-gradient fluxes is relatively negligible in comparison to the full data-set. As such the significant takeaway from the results presented within this regime is not the precise value for the saturated mixing efficiency but rather the observation that Γ appears to grow independent of Fr within this regime.

To investigate this further we sort and average our instantaneous measurements of horizontal plane measurements of $\Gamma(z,t)$ across bins of constant Fr to obtain the binned data-set of $\langle\Gamma\rangle$. Avoiding near-wall mechanics we consider all data for $z > 0.2$ and $t^0_\tau > 1$. We note that for this case we include the data near the free-surface boundary to highlight the departure point from the saturated regime towards the diffusive regime. Figure 4.4(b) shows $\langle\Gamma\rangle$ plotted against bins of corresponding $\langle Fr\rangle$ for all simulations under the conditions described above. A colour bar depicting $\langle Re_B\rangle$ is also shown for reference. When presented in this manner, it becomes clear that for $Fr \lesssim 0.3$ the mixing efficiency indeed saturates towards a constant value for all simulations, independent of Fr, a detail that is somewhat less clear in the scattered data presented in figure 4.4(a). Furthermore, it is clear that the transition from a saturated mixing efficiency to the $\Gamma \sim Fr^{-1}$ regime at $Fr \approx 0.3$ occurs irrespective of $Re_\tau, \lambda, \alpha\delta$ or vertical location z within the channel, again suggesting a degree of universality for this transitional value as argued by MBL16. Conversely no singular value of Fr appears for the transition away from the constant Γ regime within the 'left flank' of the curve. Rather as seen from the results, this corresponds to a transition to the diffusive regime at low Re_B as will be demonstrated in further detail in §4.4.5.

We note that within the 'left flank' of figure 4.4(b), following the saturated regime, case R900L5 displays a further increase in Γ with a clear peak before dropping away. The exact mechanism of this is unknown, and may be attributed to a number of influencing factors that fall outside the scope of this chapter such as large vertical displacement of fluid parcels through internal gravity waves, surface confinement effects and strong spatio-temporal intermittency of turbulence as the flow approaches the diffusive regime. Furthermore, as can be observed from the colour bar, this behaviour occurs for flow where $Re_B \ll \mathcal{O}(1)$, which can be considered essentially laminar such that the vertical transfer of buoyancy through the turbulent flux B is significantly smaller than that of molecular diffusion. Subsequently our definition of a 'turbulent' mixing efficiency through Γ begins to lose relevance. We further note similar behaviour has been observed at low Re_B in the studies of Zhou *et al.* (2017*b*) and Smith *et al.* (2021), suggesting that as ϵ_K goes to zero the diapycnal flux is not fully suppressed within this regime.

4.4.2 Ri_g framework

In this section we briefly examine the behaviour of Γ relative to the more established framework based on Ri_g, where

$$Ri_g = \frac{N^2}{S^2}, \tag{4.8}$$

where $S = \partial\overline{u}(z)/\partial z$. Figure 4.5 shows the two dimensional p.d.f. of Ri_g and R_f constructed analogously to that of figure 4.4(a). For reference we also plot the line corresponding to the linear relationship $R_f = Ri_g$ (dotted line) as well as the empirical fit corresponding to $R_f = 0.25(1 - e^{-7Ri_g})$ of Venayagamoorthy & Koseff (2016) (solid lined). From the results it is clear that in agreement with numerous studies of sheared stratified turbulence (see §4.1), the mixing efficiency displays linear monotonic dependence on Ri_g up to a critical value of $Ri_g \approx 0.25$, where it can be seen that the majority of our data is concentrated. The results add to the mounting evidence that in weak/moderate levels of stratification the diapycnal and momentum diffusivities are relatively equal such that the the turbulent Prandtl number $Pr_T \sim Ri_g/R_f$ is approximately unity. A further key observation from the results is that within our flow we clearly observe sustained turbulence and vigorous shear instability

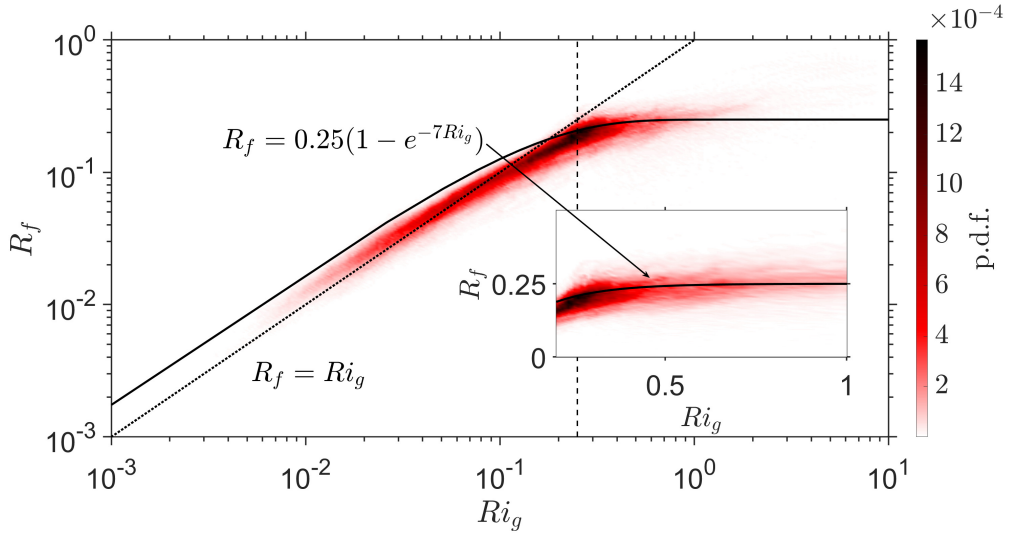

FIGURE 4.5: Two dimensional p.d.f. of the gradient Richardson number Ri_g and the the flux Richardson number R_f constructed out of the instantaneous data of all simulations within the range of $t_\tau^0 > 1$ and $0.2 \leq z/\delta \leq 0.8$. Solid line indicate the proposed empirical fit model of Venayagamoorthy & Koseff (2016). Dotted line represents a linear relationship of $R_f = Ri_g$. Vertical dashed line indicates $Ri_g = 0.25$. The axes on the insert within the figure are presented on a linear scale.

induced mixing at Ri_g values significantly higher than the critical 'Miles-Howard' limit of $Ri_{g,c} = 0.25$, suggesting exercising caution in assuming a strict upper limit of stability based on $Ri_{g,c}$ for more complex and initially turbulent flows as suggested by Galperin *et al.* (2007).

Within the 'right flank' of the curve we again observe no non-monotonic behaviour in R_f as observed in the high Pr Couette flow simulations of Zhou *et al.* (2017*b*), rather the saturation of the mixing efficiency seems very well described by the empirical fit of Venayagamoorthy & Koseff (2016) showing clear asymptotic behaviour in the limit of high Ri_g. We note in our study we maintain $Pr = 1$ for all simulations, rather than higher values of $Pr = 6 - 7$ which a are typical of stably stratified river or oceanic flows that provide the motivation behind this chapter. Past studies of shear instability driven mixing (Smyth *et al.*, 2001; Salehipour & Peltier, 2015; Salehipour *et al.*, 2015) have shown that at higher Pr the dynamics of a KHI mixing event can vary significantly to that at lower Pr, particularly the secondary instabilities that form at smaller scales. Furthermore, we note our definition of the mixing efficiency through R_f has fundamentally different behaviour at high Ri_g compared with its irreversible

counterpart used in the aforementioned studies making a direct comparison somewhat difficult. It remains unclear how higher Pr values for our flow configuration would effect the results presented in this chapter and presents direction for future work.

4.4.3 Influence of mean shear and $Fr - Ri_g$ scaling

A distinct key observation from the above analysis is that the transition to the saturated mixing efficiency regime is described well by both $Fr \approx 0.3$ and $Ri_g \approx 0.25$. However for $0.3 \lesssim Fr \lesssim 1$ and $Fr \gtrsim 1$ we have observed two distinctly different mixing regimes with separate scaling for Γ, in contrast to a simple linear dependence of the mixing efficiency on the gradient Richardson number for $Ri_g \lesssim 0.25$. Such results imply a more complex relationship between Fr and Ri_g within our flow than the $Ri_g \sim Fr^{-2}$ relationship for weakly stratified flow (Zhou *et al.*, 2017*a*). To investigate this further, we consider that the dynamics of our channel flow can be described in the conceptual framework of Mater & Venayagamoorthy (2014) as a competition of the inertial, buoyancy and shear forces within the flow, or analogously as a competition of the three respective time scales T_L, T_N, T_S, where $T_S = 1/S$ is the shear timescale. Thus we consider our channel flow within their $S^* - Fr^{-1}$ regime map, where S^* is the non-dimensional shear rate defined as

$$S^* = \frac{SE_K}{\epsilon_K}. \tag{4.9}$$

S^* has been frequently used in literature to describe sheared turbulence, both with and without the presence of buoyancy (Rogallo, 1981; Shih *et al.*, 2000; Chung & Matheou, 2012). Furthermore, It can be readily seen that $S^* = T_L/T_S$, and hence S^* represents the competition between the shear and inertial time scales in the same manner that $Fr = T_N/T_L$ analogously represents the competition of buoyancy and inertial time scales. We note that by convention, S^* is often defined by $S^* = Sq/\epsilon_K$ where $q = 2E_K$ is twice the turbulent kinetic energy. For this chapter however, we defer to the definition in (4.9) to maintain consistency in the comparison of the respective three time scales.

In this sense Mater & Venayagamoorthy (2014) propose stratified shear flow can be divided into three distinct regimes. An inertia dominated regime where flow tends to revert to isotropy

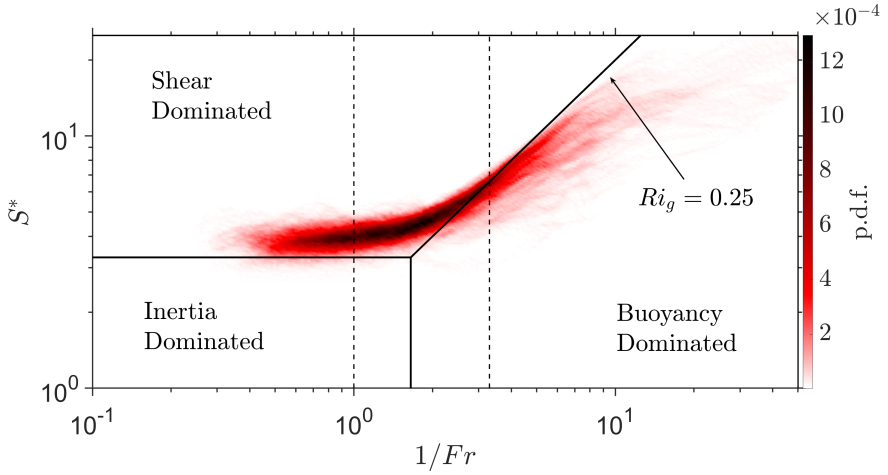

FIGURE 4.6: Two dimensional p.d.f. of the inverse of the turbulent Froude number $1/Fr$ and non-dimensional shear rate S^* in the $ST_L - NT_L$ regime map of Mater & Venayagamoorthy (2014) constructed out of the instantaneous data of all simulations within the range of $t^0_\tau > 1$ and $0.2 \leq z/\delta \leq 0.8$. Solid lines indicate the separation of the proposed inertia, buoyancy and shear dominated regimes as outlined in §4.4.2. Vertical dashed lines indicate $1/Fr = 1$ and $1/Fr = 3.33$ corresponding to $Fr = 1$ and $Fr = 0.3$ respectively.

and is defined by both $S^* < S^*_c$ and $Fr^{-1} < Fr_c^{-1}$, where S^*_c and Fr_c are some critical values at which shear and buoyancy forces become significant relative to inertia and begin to distort the isotropic flow. Meanwhile the buoyancy and shear dominated regimes are defined by $S^* > S^*_c$ and $Fr^{-1} > Fr_c^{-1}$ and separated by the diagonal line of $Ri_g = 0.25$ as it can be readily shown that $Ri_g = (T_S/T_N)^2 = (Fr^{-1}/S^*)^2$. We adopt the critical values defined in Mater & Venayagamoorthy (2014) of $S^*_c = 3.3$ and $Fr_c^{-1} = 1.65$. Furthermore, we note that the limit of $Ri_g = 0.25$ delineating the shear and buoyancy dominated regime isn't a strict limit as in the sense of the 'Miles-Howard' criterion but rather an empirical choice due to the evidence that in forced stratified sheared turbulence Ri_g tends to an upper bound of 0.25 in a stationary state (Rohr *et al.*, 1988; Chung & Matheou, 2012).

Figure 4.6 shows the two dimensional p.d.f. of our flow within $S^* - Fr^{-1}$ regime map described above, constructed in the same manner as figure 4.4. From the results we can again observe three distinct regimes of behaviour separated by $Fr = 1$ and $Fr = 0.3$.

In the weakly stratified regime for $1/Fr < 1$, buoyancy acts essentially as a passive scalar and the flow travels along a horizontal path of $S^* \approx S_c^*$ where the shear and inertial forces are in balance, much like in a neutral channel flow.

Within the moderately stratified regime we observe a transitional regime where buoyancy begins to change the dynamics of the flow. As Fr decreases and buoyancy begins to restrict the vertical velocity fluctuation w' and subsequently the turbulent shear stress $\overline{-u'w'}$, an inbalance appears in the flow between the total local shear stress and the driving pressure gradient. This causes the flow to accelerate in an effort to obtain energetic equilibrium, translating into an increase in a local measure of S, such that S^* accordingly increases. Thus, it is clear that for our flow this intermediate regime where both $S^* = \mathcal{O}(1)$ and $Fr = \mathcal{O}(1)$ represents a critical state of the flow where inertia, buoyancy and shear all play a significant and interconnected role in the dynamics of the flow.

Conversely in the saturated regime for $Fr < 0.3$ or $Ri_g > 0.25$ we observe that with further increasing stratification, the shear accordingly increases such that S^* grows large and Fr grows small. Within this regime we can thus expect inertia to become insignificant relative to the effects of shear and stratification such that $N \sim S$ and Fr becomes decoupled from Ri_g as the effects of inertia become negligible relative to buoyancy and shear. Accordingly, although the data in this regime shows some scatter we can observe that within this regime the flow tends to settle down and evolve along diagonal lines of constant Ri_g, with the majority of the data in the 'right flank' of the figure again being concentrated around the ubiquitous value of $Ri_g = 0.25$. The scatter in the data can be directly explained by the relatively slow process that is the acceleration of the mean flow from its initial state. We note that at $t_{\text{final}} = 10$ all the simulations are still significantly distant from their final equilibrium states. As such the mean shear S is still increasing to obtain shear stress equilibrium such that Ri_g is still evolving towards its stationary state. Meanwhile, the turbulent properties have adapted to the growing background stratification and Fr has essentially stabilized as observed in figure 4.1, causing the scattered trajectories of the flow in $S^* - Fr^{-1}$ space within this regime.

From the observations above it is clear that the relationship between the inertial, shear and buoyancy forces within the flow vary significantly along the three energetic regimes of the

flow. We can hence derive scaling arguments to directly relate Fr to Ri_g within our flow across the three regimes.

Within the weakly stratified, $Fr > 1$ regime we can relate Fr and Ri_g with a simple mixing length argument for S such that

$$S \sim \frac{U_*}{L_*}, \tag{4.10}$$

where U_* and L_* are some characteristic velocity and length scales pertinent to energetic mixing within the flow. Observing a balance between shear and inertial forces we can estimate $U_* \sim E_K^{1/2}$ and $L_* \sim L_I$ such that $S \sim \epsilon_K / E_K$ or conversely $T_S \sim T_L$. Thus we can obtain

$$Ri_g = \frac{N^2}{S^2} \sim \frac{N^2 E_K^2}{\epsilon_K^2} = Fr^{-2}. \tag{4.11}$$

The same scaling as derived in MBL16 or Zhou *et al.* (2017*a*).

Within the moderately stratified, intermediate $0.3 < Fr < 1$ regime we can adopt a similar mixing length argument for S as in (4.10). Having hypothesised that in this critical regime inertia, buoyancy and shear are all significant, the dimensional group that could influence the dynamics becomes (N, S, E_K, ϵ_K). Analogously to our scaling of B within this regime in (4.6), we make the assumption that the pertinent length scale is the energetic vertical buoyancy length scale such that $L_* \sim L_N$. Hence, dimensional analysis dictates that a velocity scale constructed out of the remaining dimensional quantities becomes $U_* \sim (\epsilon_K / N)^{1/2}$, where $(\epsilon_K / N)^{1/2}$ is the velocity scale analogue of the Ozmidov length scale (Shih *et al.*, 2005). Hence we obtain

$$S \sim \frac{U_*}{L_*} \sim \frac{(\epsilon_K / N)^{1/2}}{E_K^{1/2} / N} = \left(\frac{\epsilon_K N}{E_K} \right)^{1/2}. \tag{4.12}$$

Conversely this can be seen as a comparison of timescales such that

$$T_S \sim (T_L T_N)^{1/2} \tag{4.13}$$

and we can obtain a scaling relation between Fr and Ri_g within this regime

$$Ri_g = \frac{N^2}{S^2} \sim \frac{N^2 E_K}{N \epsilon_K} = \frac{N E_K}{\epsilon_K} = Fr^{-1}. \tag{4.14}$$

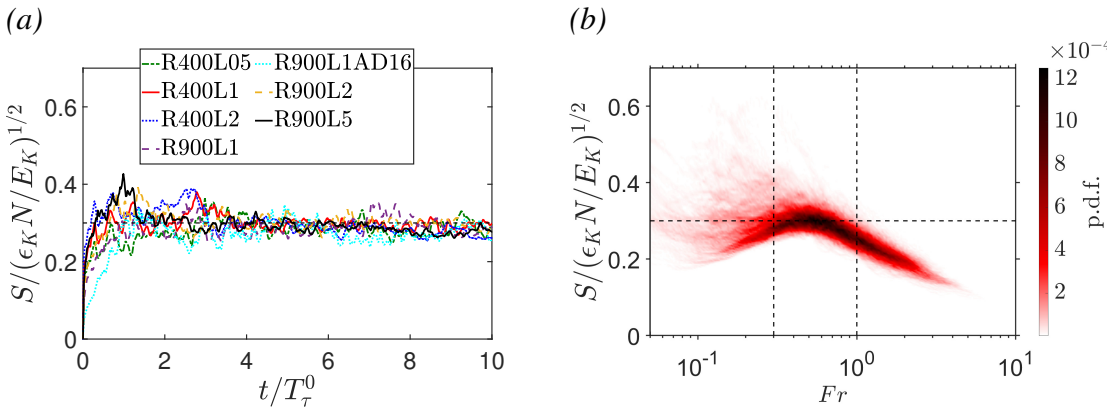

FIGURE 4.7: Mean shear rate S non-dimensionalized by $(\epsilon_K N/E_K)^{1/2}$ (a) plotted against time t for all simulations, horizontal dashed lined indicates empirically observed constant of 0.3, (b) presented in the form of a two dimensional p.d.f. with the turbulent Froude number Fr. The p.d.f. is constructed out of the instantaneous data of all simulations within the range of $t/T_\tau^0 > 1$ and $0.2 \leq z/\delta \leq 0.8$. Vertical dashed lines indicate $Fr = 0.3$ and $Fr = 1$

We note the scaling proposed in (4.12-4.14) are new scaling relationships for the $Fr = \mathcal{O}(1)$ regime and thus directly reconcile the observed $\Gamma \sim Fr^{-1}$ and $R_f \sim Ri_g$ scaling for mixing efficiency within this regime.

Finally in the $Fr < 0.3$ saturated regime we can directly imply that as T_N and T_S both become much smaller than T_L, the effects of inertia become negligible such that $N \sim S$ and Ri_g becomes decoupled from Fr.

We first test the new scaling in (4.13) explicitly by plotting the ratio $S/(\epsilon_K N/E_K)^{1/2}$ as a function of time at $z/\delta = 0.5$ in figure 4.7(a) and as a function of Fr, presented in the form of a two dimensional p.d.f. in figure 4.7(b). From the results it is clear that $S/(\epsilon_K N/E_K)^{1/2}$ approaches a constant value of approximately 0.3 that appears invariant with respect to both time and space within the defined regime of $0.3 \lesssim Fr \lesssim 1$. Again in the context of our evolving and inhomogeneous flow, such results suggest that the scaling is reasonably robust and may pertain to a wider range of stratified shear flows.

To confirm the different scaling across all regimes, we plot the two dimensional p.d.f. of Fr and Ri_g in figure 4.8(a) for our DNS results as well as from the stationary homogeneous

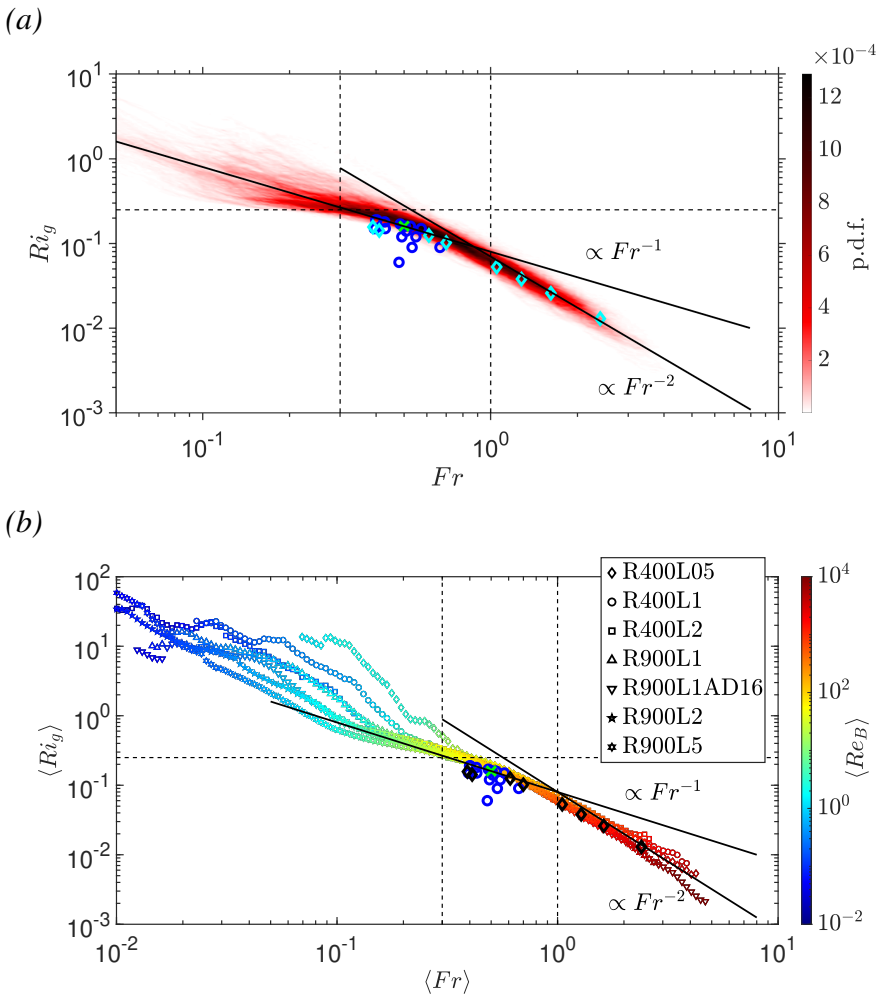

FIGURE 4.8: (a) Two dimensional p.d.f. of the turbulent Froude number Fr and the gradient Richardson number Ri_g constructed out of the instantaneous data of all simulations within the range of $t/T_\tau^0 > 1$ and $0.2 \leq z/\delta \leq 0.8$. (b) Fr bin-averaged gradient Richardon number $\langle Ri_g \rangle$ plotted against bins of corresponding $\langle Fr \rangle$ for all data points within $t/T_\tau^0 > 1$ and $z/\delta > 0.2$. Large blue circles show the data of the stationary runs in table 2 of Shih *et al.* (2000). Large diamonds (cyan in (a), black in (b)) show data of Chung & Matheou (2012). Large green 'X' shows 'tuned' values of Portwood *et al.* (2019). Solid lines indicate the proposed scaling in (4.11) and (4.14). Vertical dashed lines indicate $Fr = 0.3$ and $Fr = 1$. Horizontal dashed lines indicate $Ri_g = 0.25$

sheared turbulence studies of Shih *et al.* (2000); Chung & Matheou (2012) and Portwood *et al.* (2019). From our instantaneous results it is clear that the flow is again well divided into the three distinct regimes divided by $Fr = 1$ and $Fr = 0.3$, with clear $Ri_g \sim Fr^{-2}$ and $Ri_g \sim Fr^{-1}$ behaviour in the weakly and moderately stratified regimes respectively.

The results of the three aforementioned studies with distinctly different forcing mechanics also show clear support for the derived scaling showing excellent agreement across both regimes, suggesting a degree of universality in their application. Meanwhile the transition to the saturated regime at $Fr \approx 0.3$ and $Ri_g \approx 0.25$ corresponds to a decoupling between Fr and Ri_g as the variables become uncorrelated, although this is somewhat obscured by the scatter in the data.

To demonstrate this result more clearly we plot the Fr bin-averaged data-set of $\langle Ri_g \rangle$ plotted against corresponding bins of $\langle Fr \rangle$ in figure 4.8(b) in a similar manner to that of the process described for figure 4.4(b). A colour bar showing $\langle Re_B \rangle$ is again included for reference. From the results it is again clear that the scaling derived for the weakly and moderately stratified regimes in (4.11) and (4.14) distinctly collapses on one line and holds irrespective of external flow parameters of vertical location in the channel, with a clear transition at $Fr \approx 0.3$ or $Ri_g \approx 0.25$ at which point each simulation continues its own unique trajectory in $Fr - Ri_g$ space. It is also worth noting that the long individual 'tails' in the 'left flank' of the curve, where $Ri_g \gg \mathcal{O}(1)$ correspond to low Re_B flow that is essentially laminar and where the scaling derived above on the assumption of turbulent flow becomes invalid. Furthermore, the data of the aforementioned three studies is again plotted for visual clarity to highlight the validity of the scaling.

In addition to the stationary runs plotted in figures 4.8(a) and (b) in which Ri_g is free to evolve to its stationary state, Shih *et al.* (2000) also ran non-stationary simulations (see table 1 in Shih *et al.* (2000)) in which Ri_g and subsequently the mean gradients S, N are kept fixed for a given simulation. These simulations do not follow the proposed scaling but instead evolve along constant lines of Ri_g across all three regimes. Conversely in our study and the other data-sets shown in figure 4.8(a) and (b) neither Fr or Ri_g are known *a priori* and subsequently the both the mean and turbulent flow properties adapt to the proposed scaling.

The findings discussed in the analysis above present implications for the parametrization of stratified shear flow. Firstly, it is clear that for $Fr > 0.3$ or $Ri_g < 0.25$, in the weakly and moderately stratified regimes Fr and Ri_g become interchangeable in any parametrization schemes by using the scaling relations in (4.11 and 4.14) respectively. Such interchangeability

allows for more flexible parametrization as relationships derived through turbulent properties and Fr may be inferred in real flows from relatively simple measurements of the mean buoyancy and velocity field. Secondly, although very appealing, the simple division of stratified shear flow into two regimes along a line of $Ri_g = 0.25$ does not accurately capture the subtleties and the differences in dynamics between the distinctly different $0.3 < Fr < 1$ and $Fr > 1$ regimes. Lastly, care should be taken in any assumptions on the state of the flow by inferring relationships between Ri_g and Fr in the $Fr < 0.3$ regime, in particular in temporally evolving flow where the mean fields may exhibit appreciably long adjustment periods as the flow transitions to energetic equilibrium. Furthermore, in the context of the strongly stratified turbulence theory of Brethouwer *et al.* (2007) the apparent decoupling of Fr and Ri_g within this regime suggests that even if an upper limit fundamentally exists on the stationary value of Ri_g, it does not translate to a lower bound on Fr, suggesting the possibility of accessing the strongly stratified $Fr \ll \mathcal{O}(1)$ regime within stratified channel flow.

4.4.4 Overturning length scale framework

In this section we investigate the applicability of the $L_E/L_O - \Gamma$ and hence the more easily measurable $L_T/L_O - \Gamma$ framework of GV19 to our temporally evolving channel flow. Where we define

$$L_E = \frac{b'_{\text{rms}}}{N^2}, \qquad L_O = \left(\frac{\epsilon_K}{N^3}\right)^{1/2}, \tag{4.15a, b}$$

where L_E is the well known Ellison overturning length scale and represents the large energy containing overturns within the flow. Meanwhile the Ozmidov length L_O represents the maximum conceptual size of an isotropic eddy that is not confined by stable stratification (Smyth & Moum, 2000). In this section we use the overturning length scales L_E and L_T interchangeably when referencing different studies, due to their linear relationship in fully turbulent flow as shown in Mater *et al.* (2013).

Figure 4.9 shows the two dimensional p.d.f. of L_E/L_O and Γ for the same data-set as in figure 4.4. It is clear that Γ is accurately described through instantaneous measurements of L_E/L_O across all three regimes and scaling relationships described in GV19. Although accessing

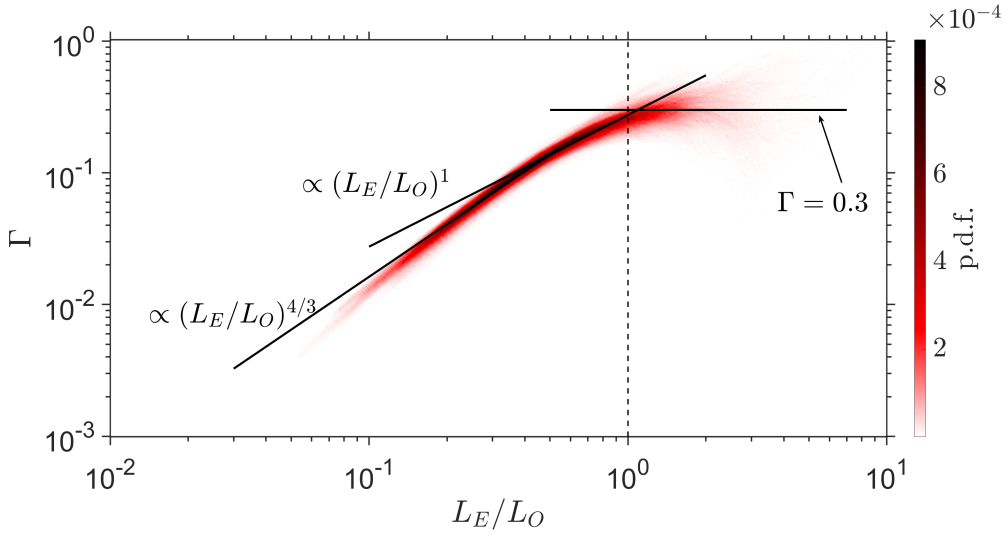

FIGURE 4.9: Two dimensional p.d.f. of the length scale ratio L_E/L_O and the mixing coefficient Γ constructed out of the instantaneous data of all simulations within the range of $t/T_\tau^0 > 1$ and $0.2 \leq z/\delta \leq 0.8$. Solid lines indicate the proposed scaling of GV19 as well as empirically observed $\Gamma = 0.3$. Vertical dashed line indicates $L_E/L_O = 1$

only a very small section of the regime, we observe a $\Gamma \sim (L_E/L_O)^{4/3}$ relationship in the weakly stratified regime in agreement with the observational oceanic study of Ijichi & Hibiya (2018). However, as L_E/L_O becomes increasingly small we note that the results appear to deviate slightly from the proposed scaling for the weakly stratified regime. We shall return to this shortly in the analysis to come. Again, we observe a distinct collapse of the data in the moderately stratified regime, showing a $\Gamma \sim (L_E/L_O)^1$ scaling that holds for almost an entire decade of (L_E/L_O). A key observation is that the transition towards the saturated regime occurs at precisely $L_E/L_O \approx 1$. Taking the approximation of $L_E \approx L_T$ and considering the visual observation of vigorous overturning induced mixing in figure 4.2, this is conceptually consistent with the work of Mashayek *et al.* (2017) who find that mixing efficiency in a KHI mixing event peaks for when $L_T \sim L_O$. That is, when energy being injected into the downscale energy cascade through the overturning of the KHI is at a scale corresponding to the upper end of the inertial sub-range such that it is not constricted by the mean stratification. In this sense $L_E/L_O \approx 1$ may offer a somewhat more conceptually appealing transitional value to the saturated regime in our flow, rather than the empirically observed $Fr \approx 0.3$ or $Ri_g \approx 0.25$.

An important observation from the above results is the appreciably large region of the channel with a distinct $\Gamma \sim (L_E/L_O)^1$ scaling within a quasi-stationary state as proposed by GV19. This is in direct contrast to the recent study of Howland *et al.* (2020) who rather find that $\Gamma \sim (L_E/L_O)^2$ within this regime. As the $L_E/L_O - \Gamma$ framework is essentially an indirect Fr based framework, we consider the scaling arguments of GV19 for the relationship between Fr and L_E/L_O.

In the weakly stratified $Fr \gg \mathcal{O}(1)$ regime, it is expected that the overturning length scale is well approximated by the inertial energy containing scale $L_T \sim L_E \sim L_I$, hence GV19 show that

$$L_T/L_O \sim L_E/L_O \sim L_I/L_O = \frac{E_K^{3/2}/\epsilon_K}{\epsilon_K^{1/2}/N^{3/2}} = \frac{E_K^{3/2}N^{3/2}}{\epsilon_K^{3/2}} = Fr^{-3/2}. \tag{4.16}$$

Conversely in the limit of strong stratification where $Fr \ll \mathcal{O}(1)$ and the effects of buoyancy strongly influence flow dynamics, the overturning scale will be expected to scale as the vertical buoyancy scale such that $L_T \sim L_E \sim L_N$, and GV19 obtain

$$L_T/L_O \sim L_E/L_O \sim L_N/L_O = \frac{E_K^{1/2}/N}{\epsilon_K^{1/2}/N^{3/2}} = \frac{E_K^{1/2}N^{1/2}}{\epsilon_K^{1/2}} = Fr^{-1/2}. \tag{4.17}$$

However in the intermediate regime the relationship between Fr and L_E/L_O becomes somewhat ambiguous. For instance in the decaying homogeneous (un-sheared) stably stratified DNS study of Mater *et al.* (2013) no such intermediate regime was observed for any appreciable range of Fr, rather the flow was divided into the two regimes described by (4.16 and 4.17) with a single critical crossover point of $L_T/L_O \sim Fr \sim 1$.

We note that the scaling in GV19 makes no assumptions about the presence of mean shear. However let us consider that in stratified shear flow it has been shown that the overturning length scale is well approximated by the turbulent shear length such that $L_T \sim L_E \sim L_S$ (Venayagamoorthy & Stretch, 2010; Mater & Venayagamoorthy, 2014), where

$$L_S = \frac{E_K^{1/2}}{S}. \tag{4.18}$$

Here L_S is the shear analogue of L_N and can be directly related back to the mixing length $L_M = \overline{-u'w'}/S$. We note that the $L_E \sim L_I$, $L_E \sim L_N$ and $L_E \sim L_S$ scaling relationships

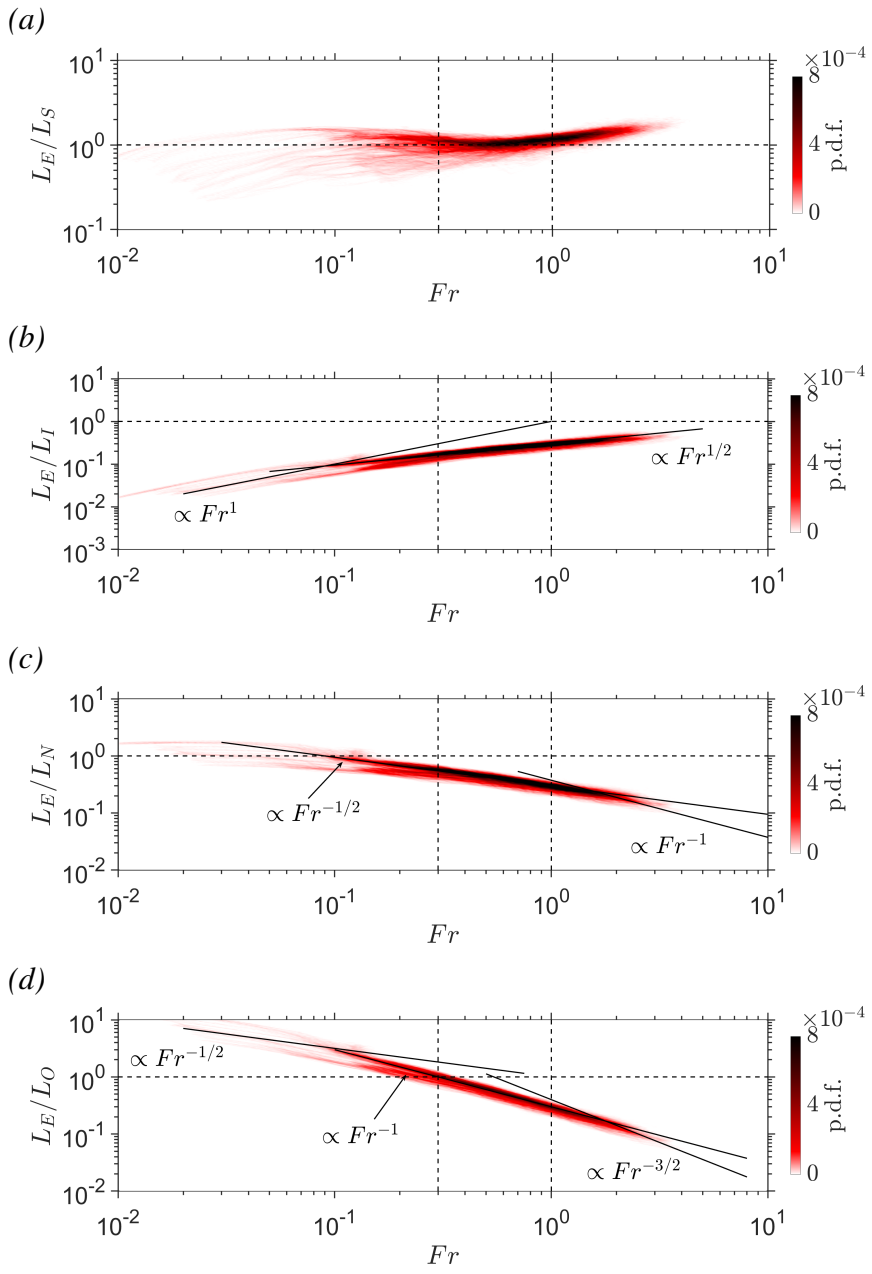

FIGURE 4.10: Two dimensional p.d.f.s of the turbulent Froude number Fr and the length scale ratios: (a) The ratio of the Ellison length L_E to turbulent shear length scale L_S, (b) The ratio of L_E to the inertial turbulent length scale L_I, (c) the ratio of L_E to vertical buoyancy length scale L_N, (d) the ratio of L_E to Ozmidov length scale L_O. All p.d.f.s. constructed out of the instantaneous data of all simulations within the range of $t/T_\tau^0 > 1$ and $0.2 \leq z/\delta \leq 0.8$. Horizontal dashed line for all figures indicates a ratio of unity. Vertical dashed lines indicate $Fr = 0.3$ and $Fr = 1$

can also be derived in the framework of dominant timescales by considering the vertical displacement of a fluid parcel from its background stratification similar to the analysis presented in §3.4, such that

$$b' \sim w' N^2 T_*, \tag{4.19}$$

where T_* is some timescale pertinent to the evolution of b' due to overturning of the buoyancy field. For instance if we consider that for the buoyancy dominated regime the pertinent timescale is T_N and by taking the approximation that $w' \sim E_K^{1/2}$ we obtain

$$L_E = \frac{b'}{N^2} \sim \frac{E_K^{1/2} N^2 T_N}{N^2} \sim E_K^{1/2} T_N = \frac{E_K^{1/2}}{N} = L_N. \tag{4.20}$$

It can hence be readily shown that a substitution of T_L or T_S into (4.19) analogously yields $L_E \sim L_I$ and $L_E \sim L_S$ respectively. In this sense and under the assumption that $L_E \sim L_T$, we present physical scaling arguments that provide support to past studies that have shown correlation between measurements of L_T and the three respective energetic length scales L_I, L_N, L_S across varying flow regimes (Mater *et al.*, 2013; Mater & Venayagamoorthy, 2014; Ijichi & Hibiya, 2018).

To investigate this further, we plot the two dimensional p.d.f.s of Fr and the ratios L_E/L_S, L_E/L_I, L_E/L_N and L_E/L_O in figure 4.10.

From figure 4.10(a) it is clear that within the moderately stratified and saturated regimes for $Fr < 1$, the L_S or alternatively T_S scaling becomes valid and the ratio L_E/L_S becomes a constant of approximately unity. In particular, the excellent correlation within the moderately stratified regime is conceptually consistent with our visual observations in figure 4.2 of vigorous overturning driven mixing arising from shear instabilities. This is further supported by the observation that in the $S^* - Fr^{-1}$ regime map in figure 4.6 the flow predominantly lies within the 'shear dominated' regime and is reflected in the $T_S \sim (T_L T_N)^{1/2}$ scaling derived in §4.4.3. The scatter in the far 'left flank' of the saturated regime can again be attributed to the relatively slow process that is acceleration of the mean flow and development of the mean shear profile in our time-varying simulations. For $Fr > 1$ where we observed the slight disagreement between the $\Gamma \sim (L_E/L_O)^{4/3}$ scaling and our results we observe a small transitional regime where L_E/L_S grows with Fr before again appearing to plateau to

a constant of $\mathcal{O}(1)$, although this behaviour is not fully developed at our parameter range. To explain this we consider our assumption that for $Fr > 1$ we expect the inertial scaling $L_E \sim L_I$ such that

$$L_E/L_S \sim L_I/L_S = \frac{E_K^{3/2}/\epsilon_K}{E_K^{1/2}/S} = \frac{SE_K}{\epsilon_K} = S^* \tag{4.21}$$

and multiplying through by N/N we obtain

$$S^*\frac{N}{N} = \frac{SE_K}{\epsilon_K}\frac{N}{N} = Ri_g^{-1/2}Fr^{-1}. \tag{4.22}$$

Now recalling $Ri_g \sim Fr^{-2}$ in the limit of high Fr as derived in (4.11) we obtain

$$L_E/L_S \sim S^* = Ri_g^{-1/2}Fr^{-1} \sim Fr^1Fr^{-1} = \text{constant}. \tag{4.23}$$

This is in agreement with our observations in figure 4.6 that S^* remains a constant of $\mathcal{O}(1)$ for $Fr > 1$.

From figure 4.10(b) however we observe that within the $Fr > 1$ regime we do not observe the expected inertial scaling of $L_E \sim L_I$ for an appreciable range of Fr. Rather we see continued growth of the ratio L_E/L_I with increasing Fr. We can explain this under two considerations. Firstly, for the data presented our highest measurements of Fr are still of $\mathcal{O}(1)$. For comparison, in the study of Mater *et al.* (2013) (their figure 6), the $L_T \sim L_I$ scaling only appears for flow where $Fr = \mathcal{O}(10)$. Secondly as seen in figure 4.1, by nature of our DNS configuration the data for high Fr inevitably occurs close to the bottom wall. At the lower vertical extent of $z = 0.2$ for which our p.d.f. results are presented, L_E, L_I, L_N and L_O are all larger than the geometric confinement length scale defined by the distance from the wall z for all simulations. As discussed in the study Taylor *et al.* (2005), this creates an additional confinement scale that changes and further complicates the relationship between the varying length scales. In this sense we find the absence of a clear $L_E \sim L_I$ scaling unsurprising and we hypothesise that a $L_E \sim L_I$ regime would manifest for our DNS configuration similar to that of Mater *et al.* (2013) if we were able to access a flow regime where $Fr \gg \mathcal{O}(1)$ and simultaneously all the relevant length scales were smaller than the physical confinement scale

z. As the confinement effects of physical boundaries on the parametrization of mixing fall outside the scope of this chapter, we leave this for future work.

Within the moderately stratified regime, we can take the $L_E \sim L_S$ scaling derived above to again obtain

$$L_E/L_I \sim L_S/L_I = 1/S^* = Ri_g^{1/2} Fr^1, \tag{4.24}$$

similarly to the derivation in (4.22). Taking the new scaling of $Ri_g = Fr^{-1}$ derived in (4.14), we obtain

$$L_E/L_I \sim Ri_g^{1/2} Fr^1 \sim Fr^{-1/2} Fr^1 = Fr^{1/2}. \tag{4.25}$$

Our results show clear support for this scaling, with a clear region of $L_E/L_I \sim Fr^{1/2}$ developing in the intermediate regime for an entire decade of Fr. This falls in direct contrast to the study of Mater *et al.* (2013) where in the absence of mean shear this scaling does not manifest but rather a $L_T/L_I \sim Fr^1$ relationship is observed for $Fr < 1$. We similarly observe an Fr^1 scaling relationship for our results, but only in the far 'left flank' of the figure within the saturated regime, suggesting a buoyancy dominated regime such that $L_E \sim L_N$ and as derived in Mater *et al.* (2013) we can obtain

$$L_E/L_I \sim L_N/L_I = \frac{E_K^{1/2}/N}{E_K^{3/2}/\epsilon_K} = \frac{\epsilon_K}{NE_K} = Fr^1. \tag{4.26}$$

From figure 4.10(c) we observe direct support for this with a clear trend that in the saturated regime L_E/L_N becomes a constant of order unity. Furthermore, we note that it can clearly be shown that

$$L_S/L_N = \frac{E_K^{1/2}/S}{E_K^{1/2}/N} = \frac{N}{S} = Ri_g^{1/2}. \tag{4.27}$$

Hence, within the saturated regime for $Fr < 0.3$ it is clear that both L_E/L_S and L_E/L_N become constant in agreement with the scaling in (4.17) and our observation that as the flow evolves towards stationarity, Ri_g will trend towards a constant critical value becoming independent of Fr. Within the the moderately stratified regime, using $L_E \sim L_S$ and $Ri_g \sim Fr^{-1}$ as derived in (4.14), we can obtain

$$L_E/L_N \sim L_S/L_N = Ri_g^{1/2} \sim Fr^{-1/2}. \tag{4.28}$$

This intermediate scaling that arises due to the presence of mean shear is again strongly supported by our results with a clear collapse of the data across a decade of Fr.

Finally for the weakly stratified regime, as shown in Mater *et al.* (2013) we can substitute the expected inertial scaling $L_E \sim L_I$ to obtain

$$L_E/L_N \sim L_I/L_N = \frac{E_K^{3/2}/\epsilon_K}{E_K^{1/2}/N} = \frac{E_K N}{\epsilon_K} = Fr^{-1}. \tag{4.29}$$

At our simulation parameter range, we cannot however confirm this scaling for our results within this regime for the reasons discussed above.

In light of the results and derivation above we now consider the ratio of L_E/L_O plotted against Fr in figure 4.10(d). Indeed it is clear that in the saturated regime we observe the respective $L_E/L_O \sim Fr^{-1/2}$ as proposed by GV19 in (4.17) and shown in the derivation above. As we barely access the weakly stratified regime we again are unable to definitively test the $L_E/L_O \sim Fr^{-3/2}$ scaling at our parameter range. For the moderately stratified regime we now consider that we have explicitly shown $L_E \sim L_S$ and also recall our scaling of $S \sim (\epsilon_K N/E_K)^{1/2}$ in (4.12) to obtain

$$L_E/L_O \sim L_S/L_O = \frac{E_K^{1/2}/S}{\epsilon_K^{1/2}/N^{3/2}} \sim \frac{E_K/\epsilon_K^{1/2}N^{1/2}}{\epsilon_K^{1/2}/N^{3/2}} = \frac{E_K N}{\epsilon_K} = Fr^{-1}, \tag{4.30}$$

which is the scaling proposed by GV19 but explicitly derived for our shear driven flow and shown to hold only for the intermediate range of $0.3 \lesssim Fr \lesssim 1$ within our flow. Hence we obtain their scaling for Γ

$$L_E/L_O \sim Fr^{-1} \Rightarrow \Gamma \sim Fr^{-1} \sim (L_E/L_O)^1. \tag{4.31}$$

As demonstrated in our results in figure 4.9.

Furthermore, due to the relationships between Ri_g and Fr derived in (4.11 and 4.14) it can be readily shown that L_E/L_O is directly related to Ri_g across the three regimes. Within the weakly stratified regime we expect

$$L_E/L_O \sim Fr^{-3/2} \sim Ri_g^{3/4}. \tag{4.32}$$

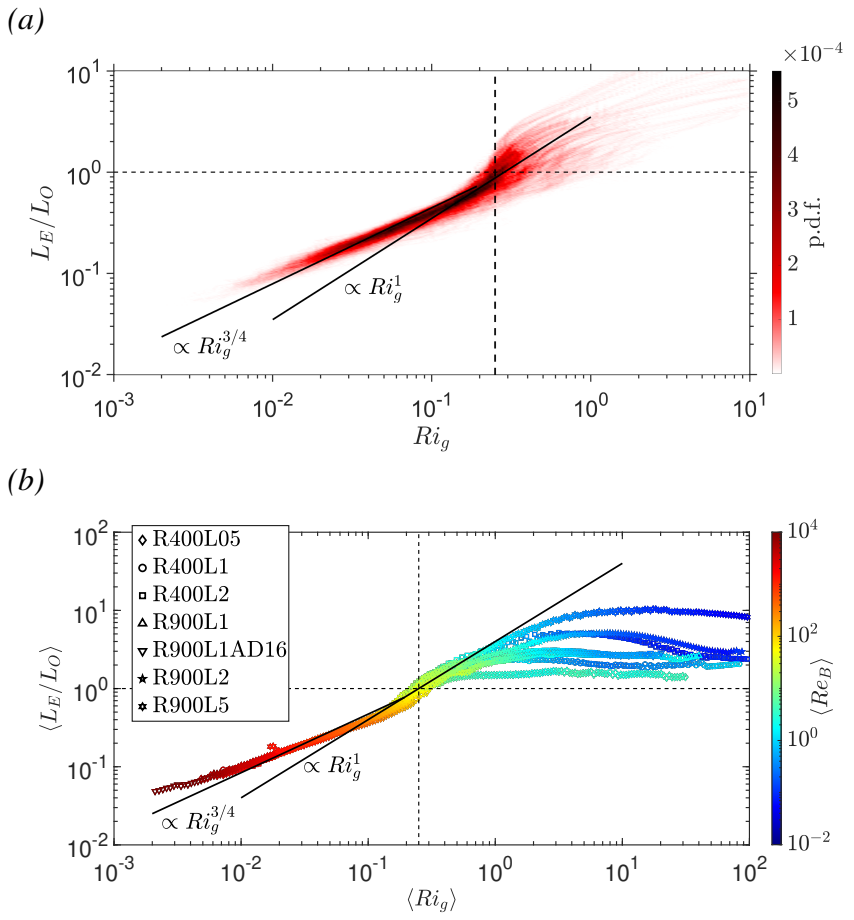

FIGURE 4.11: (a) Two dimensional p.d.f. of the gradient Richardson number Ri_g and the length scale ratio L_E/L_O constructed out of the instantaneous data of all simulations within the range of $t/T_\tau^0 > 1$ and $0.2 \leq z/\delta \leq 0.8$. (b) Ri_g bin-averaged $\langle L_E/L_O \rangle$ plotted against bins of corresponding $\langle Ri_g \rangle$ for all data points within $t/T_\tau^0 > 1$ and $z/\delta > 0.2$. Solid lines indicate the proposed scaling in (4.32 and 4.33). Vertical dashed line indicates $Ri_g = 0.25$. Horizontal dashed line indicates $L_E/L_O = 1$

Within the moderately stratified regime

$$L_E/L_O \sim Fr^{-1} \sim Ri_g^1. \tag{4.33}$$

and within the saturated regime where Ri_g and Fr become decoupled we expect that L_E/L_O will become independent of Ri_g, similar to the results of Rohr *et al.* (1988) for high Ri_g. Figure 4.11(a) the two dimensional p.d.f. of Ri_g and L_E/L_O, with reasonable collapse for the scaling of the three regimes presented above. Due to the scatter in the 'right flank' of the curve we illustrate this point more clearly by plotting the Ri_g bin-averaged set of $\langle L_E/L_O \rangle$ against

corresponding bins of $\langle Ri_g \rangle$ in figure 4.11(b). A colour bar depicting $\langle Re_B \rangle$ is again included for reference. From the results it becomes clear that for $Ri_g \lesssim 0.25$ or $L_E/L_O \lesssim 1$ the data collapses well along lines of the proposed scaling derived in (4.32 and 4.33). Meanwhile, in the 'right flank' of the curve we observe that L_E/L_O grows independent of Ri_g in agreement with the analysis above, showing separate horizontal trajectories for each simulation.

In this sense for our quasi-steady shear driven flow it becomes clear that the Fr, Ri_g and L_E/L_O frameworks for the parametrization of the mixing efficiency can all be directly reconciled across the weakly and moderately stratified regimes, with a clear transition to the saturated regime at $Fr \approx 0.3$, $Ri_g \approx 0.25$ or $L_E/L_O \approx 1$, with it being implicit that these three values are interchangeable for our flow. In light of the above analysis we find that the results of Mater *et al.* (2013) or Howland *et al.* (2020) do not contradict ours, as their studies inherently have zero mean shear and hence the $L_E \sim L_S$ scaling within the intermediate regime becomes invalid. As such, for non-sheared flows we expect that the buoyancy scaling of $L_E \sim L_N$ to hold across both the intermediate and saturated regimes for $Fr \lesssim 1$ as in Mater *et al.* (2013) and accordingly may explain the $\Gamma \sim Fr^{-1} \sim (L_E/L_O)^2$ scaling observed in Howland *et al.* (2020) for the moderately stratified regime. Hence in flows where the mean shear is not significant, we expect no appreciable range of L_E/L_O to develop a $\Gamma \sim (L_E/L_O)^1$ scaling as in the aforementioned studies. Such findings suggest that the inference of Fr and hence the state of turbulence and mixing through direct field measurements of the overturning length scale within the $Fr = \mathcal{O}(1)$ regime may prove a problematic task as it would require additional information as to the state of the flow.

4.4.5 Re_B framework and transition to diffusive regime

Since the important work of Shih *et al.* (2005), recent studies have shown that Re_B may not be an optimal parameter in the parametrization of mixing efficiency as it does not truly describe the strength of stratification within the flow in the same sense as Fr or Ri_g (Scotti & White, 2016; Maffioli *et al.*, 2016; Garanaik & Venayagamoorthy, 2019; Portwood *et al.*, 2019). Rather, it is argued that since $Re_B = (L_O/L_K)^{4/3}$, where $L_K = (\nu^3/\epsilon_K)^{1/4}$ is the

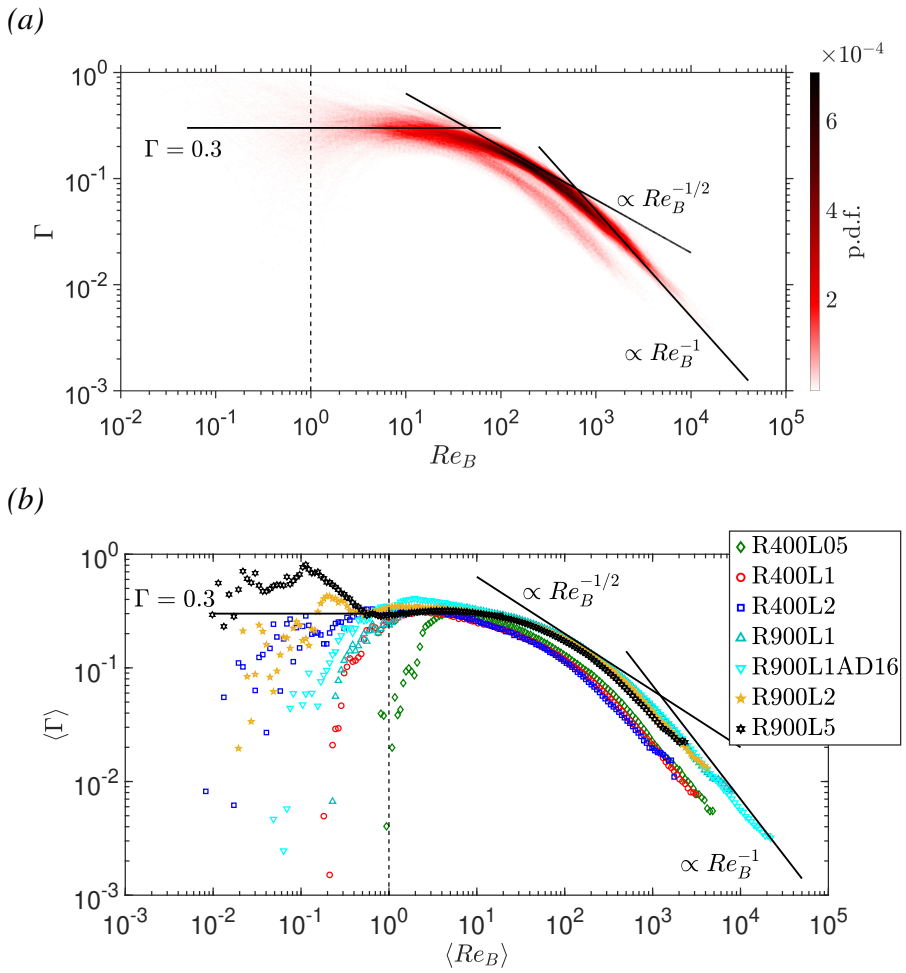

FIGURE 4.12: (a) Two dimensional p.d.f. of the buoyancy Reynolds number Re_B and the mixing coefficient Γ constructed out of the instantaneous data of all simulations within the range of $t/T_\tau^0 > 1$ and $0.2 \leq z/\delta \leq 0.8$. (b) Re_B bin-averaged mixing coefficient $\langle\Gamma\rangle$ plotted against bins of corresponding buoyancy Reynolds number $\langle Re_B\rangle$ for all data points within $t/T_\tau^0 > 1$ and $z/\delta > 0.2$. Solid lines indicate scaling lines of $\Gamma \sim Re_B^{-1/2}$ and $\Gamma \sim Re_B^{-1}$ as well as empirically observed $\Gamma = 0.3$. Vertical dashed line indicates $Re_B = 1$

well known Kolomogorov scale, its use should be restricted to a measure of the size of the inertial subrange or how 'energetic' the flow is.

We explore this by plotting the two dimensional p.d.f. of Re_B and Γ in figure 4.12(a). From the results we again observe that our flow is divided into three mixing regimes. Again we observe a clear saturated regime where Γ trends towards constancy and a distinct regime where $\Gamma \sim Re_B^{-1/2}$, in agreement with the 'intermediate' and 'energetic' regimes proposed

by Shih *et al.* (2005). Furthermore, we observe a region of the flow corresponding to the weakly stratified regime with a clear $\Gamma \sim Re_B^{-1}$ scaling, in agreement with the Couette flow results and scaling derived in Zhou *et al.* (2017*a*). The results suggest the validity of an Re_B based parametrization approach of mixing efficiency for our flow at the parameter range available. albeit with slightly more scatter in the high Re_B 'right flank' of the plot with two distinctly separate 'tails' emerging in the results. However, as described in MBL16, Re_B can be directly linked to the horizontal Reynolds number Re_h and Froude number Fr_h through the expression $Re_B = Re_h Fr_h^2$. By considering $E_K^{1/2}$ as the velocity scale instead of u_h, a similar expression can be constructed for turbulent Reynolds number Re_T and Fr such that

$$Re_B = Re_T Fr^2, \tag{4.34}$$

where $Re_T = E_K^2/(\nu\epsilon_K)$ is the turbulent Reynolds number (Mater & Venayagamoorthy, 2014). Hence the parametrization of Γ through Fr can be directly related back to Re_B. For the weakly stratified regime it is clear that

$$\Gamma \sim Fr^{-2} \Rightarrow \Gamma \sim \left(\frac{Re_B}{Re_T}\right)^{-1}. \tag{4.35}$$

For the moderately stratified regime we obtain

$$\Gamma \sim Fr^{-1} \Rightarrow \Gamma \sim \left(\frac{Re_B}{Re_T}\right)^{-1/2}. \tag{4.36}$$

And for the saturated regime, provided the flow remains turbulent, Γ will become independent of both parameters. As discussed by MBL16, in this sense and under the assumption that Γ is fundamentally linked to Fr rather than Re_B, an Re_B based parametrization inherently contains an Re_T dependence within itself. Furtheremore, taking the estimation that in weakly and moderately stratified flow $E_K^{1/2} \sim u_\tau$ and $\epsilon_K \sim u_\tau^3/\delta$, it can be clearly shown that

$$Re_T = \frac{E_K^2}{\nu\epsilon_K} \sim \frac{u_\tau^4\delta}{\nu u_\tau^3} = \frac{u_{\tau\delta}}{\nu} = Re_\tau. \tag{4.37}$$

Hence, provided the scaling in (4.35 - 4.36) is valid, we expect the flow should show Re_τ sensitivity in the parametrization of mixing efficiency through Re_B within these regimes.

To investigate this we consider an Re_B bin-averaged data-set of $\langle\Gamma\rangle$ plotted against corresponding bins of $\langle Re_B\rangle$ in figure 4.12(b) in the same manner as for the Fr sorted data in figure 4.4(b). From the results it is clear that there is no singular transitional value of Re_B from the saturated regime of constant mixing efficiency to the $\Gamma \sim Re_B^{-1/2}$ regime. Rather, two separate evolution paths develop for the $Re_{\tau,0} = 400$ and $Re_{\tau,0} = 900$ cases respectively, showing a clear Reynolds number dependence on the transition. Similarly no clear singular Re_B value emerges for the transition to the $\Gamma \sim Re_B^{-1}$ regime. In contrast with the Fr averaged results in 4.4(b) it becomes clear that an Re_B based parametrization of mixing efficiency is inherently dependant on Fr, while the reverse is untrue.

In the 'left flank' of figure 4.12(b) we can observe that the transition away from a constant Γ regime to the diffusive regime is well approximated by $Re_B \approx 1$ in agreement with the theory of Brethouwer *et al.* (2007). The exception is the data for case R400L05 (green diamonds), where due to the relatively low level of stability, the flow remains turbulent up the free surface. In this case the free surface itself rather than buoyancy acts to confine and modify the turbulence properties (Calmet & Magnaudet, 2003; Flores *et al.*, 2017), causing deviation from the constant Γ regime. The exact mechanics of this are relatively unknown and are an area of study within itself and are subsequently outside the scope of this chapter.

4.5 Conclusion

In this chapter we have investigated temporally evolving stratified open channel flow through direct numerical simulations as the flow transitions from a neutral to a stably stratified state, with the emphasis of the study being on the parametrization of mixing across varying energetic regimes within stratified channel flow and the subsequent analysis of the relationship between the relevant non-dimensional mixing diagnostics.

We find that after an initial transient adjustment period of approximately one eddy turnover time unit ($t \approx 1$), the turbulent flow within the channel is distinctly divided into weakly stratified, moderately stratified and saturated mixing regimes separated by transitional values of $Fr = 1$ and $Fr = 0.3$ across all simulations. Within the three regimes we find that

instantaneous measurements of the mixing coefficient Γ are predicted well through both the Fr and L_E/L_O parametrization frameworks as outlined in MBL16 and GV19. To our knowledge, ours is the first DNS study to extensively test both the Fr and L_E/L_O parametrization frameworks for stratified wall-bounded flow across a wide range of Fr. Considering the strong inherent vertical inhomogeneity within our sheared flow due to the depth varying flux profiles as well as the spatio-temporally evolving mean gradients S and N, the remarkable collapse of the results from purely instantaneous measurements of Fr within our flow presents a very strong argument in the favor of the case put forward by MBL16 and GV19 for the applicability of an Fr based approach to parametrization of mixing across a variety of stratified flows.

A defining characteristic of our flow is that the majority of the channel evolves into an energetically quasi-stationary state of $Fr = \mathcal{O}(1)$. Within this regime we are able to explicitly verify the novel 'moderately stratified' scaling of GV19 by showing that $B \sim E_K^{3/2}/L_N$, invariant in time and only within the range of $0.3 < Fr < 1$. By considering our flow within the inertia-shear-buoyancy regime map of Mater & Venayagamoorthy (2014), we find this regime describes a critical state where the inertial, shear and buoyancy forces are all significant in describing the energetic state of the flow. We subsequently provide physically based scaling arguments to show that $T_S \sim (T_N T_L)^{1/2}$ and $Ri_g \sim Fr^{-1}$ within this regime, hence reconciling the concept of a separate intermediate $\Gamma \sim Fr^{-1}$ scaling with the established evidence that in sheared flow and for $Ri_g < 0.25$, the turbulent Prandtl number is approximately unity resulting in a linear relationship between the mixing efficiency and Ri_g. In contrast we find that for $Fr > 1$ in the weakly stratified regime, buoyancy becomes negligible and a simple balance between shear and inertial forces leads to $Ri_g \sim Fr^{-2}$ in agreement with the arguments presented by MBL16. By considering the mixing length scaling in shear flow of $L_E \sim L_S$ within the intermediate regime we demonstrate that the remarkable collapse of the data with a distinct $\Gamma \sim (L_E/L_O)^1$ scaling for $0.3 < Fr < 1$ as proposed by GV19 comes as a direct result of the T_S scaling presented above. However, our analysis suggests that in flows devoid of mean shear, the $L_E/L_O - Fr$ and hence $L_E/L_O - \Gamma$ scaling within this regime may differ, implying limited applicability to a wider range of stratified flows under a single framework.

As such, the results suggest that for weakly and moderately stratified quasi-stationary shear flow, the three parametrization schemes become equivalent. As the unification of parametrizing mixing across various fields and applications in the study of stratified turbulence remains a pressing challenge (Caulfield, 2020), the results of our study present strong evidence of universal mixing behaviour that appears invariant under differing frameworks in these ubiquitous shear driven flows. Furthermore, as our DNS configuration is an idealisation of stratified river flows (Williamson *et al.*, 2015; Kirkpatrick *et al.*, 2019), the present results suggest that under sufficient levels of stratification an appreciable region will inevitably develop where $Fr = \mathcal{O}(1)$ and the separate scaling relationships derived in this chapter for the moderately stratified regime become physically relevant.

For flow that remains turbulent and within the regimes described by the equivalent transitional values $Fr < 0.3$, $Ri_g > 0.25$ or $L_E/L_O > 1$, we find that the mixing efficiency saturates to a constant asymptotic value, seemingly in agreement with the strongly stratified scaling of MBL16, however we note our lowest values of Fr obtained in this chapter are still significantly higher than the theoretical upper limit of the strongly stratified regime. We further find that in agreement with the theory of Brethouwer *et al.* (2007), the transition away from a saturated mixing efficiency into the diffusive regime occurs at $Re_B \approx 1$ for our flow, with the caveat that the transition occurs sufficiently far from the free surface boundary.

We would like to clarify that the primary conclusions from the results within this chapter and our comparison to GV19 is not to specify clear transitional values of $Fr, Ri_g, L_E/L_O$ between the varying mixing regimes nor to serve as direct validation for specific mixing models with direct applicability to the field. Rather due to the ambiguity in the current literature (Caulfield, 2021), the focus of this chapter was to identify and present evidence for a distinctly different 'intermediate' mixing regime where $Fr \sim \mathcal{O}(1)$ which have identified as being fundamentally different from the two more established limit regimes of $Fr \gg \mathcal{O}(1)$ and $Fr \ll \mathcal{O}(1)$. We have further expanded on the insightful scaling arguments of GV19 to develop new scaling relations in the shear/inertia/buoyancy regime space as well as in the conceptual framework of the overturning length scale. Furthermore, we have observed visually that both the physical structure of the flow and the nature of the mixing within this 'intermediate' mixing regime is

definitively different to that of the weakly stratified and hence quasi-isotropic state. Hence we substantiate our claims and primary argument that this regime is indeed dynamically distinct and care should be taken in future studies of stratified flow driven by a mean shear to properly account for the differing dynamics for flow where $Fr \sim \mathcal{O}(1)$.

CHAPTER 5

Intermittency and critical mixing in stratified open channel flow

---

In this chapter we investigate the spatio-temporal intermittency that arises in stratified open channel flow due to the suppressive nature of stable stratification. We hence present an adaptation of the unstable density gradient method of Portwood *et al.* (2016) to robustly separate instantaneous realisations of the flow into turbulent and quiescent regions. We explore the nature and mechanisms by which this intermittency manifests for our flow and quantify it through a 'local' depth varying turbulent fraction which we demonstrate is well predicted through Monin-Obhukov theory. We further investigate the resulting vertical structure of the channel from the perspective of the two conditionally averaged data sets with respect to energetic quantities and key mixing diagnostics. Finally we directly investigate the effect intermittency has on a Fr based parameterization of Γ for our flow at low Fr.

The contents of this chapter are based on the following publication:

Issaev, Vassili, Williamson, N. & Armfield, S. W. 2022, Intermittency and critical mixing in stratified channel flow. *Journal of Fluid Mechanics*, (Submitted).

5.1 Introduction

Turbulent flows subject to strong stable stratification such as in the ocean and atmosphere have been shown to exhibit strong spatio-temporal intermittency with isolated patches of vigorous 'weakly stratified' turbulence encapsulated by an essentially quiescent yet 'strongly stratified' fluid (Baker & Gibson, 1987; Van de Wiel *et al.*, 2002). As discussed in §1, this intermittency creates significant challenges in the quantification of local mixing rates from measurements

that are inherently calculated as averages over finite volumes and time periods and in which conceivably contributions from both flow regimes are present in unknown quantities. In wall-bounded stratified flows the complexity of the intermittency problem is further confounded by the inherent vertical inhomogeneiety of the flow (Armenio & Sarkar, 2002; Taylor *et al.*, 2005). Accordingly, flow properties and mixing diagnostics for wall-bounded flows are by convention presented as appropriate volumetric averages across horizontal planes (García-Villalba & del Álamo, 2011; Deusebio *et al.*, 2015; Williamson *et al.*, 2015; Zhou *et al.*, 2017*a*; Issaev *et al.*, 2022). However strong intermittency of turbulence has been observed across horizontal layers in the very same studies. In this study we explore the nature and structure of intermittency in stratified open channel flow and its effect on the estimation of local mixing rates.

Strongly stratified flows are highly anisotropic with a large separation of horizontal and vertical scales. Such flows are typically defined by a sufficiently small turbulent Froude number Fr. Additionally for turbulence to be sustained, a global buoyancy Reynolds number Re_B must be appropriately large such that the inertial range of the flow is sufficient to generate local instabilities that create turbulence (Riley & deBruynKops, 2003). In particular, much of the stratified turbulence theory developed and investigated over the past decades that underlies the prediction of mixing and energetic transfer in the ocean and atmosphere focuses on the so called 'strongly stratified' or 'layered anisotropic stratified turbulence' (LAST) regime in the limit of $Fr \ll \mathcal{O}(1)$ and $Re_B \gg \mathcal{O}(1)$ (Billant & Chomaz, 2001; Riley & deBruynKops, 2003; Lindborg, 2006; Riley & Lindborg, 2008; Maffioli & Davidson, 2016; Falder *et al.*, 2016; Maffioli, 2019; Taylor *et al.*, 2019).

Portwood *et al.* (2016) demonstrate that flow described by appropriate bulk measures of Fr and Re_B such that the flow approaches the LAST regime may be subdivided into three dynamically distinct regimes: 'turbulent patches', 'intermittent layers' and 'quiescent' flow, with conditionally averaged values of Re_B that vary by orders of magnitude across the three regimes. Of particular note, they find that although for their most stratified case of $Fr = 0.015$, the quiescent region occupies approximately 80% of the flow domain, it only accounts for less than 15% of the total dissipation rates of TKE and scalar variance. In their DNS study

de Bruyn Kops (2015) similarly find that with decreasing Fr the flow becomes increasing anistropic with an emerging bimodal distribution of the dissipation rates. In their similar DNS study of homogeneous stratified turbulence Howland *et al.* (2020) further observe the occurrence of 'spontaneous layering', such that the flow organizes into horizontal layers of vigorous and essentially isotropic turbulence as well as definitively anisotropic quiescent flow. A fundamental question of stratified turbulence is hence how such strong intermittency effects the parametrization of diapycnal mixing through non-dimensional parameters that are comprised of flow properties that display significant spatial variation over the different dynamical regions.

Of particular note, Maffioli *et al.* (2016) present scaling arguments based on the underlying theory of the LAST regime to demonstrate that for quasi-stationary flow in the limit of low Fr, Γ should become independent of Fr and asymptote to a constant value. Since their work, a number of studies with a variety of flow configurations and ranges of Fr and Re_B including the work presented in §4, have demonstrated support for this result (Garanaik & Venayagamoorthy, 2019; Howland *et al.*, 2020; Smith *et al.*, 2021; Issaev *et al.*, 2022), albeit with differing asymptotic values of Γ. However, it remains unclear how the varying intermittency in these studies influences this relationship as measurements of both Fr and Γ inherently contain contributions from both turbulent and quiescent regions of the flow.

In atmospheric boundary layer literature, the prediction of intermittency has been frequently explored through the Monin-Obhukov (M-O) framework and the M-O length L which compares the turbulence generation through the wall shear to the suppression of turbulence as a result of the surface buoyancy flux (Van de Wiel *et al.*, 2002, 2012). In their idealised DNS of the nocturnal atmospheric boundary layer, Flores & Riley (2011) demonstrate that the collapse of turbulence in channel flow subject to bottom wall cooling is well predicted by the parameter L^+, where L^+ is the M-O length normalized in viscous wall units. In a subsequent study Deusebio *et al.* (2015) demonstrate that the L^+ criterion is similarly applicable to stratified plane Couette flow for the prediction of intermittency. Chung & Matheou (2012) further show that M-O theory may be similarly applied to homogeneous stratified shear flow and intermittency displays a dependence on a 'local' normalized M-O length Λ^+. However, it

still remains unclear whether the prediction of intermittency through M-O theory is applicable to stratified flows in which the suppression of turbulence occurs 'top-down' such as the radiatively heated open channel flow framework of Williamson *et al.* (2015).

For stratified flows in the presence of a mean shear, the theme of intermittency and relaminarization has been frequently explored in literature through the gradient Richardson number: $Ri_g = N^2/S^2$, where S is the mean shear. The underlying concept being that the stabilizing forces of the background stratification suppress turbulence whilst the background shear deforms the flow leading to the formation of shear instabilities. Based on linear stability analysis Miles (1961) proposed the 'Miles-Howard Criterion' of an upper limit of $Ri_g = 1/4$ for the formation of instabilities. Since then, seemingly in agreement a wide range of studies have observed that in a stationary state, stratified sheared turbulence tends to converge to an upper critical limit of $Ri_{g,c} \approx 0.16 \sim 0.25$ (Shih *et al.*, 2000; Flores & Riley, 2011; Chung & Matheou, 2012; Williamson *et al.*, 2015; Zhou *et al.*, 2017*a*; Portwood *et al.*, 2019). However as discussed by Zhou *et al.* (2017*a*), it is unclear if this result is indeed related to the stability of the local flow as argued by Miles (1961) or is simply 'fortuitous'. Thorpe & Liu (2009) further hypothesise that stratified shear flow naturally converges to this state of 'marginal instability' that facilitates the formation of relatively efficient mixing through local shear instabilities. This work was expanded on by the studies of Salehipour *et al.* (2018) and Smyth *et al.* (2019) who use numerical and observational data to demonstrate this behaviour dubbed 'self-organised criticality' in stratified shear flows. However as noted in Caulfield (2020), due to the inherent local intermittency of stratified flows it becomes somewhat ambiguous as to what defines a local measure of the background shear and stratification and hence the appropriate measure of Ri_g. As such the role of the intermittency in the concept of a 'critical' Ri_g remains unclear.

The shear layer study of Mashayek *et al.* (2017) support the aforementioned 'self-organized criticality' demonstrating that the mixing in a KHI overturning event is most vigorous and efficient when the flow enters a critical state such that the injection of energy into the flow through overturning is precisely at the wavelength corresponding to the upper limit of the inertial sub-range such that $R_{OT} \approx 1$. Where $R_{OT} = L_O/L_T$ is the length scale ratio

of the Ozmidov length scale (L_E) characterizing the theoretical upper bound for scales largely unaffected by the background stratification to the well known Thorpe scale (L_T) describing the extent of overturning motions. Mashayek *et al.* (2021) expand on this idea, demonstrating through oceanic observational data sets that the distinct majority of field observations correspond to this 'critical' and 'optimal' state defined by a marginally unstable Ri_g and where $R_{OT} \approx \mathcal{O}(1)$. It is still however unclear how the theory and results derived in studies of singular mixing events pertains to forced quasi-stationary flows and the role of the inherent intermittency arising from stable stratification, in particular that of wall-bounded vertically inhomogeneous flows. Furthermore, it is unclear how the concept of a self-organized critical state within stratified shear flow reconciles with the numerous observations of an asymptotic Γ regime in the limit of low Fr and how intermittency effects this behaviour.

The concept of spatio-temporally intermittent mixing is directly physically relevant to stratified river flows which underlies the motivation behind this study. Persistent stratification and subsequent reduction in mixing rates in Australian rivers has been shown to create conditions that directly facilitate harmful cyanobacterial blooms and reduce vertical transport of key nutrients (i.e. CO_2, O_2) absorbed at the water/air interface (Turner & Erskine, 2005). As such the need to accurately predict the intermittency profile of the flow and to better understand the mixing dynamics in regions of intermittency are crucial to understanding such ecologically damaging processes.

In light of the discussion presented above, the work presented in this chapter falls into two key themes. Firstly, that of the robust identification and prediction of the intermittency profile in radiatively heated open channel flow. Secondly, that of the role of spatio-temporal intermittency in stratified shear flows on the estimation of mixing rates through 'local' measurements of appropriately defined mixing diagnostics, with emphasis on the concept of self-organized 'critical' mixing in stratified shear flows. We explore these ideas through our DNS of temporally evolving stratified open channel flow which due to its vertical inhomogeneity allows us to explore a wide range of local parameters with a varied intermittency profile within a single simulation. To that end the remainder of this chapter is structured as follows. In §5.2 we present the list of DNS used in this chapter. In §5.3 we present our adaption of the density

Case	Re_τ^0	λ^0	Pr	$\alpha\delta$	$L_x \times L_y \times L_z$	$N_x \times N_y \times N_z$	$\frac{t_f}{T_\tau^0}$	$\frac{t_e}{T_\tau^0}$	$\frac{z_e}{\delta}$
R400L0.5	400	0.5	1	8	$2\pi\delta \times \pi\delta \times \delta$	$512 \times 512 \times 150$	50	15	0.86
R400L0.5AD32	400	0.5	1	32	$2\pi\delta \times \pi\delta \times \delta$	$512 \times 512 \times 150$	40	15	0.89
R400L1	400	1	1	8	$2\pi\delta \times \pi\delta \times \delta$	$512 \times 512 \times 150$	50	30	0.82
R400L1LD	400	1	1	8	$8\pi\delta \times 2\pi\delta \times \delta$	$2560 \times 1280 \times 150$	40	30	0.83
R400L2	400	2	1	8	$2\pi\delta \times \pi\delta \times \delta$	$512 \times 512 \times 150$	90	50	0.71
R900L1	900	1	1	8	$2\pi\delta \times \pi\delta \times \delta$	$1152 \times 1152 \times 450$	43	33	0.91

TABLE 5.1: List of DNS performed and relevant parameters. t_f corresponds to the total simulation time, t_e corresponds to the time to obtain quasi-stationary, z_e corresponds to the upper vertical coordinate past which the stationary flow is no longer in a state of local quasi-equilibrium.

gradient inversion method of Portwood *et al.* (2016) to separate our intermittent flow into 'turbulent' and 'quiescent' regions and present our prediction of the intermittency profile through Monin-Obhukov theory. In §5.4 we demonstrate the vertical distribution of key conditionally averaged flow properties and non-dimensional parameters within the turbulent and quiescent regions of the flow . In §5.5 we explore and quantify the effect of intermittency on the parametrization of mixing rates through Fr and discuss the implications of the results for stratified shear flow. Finally in §5.6 we summarize the main findings within this study.

5.2 List of DNS performed and notation

Table 5.1 presents the list of DNS considered in this chapter. As we are interested in the vertical structure of the intermittent stationary flow, we only consider the DNS that have been substantially past stationarity as defined by t_e in §3. Furthermore, as this chapter focuses on intermittency that arises due to strong stable stratification we again only consider DNS run at $\lambda^0 \geq 0.5$. We again demonstrate that our local correlations of flow flow properties are independent of the flux profiles by considering a single $\alpha\delta = 32$ case relative to all other DNS where $\alpha\delta = 8$. We further limit our focus in this chapter on cases for which $Pr = 1$. Finally as discussed in §2, we acknowledge past studies that have shown that the size of the domain may effect the intermittent regime where laminar and turbulent patches coexist, such that a smaller domain often leads to earlier laminarization for the same set of

bulk parameters (Flores & Riley, 2011; García-Villalba & del Álamo, 2011; Brethouwer *et al.*, 2012; Deusebio *et al.*, 2015). However as shown in Williamson *et al.* (2015), our adiabatic bottom boundary condition ensures that the near-wall region remains fully turbulent, hence we do not expect the domain size to significantly influence the results presented in this study. Accordingly for computational efficiency we keep the domain size constant at $L_x \times L_y \times L_z = 2\pi\delta \times \pi\delta \times \delta$ across all simulations. However as intermittency is the core theme of this chapter we also consider case R400L1LD (long domain) for which the domain size is increased to $L_x \times L_y \times L_z = 8\pi\delta \times 2\pi\delta \times \delta$ to demonstrate the independence of our results on the domain size.

In this chapter we consider both time developing and stationary flow. We hence define that for this chapter the $\overline{(\cdot)}$ overbar operator indicates an appropriate temporal average within the stationary time period of $t_e \leq t \leq t_f$. Meanwhile, unless otherwise explicitly stated, the angle bracket $\langle . \rangle$ operator in this chapter presents an appropriate instantaneous ensemble average at time t.

5.3 Turbulent/Non-Turbulent identification algorithm

5.3.1 Method Validation

We base our turbulent flow identification algorithm on the method described in Portwood *et al.* (2016) (Henceforth denoted as PKTSC16). The underlying hypothesis being that regions of active turbulence inevitably contain some measure of local overturning down to a relevant length scale such that there exist appreciable regions in the flow where the local buoyancy gradient is unstable; i.e. $\partial b(\mathbf{x})/\partial z < 0$. We define our detector function Q as:

$$Q(\mathbf{x}) = \int_{-\infty}^{\infty} H\bigg(- \frac{\partial b(\mathbf{x}-\mathbf{r})}{\partial z} \bigg) G_{xy}(\mathbf{r}, l_f) d\mathbf{r} \tag{5.1}$$

Where H is the heavy-side function, G_{xy} is the two dimensional Gaussian function (in the $x-y$ horizontal plane) with the input variance corresponding to the filter length scale l_f and $\mathbf{r}$ is the dummy variable for the convolution of the Gaussian. We note that the inherent

vertical inhomogeneity of open channel flow creates significant variation with in the turbulent length scales of the flow with respect to the vertical coordinate z (Williamson *et al.*, 2015). Accordingly we cannot construct a sensible three-dimensional cumulative filtered density function as the detector function analogously to that of the homogeneous flow of PKTSC16 that tests the vertical extent of the density inversions. Our hypothesis however is that for active vigorous turbulence, overturns of a particular vertical extent l_f leave an 'imprint' of small scale inversions on a horizontal pancake of the same radius l_f. $Q(\mathbf{x})$ can hence be considered the smoothed probability that within the horizontal circular filter range of l_f the local buoyancy gradient at $(\mathbf{x})$ is unstable. Subsequently, for our flow the turbulent identification algorithm requires two choices, an appropriate filter size l_f and a suitable threshold value of Q^* to be defined below in (5.3).

As discussed in §5.1, for their high resolution DNS, PKTSC16 demonstrate that by defining two different filter radii based on physical length scales, their flow may be separated into three regimes with varying values of conditionally averaged Re_B: vigorous 'patch' turbulence where buoyancy inversions occur down to the buoyancy length scale L_B and where $Re_B \approx \mathcal{O}(100)$, 'layers' where buoyancy inversion occur down to the Taylor micro scale L_λ where $Re_B \approx \mathcal{O}(10)$ and 'quiescent' flow where $Re_B \approx \mathcal{O}(1)$. Where

$$L_B = \frac{u_h}{N}, \qquad L_\lambda = \sqrt{15\frac{\nu}{\epsilon_K}}\mathbf{u}'_{\text{rms}}. \tag{5.2a, b}$$

where u_h is the turbulent horizontal velocity scale, $N = (\partial\overline{b}/\partial z)^{1/2}$ and $\epsilon_K = \nu(\partial u_i'/\partial x_j)^2$. As $L_B > L_\lambda$ for all z, it is clear that regions of the flow where buoyancy inversions occur down to a length scale of L_λ incorporate both turbulent 'patch' and 'layer' regions. The vertical inhomogeneity of open channel flow creates a wide range of horizontally averaged $Re_B(z)$ that spans between $\mathcal{O}(10^5)$ near the wall to $\mathcal{O}(10^{-2})$ at the free surface (as will be shown shortly). However the same inhomogeneity of the stratification profile and modest Re_τ of our simulations ensures that we do not have sufficient dynamic range to find horizontal planes within our flow where appreciable contributions from all three regions exist. Accordingly, for our study we have chosen not to differentiate between 'patch' and 'layer' turbulence, but rather classify them together as 'turbulent' with the remaining flow considered 'quiescent'.

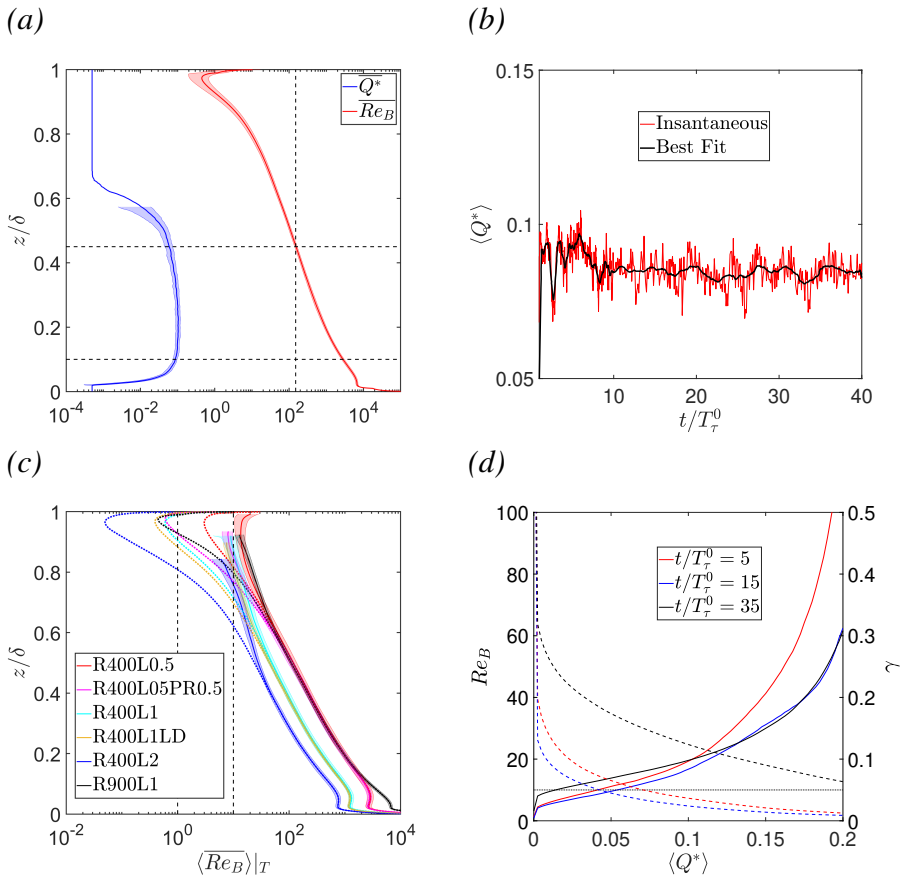

FIGURE 5.1: (a) Stationary profiles of the horizontally averaged cutoff threshold paramater $\overline{Q}^*$ and buoyancy Reynolds number $\overline{Re_B}$ as a function of z/δ. Shading indicates $\pm$ one standard deviation (Shading for $\overline{Q}^*$ cutoff to minimize noise in the plot.) Horizontal lines indicate $z/\delta(\overline{Re_B} = 150)$ and $z/\delta = 0.1$. (b) Time series of the global threshold parameter $\langle Q^* \rangle$. (c) Stationary profiles of the conditionally averaged 'turbulent' buoyancy Reynolds number $\langle \overline{Re_B} \rangle|_T$ plotted against z/δ for all simulations. Shading indicates $\pm$ one standard deviation. Plots ended at a turbulent fraction threshold of $\gamma < 0.05$. Dotted lines of same color correspond to full data set. Vertical dashed lines correspond to $Re_B = 1, 10$ (d) Variation of conditionally averaged $\langle Re_B \rangle|_T$ (left axes solid lines) and turbulent fraction γ (right axes dashed lines) with varied sampling of $\langle Q^* \rangle$ at $z/\delta = 0.875$. Figures (a),(c),(d) for case R900L1

Hence we only consider one depth varying filter size in the definition of (5.1) such that $l_f(\mathbf{x}) = L_\lambda(z)$.

In PKTSC16 the threshold criterion was derived by considering a reference simulation at high Re_B and moderate Fr where intermittency was negligible such that the entire flow domain

may be considered a turbulent 'patch'. For our study we employ similar logic by considering the bottom region of the channel is similarly described by $Fr > \mathcal{O}(1)$ and $Re_B > \mathcal{O}(10^2)$ and may be considered fully turbulent (Williamson *et al.*, 2015; Kirkpatrick *et al.*, 2019; Issaev *et al.*, 2022). We hence define a depth and time varying threshold value of $Q^*(z,t)$ such that almost the entire volume of a horizontal plane at depth z would be considered turbulent. We explicitly define this as

$$Q^*(z,t) \qquad \text{s.t.} \qquad \frac{1}{L_x L_y}\int_0^{L_x}\int_0^{L_y} H\big(Q(\mathbf{x},t) - Q^*(z,t)\big)dxdy \geq 0.99. \tag{5.3}$$

Hence we expect that for fully turbulent regions $Q^*(z,t)$ will approach a constant value and for regions with strong intermittency $Q^*(z,t)$ will trend towards zero. To demonstrate this we plot the quasi-stationary profiles of $\overline{Q}^*(z)$ and $\overline{Re_B}(z)$ against z for a typical case R900L1 in figure 5.1(a), where the $\overline{(\cdot)}$ operator denotes temporal averaging over the quasi-stationary window of $t_e \leq t \leq t_f$. Note that a reading of $\overline{Q}^*(z) = 10^{-4}$ corresponds to the finest numerical sampling size of Q^* in the algorithm to satisfy the implicit equation (5.3) and may be interpreted as essentially zero.

The results show clear support for our hypothesis showing $\overline{Q}^*(z)$ approaching a constant value of $\mathcal{O}(10^{-1})$ within a region approximately bounded by an upper vertical limit corresponding to $Re_B \approx 150$ and a lower limit of $z/\delta \approx 0.1$. The upper bound is consistent with the arguments presented in PKTSC16 for $Re_B \approx \mathcal{O}(100)$ as a criterion for vigorous turbulence where intermittency is negligible. The lower bound represents the dominance of near-wall mechanics and viscous effects that invalidate the assumption of small scale overturning as an indicator of active turbulence. Note that for the $Re_\tau = 400$ cases the corresponding depth is $z/\delta \approx 0.15$ As near-wall mechanics are outside the scope of this study, for simplicity we assume that this region is fully turbulent due to past studies showing negligible effects of stratification for channel flow with a bottom adiabatic boundary condition at a similar parameter range (Taylor *et al.*, 2005; Williamson *et al.*, 2015; Kirkpatrick *et al.*, 2019). Although not shown here, qualitatively similar behaviour occurs for all our other simulations, with variations in the asymptotic value of $\overline{Q}^*(z)$ for each simulation.

Accordingly we can construct a global threshold value of $\langle Q^*(t)\rangle$ of the form

$$\langle Q^*(t)\rangle = \frac{1}{(z(Re_B = 150) - z_l)} \int_{z_l}^{z(Re_B=150)} Q^*(z,t)dz. \tag{5.4}$$

where

$$z_l/\delta = \begin{cases} 0.15, & Re_\tau = 400 \\ 0.10, & Re_\tau = 900. \end{cases} \tag{5.5}$$

Figure 5.1(b) shows the time series of $\langle Q^*(t)\rangle$ for case R900L1, both the instantaneous realisations and a line of best fit using a moving average filter. Note we do not consider the data for $t/T^0_\tau < 1$ as this corresponds to an initial non-linear adjustment period of the flow due to the sudden imposition of buoyancy on an idealised isothermal flow field (see §3). The results show that $\langle Q^*(t)\rangle$ is well behaved, with a slight initial decline during the early 'suppression period' of the flow (Atoufi *et al.*, 2020), and approaches a constant value of $\langle Q^*(t)\rangle \approx 0.09$ with a normal distribution of the scatter about the line of best fit of the order of 0.005 in agreement with the narrow spread of $\overline{Q}^*(z)$ observed in figure 5.1(a). Accordingly we propose that provided a sufficient amount of flow falls within the fully turbulent range as defined in (5.4), a single realisation of the flow at time t and the subsequent instantaneous measurement of $\langle Q^*(t)\rangle$ is sufficient to separate the flow into turbulent and quiescent regions. Hence we define that flow is considered 'turbulent' if $Q(\mathbf{x},t) \geq \langle Q^*(t)\rangle$ and 'quiescent' or quasi-laminar if $Q(\mathbf{x},t) < \langle Q^*(t)\rangle$.

To test this we consider that as discussed in PKTSC16, a consensus has formed in stratified flow literature that for active turbulence a requirement is that $Re_B \geq \mathcal{O}(10)$. We hence define a conditionally averaged (and inherently depth varying) $\langle Re_B\rangle|_I$ such that

$$\langle Re_B\rangle|_I = \frac{\langle \epsilon_K\rangle|_I}{\nu\langle N^2\rangle|_I} \tag{5.6}$$

where the $\langle .\rangle|_I$ operator denotes conditional averaging over the set I where $|_F, |_T, |_Q$ correspond to the full (unsorted), turbulent and quiescent data sets respectively and where $\langle N^2\rangle|_I = \langle \partial b(\mathbf{x})/\partial z\rangle|_I$. Accordingly in the limit of low Re_B ,we expect that for horizontal layers with strong intermittency, the conditionally averaged $\langle Re_B\rangle|_T$ should trend towards $\mathcal{O}(10)$ if our turbulent identification algorithm is robust.

We demonstrate the validity of our method by plotting the quasi-stationary profiles of $\langle\overline{Re_B}\rangle|_T$ against z/δ for all simulations in figure 5.1(c). We restrict the plots within the limits of $0.05 < \gamma \leq 1$, as past this limit the relatively small amount of data at our flow resolution generates excessive noise in measurements of turbulent flow properties. For reference the profiles of the full data-set are also plotted (dashed lines of the same colour). From the results it is clear that for all simulations, despite the variation in the profiles of $\langle\overline{Re_B}\rangle|_F$, the turbulent counterpart $\langle\overline{Re_B}\rangle|_T$ appears to approach a limit of $\mathcal{O}(10)$ confirming the hypothesis underlying our algorithm.

To further test the robustness of our algorithm we consider the of depth $z/\delta = 0.875$ of case R900L1 where throughout the entire flow evolution $Re_B \approx \mathcal{O}(1)$ and a significant portion of the flow is quiescent. Figure 5.1(d) shows the variation of $\langle Re_B\rangle|_T$ (solid lines, left axes) and the turbulent volume fraction $\gamma = V_T/V_F$ (dashed lines, right axes) as we vary the threshold parameter $\langle Q^*\rangle$ at three arbitrarily selected instances in time. To help interpret this figure it is important to consider that $\langle Q^*(t)\rangle = 0$ corresponds to the assumption that the entire horizontal plane is considered turbulent such that $\langle Re_B\rangle|_T = \langle Re_B\rangle|_F$. From the results it is clear that the result is robust with $\langle Re_B\rangle|_T \approx \mathcal{O}(10)$ for all cases showing relative insensitivity to the noise in the instantaneous measurements of $\langle Q^*(t)\rangle$ within the expected standard deviation of 0.005 observed in figure 5.1(b). Similarly γ is well behaved, with negligible variation in the region of uncertainty relative to $\langle Q^*(t)\rangle$.

For visual reference we also verify our identification algorithm by considering flow visualizations of the ϵ_K field for case R900L1 across all three planes in figure 5.2 at $t/T^0_\tau = 35$ which has been chosen to display the full range of intermittency in the flow. The overlaying red contours display the separation of turbulent and quiescent regions as outlined in the method above. Figures 5.2(a,b) show slices in the $x-y$ plane at depths of $z/\delta = 0.75$ and $z/\delta = 0.875$ respectively and where there is significant variation in the amount of intermittency between the two depths. The results show convincing support for the robustness of our algorithm as the small-scale high dissipation regions of active turbulence are distinctly separated from quiescent regions of essentially constant near-zero dissipation.

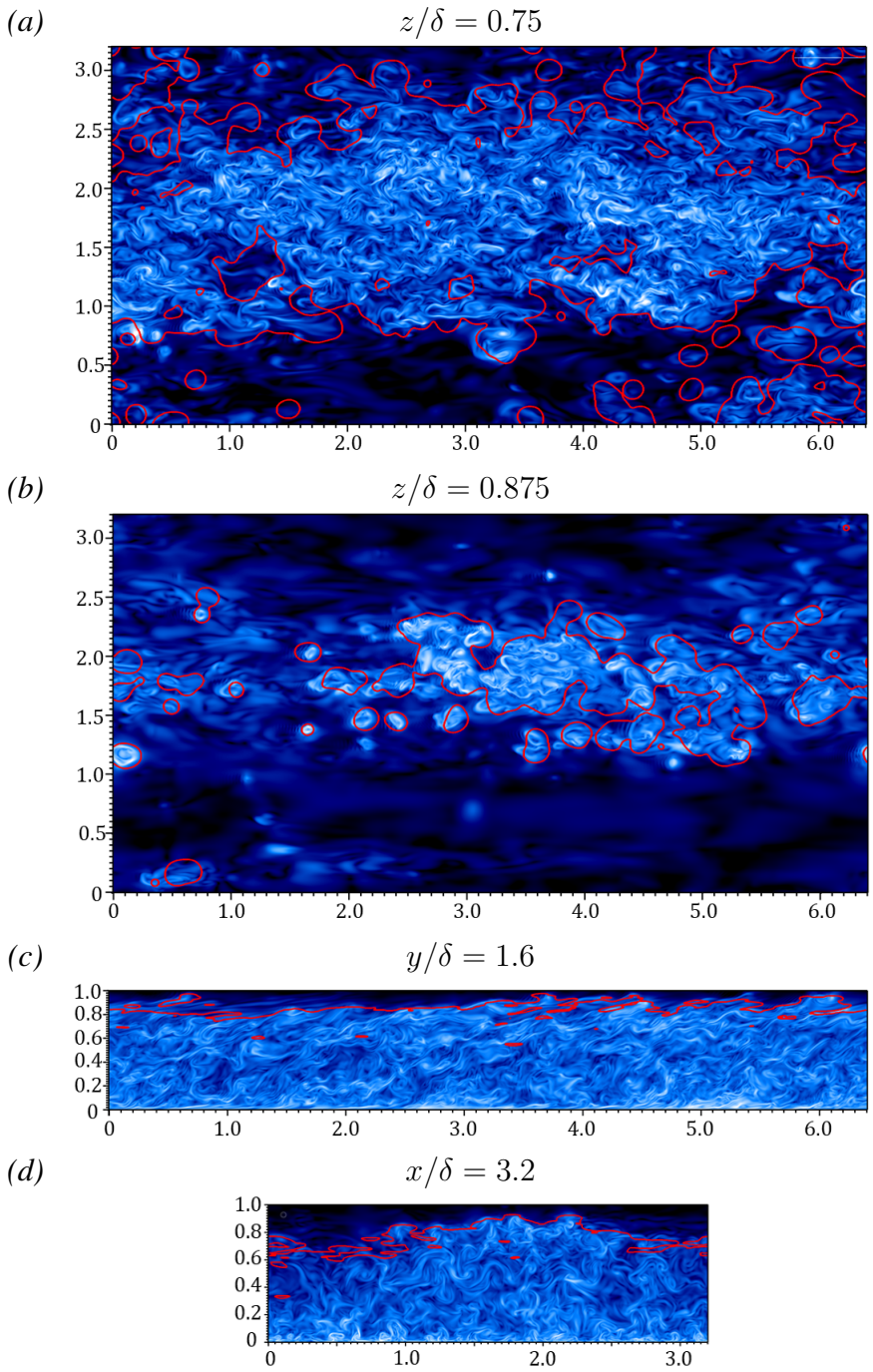

FIGURE 5.2: Instantaneous realisations of the dissipation rate of kinetic energy field ϵ_K at $t/T_\tau^0 = 35$ for case R900L1. Red lines indicate the separation of the 'turbulent' and 'quiescent' flow regions as per the algorithm in §5.3. Colour scale for all figures is logarithmic. (a,b) slices in the $x - y$ plane at $z = 0.75, 0.875$ respectively. (c) Slice in the $x - z$ plane. (d) Slice in the $y - z$ plane.

Figures 5.2(c,d) show realisations of the flow in the $x-z$ and $y-z$ planes respectively. The results clearly depict our unique flow structure with a weakly stratified fully turbulent lower region, a distinctly sheared central bulk flow and an upper quiescent or quasi- laminar layer. The results clearly highlight the inherent three dimensional aspect of the intermittency boundary in stratified open channel flow and the subsequent inaccuracy of naively using a single horizontally averaged metric to separate the transition from turbulent to quiescent flow. Here we note a fundamental feature of our flow: that the intermittency in our flow which may be interpreted as a deformed horizontal interface between the lower turbulent and upper quiescent flow. This being fundamentally different to that of past atmospheric boundary layer or Couette flow studies where intermittency originates at the wall (Flores & Riley, 2011; Deusebio *et al.*, 2015). We will return to this idea in more detail in §5.4. In particular, we highlight that the shear layer that forms between the turbulent bulk flow and upper quasi-laminar layer is notably defined by distinctly energetic overturning driven mixing that arises from the critical conditions below as the shear instability structures are ejected upwards through upwelling events. From figure 5.2(c) we note that our algorithm is able to robustly capture this mechanic identifying singular ejection events in the upper layer as 'turbulent'.

5.3.2 Intermittency profile and Monin-Obhukov scaling

Figure 5.3(a) shows the resulting intermittency profile as a result of the turbulent/quiescent identification algorithm outlined above by plotting the quasi-stationary turbulent volume fraction $\overline{\gamma}$ against z/δ for all simulations. Accordingly in agreement with the distinctly inhomogeneous profiles of Re_B, the profiles of $\overline{\gamma}$ show significant variation with z as the flow sharply transitions from its fully turbulent state in the lower portion of the channel to an entirely quiescent state at the upper boundary. We note this profile comes as a result of the deformed turbulent/quiescent interface that spontaneously forms within the flow. This allows us the opportunity to explore the effect of intermittency in wall bounded flows at a wide range of local parameters and with a distinctly inhomgeneous intermittency profile that is not effected by the suppression of near-wall mechanics.

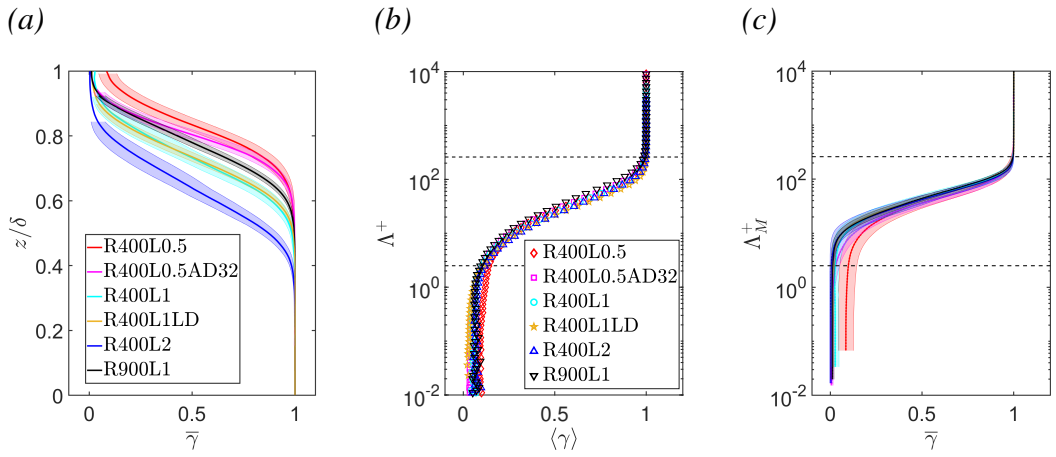

FIGURE 5.3: (a) Vertical profiles of the stationary turbulent fraction $\overline{\gamma}$ for all simulations. (b) Bin averaged values of the turbulent fraction $\langle\gamma\rangle$ plotted against corresponding bins of Λ^+. Bin averaged values constructed for all z and $t/T^0_\tau > 1$. Horizontal dashed lines indicate $\Lambda^+ = 2.5, 260$. (c) Stationary profiles of $\overline{\gamma}$ plotted against the theoretical maximum value of Λ^+_M. Shading corresponds to $\pm$ one standard deviation. Horizontal dashed lines in (b,c) indicate $\Lambda^+ = 2.5, 260$.

One of the key aims of this study is the prediction of the derived intermittency profile through appropriate non-dimensional parameters. As outlined in §5.1, the scaling of 'local' flow sufficiently far from the wall and prediction of intermittency has been extensively investigated in literature through the Monin-Obhukov framework for a variety of flow configurations (Flores & Riley, 2011; García-Villalba & del Álamo, 2011; Van de Wiel *et al.*, 2012; Chung & Matheou, 2012; Deusebio *et al.*, 2015; Williamson *et al.*, 2015; Zhou *et al.*, 2017*a*).

Flores & Riley (2011) demonstrate that the collapse of turbulence of open channel flow subject to bottom cooling was well predicted by a critical value of the parameter $L^+ \approx 100$. Here $L^+ = Lu_\tau/\delta$ being the ratio of the Monin-Obhukov (M-O) length L to the viscous wall unit ν/u_τ. In their study of stratified plane Couette flow Deusebio *et al.* (2015) showed that similarly the introduction of intermittency due to to near-wall intermittency was well predicted through $L^+ \approx 200$. Zhou *et al.* (2017*a*) further demonstrated that due to the constant turbulent flux profile of Couette flow, M-O theory accurately described the mean flow sufficiently far from the wall. Expanding on past studies of the outer stable atmospheric boundary layer such as Nieuwstadt (1984) and Sorbjan (1986), Chung & Matheou (2012) demonstrate that Monin-Obhukov scaling is applicable to homogeneous stratified shear flow

sufficiently far from the wall through the construction of a 'local' Monin-Obhukov length Λ and non-dimensional parameter Λ^+ comprised out of the local momentum and buoyancy fluxes of the form

$$\Lambda = \frac{\langle -u'w' \rangle^{3/2}}{\kappa_c B}, \qquad \Lambda^+ = \frac{\langle -u'w' \rangle^2}{\kappa_c B \nu}, \tag{5.7a, b}$$

where $B = \langle -b'w' \rangle$ is the turbulent buoyancy flux. They similarly found the flow to become noteably intermittent with horizontal layers of quiescent fluid forming for $\Lambda^+ \lesssim 260$.

As demonstrated in Williamson *et al.* (2015) this flow configuration obtains an appreciable depth range for which the flow is sufficiently stratified and obtains a state of local energetic equilibrium and where each horizontal layer may be loosely considered a slice of quasi-homogeneous sheared turbulence where we expect 'local' M-O scaling to become valid (Chung & Matheou, 2012; Zhou *et al.*, 2017*a*). Williamson *et al.* (2015) further provide scaling arguments to demonstrate that within the region of local equilibrium, $Re_B \approx \kappa_c \Lambda^+$. Accordingly we expect the intermittency profile to show dependence on a depth varying value of $\Lambda^+(z)$.

Figure 5.3(b) shows the bin-averaged values of γ plotted against corresponding bins of Λ^+. The bin averaged data includes both the transitional and quasi-stationary data and is constructed for $t/T_\tau^0 > 1$ to exclude the initial adjustment period as described above. The results show clear collapse of the data as intermittency is introduced into the flow at $\Lambda^+ \approx 260$ in direct agreement with Chung & Matheou (2012), corresponding to $Re_B \approx 100$ under the assumption that $Re_B \approx \kappa_c \Lambda^+$. The data within the intermittent region remains collapsed across all simulations as the flow transitions to a fully quiescent or quasi-laminar state at $\Lambda^+ \approx 2.5$ corresponding to $Re_B \approx 1$ as argued for the transition to the 'diffusive' regime by Brethouwer *et al.* (2007).

It is further worth noting that the data here includes both the transitional period of the flow as well as the quasi-stationary state. Furthermore, our flow is highly inhomegeneous with distinctly varying flux profiles with respect to depth. As such the excellent collapse of the results presents a further strong argument for the applicability of M-O theory in the prediction of the onset of intermittency for a variety sheared flows.

In a practical sense, the accurate prediction or measurement of the depth varying turbulent fluxes $\langle -u'w' \rangle, B$ is very challenging outside of DNS. However, an advantage of our flow configuration is that for the quasi-stationary case, the vertical profiles of the momentum and buoyancy fluxes and hence $\Lambda^+(z)$ may be roughly estimated *a priori*. For the flow to obtain a quasi-equilibrium state, the forced heating profile $q(z)$ and driving pressure gradient F seek to attain balance with the total downward buoyancy $\mathcal{B}$ and momentum $\mathcal{M}$ fluxes which are comprised of their turbulent and laminar components such that

$$\mathcal{B} = B + \kappa N^2, \qquad \mathcal{M} = \langle -u'w' \rangle + \nu S. \tag{5.8a, b}$$

For the stationary state, the equilibrium profiles of $\mathcal{B}_E$ and momentum $\mathcal{M}_E$ may be obtained analytically (Williamson *et al.*, 2015):

$$\mathcal{B}_E(z) = \frac{g\beta I_S}{C_P \rho_0 \delta}\left(z(1 - e^{(z-\delta)\alpha})\right), \qquad \mathcal{M}_E(z) = \overline{u}_\tau^2\left(1 - \frac{z}{\delta}\right). \tag{5.9a, b}$$

By neglecting the molecular terms we can hence construct a theoretical maximum value for $\Lambda_M^+(z)$ from the analytical profiles of the form

$$\Lambda_M^+(z) = \frac{\mathcal{M}_E^2(z)}{\kappa_c \mathcal{B}_E(z)\nu}. \tag{5.10}$$

In this sense $\Lambda_M^+(z)$ represents an ideal state which the flow seeks to achieve such that the turbulent flux profiles develop to obtain equilibrium.

Figure 5.3(c) shows the quasi-stationary values of $\overline{\gamma}$ plotted against $\Lambda_M^+(z)$ for all simulations. The results show excellent agreement with identical bounding values of $\Lambda_M^+ \approx 2.5 - 260$ that define the intermittent region of the flow. We observe that the slope of γ in the intermittent region is slightly reduced to that of figure 5.3(b) due to our idealised assumption of neglecting the molecular terms in Λ_M^+. However the data remains well collapsed suggesting the variation between the turbulent and molecular components due to the suppression of turbulent fluxes in captured is the idealised measure of Λ_M^+. The exception to this is the least intermittent case R400L0.5 where the stationary flow never reaches a state of $\gamma = 0$. Accordingly as the flow approaches the surface where the confinement effects modify the turbulence properties (Calmet & Magnaudet, 2003; Flores *et al.*, 2017), the assumptions of local equilibrium

underpinning the construction of Λ become somewhat invalid and the data assymptotes to the final value of γ even as Λ_M^+ continues to decrease.

As Λ_M^+ may be constructed entirely from bulk flow proprieties and the geometry of the flow, our results suggest Λ_M^+ may lend itself as a useful forecasting tool for the onset of intermittency and subsequent reduction in 'local' mixing of stratified open channel flow.

We note further from the comparison of our results of cases R400L1 and R400L1LD that their is negligible difference in the intermittency profile and its dependence on Λ^+ with increased domain size. The results hence suggest that our results pertaining to 'local' intermittency and its effect on 'local' parameters is independent of the domain size of our DNS.

5.4 Vertical distribution of conditionally averaged flow properties

5.4.1 Mean gradients and energetic quantities

We briefly present the variation in key flow properties due to intermittency for our representative case R900L1. We similarly plot both the turbulent and quiescent data sets within the limits of $0.05 \leq \gamma \leq 1$ and $0 \leq \gamma \leq 0.95$ respectively to minimize the effect of noisy measurements in the presentation of our results. Dimensional flow properties are non-dimensionalized by the friction velocity u_τ and channel height δ

Figures 5.4(a,b) show the conditionally averaged stationary profiles of the buoyancy frequency $\langle \overline{N} \rangle|_I$ and mean shear $\langle \overline{S} \rangle|_I$ respectively, where $\langle S \rangle|_I = \langle \partial u(\mathbf{x})/\partial z \rangle|_I$. As discussed above, the flow attempts to balance the imposed heating profile and pressure gradient through $\mathcal{B}$ and $\mathcal{M}$ respectively. Accordingly we find that in regions of non-trivial intermittency, the turbulent mean stratification $\langle \overline{N} \rangle|_T$ and shear $\langle \overline{S} \rangle|_T$ are appreciably reduced relative to the full data-set as the turbulent fluxes are less suppressed within these regions. Analogously the mean profiles in the quiescent data set $\langle \overline{N} \rangle|_Q$ and shear $\langle \overline{S} \rangle|_Q$ are both larger than the full data-set as the flow tends to develop steeper gradients locally to account for the strong

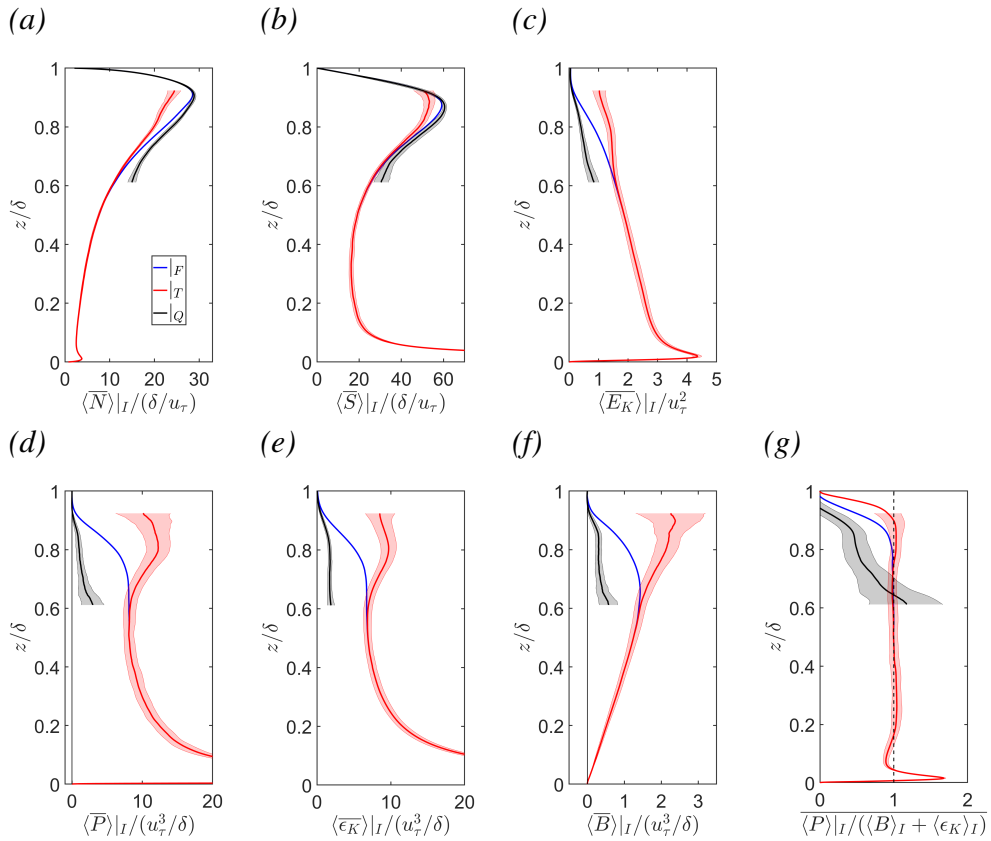

FIGURE 5.4: Stationary vertical profiles of key conditionally averaged flow properties for case R900L1. (a) Buoyancy frequency $\langle\overline{N}\rangle|_I$. (b) Mean shear rate $\langle\overline{S}\rangle|_I$. (c) Turbulent kinetic energy $\langle\overline{E}_K\rangle|_I$. (d) production of turbulent kinetic energy $\langle\overline{P}\rangle|_I$. Dissipation rate of turbulent kinetic energy $\langle\overline{\epsilon}_K\rangle|_I$. (f) The vertical buoyancy flux $\langle\overline{B}\rangle|_I$. (g) The local energetic equilibrium ratio $\overline{\langle P\rangle|_I/(\langle B\rangle|_I+\langle\epsilon_K\rangle|_I)}$. Turbulent and quiescent data sets are cutoff at $\gamma<0.05$ and $\gamma>0.95$ respectively. Shading corresponds to $\pm$ one standard deviation.

suppression of turbulence within these regions. As such our results support the concern raised in Caulfield (2020) about the validity of any assumptions made of mean gradients of buoyancy or shear, particularly from field measurements where the data-set may be limited or biased by time-dependant events.

Figure 5.4(c) shows the stationary vertical profiles of the conditionally averaged turbulent kinetic energy $\langle\overline{E_K}\rangle|_I$ where $E_K=1/2\langle u_i'u_i'\rangle$. From the results it is clear that in the region of intermittency, $\langle\overline{E_K}\rangle|_T$ does not decline towards zero with increasing distance from the wall as does the full data set, but rather plateaus to an approximately constant value within the

energetic shear mixing layer. Conversely, we observe low but non-zero TKE for the quiescent data-set as $\langle\overline{E_K}\rangle|_Q$ remains relatively small for its entire range. We conjecture that the energy remaining within the flow is kept at long wave lengths similar to the analysis presented for the diffusive regime of Brethouwer *et al.* (2007). Accordingly the results highlight the subtle difference between a 'quiescent' in the presence of nearby turbulence to that of steady laminar flow where the TKE is strictly zero.

Figure 5.4(d-f) shows the stationary conditionally averaged profiles of the dominant terms in the TKE budget, that being the production term $\langle\overline{P}\rangle|_I$, the dissipation rate of kinetic energy $\langle\overline{\epsilon}_K\rangle|_I$ and the buoyancy flux $\langle\overline{B}\rangle|_I$ where $P = \langle -u'w'\rangle S$. The results show qualitatively similar results within the intermittent region for all three quantities with the turbulent data-sets showing clear growth up to a secondary peak at $z/\delta \approx 0.8$, roughly corresponding to the location of maximum shear and where the overturning driven shear layer is observed in figure 5.2. As will be shown, this can be directly attributed to the idea of an 'energetic' mixing regime as argued by Mashayek *et al.* (2021) where the flows self organises to a critical state such that the mixing is most vigorous and becomes most efficient. Conversely, the three quantities within quiescent data set remain relatively negligible and trend towards a constant limit with increasing distance from the free surface.

Figure 5.4(g) shows the profiles of the ratio $\overline{\langle P\rangle|_I/(\langle B\rangle|_I + \langle\epsilon_K\rangle|_I)}$ which represents a measure of how close the flow is to a state of local energetic equilibrium. For horizontal layers where the ratio is unity we expect the local flow dynamics to be representative of an instance of homogeneous flow such that local scaling and parametrization becomes valid. We observe that the 'turbulent' flow exists in a state of local equilibrium for the majority of the channel depth and this region has a slightly greater vertical extent relative to the full data set as the quasi-laminar quiescent contributions are filtered out. Accordingly we define z_e as listed in table 2.1 as the upper vertical intercept for which the local equilibrium assumption holds true such that $\overline{\langle P\rangle|_T/(\langle B\rangle|_T + \langle\epsilon_K\rangle|_T)} \approx 1$ and where we expect negligible influence over local flow dynamics from the confinement effects of the upper boundary which remains poorly understood (Flores *et al.*, 2017). For the other simulations not presented here we note similar regions develop where the local equilibrium assumption is valid, albeit with

different individual values of z_e due the varying thickness of the upper fully quiescent regions as the quasi-laminar flow is unable to produce enough TKE to maintain local equilibrium. In agreement with this, we observe that in the quiescent regions where the turbulent fluxes are almost fully suppressed, the local equilibrium assumption becomes strictly invalid for all z.

5.4.2 Gradient Richardson number and 'marginal instability'

Through separation of the turbulent and quiescent data sets we can define a conditionally averaged gradient Richardson number of the form

$$\langle Ri_g \rangle|_I = \frac{\langle N^2 \rangle|_I}{\langle S^2 \rangle|_I} \tag{5.11}$$

Figures 5.5(a,b) show the quasi-stationary and conditionally averaged vertical profiles of the gradient Richardson number for the 'turbulent' $\langle \overline{Ri}_g \rangle|_T$ and 'quiescent' data sets $\langle \overline{Ri}_g \rangle|_Q$ for all simulations. For reference we include the full data-set (dashed line of same colour) on both plots.

From the results we observe that even though the mean stratification and shear vary appreciably over the intermittent region as seen in figures 5.4(a,b), Ri_g shows relatively small variation from its full data-set values as the mean profiles of N, S evolve proportionally in the turbulent and quiescent regions. Similar to past results of open channel and Poiseille flow (Armenio & Sarkar, 2002; García-Villalba & del Álamo, 2011; Williamson *et al.*, 2015), we observe the core of the channel which directly corresponds to the region of intermittency equilibrates to a constant critical value of approximately $Ri_{g,c} \approx 0.2$. Towards the free surface where $\mathcal{B}$ and $\mathcal{M}$ are comprised almost entirely through the molecular terms, Ri_g grows rapidly large as the upper boundary condition dictates the mean gradient profiles of S and N through (5.9).

A key finding from these results is that although the profiles of $\langle \overline{Ri}_g \rangle|_T$ and $\langle \overline{Ri}_g \rangle|_Q$ are qualitatively similar in the region of intermittency, the turbulent data set is marginally smaller than the visually estimated asymptotic value of $Ri_{g,c} \approx 0.2$, whilst the quiescent data set is marginally larger. To show this more clearly, figure 5.5(c) shows the ratio of $\langle \overline{Ri}_g \rangle|_T / \langle \overline{Ri}_g \rangle|_Q$ plotted against z within the region of intermittency of $0.05 \leq \gamma \leq 0.95$. The results

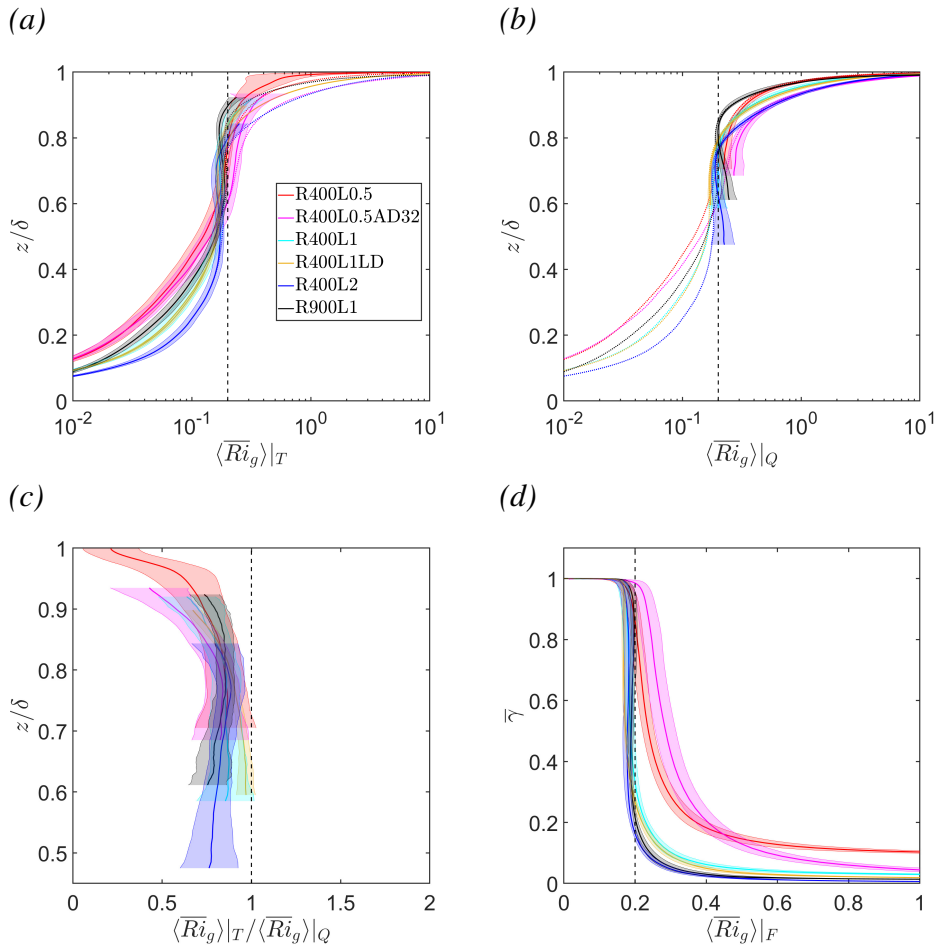

FIGURE 5.5: Stationary vertical profiles of: (a) the 'turbulent' conditionally averaged gradient Richardson number $\langle \overline{Ri}_g \rangle|_T$ (b) the 'quiescent' conditionally averaged gradient Richardson number $\langle \overline{Ri}_g \rangle|_Q$. Vertical dashed line in (a,b) indicates $Ri_g = 0.2$. Dotted lines of same colour depict full data sets in both figures. Turbulent and quiescent data sets are cutoff at $\gamma < 0.05$ and $\gamma > 0.95$ respectively. (c) Ratio of the turbulent to quiescent gradient Richardson numbers $\langle \overline{Ri}_g \rangle|_T / \overline{Ri}_g \rangle|_Q$ plotted against z within the vertical range corresponding to $0.05 \leq \gamma \leq 0.95$. (d) The 'full' unconditionally averaged gradient Richardon number $\langle \overline{Ri}_g \rangle|_F$ plotted against the corresponding turbulent fraction $\overline{\gamma}$. Shading corresponds to $\pm$ one standard deviation. Note the vertical scale in (c) is different to (a,b,d)

clearly show that sufficiently far from the upper boundary the ratio approaches a constant of approximately 0.8 for all simulations, regardless of the external parameter set. The results hence provide strong evidence for the 'marginal instability' hypothesis of Thorpe & Liu (2009). As outlined in §5.1, the underlying theory being that the mean shear and stratification

self-modulate in a cycle between states of marginal stability and instability. Under the assumption that $Ri_{g,c} \approx 0.2$ represents some critical measure of stability for our particular flow, our results suggest that the turbulent flow exists in an energetic and marginally unstable state prone to the formation of local instabilities. Meanwhile the quiescent flow remains suppressed, yet exists in a state where a marginal acceleration of the flow and increase in mean shear reverts the flow back to an unstable state defined by $Ri_g < Ri_{g,c}$. Considering the distinct inhomogeneity of the S, N vertical profiles for our flow, our results present very strong evidence for this self-modulating behaviour.

A further and crucial observation is that this critical state defined by $Ri_g = Ri_{g,c}$ only occurs within regions of intermittency. To make this clear we plot the stationary values of $\langle \overline{Ri}_g \rangle|_F$ against corresponding turbulent fraction $\overline{\gamma}$ for a given depth in figure 5.5(d). The results clearly show that the transition to $Ri_g \approx 0.2$ occurs for all simulations at precisely the location where intermittency is introduced into the flow such that γ becomes less than unity. The results hence suggest that for our flow, criticality and intermittency are fundamentally linked as a critical Ri_g represents a saturated state past which the stationary flow cannot sustain turbulence. The results hence present strong arguments for the theory of Thorpe & Liu (2009) suggesting that past observations of a stationary and critical gradient Richardson number are indeed linked to the stability of the local flow.

5.4.3 Turbulent Froude number and the mixing efficiency

As outlined in §5.1 one of the core aims of this study is to identify the effect of intermittency on the scaling arguments of Maffioli *et al.* (2016) and Garanaik & Venayagamoorthy (2019) that suggest the flux coefficient Γ trends towards a constant asymptotic value in the limit of $Fr \ll \mathcal{O}(1)$. Initially we consider the conditionally averaged vertical profiles of Fr and Γ. We hence explicitly define the conditionally averaged measures of $\langle Fr \rangle|_I$ and $\langle \Gamma \rangle|_I$ of the form

$$\langle Fr \rangle|_I = \frac{\langle \epsilon_K \rangle|_I}{\langle N \rangle|_I \langle E_K \rangle|_I}, \qquad \langle \Gamma \rangle|_I = \frac{\langle B \rangle|_I}{\langle \epsilon_K \rangle|_I}, \tag{5.12a, b}$$

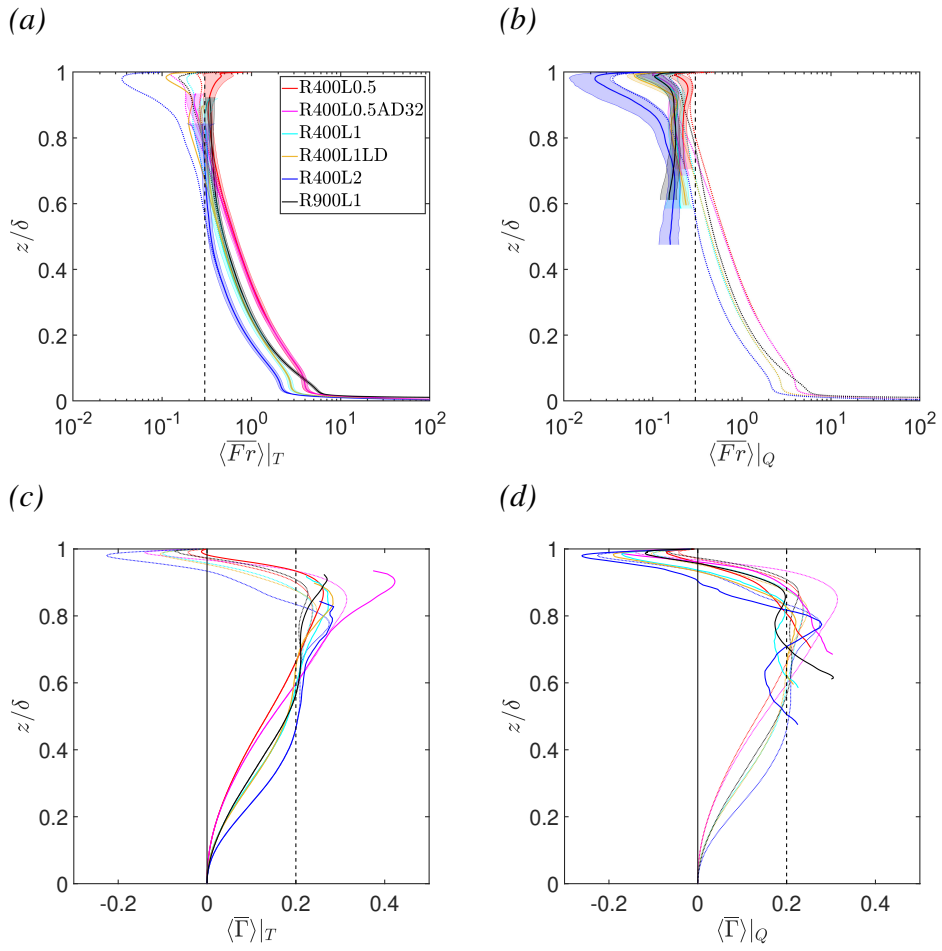

FIGURE 5.6: Stationary vertical profiles of 'turbulent' and 'quiescent' conditionally averaged: (a,b) Turbulent Froude number $\langle \overline{Fr} \rangle|_I$. Vertical dashed line corresponds to $Fr = 0.3$. (c,d) Flux coefficient Γ. Vertical dashed line corresponds to $\Gamma = 0.2$ (d-f) Same as for (a-c) but the 'quiescent data sets'. Turbulent and quiescent data sets are cutoff at $\gamma < 0.05$ and $\gamma > 0.95$ respectively. Shading where presented corresponds to $\pm$ one standard deviation. Shading not included in (c,d) due to excessive noise.

Figures 5.6(a,b) show the stationary vertical profiles of Fr within the turbulent and quiescent data sets respectively. For reference, the vertical profiles of the full data set of each simulation are plotted as the dashed lines of the same colour on all figures.

We observe the distinct trend that irrespective of the external parameter set and the subsequent range of Fr for the full data-set, the Froude number for the 'turbulent' data set appears to assymptote towards a lower critical limit of $Fr_c \approx 0.3$. The critical value being in direct agreement of the value for the maximum mixing efficiency within the homogeneous

simulations of Maffioli *et al.* (2016) and the value at which in §4 we observe the transition to the 'saturated' constant Γ regime. Accordingly, this result adds further evidence to the hypothesis of self-organized criticality of stratified shear flow, as the turbulent flow naturally converges towards an optimal or critical state that facilitates conditions for relatively 'efficient' overturning induced mixing (Thorpe & Liu, 2009; Mashayek *et al.*, 2017, 2021).

We note that similar to the results regarding Ri_g in figure 5.5, the flow obtains $Fr \approx Fr_c$ at the location in the flow where intermittency becomes appreciable. Furthermore, as observed in figure 5.3, the intermittency profile displays a clear dependence on Λ^+ and hence Re_B in direct agreement with the theory off PKTSC16. Accordingly our results which suggest criticality and intermittency are fundamentally linked for our flow, present compelling evidence for the arguments of Caulfield (2021) that active vigorous turbulence in stratified sheared flow may not be able to access the LAST regime and should not be considered 'strongly stratified' as the underlying requirements of $Re_B \gg \mathcal{O}(1)$ and $Fr \ll \mathcal{O}(1)$ are inherently unsatisfied.

Conversely, the quiescent vertical profiles of Fr essentially follow that of the full data set as the turbulent properties (ϵ_K, E_K) go towards zero and the parameters become predominantly defined by the shape of the vertical profile of the background stratification N. We observe that similarly to the lower limit for the turbulent data set, Fr appears to have an analogous asymptotic upper limits within the quiescent regime of $Fr \approx 0.3$. This is conceptually consistent with the underlying theme of criticality in stratified shear flow and our analysis in §4 that shows a functional relationship between Fr and Ri_g. Accordingly finite bounds must exist on Fr within the turbulent and quiescent regions such that the respective measurements of Ri_g remain in a marginally unstable or stable state.

Figures 5.6(c,d) show the stationary vertical profiles of Γ within the turbulent and quiescent data sets respectively. Again, the vertical profiles of the full data set of each simulation are plotted as the dashed lines of the same colour on all figures.

From the results we observe that the variation in Γ between the conditionally averaged and full data-sets is relatively subtle as the qualitative behaviour remains essentially the same. However within the region of intermittency it is clear that the 'turbulent' mixing efficiency

is slightly larger than the full data. In particular this variation is most pronounced at the secondary energetic peak corresponding to the shear mixing layer separating the turbulent and quiescent regimes. This again directly corresponds to a critical state and the 'optimal' energetic mixing regime described above.

Conversely, the results show that for the majority of the intermittent region, measurements of Γ in the quiescent regime are relatively smaller than the full data set as the quasi-laminar flow is not able to mix the flow as efficiently. We note however, with increasing distance from the free surface or analogously as the turbulent fraction $\gamma \to 1$, Γ within the quiescent flow grows larger and exceeds the full data set. As observed in Smith *et al.* (2021) in quiescent regions described by low Re_B, even as ϵ_K goes towards zero the diapycnal flux may not fully suppressed resulting in high readings of Γ. Furthermore we note that this occurs at the lower fringes of the intermittent region where the quiescent data set is relatively sparse and measurements of B become very noisy resulting in large fluctuations of Γ. It is also worth noting that the corresponding 'quiescent' Froude number for these higher values is appreciably smaller than that of the full or turbulent data sets for the same vertical location.

5.4.4 Turbulent/Quiescent interface coordinate system

A key observation from the flow visualizations in figure 5.2 and the vertical profiles of turbulent fraction γ in figure 5.3 is that the intermittency of the flow is largely defined by an upper quasi-laminar quiescent layer separated from the lower turbulent channel by a deformed horizontal interface. The exception to this being occasional detached turbulent overturning structures within the quiescent layer and localised pockets of quiescent fluid within the turbulent flow. We can hence consider the vertical distribution of flow properties and non-dimensional parameters from the reference coordinate system of the interface location analogous to past studies of turbulent/non-turbulent interface flows (Watanabe *et al.*, 2016).

Within the horizontal $(x - y)$ plane we hence define the vertical reference coordinate of the turbulent/quiescent interface $z_i(x, y) = 0$ as the upper most location that vertically separates an upper 'quiescent' and lower 'turbulent' location according to the algorithm defined in

§5.3. To ensure that we do not define the interface along a separated overturning structure we place an additional constraint such that along a one dimensional search vector of length $L/\delta = 0.2$ in the $-z$ direction originating at $z_i(x, y) = 0$, more than half of the flow must be 'turbulent'. The choice of $L/\delta = 0.2$ being the visually estimated vertical size of the largest turbulent structures within the central region of intermittency. Dimensional flow quantities (i.e. N, S, E_K, ϵ_K at a given x, y, z, t are hence calculated cell-wise relative to their reference interface location $z_i(x, y, t) = 0$ and subsequently bin-averaged into vertical bins of size $\Delta z_i^+ = 4, 2.5$ for the $Re_\tau = 400, 900$ cases respectively which correspond to the coarsest vertical grid size. Non dimensional parameters for a given z_i are constructed out of the bin-averaged dimensional quantities.

Figures 5.7(a-c) shows the stationary vertical profiles of the dominant energetic terms $\overline{P}, \overline{B}, \overline{\epsilon_K}$, normalized by their mean interfacial values $\overline{P}(z_i = 0), \overline{B}(z_i = 0), \overline{\epsilon_K}(z_i = 0)$ in the z_i reference coordinate system for all simulations. As the turbulent/quiescent interface is markedly defined by distinct overturning structures, we hypothesize that the size of the interfacial layer will scale with the size of the overturns. Accordingly, we normalize z_i by $\overline{L_E}(z_i = 0)$ calculated at the interface, where L_E is well known Ellison length describing the characteristic size of the overturns in a stratified fluid (Ellison, 1957; Shih *et al.*, 2005; Mater *et al.*, 2013), defined as:

$$L_E = \frac{b'_{\text{rms}}}{N^2}. \tag{5.13}$$

The results show clear behaviour of two distinctly different flow regimes separated by an interfacial layer where the properties rapidly change, showing qualitatively similar behaviour to the results of Watanabe *et al.* (2016). Above the interface, the energetic terms go to zero as the flow approaches quasi-laminar conditions. Below the interface the flow is actively turbulent, in particular the mixing being most energetic just below the interfacial layer as seen from the peak in B. Crucially, the interfacial layer does appear to characterized by the Ellison length, with thickness of approximately $4L_E/\delta$.

We note that on the 'turbulent-side' of the interface the energetic quantities follow individual trajectories with each simulations. This is unsurprising as the location of the vertical region of intermittency varies with each simulation, which combined with the vertically inhomogeneous

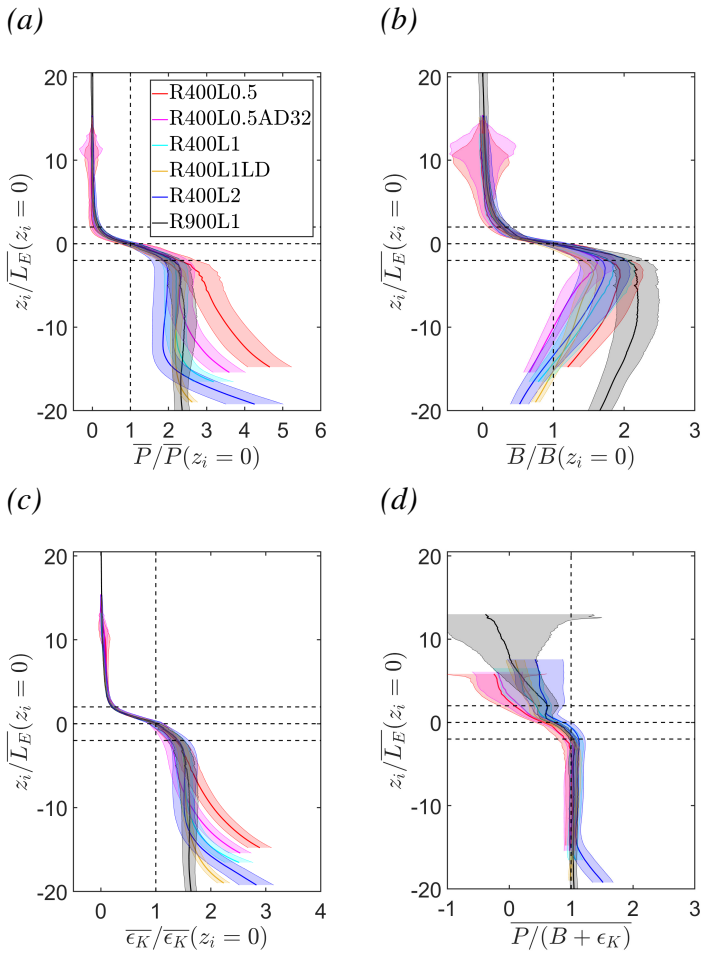

FIGURE 5.7: Stationary vertical profiles in the z_i turbulent/quiescent interface system of: (a) Turbulent kinetic energy production $\overline{P}$, (b) Buoyancy flux $\overline{B}$. (c) Turbulent kinetic energy dissipation rate $\overline{\epsilon_K}$. (d) Local equilibrium ratio $\overline{P/(B+\epsilon_K)}$. Dimensional quantities in (a-c) normalized by their respective mid-interface values at $z_i = 0$. For all figures: vertical interface location z_i normalized by the Ellison length calculated at the centre of the interface. Vertical dashed lines indicate a value of unity. Horizontal dashed lines indicate values of $z_i/\overline{L_E} = -2, 0, 2$. Shading where presented corresponds to $\pm$ one standard deviation.

nature of the depth dependant mean shear and stratification profiles causes variation in the energetic quantities with respect to the turbulent/quiescent interface.

Figure 5.7(d) shows the stationary vertical profiles of the local equilibrium ratio $\overline{P/(B+\epsilon_K)}$ in the z_i coordinate system. Note that the data in the positive z_i direction has been abbreviated to minimize excessively noise measurements of the local equilibrium ratio as all terms become

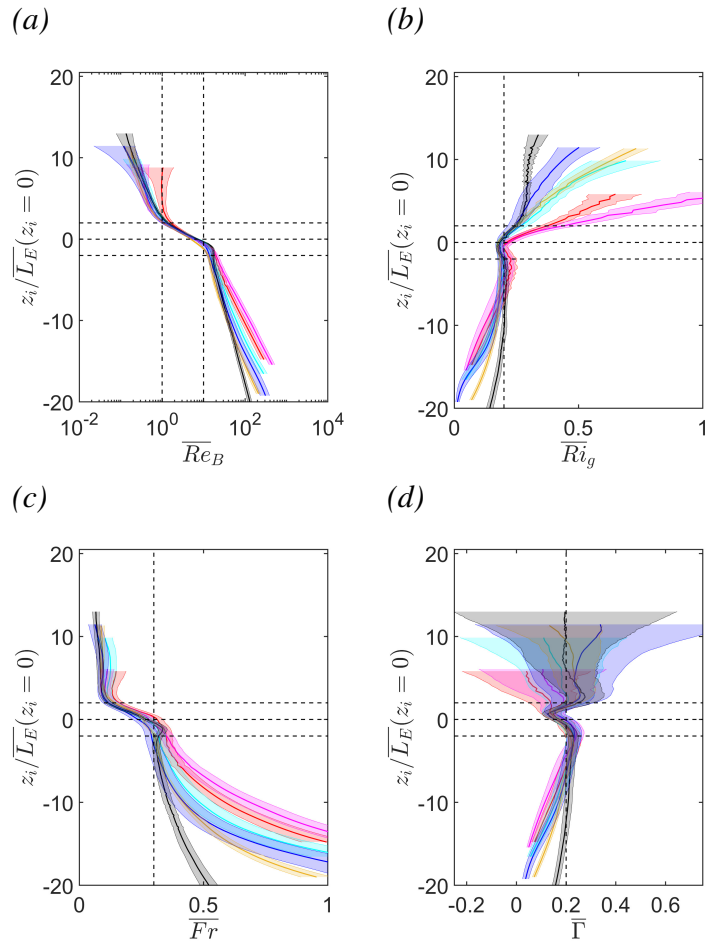

FIGURE 5.8: Stationary vertical profiles in the z_i turbulent/quiescent interface system of: (a) Buoyancy Reynolds number $\overline{Re_B}$, vertical dashed lines indicate $Re_B = 1, 10$. (b) Gradient Richardson number $\overline{Ri_g}$, vertical dashed line indicate $Ri_g = 0.2$ (c) Turbulent Froude number $\overline{Fr}$, vertical dashed line indicate $Fr = 0.3$. (d) Flux coefficient $\overline{\Gamma}$, vertical dashed line indicate $\Gamma = 0.2$. For all figures: vertical interface location z_i normalized by the Ellison length calculated at the centre of the interface. Horizontal dashed lines indicate values of $z_i/\overline{L_E} = -2, 0, 2$. Shading where presented corresponds to $\pm$ one standard deviation and has been abbreviated to minimize excessive noise in the quiescent region. Legend same as figure 5.7.

small and minor fluctuations in any quantity cause large variations in the local equilibrium ratio. A state of local energetic equilibrium is only evident for the actively turbulent flow as the suppressed momentum flux in the quiescent layer is unable to extract sufficient turbulent kinetic energy from the mean shear to maintain local equilibrium in agreement with our analysis in §5.4.

We again normalize z_i by $\overline{L_E}(z_i = 0)$ to demonstrate self-similar behaviour of the interfacial layer. Figure 5.8(a) shows the stationary profiles of the buoyancy Reynolds number $\overline{Re_B}(z_i)$. The results are well collapsed for all simulations. At the quiescent-side boundary of the interfacial layer, the flow obtains $Re_B \approx \mathcal{O}(1)$ confirming the observation of a quasi-laminar or diffusive state. Conversely at turbulent-side boundary of the interfacial layer, the flow obtains $Re_B \approx \mathcal{O}(10)$. The results are consistent with the assumptions of PKTSC16 and past work on stratified flows discussed in §5.3 regarding the lower 'local' limit of $Re_B \approx 10$ for actively turbulent flow.

Figure 5.8(b) shows the stationary profiles of the gradient Richardson number $\overline{Ri_g}(z_i)$. The results clearly show support for our argument that the criticality of the flow is inherently linked to the intermittency as the flow deviates from its critical state of $Ri_g \approx 0.2$ at precisely the interface location $z_i = 0$ for all simulations. Above the interface Ri_g rapidly grows as the flow approaches stable and quasi-laminar conditions. Further evidence to support this idea is seen in figure 5.8(c), which analogously shows that through the stationary profiles of the turbulent Froude number $\overline{Fr}(z_i)$ that the flow similarly departs from its critical state of $Fr \approx 0.3$ within the interfacial layer again suggesting that actively turbulent shear flow is unable to access $Fr \ll \mathcal{O}(1)$ locally.

Figure 5.8(d) shows the stationary profiles of the flux coefficient $\overline{\Gamma}(z_i)$. We interestingly observe non-monotonic behaviour of Γ with z_i. We note that the mixing is most efficient with a clear peak of $\Gamma \approx 0.25$ at the lower turbulent-side boundary of the interfacial layer at $z_i/L_E = -2$ rather than at $z_i = 0$, corresponding to the peak in B observed in figure 5.7(b) and where Ri_g and Fr obtain their critical values. Past this point, as $Re_B < \mathcal{O}(10)$ and the flow begins to enter a diffusive regime which is not able to mix the buoyancy field as efficiently, Γ drops slightly and approaches a constant value (albeit with a significant amount of scatter) within the quiescent regime. This suggests the asymptotic nature of a 'saturated' Γ at low Fr is linked to the quiescent flow. We will explore this concept in more detail in §5.5.

We again observe that on the 'turbulent-side' of the interface the profiles the mixing diagnostics do not universally collapse when normalized by the interfacial value of L_E. In particular, this is accentuated in our R900L1 results. This can be explained if we consider that for all cases

the transition to the intermittent interfacial region occurs at $Re_B \approx 10$, consistent with the underlying theory and our analysis so far. Furthermore, we recall that Re_B can be defined as a ratio of length scales such that

$$Re_B = \left(\frac{L_O}{L_K}\right)^{4/3}, \tag{5.14}$$

where $L_O = (\epsilon_K/N^3)^{1/2}$ is the Ozmidov length roughly defining the upper limit of the inertial subrange in stratified flow and $L_K = (\nu^3/\epsilon_K)^{1/4}$ is the Kolmogorov micro scale. Re_B hence represents an estimate of the isotropic inertial subrange of the flow. Hence if we assume L_K decreases with increasing Re_τ, then to maintain $Re_B \approx 10$ we expect L_O to similarly decrease. Furthermore as argued by Mashayek *et al.* (2021) and as will be shown directly in §5.5, we expect this region of 'optimal' or critical mixing to be defined by $L_E \approx L_O$ such that the injection of energy into the flow through overturns is precisely at the wavelength corresponding to the upper limit of the inertial subrange. Hence the interfacial value of L_E accordingly shrinks with increasing Re_τ. The vertical profiles of the $Re_\tau = 900$ appear more 'stretched' than the $Re_\tau = 400$ cases. However the significant takeaway from the results is that regardless of Reynolds number, the behaviour of the energetic quantities and mixing diagnostics within the interfacial layer as seen in figures 5.7,5.8 remains self-similar when scaled with the interfacial mean value of L_E.

5.5 Effect of intermittency on a Fr based parametrization of Γ

5.5.1 Horizontal averages

We now consider how the spatially varying distributions of the conditionally and horizontally averaged values of Fr and Γ correlate and to what effect the parametrization of the mixing efficiency is effected by highly intermittent flow. We note that a caveat to the use of our conditionally averaged data sets in this section is that the 'turbulent' and 'quiescent' patches within the horizontal layers for which statistics are calculated, must be larger than all the

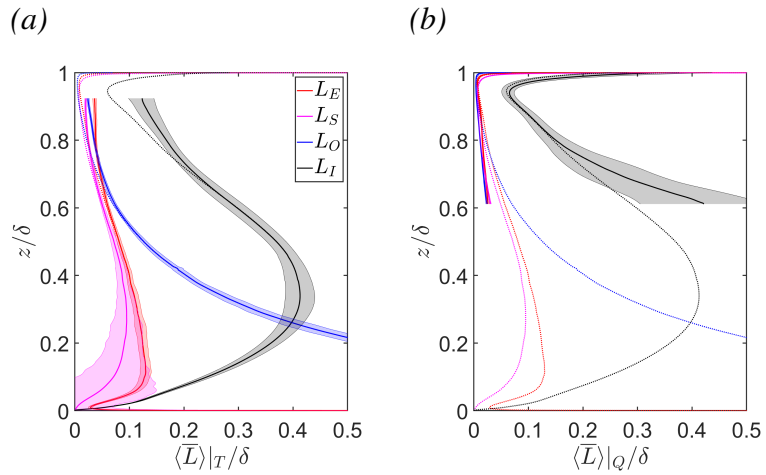

FIGURE 5.9: Stationary vertical profiles of the Ellison length $\overline{L_E}$, shear mixing length $\overline{L_S}$, Ozmidov length $\overline{L_O}$, turbulent inertial length $\overline{L_I}$ normalized by the channel height δ. (a) 'Turbulent' data set. (b) 'Quiescent' data set. Turbulent and quiescent data sets are cutoff at $\gamma < 0.05$ and $\gamma > 0.95$ respectively. Shading where presented corresponds to $\pm$ one standard deviation. Data presented for case R900L1 in both figures.

physically relevant scales such that the two regions may be seen as self-contained. If this condition is met, we conceptually expect the two flow regimes to be independent of one another and local measures of Fr to correlate with local measures of Γ.

To demonstrate that this is strictly true for our flow, we consider that the largest length scales most physically relevant to the mixing dynamics of our flow are: the Ellison length L_E defining the size of the overturns, the mean shear mixing length L_S, the Ozmidov length L_O defining the upper limit of the inertial subrange and the inertial turbulent length L_I roughly characterizing the integral scale of the flow. We hence explicitly define the above conditionally averaged lengths:

$$\langle L_E\rangle|_I = \frac{\langle b'_{\text{rms}}\rangle|_I}{\langle N^2\rangle|_I}, \qquad \langle L_S\rangle|_I = \frac{\langle E_K^{1/2}\rangle|_I}{\langle S\rangle|_I}, \tag{5.15a, b}$$

and

$$\langle L_O\rangle|_I = \left(\frac{\langle \epsilon_K\rangle|_I}{\langle N^3\rangle|_I\langle E_K\rangle|_I}\right)^{1/2}, \qquad \langle L_I\rangle|_I = \frac{\langle E_K^{3/2}\rangle|_I}{\langle \epsilon_K\rangle|_I}, \tag{5.15a, b}$$

Figures 5.9(a,b) respectively show the stationary vertical profiles of the turbulent and quiescent length scales L_E, L_S, L_O, L_I normalized by the domain height δ for case R900L1. From the

results it is clear that for both data sets, within the region of intermittency all the normalized lengths are of size $L/\delta \approx \mathcal{O}(10^{-1})$. In particular we note that within the 'turbulent' data sets L_E, L_S and L_O appear to be of similar scale and approach an asymptotic limit in agreement with the concept of criticality as argued by Mashayek *et al.* (2021) where all three length scales equate. Conversely, from our visualizations in figure 5.2 it is clear that with the exception of small isolated overturning events, contiguous turbulent or quiescent patches are of size $L/\delta \approx \mathcal{O}(1)$. Furthermore, as the turbulent and quiescent flow regions may be loosely considered two large dynamically distinct regions separated by a deformed horizontal interface, the results confirm our underlying assumption that the local dynamics describing both regions are self-contained.

We have used a singular case R900L1 to show this result for brevity. Although the size of the four aforementioned length scales vary slightly with each simulation, they all remain of size $L/\delta \approx \mathcal{O}(10^{-1})$ validating our assumption of self-contained flow within the quiescent and turbulent patches.

Figure 5.10 shows the bin averaged values of instantaneous measurements of $\langle \Gamma(z,t) \rangle|_I$, plotted against their corresponding bins of $\langle Fr \rangle|_I$ for each individual simulation. To show the spread of the instantaneous data, we plot the two-dimensional probability density functions (2D p.d.f.s) of the same variables constructed from all simulations as a single 2D p.d.f. in the insert of the figures. To demonstrate the invariance of our results to time, we include data for both the temporally evolving and quasi-stationary state such that both the bin averaged values and p.d.f.s are constructed for data where $t/T^0_\tau > 1$. Furthermore, to ensure our results are not susceptible to the confinement effects from the top and bottom boundaries, we limit the vertical range from which we construct our figures between $0.2\delta < z < z_e$. Here $z = 0.2$ corresponds to the approximate lower bound in which Williamson *et al.* (2015) observe a transition of the flow to a state of local equilibrium such that $P \approx B + \epsilon_K$ for their $Re_\tau = 395$ simulations. Meanwhile z_e as defined in §5.4 varies with each simulation. Accordingly within this vertical range we expect the mixing dynamics of the flow to be free from boundary effects and to be characterized by local processes.

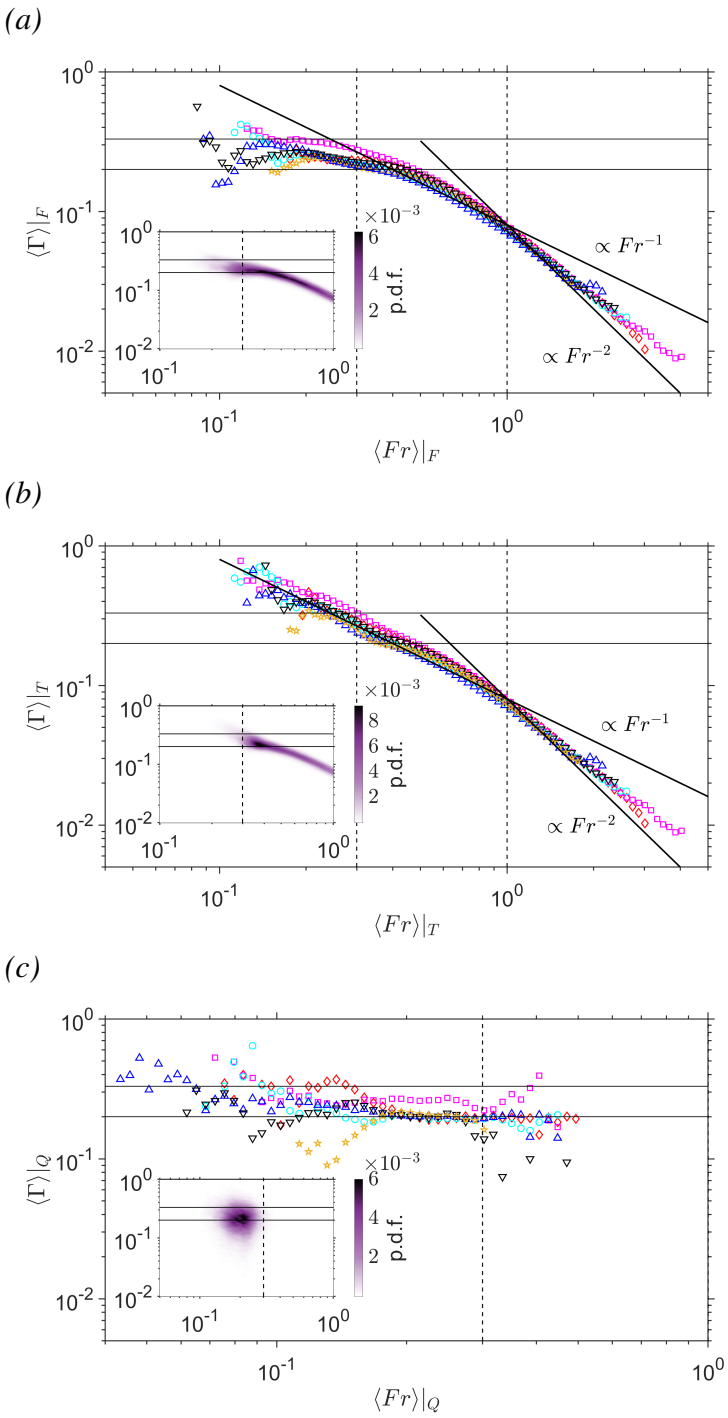

FIGURE 5.10: Bin averaged values and 2D p.d.f.s of the conditionally averaged flux coefficient $\langle\Gamma\rangle|_I$, plotted against corresponding bins of conditionally averaged $\langle Fr\rangle|_I$. Bin averaged values and 2D p.d.f. constructed with the temporal range of $t/T^0_\tau > 1$ and the vertical range of $0.2\delta < z < z_{le}$. (a) 'Full' data set. (b) 'Turbulent' data set. (c) 'Quiescent data set'. For (a,b) solid diagonal lines indicate $\Gamma \propto Fr^{-1}$ and $\Gamma \propto Fr^{-2}$. Dashed vertical lines indicate $Fr = 0.3, 1$. Horizontal thin lines in all figures indicate $\Gamma = 0.2, 0.33$. Legend same as figure 5.3(b)

For reference, figure 5.10(a) shows the the correlations between Γ with Fr for the 'full' data set. The results show the same qualitative behaviour as shown in figure 4.4, with a distinct collapse of the data along the lines of scaling as proposed by Maffioli *et al.* (2016) and Garanaik & Venayagamoorthy (2019). For $Fr \gtrsim 1$ the flow displays a $\Gamma \sim Fr^{-2}$ scaling consistent with the arguments of Maffioli *et al.* (2016) for 'weakly stratified' flow. For $0.3 \lesssim Fr \lesssim 1$ we observe the 'moderately stratified $\Gamma \sim Fr^{-1}$ scaling of Garanaik & Venayagamoorthy (2019). Importantly we observe that similarly to the results presented in §4, the full data set displays an asymptotic Γ regime for $Fr < 0.3$ which corresponds directly to the regions of the flow where we observe strong intermittency. Within this regime Γ approaches a constant value within the bounds of $\Gamma = 0.2$ as predicted by Osborn (1980) and $\Gamma = 0.33$ as predicted for the optimal mixing regime of Mashayek *et al.* (2021).

Figure 5.10(b) shows the correlations between Fr and Γ for the turbulent data set and the comparison to the full data set is striking. The results clearly show that within the turbulent data set there is no indication of a constant Γ regime. Rather for flow where $Fr \lesssim 1$, the mixing efficiency continues to display an inverse correlation with Fr, such that the $\Gamma \sim Fr^{-1}$ 'intermediate' scaling of GV19 clearly holds for an entire decade of Fr with a distinct collapse of the data for all simulations even for $Fr < Fr_c$. This is again seemingly in agreement with the arguments of Caulfield (2021) suggesting turbulent stratified shear flow is unable to access a strongly stratified buoyancy dominated regime. However as discussed in Mashayek *et al.* (2021), the emergence of an 'intermediate' $\Gamma \sim Fr^{-1}$ mixing regime under the assumption of Garanaik & Venayagamoorthy (2019) that buoyancy influences the evolution of B to leading order appears somewhat in contradiction of their primary assumption underlying the theory of self-organized criticality of stratified shear flow. Being that for the entire mixing life cycle of a shear driven overturning event, the flow is weakly stratified in the sense that the mixing of the buoyancy field defined through B is 'slaved' to that of momentum and hence the shear and inertial forces of the flow. We will return to this idea in more detail in §5.5.3.

It is important however to consider our distinct observation from figure 5.5(a) which shows that for the stationary case and when considering only the 'turbulent' flow, Fr approaches its clear critical limit of $Fr_c = 0.3$. For our results this directly corresponds to a measurement of

$\Gamma = 0.2 - 0.33$ conceptually consistent with the critical mixing regime of Mashayek *et al.* (2021) and with numerous studies for the saturated value of the mixing efficiency in the limit of strong stratification (Osborn, 1980; Ivey & Imberger, 1991; Shih *et al.*, 2005; Maffioli *et al.*, 2016; Portwood *et al.*, 2019; Howland *et al.*, 2020). This is reflected by the high concentration of data on the 2D p.d.f at the critical point in the flow.

In contrast, we note that the instances where $Fr < 0.3$ and we observe higher measurements of Γ are significantly less frequent and and can be interpreted as transient mixing events at strong levels of stratification. This interpretation of the results is conceptually consistent with the findings of numerous stratified free shear layer studies that show the mixing efficiency grows very large during an initial 'roll-up' of a KHI mixing event in a quiescent and hence more strongly stratified background fluid (Caulfield & Peltier, 2000; Peltier & Caulfield, 2003; Salehipour *et al.*, 2015; Mashayek *et al.*, 2017).

In stark contrast to the above results, figures 5.10(c) clearly show that within the quiescent flow, Γ does not show any functional relationship on Fr. Rather, the mixing efficiency appears to remain constant such that Γ ranges between $0.2 - 0.33$ for the full parameter range presented. We explain this by employing the scaling arguments of Garanaik & Venayagamoorthy (2019). Within this regime the flow is essentially quasi-laminar such that buoyancy has almost entirely suppressed turbulent motions and $Re_B \lesssim \mathcal{O}(1)$. Accordingly we expect, shear and inertial forces to be negligible and all dynamics of the flow to be characterized by processes occurring at the buoyancy time scale $T_N = 1/N$. This leads to their scaling argument of

$$B \sim \epsilon_K \sim \frac{w'^2}{T_N} \tag{5.16}$$

and subsequently

$$\Gamma = \frac{B}{\epsilon_K} \sim \frac{w'^2 T_N}{w'^2 T_N} = \text{const.} \tag{5.17}$$

We note within this quiescent data set there is a significant amount of spread in the results as B and ϵ_K approach zero and small fluctuations in either quantities cause large variations in Γ. However, the main observation from the results that Γ appears independent of Fr within the quiescent regions of the flow remains distinctly clear.

The results clearly show that at our parameter range and for our flow configuration, flow described by a global (unconditionally averaged) $Fr < Fr_c$ and hence low Re_B corresponds to highly intermittent flow with appreciable contributions from both the turbulent and quiescent data sets. Accordingly for our flow the transition observed in figures 5.10(a) at the critical point of $Fr_c = 0.3$ from the $\Gamma \sim Fr^{-1}$ regime to a 'saturated' constant Γ regime occurs due to the increasing contributions from the quiescent flow regions leading to a plateau in a 'global' measure of Γ. Hence assuming that $Fr \approx 0.3$ represents a critical lower bound for our sheared flow in the same sense that $Ri_{g,c} \approx 0.2$ represents an upper bound, the results suggest that the manifestation of a constant Γ regime within stratified shear flows in the limit of low Fr as argued by Maffioli *et al.* (2016) and Garanaik & Venayagamoorthy (2019) occurs directly due to the intermittency of the flow as the 'saturated' flow cannot exceed critical conditions. The results again provide clear evidence for the concept that the self organized criticality of stratified shear flow is linked with and arises directly due to the strong spatio-temporal intermittency of the flow. Although this concept has been previously discussed in past studies (Caulfield, 2020, 2021; Mashayek *et al.*, 2021), to our knowledge ours is the first study to directly demonstrate this with DNS data. Furthermore, considering the collapse of the results irrespective of the external parameter set, time or vertical location, we believe this behaviour will display a degree of universality for a variety of forced stratified shear flows.

Furthermore, it becomes clear that for rare transient mixing events where $Fr < Fr_c$, Γ can significantly vary for a single measured value of Fr depending on whether the composition of the flow is turbulent, quiescent or contains varied contributions from both flow regimes.

5.5.2 Interface based parametrization within the region of intermittency

We also investigate a Fr based parametrization of Γ within the turbulent/quiescent interface based coordinate system. Figure 5.11 shows the bin averaged values and the 2D p.d.f of $\langle\Gamma\rangle|(z_i,t)$ plotted against corresponding bins of $\langle Fr\rangle|(z_i,t)$ constructed out of instantaneous measurements of $\Gamma(z_i,t)$ and $Fr(z_i,t)$, which are constructed from the instantaneous z_i bin averaged dimensional quantities, i.e. $B(z_i,t), \epsilon_K(z_i,t), E_K(z_i,t), N(z_i,t)$.

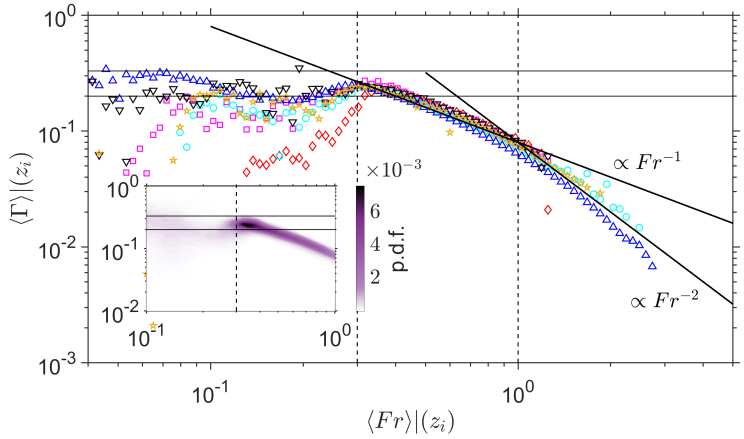

FIGURE 5.11: Bin averaged values and 2D p.d.f.s of the flux coefficient $\langle\Gamma\rangle|_I(z_i)$, plotted against corresponding bins of conditionally averaged $\langle Fr\rangle|_I(z_i)$ calculated within the z_i turbulent/quiescent interface based co-ordinate system. Bin averaged values and 2D p.d.f. constructed with the temporal range of $t/T_\tau^0 > 1$. Solid diagonal lines indicate $\Gamma \propto Fr^{-1}$ and $\Gamma \propto Fr^{-2}$. Dashed vertical lines indicate $Fr = 0.3, 1$. Horizontal thin lines in all figures indicate $\Gamma = 0.2, 0.33$. Legend same as figure 5.3(b)

However in contrast to our horizontally averaged results we observe non-monotonic behaviour of Γ in the left flank of the figure. Here the critical value of $Fr(z_i) \approx 0.3$ corresponds to a clear peak in the mixing efficiency consistent with the underlying theme of this study being the concept of optimal and most 'efficient' mixing under critical conditions defined by $Fr = 0.3$. Past this critical point, the mixing efficiency drops off slightly before plateauing to an 'Osborne' constant value at approximately $\Gamma \approx 0.2$, although this is somewhat unclear due to the significant scatter in the measurements of Γ within this regime.

The results here are consistent with the findings and arguments of Maffioli *et al.* (2016) who similarly find a peak in the mixing efficiency at $Fr = 0.3$ in their high resolution DNS study. We note that although the nature of the mixing in their body-forced homogeneous DNS is appreciably different to ours being driven by the mean shear, we find their results conceptually consistent with our hypothesis that intermittency in stratified flows is responsible for the asymptotic nature of Γ at low Fr. In their study, flow for which $Fr < 0.3$ and where they observe a constant Γ regime corresponds to flow where $Re_B \approx \mathcal{O}(10)$ and we expect strong intermittency. Conversely their $Fr = 0.3$ case where they observe a peak in mixing

efficiency corresponds to $Re_B \approx \mathcal{O}(10^3)$ and hence we expect intermittency to be negligible. Accordingly, the results presented in this section provide further strong evidence not only for the concept of self organized criticality manifesting due to the intermittency of the flow. But also for our hypothesis that within stratified flow the asymptotic behaviour of Γ for $Fr \lesssim 0.3$ comes directly as a result of the intermittency and contributions from quasi-laminar quiescent flow. How this result pertains to a wide variety of stratified flows and at significantly higher Reynolds presents clear direction for future high resolution DNS studies.

5.5.3 Underlying assumptions of the 'intermediate' mixing regime

In light of our results in figures 5.10, 5.11 and the discussion presented in Mashayek *et al.* (2021) (henceforth denoted as MCA21 in this chapter) regarding the potential discrepancies of the 'intermediate' $\Gamma \sim Fr^{-1}$ scaling of Garanaik & Venayagamoorthy (2019) (henceforth denoted as GV19 in this chapter) and their assumptions of stratified shear flow, we explore this regime and the scaling arguments of both studies. In particular our data-set for which the majority of the flow falls within $0.3 \lesssim Fr \lesssim 1$ 'intermediate' regime within a quasi-steady state allows us to explore this in more detail than previously reported in literature.

Central to the scaling arguments of MCA21 are two key assumptions. Firstly, that within the critical mixing regime, the flow approaches a critical state defined by $Ri_g \approx Ri_{g,c}$. Secondly, that buoyancy in stratified shear flows inherently never dominates the dynamics of the flow such that the mixing of the buoyancy field is 'slaved' to that of the momentum field resulting in $Pr_T = K_M/K_\rho \approx 1$ for all stages of the shear instability mixing cycle. Where K_M and K_ρ are the eddy viscosity and diffusivity defined as

$$K_M = \frac{\langle -u'w' \rangle}{S}, \qquad K_\rho = \frac{B}{N^2}. \tag{5.18a, b}$$

Figures 5.12(a,b) respectively show the 'turbulent' conditionally bin- averaged values and 2D p.d.f.s of $\langle Ri_g \rangle|_T$ and $\langle Pr_T \rangle|_T$ plotted against corresponding bins of $\langle Fr \rangle|_T$ for all simulations. The plots are constructed analogously to figure 5.10. The results distinctly

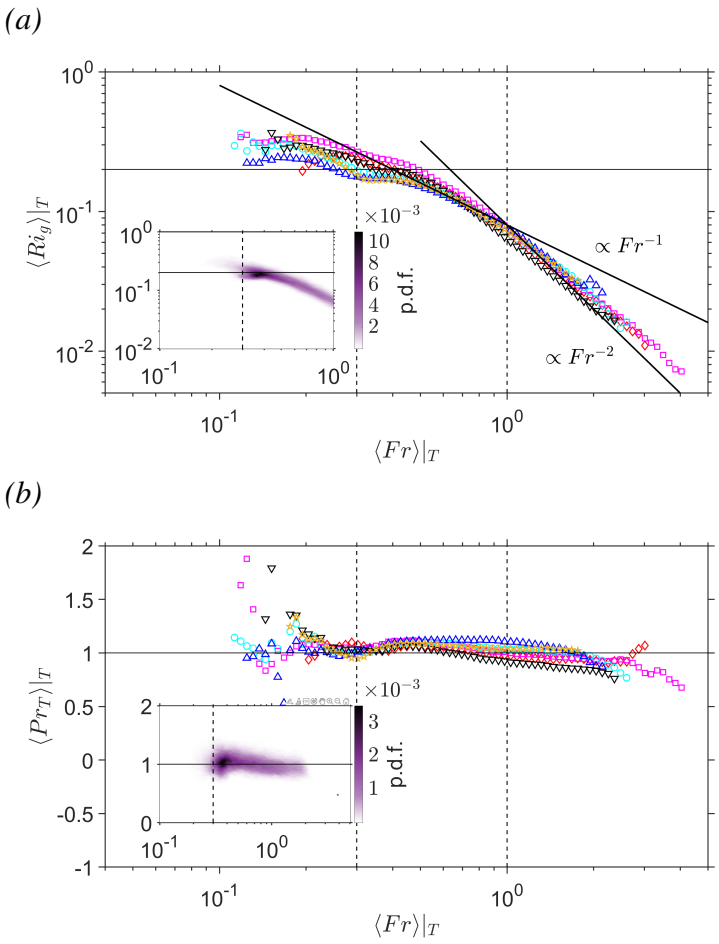

FIGURE 5.12: Bin averaged values and 2D p.d.f.s of the (a) the conditionally averaged gradient Richardson number within the turbulent data set $\langle Ri_g \rangle|_T$, thin horizontal line indicates $Ri_g = 0.2$. Diagonal lines indicate $Ri_g \propto Fr^{-1}$ and $Ri_g \propto Fr^{-2}$. (b) conditionally averaged turbulent Prandtl number within the turbulent data set $\langle Pr_T \rangle|_T$ plotted against corresponding bins of conditionally averaged $\langle Fr \rangle|_T$, thin horizontal line indicates $Pr_T = 1$. Bin averaged values and 2D p.d.f. constructed with the temporal range of $t/T^0_\tau > 1$ and the vertical range of $0.2\delta < z < z_{le}$. Vertical dashed lines indicate $Fr = 0.3, 1$. Legend same as figure 5.3(b).

present confirmation of the two assumptions of MCA21. In agreement with our past analysis, it is clear from the high concentration of data that the flow organizes towards a critical point of $Fr = Fr_c \approx 0.3$ and $Ri_g = Ri_{g,c} \approx 0.2$. For $Fr \geq 1$, we obtain the classic scaling of $Ri_g \sim Fr^{-2}$ for weakly stratified flow (Maffioli *et al.*, 2016; Zhou *et al.*, 2017*a*). And for the 'intermediate' regime of $0.3 \lesssim Fr \lesssim 1$ and, the flow displays the transitional scaling of $Ri_g \sim Fr^{-1}$ between the weakly stratified and critical states as derived in §4. For $Fr \lesssim 0.3$

we observe that Ri_g seems to remain constant and become independent of Fr in agreement with our scaling analysis in §4. Furthermore, from the results it is clear that for all Fr, we obtain $Pr_T \approx 1$ as argued in MCA21, albeit with significant scatter the the left tail of the figure for $Fr \lesssim 0.3$ where the data set becomes quite scarce.

As discussed in MCA21, the scaling arguments of GV19 for the intermediate regime of $B \sim E_K N$ (to be derived in more detail shortly) presents an apparent contradiction of the $Pr_T \approx 1$ assumption. If we employ this scaling and initially assume that $E_K \sim \langle -u'w' \rangle$, we can show that

$$Pr_T = \frac{K_M}{K_\rho} = \frac{\langle -u'w' \rangle N^2}{BS} \sim \frac{\langle -u'w' \rangle N^2}{E_K N S} \sim \frac{N}{S} = Ri_g^{1/2}. \tag{5.19}$$

And from the results presented in figure 5.12(a) this implies that Pr_T has an inverse and functional relationship with Fr for $Fr > 0.3$. However, the results in 5.12(b) demonstrate this to be untrue.

We hence consider the arguments of GV19. They argue that the evolution of the buoyancy perturbation b' evolves due to a turbulent vertical displacement of a fluid parcel from its background stratification such that

$$b' \sim w' N^2 T_*, \tag{5.20}$$

where T_* is the time-scale relative to the mixing dynamics of the local flow. Hence by multiplying both sides of (5.20) by w' we can obtain

$$b'w' \sim B \sim w'^2 N^2 T_* \sim E_K N^2 T_*. \tag{5.21}$$

Accordingly they argue that for the weakly stratified regime, inertial effects are dominant such that $T_* = T_L$, where $T_L = E_K/\epsilon_K$ is the turbulent time scale. And for the 'intermediate' regime GV19 propose that buoyancy dominates the evolution of B such that $T_* = T_N$. Accordingly they derive

$$\Gamma = \frac{B}{\epsilon_K} \sim \frac{E_K N^2 T_L}{\epsilon_K} = \frac{E_K^2 N^2}{\epsilon_K^2} = Fr^{-2} \tag{5.22}$$

for the weakly stratified regime and

$$\Gamma = \frac{B}{\epsilon_K} \sim \frac{E_K N^2 T_N}{\epsilon_K} = \frac{E_K N}{\epsilon_K} = Fr^{-1} \tag{5.23}$$

for the intermediate regime. However note that inherent within (5.20) lie two key assumptions. Firstly, that the separation of vertical and horizontal scales is negligible such that $w'^2 \sim E_K$. A similar assumption in (5.19) leads to $E_K \sim \langle -u'w' \rangle$. Secondly considering the statistical nature of B, that the multiplication of the root-mean-square (rms) values of b'_{rms} and w'_{rms} corresponds to the correlation between their local values such that $b'_{\text{rms}} w'_{\text{rms}} \sim B$. We can directly investigate the validity of these assumptions by defining the ratios

$$C_1 = \frac{w'^2_{\text{rms}}}{E_K}, \qquad C_2 = \frac{\langle -u'w' \rangle}{E_K}, \qquad C_3 = \frac{B}{b'_{\text{rms}} w'_{\text{rms}}}. \tag{5.24a, b, c}$$

To test this figure 5.13 shows the 'turbulent' conditionally bin-averaged values and 2D p.d.f.s of $\langle C_1 \rangle|_T$, $\langle C_2 \rangle|_T$ and $\langle C_3 \rangle|_T$ plotted against corresponding bins of $\langle Fr \rangle|_T$. For the weakly stratified case of $Fr \gtrsim 1$, the assumptions are clearly valid and all three ratios approach a constant asymptotic value as buoyancy effects are neglible and the flow remains in a state of relative isotropy. However for $Fr \lesssim 1$ the assumptions become distinctly invalid as all three ratios grow smaller with decreasing Fr such that we can empirically observe

$$C_1 \sim C_2 \sim C_3 \sim \begin{cases} \text{const}, & Fr \geq 1 \\ Fr^{1/2}, & Fr \leq 1. \end{cases} \tag{5.25}$$

Conceptually this is consistent with the stratified turbulence theory of Billant & Chomaz (2001) and Lindborg (2006) if we consider that Fr may be interpreted as a ratio of length scales such that

$$Fr = \left(\frac{L_O}{L_I} \right)^{2/3}, \tag{5.26}$$

Accordingly as $Fr < 1$, we obtain $L_O < L_I$ such that buoyancy begins to constrain the vertical component of the largest energetic scales leading to large scale anisotropy. Hence we observe that the vertical and horizontal velocity scales diverge as seen in the evolution of C_1 and C_2. Similarly as Fr grows smaller and b' becomes increasingly effected by motions due to the resulting internal waves of the stable flow field (Itsweire *et al.*, 1993), we similarly

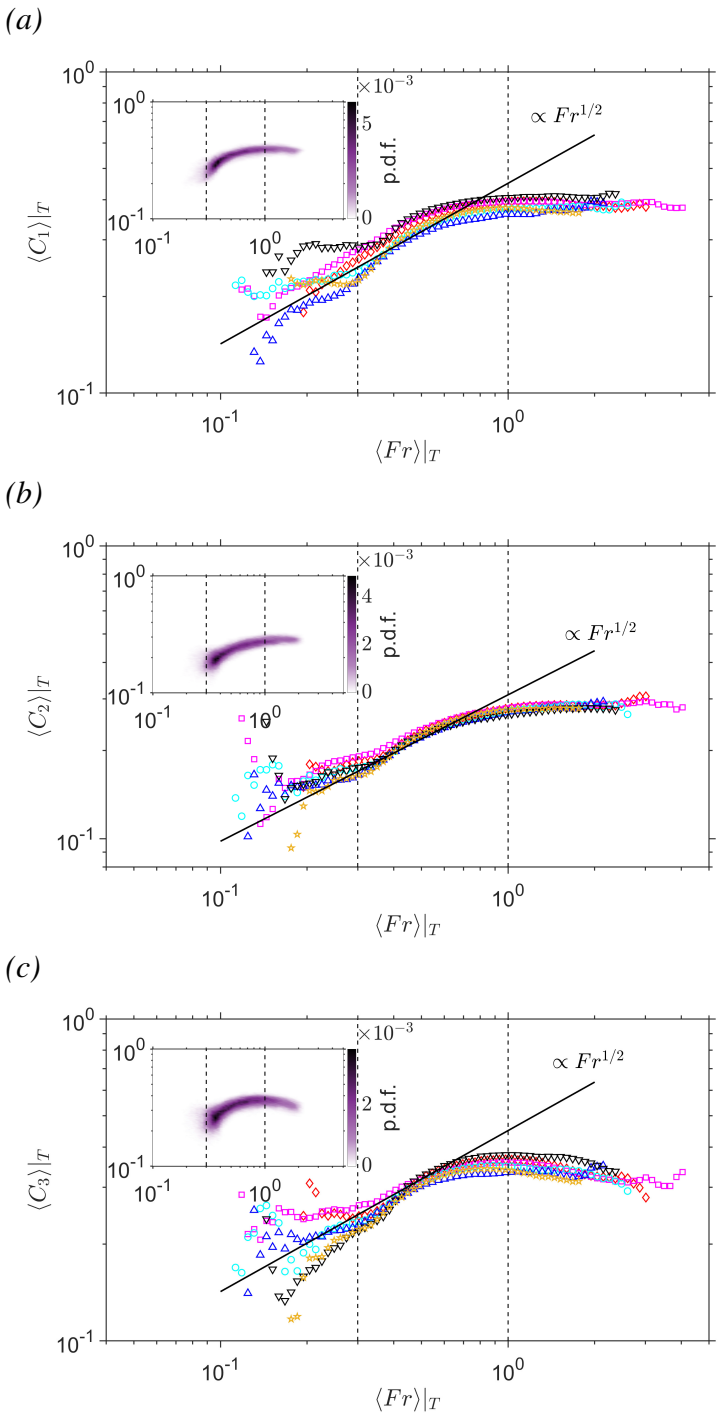

FIGURE 5.13: Bin averaged values and 2D p.d.f.s of: (a) $\langle C_1\rangle|_T$, (b) $\langle C_2\rangle|_T$ and (c) $\langle C_3\rangle|_T$ as defined in (5.24) within the turbulent data set plotted against corresponding bins of conditionally averaged $\langle Fr\rangle|_T$. Bin averaged values and 2D p.d.f. constructed with the temporal range of $t/T_\tau^0 > 1$ and the vertical range of $0.2\delta < z < z_{le}$. Solid diagonal lines in all figures indicate $C \propto Fr^{1/2}$. Vertical dashed lines indicate $Fr = 0.3, 1$.Legend same as figure 5.3(b).

observe C_3 to grow smaller. We note that for $Fr < 0.3$ there is significant scatter in the results as the data-set becomes sparse, corresponding to the rare high stratification mixing events. However it is still reasonably clear that a positive correlation continues to exist between C_1, C_2, C_3 and Fr. These results are consistent with the experimental findings of Ivey & Imberger (1991) who demonstrate that the correlation coefficient between the vertical density flux and rms values of vertical velocity and density fluctuations goes to zero as $Fr \to 0$.

We can now rewrite (5.21) explicitly incorporating the above assumptions

$$B \sim C_1 C_3 E_K N^2 T_*. \tag{5.27}$$

Hence if we take the assumption of MCA21 that active turbulence in stratified shear flow may always be considered 'weakly stratified' for all Fr, we take $T_* = T_L$ to obtain

$$\Gamma = \frac{B}{\epsilon_K} \sim \frac{C_1 C_3 E_K N^2 T_L}{\epsilon_K} = C_1 C_3 Fr^{-2}. \tag{5.28}$$

Accordingly for $Fr > 1$, the flow approaches relative isotropy and buoyancy acts as a passive scalar such that $C_1 \sim C_3 \sim$ const and hence we recover the $\Gamma \sim Fr^{-2}$ scaling of Maffioli *et al.* (2016) and GV19.

For the $0.3 \leq Fr \leq 1$ 'intermediate' transitional regime, the flow begins to develop the shear and large scale anisotropy to reach its critical and 'optimal' state such that $C_1 \sim C_3 \sim Fr^{1/2}$. Accordingly we obtain

$$\Gamma \sim C_1 C_3 Fr^{-2} \sim Fr^{1/2} Fr^{1/2} Fr^{-2} \sim Fr^1, \tag{5.29}$$

the same as the results presented in GV19 and directly supported by our results in this study. We now directly reconcile this with the primary assumption of MCA21 by rewriting (5.19) using (5.24) and (5.27) to obtain

$$Pr_T = \frac{K_M}{K_\rho} = \frac{\overline{-u'w'}N^2}{BS} \sim \frac{1}{C_1 C_3} \frac{\overline{-u'w'}}{E_K} \frac{N^2}{N^2} \frac{T_S}{T_*} \sim \frac{C_2}{C_1 C_3} \frac{T_S}{T_L}, \tag{5.30}$$

where $T_S = 1/S$ is the shear time scale. We also recall that Ri_g and Fr may be interpreted as a ratio of time scales such that

$$Ri_g = \frac{T_S^2}{T_N^2}, \qquad Fr = \frac{T_N}{T_L}. \tag{5.31a, b}$$

Accordingly from the results in figure 5.9(a) we obtain

$$Ri_g \sim Fr^{-2} \rightarrow T_S/T_L = \text{const}, \quad Fr \geq 1 \tag{5.32}$$

and

$$Ri_g \sim Fr^{-1} \rightarrow T_S/T_L \sim Fr^{1/2}, \quad 0.3 \leq Fr \leq 1. \tag{5.33}$$

Hence for the $Fr \geq 1$ regime we recall that $C_1 \sim C_2 \sim C_3 \sim$ const to obtain

$$Pr_T \sim \frac{C_2}{C_1 C_3}\frac{T_S}{T_L} \sim \text{const} \tag{5.34}$$

and for the intermediate regime we recall that $C_1 \sim C_2 \sim C_3 \sim Fr^{1/2}$ to obtain

$$Pr_T \sim \frac{C_2}{C_1 C_3}\frac{T_S}{T_L} \sim \frac{Fr^{1/2}}{Fr^{1/2}Fr^{1/2}} Fr^{1/2} \sim \text{const}. \tag{5.35}$$

This is consistent with our observations that $Pr_T \approx 1$ across both the weakly stratified and intermediate regimes. Hence we reconcile a $\Gamma \sim Fr^{-1}$ mixing regime with the $Pr_T \approx 1$ assumption of MCA21 by accounting for the large scale anisotropy of the flow at $Fr \lesssim \mathcal{O}(1)$. For the super-critical regime of $Fr < 0.3$ where Ri_g becomes constant we hence expect no correlation between T_S and T_L. Due to the sparsity of data and scatter of our results in figures 5.12 and 5.13 within this regime in our study, it becomes somewhat unclear if Pr_T would remain constant with further decreasing Fr. However as $Fr \approx 0.3$ represents a critical state for the stationary flow, we expect the infrequent deviations from this state to be relatively small and hence the $Pr_T \approx 1$ assumption to hold.

As such our results and analysis directly support the arguments of Caulfield (2021) that vigorous turbulence in stratified shear flow should never be considered ‘strongly stratified’ in the same sense as the LAST regime where buoyancy effects dominate the flow dynamics to leading order. However our results distinctly show that for $Fr \leq 1$, the assumption that buoyancy acts purely as a passive scalar is also invalid. The results suggest, that as argued by

GV19, the emergence of a $\Gamma \sim Fr^{-1}$ intermediate mixing regime indeed manifests due to buoyancy beginning to influence flow dynamics. However, the results imply that this occurs due to the secondary effect of buoyancy distorting the large scales of the flow towards an optimal anisotropic state rather than buoyancy playing a leading order role in the evolution of b' and hence B.

5.6 Conclusions

In summary, we have investigated the behaviour of spatio-temporal intermittency in our DNS of stratified open channel flow due to the suppression of turbulence through the stabilising effects of buoyancy. In particular our study focuses on the prediction of the vertical intermittency profile and on the effect of the inherent intermittency in stratified shear flows on the accurate parameterization of the flux coefficient Γ.

By adapting the density inversion criterion method of PKTSC16 to our inhomogeneous flow we are able to robustly separate the flow into regions of active turbulence defined by $Re_B \gtrsim \mathcal{O}(10)$ and the surrounding quiescent fluid which approaches a quasi-laminar state. Our method demonstrates that we are able to construct our reference state of 'fully turbulent' flow from a single instantaneous realisation of the flow, provided a sufficient vertical range emerges in the flow where $Re_B > \mathcal{O}(100)$.

We find our flow configuration modelled as a canonical representation of radiatively heated stratified river flows in the framework of Williamson *et al.* (2015) is distinctly defined by an intermittency profile that is highly inhomogeneous in the vertical direction that results from the spontaneous formation of an interface separating the upper quiescent flow from the turbulent bulk flow. We quantify this local intermittency through a depth varying turbulent volume fraction γ. The flow displays a fully turbulent and weakly stratified lower region near the wall defined by $\gamma = 1$, $Re_B > \mathcal{O}(100)$ and $Fr > \mathcal{O}(1)$. Conversely, at our parameter range (with the exclusion of our most weakly stratified case case R400L0.5) the region at the top free surface transitions into a fully quiescent quasi-laminar state defined by $\gamma = 0$, $Re_B < \mathcal{O}(1)$ and $Fr \ll \mathcal{O}(1)$. The central bulk flow hence develops as region of vertically

varying intermittency separating the two regions. By applying local Monin-Obhukov scaling we find that γ is well predicted by a locally defined Obhukov length (normalized in wall units) Λ^+ across all simulations and their respective external bulk parameter set. We find that in direct agreement with the analysis of Chung & Matheou (2012), the transition away from the fully turbulent regime occurs at $\Lambda^+ \approx 260$, while the flow approaches quasi-laminar conditions at $\Lambda^+ \approx 2.5$. As such our results add further evidence that the Monin-Obhukov framework is highly applicable for the prediction of intermittency in a variety of stratified shear flows where the flow exists in a state of balance between the production of turbulence through the mean shear and suppressing nature of buoyancy and viscosity.

We find that within the region of intermittency, the background stratification N and shear S are marginally lower in the 'turbulent' flow relative to the surrounding quiescent fluid as the suppression of the turbulent fluxes causes the quiescent flow to develop steeper mean gradients such that the total buoyancy and momentum fluxes are in balance with the forcing terms of the flow. Accordingly we find this region to be described by a critical value of $Ri_{g,c} \approx 0.2$ and where the turbulent and quiescent flow respectively organizes towards local Ri_g values marginally smaller and larger than the conceptual critical value for stability suggesting the flow exists in a state of 'marginal instability' as argued by Thorpe & Liu (2009). This region is notably defined by vigorous overturning shear instability driven mixing that form in these critical conditions and where we find that the dominant energetic terms within the 'turbulent' flow P, B, ϵ_K all come to a local maxima. In agreement with the concept of optimal mixing under critical conditions as argued by Mashayek *et al.* (2021), we find that within this region the turbulent flow is described by $\Gamma \approx 0.2 - 0.33$. Considering the distinct vertical inhomogeneity in the profiles of the mean and turbulent flow, our results strongly suggest as to a degree of universality for the self-organization of stratified shear flows towards this 'optimal' state. Furthermore, we find that within this region of critical flow, the stationary profiles of Fr within the 'turbulent' flow all clearly converge to a clear lower critical limit of $Fr_c \approx 0.3$ in direct agreement to the transitional value towards an asymptotic regime proposed by Maffioli *et al.* (2016). Hence we provide further evidence for the arguments of Caulfield (2021) that active and vigorous turbulence in stratified shear flow should not be

considered ‘strongly stratified’ in the same theoretical sense as the LAST regime due to a clear lower limit on Fr.

By considering the flow from the z_i turbulent/quiescent interface reference coordinate system, we find that the thickness of the interfacial layer separating the two regimes to scale with the Ellison length L_E. This being in direct agreement with our visual observations of overturning within this region. In particular we find that the critical values of $Ri_{g,c} \approx 0.2$, $Fr_c \approx 0.3$ and the peak in Γ occur directly at the lower bound of the interfacial layer. Accordingly our results directly suggest that criticality and intermittency are intrinsically linked within stratified open channel consistent with the concept of self organized criticality in stratified shear flows as argued by Smyth *et al.* (2019).

By examining the correlations between horizontal averages of Fr and Γ across the conditionally averaged data sets we show that in the limit of low Fr, Γ shows continued dependence on Fr within the ’turbulent’ flow such that the flow continues to display $\Gamma \sim Fr^{-1}$ behaviour in for $Fr < Fr_c$. Conversely, within the quiescent regions of the flow we find Γ is independent of Fr for the full parameter range presented and maintains a constant value of $\Gamma \approx 0.2 - 0.33$. The emergence of an asymptotic constant Γ regime for $Fr \leq 0.3$ in the full data set comes directly as a result of the intermittency of the flow and increasing contributions to measurements of Fr and Γ from the surrounding quiescent fluid. We argue that the observation of a ‘saturated’ Γ regime in numerous past studies of stratified shear flow is fundamentally linked to the inherent intermittency of the flow at finite Re_B.

Within the turbulent patches of the flow, we observe the emergence of a $\Gamma \sim Fr^{-1}$ intermediate regime for $Fr \leq 1$ manifests due to the separation of the vertical and horizontal velocity scales within such patches as buoyancy and the mean shear distorts the flow towards an anisotropic state to facilitate efficient mixing through shear instabilities. As such, our results present evidence for the arguments of MCA21 that suggest when considering energetic turbulent patches within stratified shear flow, buoyancy does not play a leading order role in the evolution of the mixing rate but rather it is ‘slaved’ to the mixing of momentum such that $Pr_T \approx 1$ for all Fr.

CHAPTER 6

Conclusion

The primary aim of this dissertation has been to investigate and improve our understanding of the nature, mechanics and accurate parameterization of turbulent mixing within vertically inhomogeneous stratified flows. To that end, we have performed an extensive series of direct numerical simulations of stratified open channel flow in the framework of Williamson *et al.* (2015). We have employed a canonical 'sunrise' configuration whereby we consider the temporally evolving flow of a neutral turbulent open channel subject to sudden radiative heating. This has allowed us to explore a wide and distinctly inhomogeneous 'local' parameter range of Fr, Re_B, Ri_g, Γ within a single simulation as the flow evolves towards stationarity. Furthermore and in the context of regulated stratified river flows, a secondary aim of this thesis has been to provide a detailed qualitative description of the transient response of the temporally evolving flow as well as a bulk parameterization for the global stratification process. A summary of the key research outcomes of this thesis is presented below.

6.1 Main research outcomes

In chapter §3 we have demonstrated that the transient response of the turbulent channel flow can be defined by two transient periods. Firstly the flow undergoes 'rapid suppression' as the sudden imposition of stratification causes a reduction in w' and hence the turbulent momentum flux $\overline{u'w'}$. This causes an inbalance between the total momentum flux and the driving pressure gradient as well as an inbalance in the TKE budget causing a global loss of TKE across the channel. Secondly, the flow enters a 'slow recovery' period as the flow accelerates to develop the mean shear profile required such that the flow is able to extract sufficient TKE from the

mean flow to obtain an equilibrium stratified state. Within the region of increased shear we observe that the flow structure changes such that mixing becomes predominantly driven by overturning shear instabilities that manifest locally rather than wall-bounded turbulence from below as in neutral channel flow. A description of the changing vertical structure of the channel with respect to mean shear and stratification gradients, second order statistics and energetic quantities has been presented for both periods of the flow.

We have presented scaling arguments to demonstrate that the global suppression of turbulent mixing within the temporally evolving channel flow defined by normalized bulk measures of the eddy diffusivity and viscosity $\langle K_\rho \rangle / \kappa Pr$ and $\langle K_M \rangle / \nu$ can be parameterized across three regimes by the mixed parameter $Ri_\tau^{-1} Re_\tau$:

For $Ri_\tau^{-1} Re_\tau \gtrsim 100$ the flow approaches neutral (asymptotic) conditions such that

$$\frac{\langle K_\rho \rangle}{\kappa Pr} \sim \frac{\langle K_M \rangle}{\nu} \sim \text{const.} \tag{6.1}$$

For $10 \lesssim Ri_\tau^{-1} Re_\tau \lesssim 100$ the flow enters a 'intermediate' state in which buoyancy begins to suppress the turbulent fluxes such that

$$\frac{\langle K_\rho \rangle}{\kappa Pr} \sim \frac{\langle K_M \rangle}{\nu} \sim (Ri_\tau^{-1} Re_\tau)^{1/4}. \tag{6.2}$$

And for $Ri_\tau^{-1} Re_\tau \lesssim 10$ the flow enters a strongly suppressed regime with relaminarization in the upper layer such that

$$\frac{\langle K_\rho \rangle}{\kappa Pr} \sim \frac{\langle K_M \rangle}{\nu} \sim (Ri_\tau^{-1} Re_\tau)^{1/2}. \tag{6.3}$$

We note that this is a new scaling relationship derived for both time-varying and stationary flow and hence propose that $Ri_\tau^{-1} Re_\tau$ may form the basis of a forecasting tool used in stratified river flows for the prediction of suppressed mixing in the upper layer. We note again however that at the limited $Re_\tau - Ri_\tau$ parameter range explored in this thesis it remains to be seen as to the universality of these transitional values.

We have demonstrated that the convergence of the buoyancy and momentum fluxes as well as the TKE towards an equilibrium state is a global parabolic process governed by a single

timescale such that the flow obtains equilibrium at all depths simultaneously at $t = t_e$. We find that t_e similarly defines the time at which local mixing dynamics have reached stationarity such that key non-dimensional mixing diagnostics (i.e. Ri_g, R_f, Fr, Re_B etc) reach their final stationary values.

By employing our previously derived bulk parameterization of $\langle K_\rho \rangle$ we provide further scaling arguments and demonstrate that t_e can be predicted such that the flow obtains stationarity at $Ri_\tau^{-1/2}(t/T_\tau) \approx 2$ provided that $Ri_\tau^{-1} Re_\tau \lesssim 100$. Our results which support our scaling across the full external parameter set are consistent with the past 'sunset' studies of Kirkpatrick *et al.* (2019, 2020) which similarly show a $Ri_\tau^{-1/2}$ dependence on the convergence of the destratifying flow towards neutral equilibrium.

As Ri_τ and Re_τ are parameters that may be readily obtained from field measurements, the results presented in this chapter provide a clear practical application for stratified river flows for both the time-varying prediction of suppressed mixing as well as an estimation for the time at which the initially and presumably well mixed 'sunrise' flow obtains stationarity such that local mixing diagnostics obtain their established stationary values as shown in the study of Williamson *et al.* (2015).

In chapter §4 we have robustly investigated the parameterization of the flux coefficient Γ within $Fr, Ri_g, L_E/L_O$ and Re_B frameworks within stratified open channel flow by considering instantaneous horizontal averages of the flow. In particular our vertically inhomogeneous and temporally evolving flow configuration has allowed us to investigate this at a broad local parameter range and without the *a priori* assumptions of stationarity or local equilibrium.

We demonstrate that the local flow is described by three dynamically different mixing regimes defined by transitional values of Fr and where despite the spatio-temporal inhomogeneity, Γ is well predicted by the Fr based parameterization schemes of Maffioli *et al.* (2016) and Garanaik & Venayagamoorthy (2019).

For $Fr \gtrsim 1$, the flow is only weakly affected by stratification and displays a $\Gamma \sim Fr^{-2}$ relationship. For $0.3 \lesssim Fr \lesssim 1$, the flow enters an 'intermediate' regime where stratification begins to modify the turbulence structure and the flow displays $\Gamma \sim Fr^{-1}$ relationship. For

$Fr \lesssim 0.3$ the flow enters a 'saturated' regime as Γ approaches a constant value. In particular our observed transitional value of $Fr \approx 0.3$ to the saturated regime is directly in agreement with the analysis of Maffioli *et al.* (2016). Considering the strong inhomogeneity of our flow with respect to both z and t, the results strongly suggest a degree of universality on the relationship between Fr and Γ as argued in their study.

In contrast we find that only two mixing become apparent when considering the flow in a Ri_g framework. For $Ri_g \lesssim 0.25$ the flow displays a classic linear relationship of $R_f \sim Ri_g$ as observed in past studies (Shih *et al.*, 2005; García-Villalba & del Álamo, 2011; Zhou *et al.*, 2017*a*). And for $Ri_g \gtrsim 0.25$, R_f approaches a constant value analogous to the saturated regime described above. We provide new scaling arguments to show that in the 'intermediate' regime, shear, inertial and buoyancy forces are all significant such that the flow obtains a transitional $Ri_g \sim Fr^{-1}$ relationship. For $Fr \gtrsim 1$ we observe that the classic inertial scaling leads to $Ri_g \sim Fr^{-2}$ as observed in past studies (Zhou *et al.*, 2017*a*). We present support for our new intermediate scaling from a variety of DNS data sets of stratified shear flow suggesting a degree of universality to this behaviour (Shih *et al.*, 2000; Chung & Matheou, 2012; Portwood *et al.*, 2019). We hence reconcile the two parameterization frameworks for stratified shear flow across all three mixing regimes defined by Fr. In particular the new scaling relationship for the intermediate regime highlights the complexity of mixing dynamics in stratified shear flow and directly bridges the gap in literature between the two limit regimes. Considering the distinctly different dynamics and mixing mechanics of the weakly and moderately stratified regimes, the results suggest that a local measure of Fr may offer a more nuanced and insightful perspective into mixing dynamics than Ri_g.

We demonstrate that Γ within the temporally evolving flow is also well parameterized by the length scale ratio L_E/L_O across all three mixing regimes as argued by Garanaik & Venayagamoorthy (2019). In particular we observe a distinct $\Gamma \sim (L_E/L_O)^1$ scaling for the intermediate regime that holds for an entire decade of L_E/L_O. We present scaling analysis to demonstrate that for our shear driven quasi-steady (forced) class of flow, this occurs directly due to the presence of mean shear and the resulting $L_E \sim L_S$ scaling within the intermediate regime. We further present scaling arguments to propose why past studies of homogeneous

(un-sheared) stratified flow have not displayed an appreciable range of $\Gamma \sim (L_E/L_O)^1$ within their DNS (Mater *et al.*, 2013; Howland *et al.*, 2020). We hence demonstrate, that for our shear driven flow, the Fr, Ri_g and L_E/L_O frameworks are directly equivalent across all three mixing regimes.

We demonstrate that although the flow qualitatively displays all three mixing regimes based on Re_B as argued by the seminal work Shih *et al.* (2005), there exists no universal transitional value of Re_B between the varying regimes. Rather we find that the transition between the three mixing regimes displays a clear Re_T and hence Re_τ dependence in agreement with the analysis of Maffioli *et al.* (2016). Our results add further evidence to recent studies that suggest Re_B is not an optimal single parameter for the accurate estimation of Γ (Scotti & White, 2016).

In chapter §5 we have investigated the spatio-temporal intermittency that manifests in our flow due to stable stratification. We have demonstrated that the density inversion criterion method of Portwood *et al.* (2016) can be adapted to our vertically inhomogeneous flow such that we are able to robustly separate the flow into turbulent regions where $Re_B \gtrsim \mathcal{O}(10)$ and surrounding quiescent flow within a single instantaneous realisation of the flow.

We have demonstrated that the resulting depth varying turbulent volume fraction $\gamma(z)$ is well predicted by Monin-Obhukov theory through the normalized (by viscous units) local M-O length Λ^+, such that intermittency manifests within the range of $2.5 \lesssim \Lambda^+ \lesssim 260$. This corresponds directly to a buoyancy Reynolds number range of $1 \lesssim Re_B \lesssim 100$ and falls directly in agreement with the analysis of Chung & Matheou (2012), suggesting a degree of universality in the prediction of intermittency for a wide range of stratified shear flows through local M-O scaling. Again, in the direct context of stratified river flows where the flux profiles may be roughly estimated *a priori* through knowledge of bulk flow properties, our results present direct applicability for the forecasting of suppressed mixing in rivers due to intermittency. Furthermore, due to the the inhomogeneity of the flux profiles, the intermittency within our flow manifests spontaneously as a deformed horizontal interface that separates an upper quiescent quasi-laminar layer from the lower bulk and highly turbulent flow. By considering the flow from an interfacial coordinate system we further demonstrate that the

thickness of the resulting interfacial layer scales with the overturning length L_E such that energetic quantities and non-dimensional mixing diagnostics display self-similar behaviour within the interfacial layer irrespective of the external parameter set.

By considering conditional horizontal averages of the 'turbulent' and 'quiescent' flow regions we demonstrate that critical mixing conditions defined by asymptotic limit values of $Ri_g \approx 0.2, \Gamma \approx 0.25$ and $Fr \approx 0.3$ only manifest within regions of appreciable intermittency. Our results suggest that for our flow, these critical mixing conditions directly arise from the intermittency in the flow and presents direct support for the theory 'optimal mixing' and self-organized criticality that has been observed in a variety of stratified shear flows (Thorpe & Liu, 2009; Salehipour *et al.*, 2018; Smyth *et al.*, 2019; Mashayek *et al.*, 2021).

We show that when considering a conditionally averaged Fr based parameterization of Γ, the 'turbulent' flow does not display a saturated regime at low Fr, but rather continues to display a $\Gamma \sim Fr^{-1}$ intermediate scaling for $Fr \lesssim 1$. Conversely, the quiescent flow displays no correlation between Fr and Γ such that Γ remains constant for all Fr. We directly demonstrate that the emergence of an asymptotic mixing regime for $Fr \lesssim 0.3$ as observed in chapter §4 manifests directly due to the intermittency in the flow and increasing contributions to 'global' measures of Fr and Γ from the quiescent flow. To our knowledge ours is the first study that has demonstrated this behaviour directly through DNS data. Considering the ubiquitous appearance of $Fr \approx 0.3 - 0.5$ in literature (Chung & Matheou, 2012; Portwood *et al.*, 2019; Smith *et al.*, 2021) as well as the original scaling arguments of Maffioli *et al.* (2016), we argue that this behaviour is a fundamental characteristic of a wide variety of quasi-steady stratified shear flows and presents evidence for the arguments of Caulfield (2021) that active turbulence in stratified shear flow is unable to access the LAST regime as defined by $Re_B \gg \mathcal{O}(1)$ and $Fr \ll \mathcal{O}(1)$. In the context of the frequent observations of spatio-temporal intermittency or so called 'patchiness' of turbulence in various geophysical flows (Caulfield, 2021), our results in this chapter highlight the importance of accurately understanding both the mechanisms by which intermittency manifests as well as the need for robust and accurate methods to quantify its effect on global mixing rates.

6.2 Future outlook

A particular key result of this thesis has been the observation that critical flow conditions characterized by efficient overturning driven mixing and limit values of Ri_g, Fr occurs directly within regions of appreciable intermittency, seemingly in agreement with the SOC theory of Smyth *et al.* (2019). However, as seen from our results in chapter §4 (figures 4.4 and 4.12), at our modest resolution and Re_τ values considered in this DNS, strongly stratified regions where $Fr \approx \mathcal{O}(10^{-1})$ corresponds to flow defined by low Re_B. It is not clear if this behaviour is a fundamental characteristic of stratified shear flow or an implicit result due to the correlation of Fr and Re_B at our paramater range. As $Re_B = Re_T Fr^2$ and $Re_T \sim Re_\tau$, future studies at significantly higher Re_τ would be able to test this result explicitly. It would be further extremely useful to rigorously test this behaviour in DNS of other stratified shear flow configurations at a presumably intermittent local Re_B range of $1 \lesssim Re_B \lesssim 100$ while similarly maintaining Re_T as a control variable.

For the most part, in this thesis we have explicitly excluded flow statistics close to the upper free surface boundary where the confinement effects on mixing dynamics remain relatively uninvestigated in current literature. In the context of stratified river flows and reduction of vertical scalar transport absorbed at the water-air interface it is clear that the free surface dynamics become extremely relevant and crucial to the understanding of such flows. Calmet & Magnaudet (2003) use scaling arguments and their LES data set to show that for unstratified channel flow an upper surface effected 'source layer' is approximately of the order 0.2δ. However in chapter 5 we have demonstrated that for case R900L1, when considering only the turbulent flow, the local equilibrium region extends up to $z/\delta = 0.91$. This suggests that the reduction w' and subsequent anisotropic nature of stratified turbulence acts to reduce the thickness of the proposed 'source layer'. Furthermore, at the paramater range explored within our study the upper layer generally is described by $Re_B \lesssim \mathcal{O}(10)$ and the issue is confounded by intermittency and relaminarization making it very challenging to analyze the surface confinement dynamics separately. As such future studies where DNS run at significantly higher Re_τ while concurrently maintaining high λ such that the upper layer is described by $Re_B \gtrsim \mathcal{O}(10)$, while the core channel remains $Fr \lesssim \mathcal{O}(1)$ would be able to

investigate this in a detailed and rigorous manner. Furthermore, we have demonstrated in chapter 3, that our bulk scaling for the stratification rate $\mathcal{S} \sim 1 - 0.5Ri_\tau^{-1/2}(t/T_\tau)$ breaks down due to relaminarization at the upper layer. Again DNS at higher Re_τ and λ as expected in real river flows would be able to test whether a linear relationship develops as per the scaling arguments.

Finally we must address that for the entirety of this thesis, with the exception of a single case we have only considered a molecular Prandtl number of unity for computational efficiency. This being in stark contrast to $Pr = 6 - 7$ expected in stratified river flows. As shown in past studies Γ has been shown to decrease monotonically with increasing Pr (Salehipour *et al.*, 2015; Zhou *et al.*, 2017*b*). How this result pertains to the parameterization of Γ within our flow in chapters 4 and 5 remains to be seen. Although it does not arise in our scaling arguments, it is unclear how high Pr would effect the bulk parameterization of reduced mixing or equilibrium time derived in chapter 3. Future studies run at higher Pr would be able to answer these open questions.

Bibliography

ARMENIO, VINCENZO & SARKAR, SUTANU 2002 An investigation of stably stratified turbulent channel flow using large-eddy simulation. *Journal of Fluid Mechanics* **459**.

ARMFIELD, S., MORGAN, P., NORRIS, S. & STREET, R. 2003 A Parallel Non-Staggered Navier-Stokes Solver Implemented on a Workstation Cluster. In *Computational Fluid Dynamics 2002* (ed. Steve W. Armfield, Patrick Morgan & Karkenahalli Srinivas), pp. 30–45. Springer Berlin Heidelberg.

ATOUFI, AMIR, SCOTT, K. ANDREA & WAITE, MICHAEL L. 2020 Characteristics of quasistationary near-wall turbulence subjected to strong stable stratification in open-channel flows. *Physical Review Fluids* **5** (6), 064603.

ATOUFI, AMIR, SCOTT, K. ANDREA & WAITE, MICHAEL L. 2021 Kinetic energy cascade in stably stratified open-channel flows. *Journal of Fluid Mechanics* **925**, publisher: Cambridge University Press.

BAKER, MARK A. & GIBSON, CARL H. 1987 Sampling Turbulence in the Stratified Ocean: Statistical Consequences of Strong Intermittency. *Journal of Physical Oceanography* **17** (10), 1817–1836.

BASAK, S. & SARKAR, S. 2006 Dynamics of a stratified shear layer with horizontal shear. *Journal of Fluid Mechanics* **568**, 19.

BILLANT, PAUL & CHOMAZ, JEAN-MARC 2001 Self-similarity of strongly stratified inviscid flows. *Physics of Fluids* **13** (6), 1645–1651.

BORMANS, MYRIAM & WEBSTER, IAN 1998 Dynamics of Temperature Stratification in Lowland Rivers. *Journal of Hydraulic Engineering-asce - J HYDRAUL ENG-ASCE* **124**.

BRETHOUWER, G., BILLANT, P., LINDBORG, E. & CHOMAZ, J.-M. 2007 Scaling analysis and simulation of strongly stratified turbulent flows. *Journal of Fluid Mechanics* **585**, 343.

BRETHOUWER, G., DUGUET, Y. & SCHLATTER, P. 2012 Turbulent–laminar coexistence in wall flows with Coriolis, buoyancy or Lorentz forces. *Journal of Fluid Mechanics* **704**,

137–172.

BROOKS, BRYAN W., LAZORCHAK, JAMES M., HOWARD, MEREDITH D. A., JOHNSON, MARI-VAUGHN V., MORTON, STEVE L., PERKINS, DAWN A. K., REAVIE, EUAN D., SCOTT, GEOFFREY I., SMITH, STEPHANIE A. & STEEVENS, JEFFERY A. 2016 Are harmful algal blooms becoming the greatest inland water quality threat to public health and aquatic ecosystems? *Environmental Toxicology and Chemistry* **35** (1), 6–13.

DE BRUYN KOPS, STEPHEN M. 2015 Classical scaling and intermittency in strongly stratified Boussinesq turbulence. *Journal of Fluid Mechanics* **775**, 436–463.

DE BRUYN KOPS, STEPHEN M. & RILEY, JAMES J. 2019 The effects of stable stratification on the decay of initially isotropic homogeneous turbulence. *Journal of Fluid Mechanics* **860**, 787–821.

BUREN, TYLER VAN, WILLIAMS, OWEN & SMITS, ALEXANDER J. 2017 Turbulent boundary layer response to the introduction of stable stratification. *Journal of Fluid Mechanics* **811**, 569–581, publisher: Cambridge University Press.

CALMET, ISABELLE & MAGNAUDET, JACQUES 2003 Statistical structure of high-Reynolds-number turbulence close to the free surface of an open-channel flow. *Journal of Fluid Mechanics* **474**.

CAULFIELD, C.P. 2021 Layering, Instabilities, and Mixing in Turbulent Stratified Flows. *Annual Review of Fluid Mechanics* **53** (1), 113–145, _eprint: https://doi.org/10.1146/annurev-fluid-042320-100458.

CAULFIELD, COLM-CILLE P. 2020 Open questions in turbulent stratified mixing: Do we even know what we do not know? *Physical Review Fluids* **5** (11), 110518.

CAULFIELD, C. P. & PELTIER, W. R. 2000 The anatomy of the mixing transition in homogeneous and stratified free shear layers. *Journal of Fluid Mechanics* **413**, 1–47.

CHUNG, D. & MATHEOU, G. 2012 Direct numerical simulation of stationary homogeneous stratified sheared turbulence. *Journal of Fluid Mechanics* **696**, 434–467.

DEUSEBIO, ENRICO, CAULFIELD, C. P. & TAYLOR, J. R. 2015 The intermittency boundary in stratified plane Couette flow. *Journal of Fluid Mechanics* **781**, 298–329.

ELLISON, T. H. 1957 Turbulent transport of heat and momentum from an infinite rough plane. *Journal of Fluid Mechanics* **2** (5), 456–466, publisher: Cambridge University Press.

FALDER, MATTHEW, WHITE, N. J. & CAULFIELD, C. P. 2016 Seismic Imaging of Rapid Onset of Stratified Turbulence in the South Atlantic Ocean. *Journal of Physical Oceanography* **46** (4), 1023–1044, publisher: American Meteorological Society Section: Journal of Physical Oceanography.

FERNANDO, H J S 1991 Turbulent Mixing in Stratified Fluids. *Annual Review of Fluid Mechanics* **23** (1), 455–493, publisher: Annual Reviews.

FLORES, O. & RILEY, J. J. 2011 Analysis of Turbulence Collapse in the Stably Stratified Surface Layer Using Direct Numerical Simulation. *Boundary-Layer Meteorology* **139** (2), 241–259.

FLORES, OSCAR, RILEY, JAMES J. & HORNER-DEVINE, ALEXANDER R. 2017 On the dynamics of turbulence near a free surface. *Journal of Fluid Mechanics* **821**, 248–265.

GALPERIN, BORIS, SUKORIANSKY, SEMION & ANDERSON, PHILIP S. 2007 On the critical Richardson number in stably stratified turbulence. *Atmospheric Science Letters* **8** (3), 65–69, _eprint: https://rmets.onlinelibrary.wiley.com/doi/pdf/10.1002/asl.153.

GARANAIK, AMRAPALLI & VENAYAGAMOORTHY, SUBHAS KARAN 2018 Assessment of small-scale anisotropy in stably stratified turbulent flows using direct numerical simulations. *Physics of Fluids* **30** (12), 126602, publisher: American Institute of Physics.

GARANAIK, AMRAPALLI & VENAYAGAMOORTHY, SUBHAS K. 2019 On the inference of the state of turbulence and mixing efficiency in stably stratified flows. *Journal of Fluid Mechanics* **867**, 323–333.

GARCÍA-VILLALBA, MANUEL & DEL ÁLAMO, JUAN C. 2011 Turbulence modification by stable stratification in channel flow. *Physics of Fluids* **23** (4), 045104.

GARG, RAJAT P., FERZIGER, JOEL H., MONISMITH, STEPHEN G. & KOSEFF, JEFFREY R. 2000 Stably stratified turbulent channel flows. I. Stratification regimes and turbulence suppression mechanism. *Physics of Fluids* **12** (10), 2569–2594, publisher: American Institute of Physics.

GREGG, M.C. 1987 Diapycnal mixing in the thermocline: A review. *Journal of Geophysical Research: Oceans* **92** (C5), 5249–5286, _eprint: https://onlinelibrary.wiley.com/doi/pdf/10.1029/JC092iC05p05249.

GREGG, M.C., D'ASARO, E.A., RILEY, J.J. & KUNZE, E. 2018 Mixing Efficiency in the Ocean. *Annual Review of Marine Science* **10** (1), 443–473, _eprint: https://doi.org/10.1146/annurev-marine-121916-063643.

HEBERT, DAVID A. & DE BRUYN KOPS, STEPHEN M. 2006 Predicting turbulence in flows with strong stable stratification. *Physics of Fluids* **18** (6), 066602.

HOWLAND, C. J., TAYLOR, J. R. & CAULFIELD, C. P. 2018 Testing linear marginal stability in stratified shear layers. *Journal of Fluid Mechanics* **839**, R4.

HOWLAND, CHRISTOPHER J., TAYLOR, JOHN R. & CAULFIELD, C. P. 2020 Mixing in forced stratified turbulence and its dependence on large-scale forcing. *Journal of Fluid Mechanics* **898**, publisher: Cambridge University Press.

HOWLAND, CHRISTOPHER J., TAYLOR, JOHN R. & CAULFIELD, C. P. 2021 Quantifying mixing and available potential energy in vertically periodic simulations of stratified flows. *Journal of Fluid Mechanics* **914**, publisher: Cambridge University Press.

IJICHI, TAKASHI & HIBIYA, TOSHIYUKI 2018 Observed Variations in Turbulent Mixing Efficiency in the Deep Ocean. *Journal of Physical Oceanography* **48** (8), 1815 – 1830, place: Boston MA, USA Publisher: American Meteorological Society.

ISSAEV, VASSILI, WILLIAMSON, N., ARMFIELD, S. W. & NORRIS, S. E. 2022 Parameterization of mixing in stratified open channel flow. *Journal of Fluid Mechanics* **935**, publisher: Cambridge University Press.

ITSWEIRE, E. C., KOSEFF, J. R., BRIGGS, D. A. & FERZIGER, J. H. 1993 Turbulence in Stratified Shear Flows: Implications for Interpreting Shear-induced Mixing in the Ocean. *Journal of Physical Oceanography* **23** (7), 1508–1522, publisher: American Meteorological Society Section: Journal of Physical Oceanography.

IVEY, G.N., WINTERS, K.B. & KOSEFF, J.R. 2008 Density Stratification, Turbulence, but How Much Mixing? *Annual Review of Fluid Mechanics* **40** (1), 169–184.

IVEY, GREGORY N., BLUTEAU, CYNTHIA E. & JONES, NICOLE L. 2018 Quantifying Diapycnal Mixing in an Energetic Ocean. *Journal of Geophysical Research: Oceans* **123** (1), 346–357, _eprint: https://agupubs.onlinelibrary.wiley.com/doi/pdf/10.1002/2017JC013242.

IVEY, G. N. & IMBERGER, J. 1991 On the Nature of Turbulence in a Stratified Fluid. Part I: The Energetics of Mixing. *Journal of Physical Oceanography* **21** (5), 650–658.

KARIMPOUR, FARID & VENAYAGAMOORTHY, SUBHAS KARAN 2015 On turbulent mixing in stably stratified wall-bounded flows. *Physics of Fluids* **27** (4), 046603.

KE, JUNHAO, WILLIAMSON, N., ARMFIELD, S. W., KOMIYA, A. & NORRIS, S. E. 2021 High Grashof number turbulent natural convection on an infinite vertical wall. *Journal of Fluid Mechanics* **929**, publisher: Cambridge University Press.

KE, JUNHAO, WILLIAMSON, N., ARMFIELD, S. W., MCBAIN, G. D. & NORRIS, S. E. 2019 Stability of a temporally evolving natural convection boundary layer on an isothermal wall. *Journal of Fluid Mechanics* **877**, 1163–1185, publisher: Cambridge University Press.

KE, JUNHAO, WILLIAMSON, N., ARMFIELD, S. W., NORRIS, S. E. & KOMIYA, A. 2020 Law of the wall for a temporally evolving vertical natural convection boundary layer. *Journal of Fluid Mechanics* **902**, publisher: Cambridge University Press.

KIRKPATRICK, MICHAEL P., WILLIAMSON, N., ARMFIELD, S. W. & ZECEVIC, V. 2019 Evolution of thermally stratified turbulent open channel flow after removal of the heat source. *Journal of Fluid Mechanics* **876**, 356–412.

KIRKPATRICK, MICHAEL P., WILLIAMSON, N., ARMFIELD, S. W. & ZECEVIC, V. 2020 Destratification of thermally stratified turbulent open-channel flow by surface cooling. *Journal of Fluid Mechanics* **899**, A29.

KOMORI, SATORU, UEDA, HIROMASA, OGINO, FUMIMARU & MIZUSHINA, TOKURO 1983 Turbulence structure in stably stratified open-channel flow. *Journal of Fluid Mechanics* **130** (-1), 13.

LEWIN, S.F. & CAULFIELD, C.P. 2021 The influence of far field stratification on shear-induced turbulent mixing. *Journal of Fluid Mechanics* **928**, A20.

LEWIN, S. F. & CAULFIELD, C. P. 2022 Stratified turbulent mixing in oscillating shear flows. *Journal of Fluid Mechanics* **944**, publisher: Cambridge University Press.

LINDBORG, ERIK 2006 The energy cascade in a strongly stratified fluid. *Journal of Fluid Mechanics* **550** (-1), 207.

LORENZ, EDWARD N. 1955 Available Potential Energy and the Maintenance of the General Circulation. *Tellus* **7** (2), 157–167, _eprint: https://onlinelibrary.wiley.com/doi/pdf/10.1111/j.2153-3490.1955.tb01148.x.

LOZOVATSKY, I. D. & FERNANDO, H. J. S. 2013 Mixing efficiency in natural flows. *Philosophical Transactions of the Royal Society A: Mathematical, Physical and Engineering Sciences* **371** (1982), 20120213, publisher: Royal Society.

MAFFIOLI, ANDREA 2017 Vertical spectra of stratified turbulence at large horizontal scales. *Physical Review Fluids* **2** (10), 104802.

MAFFIOLI, ANDREA 2019 Asymmetry of vertical buoyancy gradient in stratified turbulence. *Journal of Fluid Mechanics* **870**, 266–289.

MAFFIOLI, A., BRETHOUWER, G. & LINDBORG, E. 2016 Mixing efficiency in stratified turbulence. *Journal of Fluid Mechanics* **794**, R3.

MAFFIOLI, A. & DAVIDSON, P. A. 2016 Dynamics of stratified turbulence decaying from a high buoyancy Reynolds number. *Journal of Fluid Mechanics* **786**, 210–233.

MASHAYEK, A., CAULFIELD, C. P. & ALFORD, M. H. 2021 Goldilocks mixing in oceanic shear-induced turbulent overturns. *Journal of Fluid Mechanics* **928**, publisher: Cambridge University Press.

MASHAYEK, A., CAULFIELD, C. P. & PELTIER, W. R. 2013 Time-dependent, non-monotonic mixing in stratified turbulent shear flows: implications for oceanographic estimates of buoyancy flux. *Journal of Fluid Mechanics* **736**, 570–593.

MASHAYEK, A., CAULFIELD, C. P. & PELTIER, W. R. 2017 Role of overturns in optimal mixing in stratified mixing layers. *Journal of Fluid Mechanics* **826**, 522–552, publisher: Cambridge University Press.

MATER, BENJAMIN D., SCHAAD, SIMON M. & VENAYAGAMOORTHY, SUBHAS KARAN 2013 Relevance of the Thorpe length scale in stably stratified turbulence. *Physics of Fluids* **25** (7), 076604.

MATER, BENJAMIN D. & VENAYAGAMOORTHY, SUBHAS KARAN 2014 A unifying framework for parameterizing stably stratified shear-flow turbulence. *Physics of Fluids* **26** (3), 036601.

MILES, JOHN W. 1961 On the stability of heterogeneous shear flows. *Journal of Fluid Mechanics* **10** (4), 496–508, publisher: Cambridge University Press.

MOSER, ROBERT D., KIM, JOHN & MANSOUR, NAGI N. 1999 Direct numerical simulation of turbulent channel flow up to ReT=590. *Physics of Fluids* **11** (4), 943–945, publisher:

American Institute of Physics.

MOUM, J. N. & NASH, J. D. 2009 Mixing Measurements on an Equatorial Ocean Mooring. *Journal of Atmospheric and Oceanic Technology* **26** (2), 317–336, publisher: American Meteorological Society Section: Journal of Atmospheric and Oceanic Technology.

MÉTAIS, OLIVIER & HERRING, JACKSON R. 1989 Numerical simulations of freely evolving turbulence in stably stratified fluids. *Journal of Fluid Mechanics* **202**, 117–148.

NIEUWSTADT, F. T. M. 1984 Some aspects of the turbulent stable boundary layer. *Boundary-Layer Meteorology* **30** (1), 31–55.

NORRIS, STUART EDWARD 2000 A Parallel Navier Stokes Solver for Natural Convection and Free Surface Flow. Thesis, accepted: 2006-03-24.

OGLETHORPE, R. L. F., CAULFIELD, C. P. & WOODS, ANDREW W. 2013 Spontaneous layering in stratified turbulent Taylor–Couette flow. *Journal of Fluid Mechanics* **721**, publisher: Cambridge University Press.

OSBORN, T. R. 1980 Estimates of the Local Rate of Vertical Diffusion from Dissipation Measurements. *Journal of Physical Oceanography* **10** (1), 83–89.

OSBORN, THOMAS R. & COX, CHARLES S. 1972 Oceanic fine structure. *Geophysical and Astrophysical Fluid Dynamics* **3**, 321–345.

PELTIER, W. R. & CAULFIELD, C. P. 2003 Mixing efficiency in stratified shear flows. *Annual Review of Fluid Mechanics* **35** (1), 135–167.

POPE, STEPHEN B. 2000 *Turbulent Flows*. Cambridge: Cambridge University Press.

PORTWOOD, G. D., DE BRUYN KOPS, S. M. & CAULFIELD, C. P. 2019 Asymptotic Dynamics of High Dynamic Range Stratified Turbulence. *Phys. Rev. Lett.* **122** (19), 194504, publisher: American Physical Society.

PORTWOOD, G. D., DE BRUYN KOPS, S. M., TAYLOR, J. R., SALEHIPOUR, H. & CAULFIELD, C. P. 2016 Robust identification of dynamically distinct regions in stratified turbulence. *Journal of Fluid Mechanics* **807**, R2.

RILEY, JAMES J. & DEBRUYNKOPS, STEPHEN M. 2003 Dynamics of turbulence strongly influenced by buoyancy. *Physics of Fluids* **15** (7), 2047–2059.

RILEY, JAMES J. & LELONG, MARIE-PASCALE 2000 Fluid Motions in the Presence of Strong Stable Stratification. *Annual Review of Fluid Mechanics* **32** (1), 613–657.

RILEY, JAMES J. & LINDBORG, ERIK 2008 Stratified Turbulence: A Possible Interpretation of Some Geophysical Turbulence Measurements. *Journal of the Atmospheric Sciences* **65** (7), 2416–2424.

ROGALLO, R. S. 1981 Numerical experiments in homogeneous turbulence. *NASA STI/Recon Technical Report N* **81**.

ROHR, J. J., ITSWEIRE, E. C., HELLAND, K. N. & ATTA, C. W. VAN 1988 Growth and decay of turbulence in a stably stratified shear flow. *Journal of Fluid Mechanics* **195**, 77–111, publisher: Cambridge University Press.

SALEHIPOUR, HESAM & PELTIER, W. R. 2015 Diapycnal diffusivity, turbulent Prandtl number and mixing efficiency in Boussinesq stratified turbulence. *Journal of Fluid Mechanics* **775**, 464–500.

SALEHIPOUR, HESAM, PELTIER, W. R. & CAULFIELD, C. P. 2018 Self-organized criticality of turbulence in strongly stratified mixing layers. *Journal of Fluid Mechanics* **856**, 228–256, publisher: Cambridge University Press.

SALEHIPOUR, H., PELTIER, W. R. & MASHAYEK, A. 2015 Turbulent diapycnal mixing in stratified shear flows: the influence of Prandtl number on mixing efficiency and transition at high Reynolds number. *Journal of Fluid Mechanics* **773**, 178–223, publisher: Cambridge University Press.

SALEHIPOUR, H., PELTIER, W. R., WHALEN, C. B. & MACKINNON, J. A. 2016 A new characterization of the turbulent diapycnal diffusivities of mass and momentum in the ocean. *Geophysical Research Letters* **43** (7), 3370–3379, _eprint: https://agupubs.onlinelibrary.wiley.com/doi/pdf/10.1002/2016GL068184.

SCOTTI, ALBERTO & WHITE, BRIAN 2014 Diagnosing mixing in stratified turbulent flows with a locally defined available potential energy. *Journal of Fluid Mechanics* **740**, 114–135, publisher: Cambridge University Press.

SCOTTI, ALBERTO & WHITE, BRIAN 2016 The Mixing Efficiency of Stratified Turbulent Boundary Layers. *Journal of Physical Oceanography* **46** (10), 3181–3191, publisher: American Meteorological Society Section: Journal of Physical Oceanography.

SHIH, LUCINDA H., KOSEFF, JEFFREY R., FERZIGER, JOEL H. & REHMANN, CHRIS R. 2000 Scaling and parameterization of stratified homogeneous turbulent shear flow. *Journal*

of Fluid Mechanics **412**, 1–20.

SHIH, LUCINDA H., KOSEFF, JEFFREY R., IVEY, GREGORY N. & FERZIGER, JOEL H. 2005 Parameterization of turbulent fluxes and scales using homogeneous sheared stably stratified turbulence simulations. *Journal of Fluid Mechanics* **525**, 193–214.

SMITH, KATHERINE M., CAULFIELD, C. P. & TAYLOR, J. R. 2021 Turbulence in forced stratified shear flows. *Journal of Fluid Mechanics* **910**, publisher: Cambridge University Press.

SMYTH, WILLIAM D. & MOUM, JAMES N. 2000 Length scales of turbulence in stably stratified mixing layers. *Physics of Fluids* **12** (6), 1327–1342.

SMYTH, W. D., MOUM, J. N. & CALDWELL, D. R. 2001 The Efficiency of Mixing in Turbulent Patches: Inferences from Direct Simulations and Microstructure Observations. *Journal of Physical Oceanography* **31** (8), 1969–1992, publisher: American Meteorological Society.

SMYTH, W. D., NASH, J. D. & MOUM, J. N. 2019 Self-organized criticality in geophysical turbulence. *Scientific Reports* **9** (1), 3747.

SORBJAN, ZBIGNIEW 1986 On similarity in the atmospheric boundary layer. *Boundary-Layer Meteorology* **34** (4), 377–397.

TAYLOR, J. R., DE BRUYN KOPS, S. M., CAULFIELD, C. P. & LINDEN, P. F. 2019 Testing the Assumptions Underlying Ocean Mixing Methodologies Using Direct Numerical Simulations. *Journal of Physical Oceanography* **49** (11), 2761–2779.

TAYLOR, JOHN R., SARKAR, SUTANU & ARMENIO, VINCENZO 2005 Large eddy simulation of stably stratified open channel flow. *Physics of Fluids* **17** (11), 116602.

THORPE, S. A. 1973 Experiments on instability and turbulence in a stratified shear flow. *Journal of Fluid Mechanics* **61** (4), 731–751, publisher: Cambridge University Press.

THORPE, S. A. & LIU, ZHIYU 2009 Marginal Instability? *Journal of Physical Oceanography* **39** (9), 2373–2381, publisher: American Meteorological Society Section: Journal of Physical Oceanography.

THORPE, S. A., SMYTH, W. D. & LI, LIN 2013 The effect of small viscosity and diffusivity on the marginal stability of stably stratified shear flows. *Journal of Fluid Mechanics* **731**, 461–476, publisher: Cambridge University Press.

TURNER, LISA & ERSKINE, WAYNE D. 2005 Variability in the development, persistence and breakdown of thermal, oxygen and salt stratification on regulated rivers of southeastern Australia. *River Research and Applications* **21** (2-3), 151–168, _eprint: https://onlinelibrary.wiley.com/doi/pdf/10.1002/rra.838.

VANDINE, ALEXANDRA, PHAM, HIEU T. & SARKAR, SUTANU 2021 Turbulent shear layers in a uniformly stratified background: DNS at high Reynolds number. *Journal of Fluid Mechanics* **916**, publisher: Cambridge University Press.

VENAYAGAMOORTHY, SUBHAS K. & KOSEFF, JEFFREY R. 2016 On the flux Richardson number in stably stratified turbulence. *Journal of Fluid Mechanics* **798**, R1.

VENAYAGAMOORTHY, SUBHAS K. & STRETCH, DEREK D. 2006 Lagrangian mixing in decaying stably stratified turbulence. *Journal of Fluid Mechanics* **564**, 197.

VENAYAGAMOORTHY, SUBHAS K. & STRETCH, DEREK D. 2010 On the turbulent Prandtl number in homogeneous stably stratified turbulence. *Journal of Fluid Mechanics* **644**, 359–369.

VERTESSY, ROBERT, BARMA, DAREN, BAUMGARTNER, LEE, MITROVIC, SIMON, SHELDON, FRAN & BOND, NICK 2019 *Independent assessment of the 2018-19 fish deaths in the Lower Darling: Final report*. Australia: Australian Government.

WAITE, MICHAEL L. 2011 Stratified turbulence at the buoyancy scale. *Physics of Fluids* **23** (6), 066602.

WATANABE, TOMOAKI, RILEY, JAMES J., DE BRUYN KOPS, STEPHEN M., DIAMESSIS, PETER J. & ZHOU, QI 2016 Turbulent/non-turbulent interfaces in wakes in stably stratified fluids. *Journal of Fluid Mechanics* **797**, R1.

WATERHOUSE, AMY F., MACKINNON, JENNIFER A., NASH, JONATHAN D., ALFORD, MATTHEW H., KUNZE, ERIC, SIMMONS, HARPER L., POLZIN, KURT L., LAURENT, LOUIS C. ST, SUN, OLIVER M., PINKEL, ROBERT, TALLEY, LYNNE D., WHALEN, CAITLIN B., HUUSSEN, TYCHO N., CARTER, GLENN S., FER, ILKER, WATERMAN, STEPHANIE, GARABATO, ALBERTO C. NAVEIRA, SANFORD, THOMAS B. & LEE, CRAIG M. 2014 Global Patterns of Diapycnal Mixing from Measurements of the Turbulent Dissipation Rate. *Journal of Physical Oceanography* **44** (7), 1854–1872, publisher: American Meteorological Society Section: Journal of Physical Oceanography.

WEBSTER, I. T., JONES, G., OLIVER, R. L., BORMANS, M. & SHERMAN, B. S. 1996 Control strategies for cyanobacterial blooms in weir pools. Final grant report to the National Resource Management Strategy .

VAN DE WIEL, B. J. H., MOENE, A. F. & JONKER, H. J. J. 2012 The Cessation of Continuous Turbulence as Precursor of the Very Stable Nocturnal Boundary Layer. *Journal of the Atmospheric Sciences* **69** (11), 3097–3115.

VAN DE WIEL, B. J. H., RONDA, R. J., MOENE, A. F., DE BRUIN, H. A. R. & HOLTSLAG, A. A. M. 2002 Intermittent Turbulence and Oscillations in the Stable Boundary Layer over Land. Part I: A Bulk Model. *Journal of the Atmospheric Sciences* **59** (5), 942–958.

WILLIAMSON, N., ARMFIELD, S. W., KIRKPATRICK, M. P. & NORRIS, S. E. 2015 Transition to stably stratified states in open channel flow with radiative surface heating. *Journal of Fluid Mechanics* **766**, 528–555.

WINTERS, KRAIG B., LOMBARD, PETER N., RILEY, JAMES J. & D'ASARO, ERIC A. 1995 Available potential energy and mixing in density-stratified fluids. *Journal of Fluid Mechanics* **289**, 115–128.

ZHOU, QI, TAYLOR, JOHN R. & CAULFIELD, C. P. 2017*a* Self-similar mixing in stratified plane Couette flow for varying Prandtl number. *Journal of Fluid Mechanics* **820**, 86–120.

ZHOU, QI, TAYLOR, J. R., CAULFIELD, C. P. & LINDEN, P. F. 2017*b* Diapycnal mixing in layered stratified plane Couette flow quantified in a tracer-based coordinate. *Journal of Fluid Mechanics* **823**, 198–229, publisher: Cambridge University Press.

1 Appendix A

Something